



北京大学

博士研究生学位论文

题目： 奇异态强子在 LHCb 上的寻找以及电磁量能二期升级模拟

姓 名： 许泽华

学 号： 1601111861

院 系： 物理学院

专 业： 粒子物理与原子核物理

研究方向： 高能实验物理

导 师： 高原宁教授

二〇二一年六月



Exotic Hadrons Searching at LHCb and ECAL Simulation Study for Upgrade II

Dissertation Submitted to
Peking University
in partial fulfillment of the requirement
for the degree of
Doctor of Philosophy
in
Physics
by
Zehua Xu

Dissertation Supervisor : Professor GAO Yuanning

June, 2021

版权声明

任何收存和保管本论文各种版本的单位和个人，未经本论文作者同意，不得将本论文转借他人，亦不得随意复制、抄录、拍照或以任何方式传播。否则一旦引起有碍作者著作权之问题，将可能承担法律责任。

摘要

关键词：其一，其二

Exotic Hadrons Searching at LHCb and ECAL Simulation

Study for Upgrade II

Zehua Xu (High Energy Physics)

Directed by Prof. Gao Yunning

ABSTRACT

Exotic hadrons, with quark configurations other than three quarks or quark-antiquark, are capable of revealing new or hidden aspects of the dynamics of the strong interactions, which is described by quantum chromodynamics. This dissertation examines the experimental evidences of exotic states over the decades, especially some results and potential studies at LHCb. Besides, some theoretical explanations to exotic hadrons are also simply investigated.

More than twenty non-standard hadrons that contain $c\bar{c}$ or $b\bar{b}$ quarks have been found and studied, among which charged states like $Z_c(3900)^+$ and $Z_c(4430)^+$ are smoking-gun evidence for tetraquark exotic states, because light quarks are apparent to account for the non-zero electric charge, in addition to the heavy quarkonium. Previously, only the u or d were observed to constitute the light quarks in such charged exotic states. For the first time, we observe two Z_{cs}^+ states decaying into $J/\psi K^+$ and several X states decaying into $J/\psi \phi$ from a 6-dimentional amplitude analysis of $B^+ \rightarrow J/\psi \phi K^+$ decays by using the data sample collected at LHCb during Run 1 and Run 2. The most significant states are $1^+ Z_{cs}(4000)^+$ hadron with a width of $131 \pm 15 \pm 26$ MeV and $1^{++} X(4685)$ state, and both states present a significance over 15σ . It should also be mentioned that four $X \rightarrow J/\psi \phi$ states previously observed by LHCb and their J^{PC} measurements are also confirmed.

Open-charm pentaquark will open a major new window in exotic hadron study, thus searching for this kind of state is performed in $\Lambda_b^0 \rightarrow \Lambda_c^+ K^+ K^- \pi^-$ decay through a data sample of proton-proton collisions at centre-of-mass energies of $\sqrt{s} = 7$ and 8 TeV collected by the LHCb detector. However, no obvious open-charm pentaquark structure appeared, so this dissertation reports the first observation of $\Lambda_b^0 \rightarrow \Lambda_c^+ K^+ K^- \pi^-$ decay. The ratio of branching fractions between the $\Lambda_b^0 \rightarrow \Lambda_c^+ K^+ K^- \pi^-$ and the $\Lambda_b^0 \rightarrow \Lambda_c^+ D_s^-$ decays is measured to be $\mathcal{B}(\Lambda_b^0 \rightarrow \Lambda_c^+ K^+ K^- \pi^-) / \mathcal{B}(\Lambda_b^0 \rightarrow \Lambda_c^+ D_s^-) = (9.26 \pm 0.29 \pm 0.46 \pm 0.26) \times 10^{-2}$, where the first uncertainty is statistical, the second systematic and the third is due to the knowledge of the

$D_s^- \rightarrow K^+ K^- \pi^-$ branching fraction.

The LHCb spectrometer will run in uttermost high luminosity situation after Upgrade II, which will provide the opportunity to investigate many open questions in flavour physics. However, high luminosity will deteriorate particle reconstruction ability of LHCb detectors, especially for ECAL. In view of this situation, a parameterized simulation tool was developed to study the impact of high luminosity in several physics decay channels containing γ or π^0 . It was found that small cell size and precision timing can not only play an important role in counteracting the overlapping effect, but also improve the mass resolution and reconstruction efficiency for B-mesons. Subsequently, a standalone simulation framework for multi-layer silicon-tungsten (Si-W) ECAL was constructed. Via the simulation, the Si-W ECAL performs well in some physics channels with high luminosity situation, and conclusions obtained from parameterized simulation were verified as well. In consideration of the cost, the idea to measure time using 3 Si-W layers is also proposed.

KEYWORDS: Exotic hadrons, LHCb, Z_{cs} , Pentaquark, ECAL

Contents

Chapter 1 Introduction	1
1.1 Derivation	1
1.1.1 The standard model	1
1.1.2 Quark model and QCD	2
1.1.3 Multiquark states	6
1.2 Experimental evidences of heavy-flavour multiquark candidates	7
1.2.1 Neutral X and Y multiquark candidates	7
1.2.2 Charged multiquark candidates Z_c and Z_{cs}	18
1.2.3 Pentaquark candidates	23
1.3 Theoretical models of multiquark states	26
1.3.1 Multiquark states as molecules	26
1.3.2 Chromomagnetic interaction	27
1.3.3 Hadrocharmonium	27
1.3.4 Rescattering-induced kinematic effects	27
Chapter 2 LHC and LHCb	29
2.1 The large hadron collider	29
2.2 The LHCb detector	32
2.2.1 Tracking	34
2.2.2 Particle identification	40
2.2.3 Trigger	45
Chapter 3 Observation of Z_{cs} states in $B^+ \rightarrow J/\psi \phi K^+$ decay	51
3.1 Study motivation	51
3.1.1 Previous studies	51
3.1.2 This analysis	51
3.2 Selection	52
3.2.1 Dataset	52
3.2.2 Reconstruction and pre-selection	52
3.2.3 Multivariate analysis	55
3.3 Invariant B mass fit and Dalitz plot distributions	57

3.3.1	Signal yields	57
3.3.2	Non- ϕ background fraction	60
3.4	The amplitude fitting formula	65
3.4.1	Helicity formalism and notation	65
3.4.2	Matrix element for the $K^{*+} \rightarrow \phi K^+$ decay chain	69
3.4.3	Matrix element for the $Z^+ \rightarrow \psi K^+$ chain	73
3.4.4	Matrix element for the $X \rightarrow \psi\phi$ chain	75
3.4.5	Usage of LS couplings	78
3.4.6	$cFit$ technique	80
3.5	The amplitude fitting results	85
3.5.1	Kaon excitations in $B^+ \rightarrow J/\psi \phi K^+$	85
3.5.2	Changes to the previous amplitude model	85
3.5.3	Nominal amplitude model	90
3.5.4	Extended K^* model	91
3.5.5	Flatté function for the $X(4140)$ and $Z_{cs}(4000)$ components	97
3.6	Spin and parity study	102
3.7	Argand diagrams	105
3.8	Systematic uncertainties	105
3.9	Conclusions	109
Chapter 4	Open-charm pentaquark search in $\Lambda_b^0 \rightarrow \Lambda_c^+ K^+ K^- \pi^-$ decay	115
4.1	Study motivation	115
4.2	Selection	116
4.2.1	Dataset	116
4.2.2	Preselection	117
4.2.3	Removal of internal track clone candidates	120
4.2.4	Multiple candidates	121
4.2.5	Multivariate Analysis	121
4.2.6	Potential Resonances	126
4.3	Signal extraction	126
4.3.1	Fit description	126
4.3.2	Signal shape	127
4.3.3	Physics background	128
4.3.4	Combinatorial background	129

4.3.5	Fit results	130
4.4	Tuning MC sample	131
4.4.1	IP smearing	131
4.4.2	p_T , y , nTracks reweight	131
4.4.3	Λ_c^+ Dalitz reweight	133
4.4.4	Λ_c^+ polarization	133
4.4.5	Resonances in $\Lambda_b^0 \rightarrow \Lambda_c^+ K^+ K^- \pi^-$	135
4.4.6	Check the Reweighting	137
4.5	Efficiency	138
4.5.1	Geometrical acceptance	139
4.5.2	Reconstruction, selection and HLT efficiency	139
4.5.3	Tracking efficiency	140
4.5.4	L0 Trigger efficiency	140
4.5.5	PID selection efficiency	140
4.6	Branching fraction	140
4.7	Systematic	141
4.7.1	Background model	141
4.7.2	Signal model	141
4.7.3	MC statistics	142
4.7.4	p_T , y and nTracks reweight	142
4.7.5	Dalitz reweight	143
4.7.6	Trigger efficiency	143
4.7.7	PID efficiency	143
4.7.8	$\Lambda_c^+ \pi$, $K^+ K^-$ and $\Lambda_c^+ K^+ K^-$ mass inconsistency and Λ_b^0 IP smearing	144
4.7.9	Physical background effect	144
4.7.10	$\Lambda_b^0 \rightarrow \Lambda_c^+ K^+ K^- \pi^-$ in normalization channel	145
4.7.11	Fraction of different MC sample	145
4.8	Conclusion	145
Chapter 5	ECAL simulation study for Upgrade II	147
5.1	Introduction	147
5.2	Parameterized simulation	147
5.2.1	Parameterization of shower	148
5.2.2	Reconstruction and calibration	149

5.2.3	Neutral particle identification	150
5.2.4	Performance in $B_s^0 \rightarrow \phi\gamma$ decay	155
5.2.5	Performance in $B_s^0 \rightarrow J/\psi\pi^0$ decay	160
5.2.6	From parameterized simulation to GEANT4 simulation	163
5.3	Silicon-tungsten ECAL simulation	164
5.3.1	Simulation model in GEANT4	164
5.3.2	Reconstruction and calibration	167
5.3.3	Physical performance with silicon of different thickness	173
5.3.4	Bremsstrahlung recovery and $B^0 \rightarrow K^*e^-e^+$ performance	175
5.4	Conclusions	177
Chapter 6	Summary and Implication	179
6.1	Exotic hadrons study at LHCb	179
6.2	ECAL simulation for Upgrade II at LHCb	180
Appendix A	Hiddern-charm pentaquark states in $\Lambda_b^0 \rightarrow J/\psi pK^-$ decay	181
A.1	Selection	181
A.1.1	Reconstruction and pre-selection	181
A.1.2	Multivariate analysis	182
A.2	One dimentional fit and mass resolution	184
Appendix B	Evidence of pentaquark states in $\Lambda_b^0 \rightarrow J/\psi p\pi^-$ decay	187
B.1	Study motivation	187
B.2	Selection	188
B.2.1	Dataset	188
B.2.2	Reconstruction and pre-selection	189
B.2.3	Reflections vetoing	191
B.2.4	Multivariate analysis	191
B.3	Invariant B mass fit and Dalitz plot distributions	193
B.4	Amplitude analysis	195
B.4.1	Likelihood construction with sPlot technique	197
B.4.2	N^* resonances	198
B.4.3	Parameters describing the P_c^+ states	200
Appendix C	Z_{cs} states in $B^+ \rightarrow J/\psi\phi K^+$ decay	201
C.1	Angular moments	201

C.2 Model-independent	201
C.3 Check on the non- ϕ sideband	207
C.4 Kmatix model	208
C.5 Check of the background PDF on B mass sidebands	209
References	213
Acknowledgements	223
Vita	225
Declaration	227

List fo Figures

1.1	The elementary particle in the standard model.	1
1.2	The particle zoo before 1964.	2
1.3	Summary of measurements of $\alpha_s(Q)$ as a function of hte respective energy scale Q. Figure taken from Ref. 52	5
1.4	The level scheme of meson states containing a minimal quark content $c\bar{c}$. The name of a state is determined by its quantum number $I^G J^{PC}$. The arrows indicate the most dominate hadronic transitions. Taken from Ref. [127].	7
1.5	Signal-band projections of (a) M_{bc} , (b) $\Delta E_{c.m.}$, and (c) $M(\pi^+\pi^-J/\psi)$ distributions in signal region with the results of the unbinned fit ^[71]	8
1.6	The log-likelihood ratio distribution between 1^{++} and 2^{-+} is shown above, a Gaussian fit to the 2^{-+} distribution is performed ^[3]	8
1.7	The decay $X(3915) \rightarrow \omega J/\psi$ states in $B \rightarrow K\omega J/\psi$ decay from Belle ^[53] (left), and BaBar ^[41] (right).	10
1.8	The $\Delta M = M(J/\psi\phi) - M(J/\psi)$ distribution of $B^+ \rightarrow J/\psi\phi K^+$ decays candidates from CDF experiment in left ^[24] ; The number of $B^+ \rightarrow J/\psi\phi K^+$ candidates as a function of $\Delta m = m(\mu^+\mu^-K^+K^-) - m(\mu^+\mu^-)$ at CMS in right ^[26]	11
1.9	The $\Delta M = M(J/\psi\phi) - M(J/\psi)$ distribution of $B^+ \rightarrow J/\psi\phi K^+$ decays candidates from CDF experiment in left ^[24] ; The number of $B^+ \rightarrow J/\psi\phi K^+$ candidates as a function of $\Delta m = m(\mu^+\mu^-K^+K^-) - m(\mu^+\mu^-)$ at CMS in right ^[26]	12
1.10	Distributions of ϕK^+ (left) and $J/\psi\phi$ (right) invariant masses for the $B^+ \rightarrow J/\psi\phi K^+$ candidates (black data points) compared with the results of the default amplitude fit to the Run 1 data ^[16]	12
1.11	The distribution of masses recoiling from the J/ψ at Belle ^[27] (above). The distribution of masses recoiling from a reconstructed J/ψ and D-meson in $e^+e^- \rightarrow J/\psi DX$ annihilation (bottom left) and $D\bar{D}$ invariant mass distribution (bottom right) ^[130]	14
1.12	The $J/\psi\pi^+\pi^-$ invariant mass distribution in the process $e^+e^- \rightarrow \gamma\pi^+\pi^-J/\psi$ at BaBar ^[47]	16
1.13	The $J/\psi\pi^+\pi^-$ invariant mass distribution in the process $e^+e^- \rightarrow \gamma\pi^+\pi^-J/\psi$ at BaBar ^[47]	17

1.14 The cross section for $e^+e^- \rightarrow \gamma\pi^+\pi^-J/\psi$ at BESIII, right one for "high luminosity" scan, left one is "low luminosity" scan ^[28]	18
1.15 The $M(\psi\pi)$ distribution in $\bar{B} \rightarrow \psi\pi^+K^-$ decay at Belle ^[29] , the $M^2(\psi\pi)$ in $\bar{B} \rightarrow \psi\pi^+K^-$ from LHCb ^[8]	19
1.16 The real and imaginary parts of the amplitude for $Z_c(4430) \rightarrow \psi\pi^+$ decay at LHCb ^[8] , the $Z_c(4200) \rightarrow J/\psi\pi^+$ decay from Belle ^[70]	19
1.17 Distribution of the larger of two $J/\psi\pi^\pm$ masses in $e^+e^- \rightarrow J/\psi\pi^+\pi^-$ events collected in BESIII at $E_{cm} = 4260$ MeV ^[29] (left), The D^0D^{*-} invariant mass distribution in $e^+e^- \rightarrow D^0D^{*-}\pi^+$ events collected in BESIII at $E_{cm} = 4260$ MeV ^[34] (right)	20
1.18 Distribution of the larger of two $h_c\pi^\pm$ masses in $e^+e^- \rightarrow h_c\pi^+\pi^-$ events collected in BESIII at $E_{cm} = 4260$ MeV and $E_{cm} = 4360$ MeV ^[33] (left), The $h_c\pi^0$ invariant mass distribution in $e^+e^- \rightarrow h_c\pi^0\pi^0$ events collected in BESIII at BESIII ^[30] (right)	21
1.19 Simultaneous unbinned maximum likelihood fit to the K^+ recoil-mass spectra in data at 4.681 GeV (left) and 4.628 GeV (right) ^[36]	22
1.20 Dalitz plots for $B^+ \rightarrow J/\psi\phi K^+$ candidates in a region ± 15 MeV around the B^+ mass peak.	22
1.21 Fit projections onto $m_{J/\psi K^+}$ in two slices of $m_{J/\psi\phi}$ for the default model and the default model without the 1^+ Z_{cs} states (left and middle) . Fitted values of the $Z_{cs}(4000)^+$ amplitude in eight $m_{J/\psi K^+}$ bins, shown on an Argand diagram (blue points). The red curve represents the expected Breit-Wigner behaviour between $-1.4\Gamma_0$ to $1.4\Gamma_0$ around the $Z_{cs}(4000)^+$ mass. The green curve is the same as the red curve but the mass is extended to the reachable range in the $B^+ \rightarrow J/\psi\phi K^+$ channel (right).	23
1.22 Dalitz plot of $\Lambda_b^0 \rightarrow J/\psi p K^-$ with Run 1 data sample (left) ^[12] , with Run 1 and Run 2 data sample together (right) ^[19]	24
1.23 Fit projection for $m_{J/\psi p}$ with two P_c states (left) ^[12] . Fit to $m_{J/\psi p}$ distribution with three BW discribed P_c states (right) ^[19]	25
1.24 Projections of the amplitude fit onto $m_{p\pi}$ (left) and $m_{J/\psi p}$ data distribution for $\Lambda_b^0 \rightarrow J/\psi p\pi^-$ decay in LHCb ^[13]	26

2.1	The CERN accelerator complex. The LHC is the last ring (dark grey line) in a complex chain of particle accelerators. The smaller machines are used in a chain to help boost the particles to their final energies and provide beams to a whole set of smaller experiments, which also aim to uncover the mysteries of the Universe ^[94]	30
2.2	Transverse slice through the CMS detector, the particle type can be inferred by combining the detector response in the different subdetectors. ^[125]	31
2.3	View of the LHCb detector ^[39]	33
2.4	Display of $b\bar{b}$ production angles as simulated with PYTHIA 8. The LHCb acceptance is shown in red.	33
2.5	Schematic of the tracking compoents with different types of tracking definitions in the tracking reconstruction ^[10]	35
2.6	Overview of the VELO as seen in the (x, z) plane, at y=0, at top. The front face of the modules in the (x,y) plane, for both closed (left) and oprn (right) positions, at bottom ^[39]	35
2.7	Perspective overview of dipole magnet(units in mm) ^[39]	37
2.8	Overview of the TT (top) and IT (bottom) ^[39]	38
2.9	Left: The three OT stations surrounding the three IT stations (purgple). Right: Overview of the OT bridge carrying the C-frames ^[39]	39
2.10	Sideview of the RICH1 detector (Left) and top view of the RICH2 detector ^[39]	41
2.11	The lateral segmentation of the SPD /PS and ECAL (left) and the HCAL (right) for a quarter of the detector front ^[39]	42
2.12	Shashlik construction of ECAL in the inner zone ^[42]	43
2.13	Sideview of the muon system ^[39]	44
2.14	Flow-diagram of the different trigger sequences ^[39]	45
2.15	Overview of the L0 trigger ^[39]	46
2.16	Track and vertex reconstruction in the HLT1 trigger ^[22]	47
2.17	Track and vertex reconstruction in the HLT2 trigger ^[22]	48
2.18	Dataflow in the upgraded LHCb detector ^[108]	49
3.1	Distributions of $J/\psi K^+$ invariant masses for the $B^+ \rightarrow J/\psi \phi K^+$ candidates (black data points) compared with the results of the default amplitude fit (left) and amplitude fit with a Z_{cs}^+ (right) in Run 1 analysis ^[58] . The Z_{cs}^+ contribution is shown by large black square point.	53

3.2	Discriminating variables used in the MVA training for Run 1	56
3.3	Discriminating variables used in the MVA training for Run 2	56
3.4	(left) ROC curves for different MVA methods and (right) the BDTG output distribution for signals and the background in the training sample and the test sample for Run 1.	58
3.5	(left) ROC curves for different MVA methods and (right) the BDTG output distribution for signals and the background in the training sample and the test sample for Run 2.	58
3.6	Signal significance (arbitrary units) for different cuts on BDTG and track-ghost probability for kaons for Run 1.	58
3.7	Signal significance (arbitrary units) for different cuts on BDTG and track-ghost probability for kaons for Run 2.	59
3.8	FOM versus BDTG, FOM versus ghost probability of kaons for run1 and run2	59
3.9	Invariant mass distribution of the $B^+ \rightarrow J/\psi \phi K^+$ decay and the fitted curve for Run 1 (top) and Run 2 (bottom).	61
3.10	The log scale invariant mass distribution of the $B^+ \rightarrow J/\psi \phi K^+$ decay and the fitted curve for Run 1 (top) and Run 2 (bottom).	62
3.11	Dalitz-plot distribution of $J/\psi \phi$ vs $J/\psi K$, where the background is subtracted by <i>sPlot</i> technique.	63
3.12	Dalitz-plot distribution of $J/\psi \phi$ vs ϕK , where the background is subtracted by <i>sPlot</i> technique.	63
3.13	Dalitz-plot distribution of ϕK vs $J/\psi K$, where the background is subtracted by <i>sPlot</i> technique.	64
3.14	Projections of the 2D fit to m_ϕ vs. $m_{J/\psi K^+ K^-}$ (notice the log scale!). The deep blue line is the total pdf. The red line is the component where phi is background (modelled by phase-space) but B^\pm is signal (hypathia function). The green line is the component where phi is signal (Breit-Wigner) and B^\pm is signal as well. The black line is the component where phi is signal but B^\pm is background (linear polynomial). The light blue line is the component where phi and B^\pm are both background.	64

3.15 Coordinate axes for the spin quantization of particle A (bottom part), chosen to be the helicity frame of A ($\hat{z}_0 \parallel \vec{p}_A$ in the rest frame of its mother particle or in the laboratory frame), together with the polar ($\theta_B^{\{A\}}$) and azimuthal ($\phi_B^{\{A\}}$) angles of the momentum of its daughter B in the B rest frame (top part). Notice that the directions of these coordinate axes, denoted as ($x_0^{\{A\}}$, $y_0^{\{A\}}$ and $z_0^{\{A\}}$), do not change when boosting from the helicity frame of A to its rest frame. After the Euler rotation $\mathcal{R}(\alpha = \phi_B^{\{A\}}, \beta = \theta_B^{\{A\}}, \gamma = 0)$ (see the text), the rotated z axis, $\hat{z}_2^{\{A\}}$, is aligned with the B momentum; thus the rotated coordinates become the helicity frame of B . If B has a sequential decay, then the same boost-rotation process is repeated to define the helicity frame for its daughters.	66
3.16 Definaton of decay angles in the K^* chain.	72
3.17 Definaton of decay angles in the Z^+ chain.	74
3.18 Definaton of decay angles in the X chain.	77
3.19 Parameterized efficiency representation in the Dalitz plane ($m_{J/\psi\phi}^2, m_{\phi K}^2$). Function values corresponding to the color encoding are given on the right. The normalization arbitrarily corresponds to unity when averaged over the phase space.	82
3.20 Parameterized efficiency $\epsilon_2(\cos \theta_\phi m_{\phi K})$, $\epsilon_3(\cos \theta_{J/\psi} m_{\phi K})$, $\epsilon_4(\Delta\phi_{K^*,\phi} m_{\phi K})$, $\epsilon_5(\Delta\phi_{K^*,J/\psi} m_{\phi K})$ functions. Function values corresponding to the color encoding are given on the right. By construction each function integrates to unity at each $m_{\phi K}$ value. The structure in $\epsilon_2(\cos \theta_\phi m_{\phi K})$ present between 1500 and 1600 MeV is an artifact of removing $B^+ \rightarrow J/\psi K^+ K^- K^+$ events in which both $K^+ K^-$ combinations pass the ϕ mass selection window.	83
3.21 Parameterized background representation in the Dalitz plane ($m_{J/\psi\phi}^2, m_{\phi K}^2$). Function values corresponding to the color encoding are given on the right. The normalization arbitrarily corresponds to unity when averaged over the phase space.	83
3.22 Parameterized background functions: $P_{\text{bkg}2}^u(\cos \theta_\phi m_{\phi K})$, $P_{\text{bkg}3}^u(\cos \theta_{J/\psi} m_{\phi K})$, $P_{\text{bkg}4}^u(\Delta\phi_{K^*,\phi} m_{\phi K})$, $P_{\text{bkg}5}^u(\Delta\phi_{K^*,J/\psi} m_{\phi K})$. Function values corresponding to the color encoding are given on the right. By construction each function integrates to unity at each $m_{\phi K}$ value.	84

3.23	Kaon excitations predicted by Godfrey–Isgur ^[Godfrey:1985xj] (horizontal black lines) labeled with their intrinsic quantum numbers: $n^{2S+1}L_J$ (see the text). Well established states are shown with narrower solid blue boxes extending to $\pm 1\sigma$ in mass and labeled with their PDG names ^[126] . Unconfirmed states are shown with dashed green boxes. The long horizontal red lines indicate the ϕK mass range probed in $B^+ \rightarrow J/\psi \phi K^+$ decays.	86
3.24	Fit projections of (a) $m_{\phi K}$, (b) $m_{J/\psi \phi}$, (c) $m_{J/\psi K}$ by fitting Run 1 model to the new Run 1+2 data sample.	89
3.25	Fit projections of (a) $m_{\phi K}$, (b) $m_{J/\psi \phi}$, (c) $m_{J/\psi K}$ from the 9K+5X+2X+2Z model.	92
3.26	Dalitz-plot distributions of signal from the nominal fit model.	93
3.27	Fit projections of $m_{J/\psi K}$ in two slices of $m_{J/\psi \phi}$ from the nominal model (top) and the nominal model without $1^+ Z_{cs}$ (bottom). The narrow Z_{cs} is evident in the two $m_{J/\psi \phi}$ slices. Including $1^+ Z_{cs}$ improve the χ^2/n_{bin} from 85/46 to 48/46 (left slice), and from 97/49 to 47/49 (right slice). Bottom figure shows the two slices of $m_{J/\psi \phi}$ regions.	94
3.28	Fit projections of $m_{J/\psi K}$ from the nominal model without $1^+ Z_{cs}$	97
3.29	Fit projections of angles in the ϕK decay chain.	98
3.30	Fit projections of (a) $m_{\phi K}$, (b) $m_{J/\psi \phi}$, (c) $m_{J/\psi K}$ from the Extended K+5X+2X+2Z model.	99
3.31	Comparison of the standard deviations between the data and the fit model, contributing to χ^2_{2D} value, for (a) the nominal fit, and (b) the fit without the two new X states. Some improvements are seen in (a) at $m^2(J/\psi \phi) = 22 \text{ GeV}^2$, as compared to (b).	100
3.32	The pull distributions of χ^2_{2D} value in Figure. 3.31, The RMS of the pull distribution is smaller when additional X components are introduced.	100
3.33	Projections of $m_{J/\psi \phi}$ from fits of Flatté function for describing $X(4140)$ in different resonance models (a) nominal K and $1^- Z(4220)$, (b) nominal K and $1^+ Z_{cs}(4220)$, (c) extended K and $1^- Z_{cs}(4220)$, (b) extended K and $1^+ Z(4220)$	102
3.34	Lineshapes of Flatté parameterization of the $X(4140)$ resonance.	103
3.35	Projections onto $m_{J/\psi K}$ from the fit with the Flatté function for describing $Z_{cs}(4000)^+$	103

3.36 Fitted values of the $Z_{cs}(4000)^+$ amplitude in eight $m_{J/\psi K^+}$ bins, shown on an Argand diagram (blue points). The red line represents the expected Breit-Wigner behaviour in between $-1.4\Gamma_0$ to $1.4\Gamma_0$ around the $Z_{cs}(4000)^+$ mass. The green line is the reachable mass range in the $B^+ \rightarrow J/\psi \phi K^+$ channel.	105
4.1 Possible Feynman diagrams contributing to the decay of $\Lambda_b^0 \rightarrow \Lambda_c^+ K^- K^+ \pi^-$	116
4.2 The mass distribution of $K^+ K^- \pi^-$ in the background subtracted data and MC	120
4.3 The distribution of the angle between K^- and π^- from the $\Lambda_b^0 \rightarrow \Lambda_c^+ K^- K^+ \pi^-$ decays. The unit of X-axis is rad. The peak near zero is generated from the clone track pairs, most of which has an angle less than 0.5 mrad.	121
4.4 Distributions of variables used in BDTG for $\Lambda_b^0 \rightarrow \Lambda_c^+ K^- K^+ \pi^-$ decays.	123
4.5 Correlation matrix of the training variables with TMVA toolkit for $\Lambda_b^0 \rightarrow \Lambda_c^+ K^- K^+ \pi^-$ decays for the background (left) and the signal (right).	124
4.6 BDTG (left) and MLP (right) distributions for the signal and background for $\Lambda_b^0 \rightarrow \Lambda_c^+ K^- K^+ \pi^-$ decays.	125
4.7 Curves showing the signal and background efficiencies as a function of the BDTG (left) and MLP (right) cut value for signal channel.	125
4.8 ROC curves for different MVA methods for signal channel.	125
4.9 2-D distribution of combined invariant mass.	126
4.10 Signal shape for $\Lambda_b^0 \rightarrow \Lambda_c^+ K^- K^+ \pi^-$ (left) and $\Lambda_b^0 \rightarrow \Lambda_c^+ D_s^-$ (right) in the simulated events.	127
4.11 Shape for $\Lambda_b^0 \rightarrow \Lambda_c^+ D_s^*$ reconstructed as $\Lambda_b^0 \rightarrow \Lambda_c^+ D_s^-$	128
4.12 $\Lambda_b^0 \rightarrow \Lambda_c^+ K^- K^+ \pi^-$ where the $KK\pi$ mass is in the sideband of the D_s^- . The blue line is full fit, the blue dashed line is the combinatorial background, and the red line is the signal shape.	129
4.13 The distribution gained from $\Lambda_b^0 \rightarrow \Sigma_c K^- K^+ \pi^-$ MC sample.	129
4.14 Reconstructed mass distribution for $\Lambda_b^0 \rightarrow \Lambda_c^+ K^- K^+ \pi^-$ candidates. A fit is overlaid, as described in the text. The blue line is full fit, the blue dashed line is the combinatorial background, the green dashed line is $\Lambda_b^0 \rightarrow \Sigma_c K^- K^+ \pi^-$ background and the red dashed line is the signal shape.	130

4.15 Reconstructed mass distributions for $\Lambda_b^0 \rightarrow \Lambda_c^+ D_s^-$ candidates. A fit is overlaid, as described in the text. The blue line is full fit, the blue dashed line is the combinatorial background, the green dashed line is the physical background, the red line is the signal shape, the pink dash line is $\Lambda_b^0 \rightarrow \Lambda_c^+ K^+ K^- \pi^-$ background.	131
4.16 The comparison of background subtracted data and signal MC for and $\Lambda_b^0 \rightarrow \Lambda_c^+ K^+ K^- \pi^-$ (top) and $\Lambda_b^0 \rightarrow \Lambda_c^+ D_s^-$ (bottom), and the s-plot method is used to get the background subtracted data. The red line is the MC signal and blue is data. Left is the distribution before smearing and Right is after smearing.	132
4.17 Relative yields between background-subtracted data and signal MC of $\Lambda_b^0 \rightarrow \Lambda_c^+ \pi^-$ as function of p_T and y of Λ_b^0 baryons. The relative yield in each bin is shown with the color sized Z axis, and it's larger when it goes yellow.	133
4.18 The distribution of invariant mass of combination of Λ_c^+ daughters in $\Lambda_b^0 \rightarrow \Lambda_c^+ D_s^-$ channel	133
4.19 The distribution of invariant mass of combination of Λ_c^+ daughters in $\Lambda_b^0 \rightarrow \Lambda_c^+ K^+ K^- \pi^-$ channel	134
4.20 The distribution of combination invariable mass of Λ_c^+ daughters in $\Lambda_b^0 \rightarrow \Lambda_c^+ D_s^-$ channel (left) and $\Lambda_b^0 \rightarrow \Lambda_c^+ K^+ K^- \pi^-$ channel (right)	134
4.21 The distribution of some polarization angle in normalization channel	135
4.22 The distribution of polarization angle in signal channel	136
4.23 The projection from two dimentions fit, the black points are data, red line is PHSP sample, blue dash line is MC sample with K^* , green dash line is MC sample with $a1$ and blue line is full fit result.	136
4.24 The invariant mass distribution of two body combination for $\Lambda_b^0 \rightarrow \Lambda_c^+ K^+ K^- \pi^-$ in the background subtracted data and MC.	137
4.25 The invariant mass distribution of three body combination for $\Lambda_b^0 \rightarrow \Lambda_c^+ K^+ K^- \pi^-$ in the background subtracted data and MC.	138
4.26 Comparison of variables between background subtracted data and weighted MC in the $\Lambda_b^0 \rightarrow \Lambda_c^+ D_s^-$ channel.	138
4.27 Comparison of variables between background subtracted data and weighted MC in the $\Lambda_b^0 \rightarrow \Lambda_c^+ K^+ K^- \pi^-$ channel.	139

4.28	Invariant mass distributions for the $\Lambda_b^0 \rightarrow \Lambda_c^+ K^+ K^- \pi^-$ sample(left) and $\Lambda_b^0 \rightarrow \Lambda_c^+ D_s^-$ sample(right) with fit and residuals. The signal shape is described by Hypatia function and background shape is the nominal one. The blue line is full fit, the blue dashed line is the combinatorial background, the red line is the signal shape, the pink dashed line is $\Lambda_b^0 \rightarrow \Lambda_c^+ K^+ K^- \pi^-$ background.	142
4.29	Invariant mass distributions for the $\Lambda_b^0 \rightarrow \Lambda_c^+ K^+ K^- \pi^-$ sample. The blue line is full fit, the blue dashed line is the combinatorial background, the red line is the signal shape.	145
5.1	The simulation process in the parameterized simulation.	148
5.2	The difference between the reconstructed energy and generated level energy (left), and the relation between the energy resolution and particle energy after calibration (right).	149
5.3	The relation between the true position and reconstructed position before (left) and after (right) calibration.	150
5.4	The relation between the π^0 energy and the distance of two γ on the ECAL plane.	151
5.5	The distribution of discriminant variables used for cluster identification.	153
5.6	The distribution of BDTG of the signal sample (γ) and background sample (merged π^0).	154
5.7	Performance of different methods used on the simulation samples. The left one presents the performance of γ and π^0 separation with the timing information included, right one with the timing information excluded.	154
5.8	Performance of different methods used on the simulation samples. The left one presents the performance of γ and random overlapping cluster separation with the timing information included, right one with the timing information excluded.	154
5.9	Performance of different methods used on the simulation samples. The left one presents the performance of π^0 and random overlapping cluster separation with the timing information included, right one with the timing information excluded.	155
5.10	The mass distribution of B_s^0 in $B_s^0 \rightarrow \phi\gamma$ decay with different luminosities. .	156
5.11	The diagram of ECAL cell size segmentation proposed by Phillip Roloff for LHCb.	157

5.12 The relation between signal efficiency and combinatorial background rejection fraction with different Δt cuts applied, in Phillip's segmentation (top) and Si-W segmentation (bottom) respectively.	158
5.13 The relation between signal efficiency and significance with different Δt cuts applied, in Phillip's segmentation (top) and Si-W segmentation (bottom) respectively.	159
5.14 The mass distribution of B_s^0 in $B_s^0 \rightarrow J/\psi\pi^0$ decay with different luminosities.	161
5.15 The relation between signal efficiency and combinatorial background rejection fraction with different $R(t)$ cuts applied, in Phillip's segmentation (top) and Si-W segmentation (bottom) respectively.	162
5.16 The relation between signal efficiency and significance with different $R(t)$ cuts applied, in Phillip's segmentation (top) and Si-W segmentation (bottom) respectively.	163
5.17 The simulation process with Si-W ECAL model in GEANT4.	165
5.18 Geometry of the SiW ECAL used in the Geant4 simulation. Displayed is a shower of a 50 GeV photon.	166
5.19 The detection efficiency of sensors for γ with different energy and incident directions to the ECAL plane.	166
5.20 The relation between particle true energy and reconstructed cluster shower energy.	168
5.21 The energy resolution in different particle energy regions.	169
5.22 The seed cell energy fraction for each layer (left). The estimated Moliere radius (right).	169
5.23 Energy resolution of electron showers as a function of the incident electron energy for different thicknesses of the silicon layers. The cell size is $1.0 \times 1.0 \text{ cm}^2$ and the thickness of the tungsten layers is 3.5 mm.	170
5.24 The relative position to the cell between true layer cluster and true layer cluster of the 15th layer (left). The position resolution (right).	171
5.25 The time difference between the seed cell time with the measured value around cells in 9th layer	171
5.26 The time resolution of each layer with different γ energy and incident angle.	172
5.27 The time distribution for each layer before(a) and after(b) calibration.	172
5.28 The time difference measured in each layer.	173

5.29	The shower time resolution with three layers to measure shower time, the right plot shows the low energy result.	173
5.30	Mass distributions of the B_s^0 mesons from $B_s^0 \rightarrow \phi\gamma$ decays. The thickness of silicon sensor is 2 mm, no copper cryostat applied (left). The thickness of silicon sensor is 2 mm, 26 cooling copper plane added against silicon layers.	174
5.31	Mass distributions of the π^0 mesons from $B_s^0 \rightarrow J/\psi\pi^0$ decays. The thickness of silicon sensor is 2 mm, no copper cryostat applied (left). The thickness of silicon sensor is 2 mm, 26 cooling copper plane added against silicon layers.	175
5.32	The B_s^0 mass distribution reconstructed from $B_s^0 \rightarrow J/\psi\pi^0$ decay. The thickness of silicon sensor is 2 mm, no copper cryostat applied (left). The thickness of silicon sensor is 2 mm, 26 cooling copper plane added against silicon layers.	175
5.33	The electron energy(left) and transverse momentum(right) distribution in $B^0 \rightarrow K^*e^-e^+$ decay.	176
5.34	Left: the distance between the electron and bremsstrahlung photon on the ECAL plane; Right: the relation between the electron energy and the x distance on the ECAL plane.	176
5.35	Left: the time difference between the electron and bremsstrahlung photon. Right: the B^0 mass distribution before(blue point) or after bremsstrahlung recovery with time-matching included(red line).	176
A.1	Discriminating variables used in the MVA training of Run 2 sample.	184
A.2	The BDTG output distribution for signals and the background in the training sample and the test sample of Run 2 sample.	185
A.3	The $m_{J/\psi p}$ resolution depended on the mass itself.	186
B.1	Feynman diagrams of the $\Lambda_b^0 \rightarrow P_c\pi$ decay via (left) the external and (right) the internal W^- emissions.	187
B.2	Feynman diagram of $\Lambda_b^0 \rightarrow P_c^+M$ via the charmless $b \rightarrow u\bar{u}q$ transition suggested by Ref. [98], where $M(q)$ can be $K^-(s)$ or $\pi^-(d)$	188
B.3	Invariant mass distributions of the $\Lambda_b^0 \rightarrow J/\psi p\pi^-$ candidate with the p and the π^- assumed to be other hadrons for those Λ_b^0 candidates in the ± 20 MeV/ c^2 mass window around the know Λ_b^0 mass. The lablels $h \rightarrow h'$ indicate that the h hadron in the $\Lambda_b^0 \rightarrow J/\psi p\pi^-$ decay is assumed as a h' hadron.	192
B.4	Discriminating variables used in the MVA training of Run 1 sample.	194

B.5	The BDTG output distribution for signals and the background in the training sample and the test sample of Run 1(left) and Run 2(right) samples.	195
B.6	Signal significance (arbitrary unit) for different BDTG cut values of Run 1(left) and Run 2(right) samples.	195
B.7	Distribution of the invariant mass of $\Lambda_b^0 \rightarrow J/\psi p K^-$ candidates reconstructed as $\Lambda_b^0 \rightarrow J/\psi p \pi^-$	195
B.8	Invariant mass distribution of the $\Lambda_b^0 \rightarrow J/\psi p \pi^-$ decay and the fitted curve for Run 1(left) and Run 2(right) samples.	196
B.9	Invariant mass squared of $p\pi$ versus either $J/\psi p$ (top) or $J/\psi \pi$ (bottom) for candidates with <i>sWeights</i> to subtract background contribution. The hatched area shows the kinematic allowed region.	196
C.1	Angular moments of $J/\psi \phi$ helicity angle as a function of $m_{J/\psi \phi}$ compared between the background subtracted data, and PDFs from run1 model (blue dashed) and the nominal model (red solid). The $\chi^2/nbin$ for the fit of nominal model (run1 model) are 83(136)/69, 59(117)/35, 48(89)/35, 33(89)/35, 42(81)/35, 55(65)/35 for order from 0 to 5, respectively.	202
C.2	Signal angular moments of ϕK helicity angle as a function of $m_{\phi K}$ compared between the background subtracted data, and PDFs from run1 model (blue dashed) and the nominal model (red solid). The $\chi^2/nbin$ for the fit of nominal model (run1 model) are 66(79)/69, 37(86)/35, 49(48)/35, 35(59)/35, 46(44)/35, 36(74)/35 for order from 0 to 5, respectively.	202
C.3	Angular moments of $J/\psi K$ helicity angle as a function of $m_{\phi K}$ compared between the background subtracted data, and PDFs from run1 model (blue dashed) and the nominal model (red solid). The $\chi^2/nbin$ for the fit of nominal model (run1 model) are 77(138)/69, 50(108)/35, 30(75)/35, 60(81)/35, 31(41)/35, 44(68)/35 for order from 0 to 5, respectively.	203
C.4	(a) Amplitude squared and (b) phase motion for $1^+ Z$ wave obtained from the model-independent method (red open) and the nominal BW-sum fit (black solid). The BW-sum model has poles at $M_0 - i\Gamma_0/2 = 4003 - i 131/2$ and $4216 - i 233/2$ MeV, obtained from sum of the lowest L waves for a reference.	204

C.5 Argand plot of $1^+ Z$ waves obtained from the model-independent method (red open) and the nominal BW-sum fit (black solid). The BW-sum model has poles at $M_0 - i\Gamma_0/2 = 4003 - i 131/2$ and $4216 - i 233/2$ MeV, obtained from sum of the lowest L waves for a reference.	204
C.6 (a) Amplitude squared and (b) phase motion for $1^+ X$ lowest L wave obtained from the model-independent method (red open) and the nominal BW-sum fit (black solid). The BW-sum model has poles at $M_0 - i\Gamma_0/2 = 4118 - i 162/2$, $4294 - i 53/2$ and $4684 - i 126/2$ MeV, obtained from sum of the lowest L waves for a reference.	204
C.7 (a) Amplitude squared and (b) phase motion for $0^+ X$ lowest L wave obtained from the model-independent method (red open) and the nominal BW-sum fit (black solid). The BW-sum model has poles at $M_0 - i\Gamma_0/2 = 4474 - i 77/2$, $4694 - i 87/2$ MeV and the NR contribution, obtained from sum of the lowest L waves for a reference.	205
C.8 (Left) Argand plot of $1^+ X$ waves obtained from the model-independent method (red open) and the nominal BW-sum fit (black solid). The BW-sum model has poles at $M_0 - i\Gamma_0/2 = 4118 - i 162/2$, $4294 - i 53/2$ and $4684 - i 126/2$ MeV, obtained from sum of the lowest L waves for a reference. (Right) Argand plot of $0^+ X$ waves obtained from the model-independent method (red open) and the nominal BW-sum fit (black solid). The BW-sum model has poles at $M_0 - i\Gamma_0/2 = 4118 - i 162/2$, $4294 - i 53/2$ and $4684 - i 126/2$ MeV, obtained from sum of the lowest L waves for a reference.	205
C.9 (a) Amplitude squared and (b) phase motion for $1^- X$ wave obtained from the model-independent method (red open) and the nominal BW-sum fit (black solid). The BW-sum model has one pole at $M_0 - i\Gamma_0/2 = 4626 - i 174/2$ MeV.	205
C.10 (a) Amplitude squared and (b) phase motion for $2^- X$ wave obtained from the model-independent method (red open) and the nominal BW-sum fit (black solid). The BW-sum model has one pole at $M_0 - i\Gamma_0/2 = 4146 - i 135/2$ MeV.	206
C.11 (Left) Argand plot of $1^- X$ waves obtained from the model-independent method (red open) and the nominal BW-sum fit (black solid). The BW-sum model has poles at $M_0 - i\Gamma_0/2 = 4626 - i 174/2$ MeV. (Right) Argand plot of $2^- X$ waves obtained from the model-independent method (red open) and the nominal BW-sum fit (black solid). The BW-sum model has poles at $M_0 - i\Gamma_0/2 = 4146 - i 135/2$ MeV.	206

C.12	The mass distribution of $m_{J/\psi K}$, $m_{J/\psi \phi}$ and $m_{\phi K}$ with phi sideband sample.	207
C.13	The mass distribution of $m_{J/\psi K}$ with $m_{J/\psi \phi} \in (4.25, 4.35) \text{ MeV}$	208
C.14	The dalitz plot with phi sideband sample.	208
C.15	Fit projections of (a) $m_{\phi K}$, (b) $m_{J/\psi \phi}$, (c) $m_{J/\psi K}$ from the nominal $K+5X+2X+2Z$ model with K-Matrix for describing the K^* resonances.	209
C.16	Fit projections of (a) $m_{\phi K}$, (b) $m_{J/\psi \phi}$, (c) $m_{J/\psi K}$ from the nominal $2K(\text{KMatrix})+7K+5X+2X+2Z$ model.	209
C.17	Comparison between the parametrized background PDF used in the default cFit (red dots) with the B sideband data (blue dots) for all masses and angles used in nominal fit, for K^* chain (left) X chain (middle) and Z_{cs} chain (right).	211
C.18	Comparison between the alternative parametrized background PDF (red dots) with the B sideband data (blue dots) for all masses and angles used in nominal fit, for K^* chain (left) X chain (middle) and Z_{cs} chain (right).	212

List of Tables

1.1	Some quantum numbers of quarks.	3
1.2	Results related to the $X(4140) \rightarrow J/\psi\phi$ mass peak, first observed in $B^+ \rightarrow J/\psi\phi K^+$ decays. The first (second) significance quoted for Ref. [26] is for the non-prompt (prompt) production components (the mass and width were determined from the non-prompt sample). The last column gives a fraction of $B^+ \rightarrow J/\psi\phi K^+$ rate attributed to the $X(4140)$ structure, however, the CDF and D0 results were normalized to a $B^+ \rightarrow J/\psi\phi K^+$ rate that excluded the high $J/\psi\phi$ mass range.	15
1.3	Results related to $J/\psi\phi$ mass structures heavier than the $X(4140)$ peak. The unpublished results are shown in italics. The last column gives a fraction of the total $B^+ \rightarrow J/\psi\phi K^+$ rate attributed to the given structure.	16
1.4	Mass threshold and S-wave J^P of $D_s^+D_s^-$ containing $c\bar{c}s\bar{s}$	17
1.5	Mass threshold and S-wave J^P of $D_s^+\bar{D}^0$ containing $c\bar{c}u\bar{s}$	23
2.1	Properties of the calorimeter sub-detector.	43
3.1	Results from previous publication based on Run 1 data at LHCb ^[16]	52
3.2	Z_{cs}^+ tests of LHCb Run 1 analysis ^[58]	53
3.3	The statistics and simulation version of MC. MU is magnet up, MD is magnet down.	54
3.4	stripping version	54
3.5	Stripping selections of J/ψ candidates in the line <code>FullDSTDiMuonJpsi2MuMuDetachedLine</code>	54
3.6	Tigger requirements on B^+ candidates.	55
3.7	All pre-selections of $B^+ \rightarrow J/\psi\phi K^+$ candidates including stripping and offline levels.	57
3.8	The yields of 2D fit.	65
3.9	Allowed LS for various J^P in the $K_n^* \rightarrow \phi K$ decay chain.	79
3.10	Allowed LS for various J^P in the $X \rightarrow J/\psi\phi$ decay chain.	80

3.11 Possible contribution of kaon excitations to $B^+ \rightarrow J/\psi \phi K^+$ decays. For those states in bold, their masses and widths are fixed to listed values, in which 2014 PDG values to remove the contribution from the previous LHCb publication is used. That of the other states are varied in the fit.	87
3.12 Improvement on $\ln \mathcal{L}$ by adding one X or Z or K with different J^P hypothesis.	90
3.13 Fit results from the 9K+5X+3X+2Z model with $Z_{cs}(4220)$ $J^P = 1^+$. Significance is evaluated from the change of the $2 \ln \mathcal{L}$ assuming ndf to be twice the reduction in number of free parameters when removing the component in the fit. The ndf is not multiply by two for the K^* resonance whose mass and width are fixed.	95
3.14 Fit results from Extended K+5X+3X+2Z model for $X(4220)$ with $J^P = 1^+$. Significance is evaluated from the change of the $2 \ln \mathcal{L}$ assuming ndf to be twice the reduction in number of free parameters when removing the component in the fit. The factor of two is not applied when mass and width are fixed. The two F K states have almost zero fit fractions and significances, therefore, their masses and widths from the fit are meaningless and not shown.	96
3.15 Comparison for $X(4140)$ resonance with Flatté and constant-width Breit-Wigner functions. The numbers between horizontal bands, the first (second), correspond to $Z(4220)$ with $J^P = 1^{-(+)}$. Also shown are the $\ln \mathcal{L}$ and 2D χ^2 of Dalitz-plot distribution in the $m_{J/\psi \phi}^2$ vs. $m_{J/\psi K}^2$ plane with 1018 adaptive bins.	101
3.16 Statistical significance of J^P preference for the X and Z_{cs} states in the default model. For the states with two lines, the upper (lower) row corresponds to the tests with $Z_{cs}(4220)$ $J^P = 1^{-(+)}$. The bold numbers highlight J^P values which cannot be ruled out with at least 5σ significance.	104
3.17 Statistical significance of J^P preference for the X and Z_{cs} states in the extended model. For the states with two lines, the upper (lower) row corresponds to the tests with $Z_{cs}(4220)$ $J^P = 1^{-(+)}$. The bold numbers highlight J^P values which cannot be ruled out with at least 5σ significance.	104
3.18 Fit results from the 9K+5X+3X+2Z model with $Z_{cs}(4220)$ $J^P = 1^-$. Significance is evaluated from the change of the $2 \ln \mathcal{L}$ assuming ndf to be twice the reduction in number of free parameters when removing the component in the fit. The ndf is not multiply by two for the K^* resonance whose mass and width are fixed.	106

3.19	Summary of the systematic errors on the parameters of the $K^{*+} \rightarrow \phi K^+$ states with $J^P = 1^+$. All numbers for masses and width are in MeV and fit fraction in %.	109
3.20	Summary of the systematic errors on the parameters of the $K^{*+} \rightarrow \phi K^+$ states with $J^P = 1^-$ and $J^P = 2^-$. All numbers for masses and width are in MeV and fit fraction in %.	110
3.21	Summary of the systematic errors on the parameters of the $K^{*+} \rightarrow \phi K^+$ states with $J^P = 2^+$ and $J^P = 0^-$. All numbers for masses and width are in MeV and fit fraction in %.	110
3.22	Summary of the systematic errors on the parameters of the $X \rightarrow J/\psi \phi$ states with $J^P = 0^+$. All numbers for masses and width are in MeV and fit fraction in %.	111
3.23	Summary of the systematic errors on the parameters of the $X \rightarrow J/\psi \phi$ states with $J^P = 1^+$. All numbers for masses and width are in MeV and fit fraction in %.	111
3.24	Summary of the systematic errors on the parameters of the $X \rightarrow J/\psi \phi$ states with $J^P = 1^-$ and $J^P = 2^-$. All numbers for masses and width are in MeV and fit fraction in %.	112
3.25	Summary of the systematic errors on the parameters of the $Z \rightarrow J/\psi K^+$ states with $J^P = 1^+$. All numbers for masses and width are in MeV and fit fraction in %.	112
3.26	Fit results from the 9K+5X+3X+2Z model with $Z(4220)$ $J^P = 1^+$. Significance is evaluated from the change of the $2 \ln \mathcal{L}$ assuming ndf to be twice the reduction in number of free parameters when removing the component in the fit. The ndf is not multiply by two for the K^* resonance whose mass and width are fixed.	113
4.1	Trigger lines for the $\Lambda_b^0 \rightarrow \Lambda_c^+ K^+ K^- \pi^-$ and $\Lambda_b^0 \rightarrow \Lambda_c^+ D_s^-$ candidates.	117
4.2	Stripping selections on the $\Lambda_b^0 \rightarrow \Lambda_c^+ K^+ K^- \pi^-$ and $\Lambda_b^0 \rightarrow \Lambda_c^+ D_s^-$ candidates.	118
4.3	The shared preselections on the $\Lambda_b^0 \rightarrow \Lambda_c^+ K^+ K^- \pi^-$ and $\Lambda_b^0 \rightarrow \Lambda_c^+ D_s^-$ candidates.	119
4.4	The rejected fraction by vetos for the signal and normalization channels.	120
4.5	BDTG training variables.	122
4.6	Rank of MLP trained variables	124

4.7	Fit result of simulated $\Lambda_b^0 \rightarrow \Lambda_c^+ K^+ K^- \pi^-$, $\Lambda_b^0 \rightarrow \Lambda_c^+ D_s^-$ ($D_s^- \rightarrow K^+ K^- \pi^-$) mass spectrum	128
4.8	Fit result of $\Lambda_b^0 \rightarrow \Lambda_c^+ K^+ K^- \pi^-$ mass spectrum in data sample.	130
4.9	Fit result of $\Lambda_b^0 \rightarrow \Lambda_c^+ D_s^-$ mass spectrum in data sample.	130
4.10	Fit result of $\Lambda_b^0 \rightarrow \Lambda_c^+ K^+ K^- \pi^-$ using MC smaples.	135
4.11	Relative efficiency values. Uncertainties listed are due to finite MC statistic, and are discussed in detail in Sec. 4.7	139
4.12	Summary of systematic uncertainties, and for the relative branching fraction ratio in unit of %.	141
5.1	Identification variables and corresponding functions.	155
5.2	Selection criteria in $B_s^0 \rightarrow \phi \gamma$ channel.	155
5.3	The physical performance in different luminosities with different ECAL cell segmentation.	158
5.4	Selection criteria in $B_s^0 \rightarrow J/\psi \pi^0$ channel.	160
5.5	The physical performance in different luminosities with different ECAL cell segmentation.	161
A.1	Stripping selections of J/ψ candidates in the line <code>FullDSTDiMuonJpsi2MuMuDetachedLine</code>	182
A.2	Pre-selections of $\Lambda_b^0 \rightarrow J/\psi p \pi^-$ candidates between old Run 1 analysis and this one.	183
A.3	Variables used in TMA study.	183
B.1	Stripping selections of J/ψ candidates in the line <code>FullDSTDiMuonJpsi2MuMuDetachedLine</code>	190
B.2	Pre-selections of $\Lambda_b^0 \rightarrow J/\psi p \pi^-$ candidates between old Run 1 analysis and this one.	190
B.3	Variables used in TMA between previous Run1 and this study.	193
B.4	The N^* resonances used in the different fits. Parameters are taken from the PDG ^[145] . The number of LS couplings is also listed for the “Nominal Model” (NM) and “Extended Model” (EM). To fix overall phase and magnitude conventions, which otherwise are arbitrary, the $N(1535)$ coupling of lowest LS is set to be (1,0). A zero entry means the state is excluded from the fit.	200
C.1	The signal and combinatorial background yields in the ± 15 MeV range around the B mass peak for $B \rightarrow J/\psi K K K$ candidates in the ϕ sideband (see the text).	207

Chapter 1 Introduction

1.1 Derivation

1.1.1 The standard model

In the field of particle physics, tremendous success have been achieved in standard model, which is a systematic theory that describes three known basic forces (the electromagnetic, weak and strong interactions, except gravitational force) and classifies all known elementary particles. As shown in Figure. 1.1, there are two kinds of elementary particles, one is called fermions with spin number equal to $1/2$, while the other is named as bosons with integral spin number. The basic fermions include 6 quarks and 6 leptons, the quarks carry the color charge and interact via the strong interaction, which is described by quantum chromodynamics (QCD), more details about this theory will be discussed later. Leptons can participate the weak and electromagnetic forces, and the electroweak sector is described by gauge theory with the symmetry group $U(1) \times U(2)$.

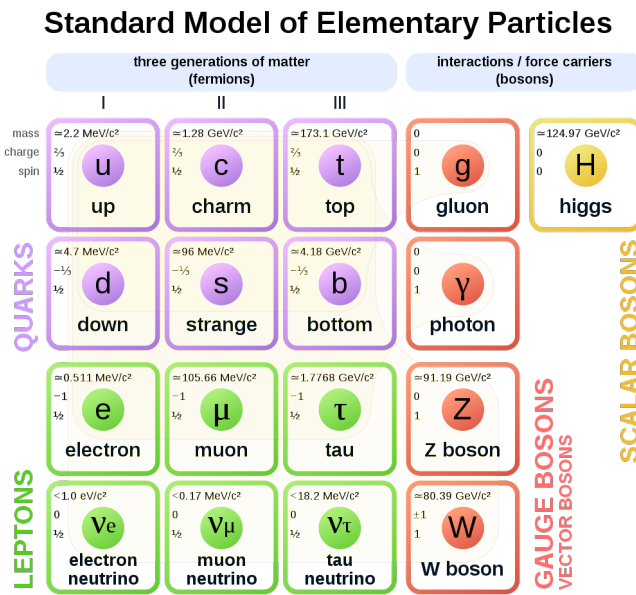


Figure 1.1 The elementary particle in the standard model.

1.1.2 Quark model and QCD

Circa 1950, the first particle accelerator began to uncover many new particles, and most of these particles are unstable and decay very quickly, and hence had not been seen in cosmic ray experiment, as shown in the Figure. 1.2. With the particle "Zoo" proliferation, people suspected that if all these particles are fundamental, and W. Lamb joked that he had heard it said that "the finder of a new elementary particle used to be rewarded by a Nobel Prize, but such a discovery now ought to be punished by a \$10,000 fine."^[101] The prosperity of new particles observed from experiments promoted emergence of many new models, which concocted to try to explain why these particles exist, such as, the model of pion composed of nucleons and anti-nucleons from Fermi and Yang^[85], which was proposed before the discovery of anti-proton. The quark model was constructed in the early 1960s by M. Gell-Mann and G. Zweig independently to classify scheme for hadrons^[90,155], which gives a natural explanation for isospin and strangeness. Besides, this model predicted the existence of the spin $-3/2$ Ω^- , which is a member of the ground-state decuplet, and the observation for this particle offered a strong evidence of correctness of quark model^[48].

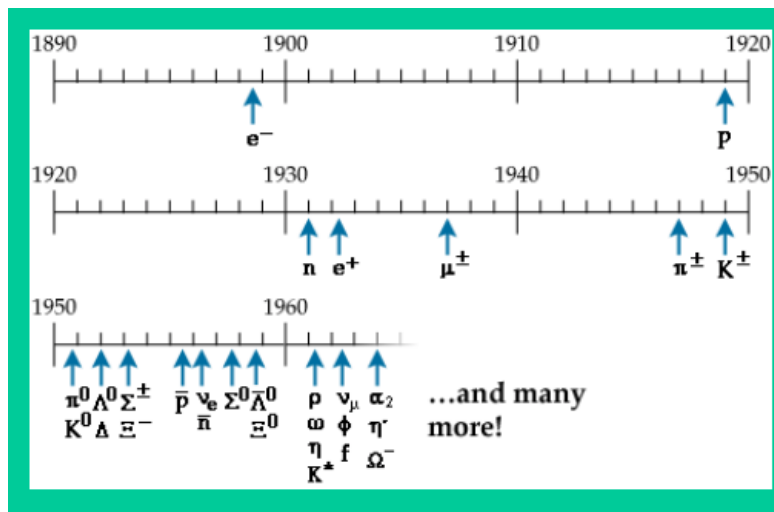


Figure 1.2 The particle zoo before 1964.

1.1.2.1 Quark model

The quark model is a description of hadronic properties which strongly emphasizes the role of the minimum-quark-content part of the wave function of hadron^[156]. In this model, the quarks are strongly interacting fermions with spin 1/2 and positive parity, while the antiquarks have negative parity. The Table 1.1 lists all quantum numbers of 6 kinds of quarks. All of them

are related with each other through the generalized Gell-Mann-Nishijima formula:

$$Q = I_z + \frac{\mathcal{B} + S + C + B + T}{2} \quad (1.1)$$

This convention imply the charged meson has the same sign as its charge. Besides, the hypercharge is another useful quantum number, which is defined as:

$$Y = \mathcal{B} + S - \frac{C - B + T}{3} \quad (1.2)$$

Table 1.1 Some quantum numbers of quarks.

	d	u	s	c	b	t
Q (electric charge)	$-\frac{1}{3}$	$+\frac{2}{3}$	$-\frac{1}{3}$	$+\frac{1}{3}$	$-\frac{1}{3}$	$+\frac{1}{3}$
I (isospin)	$\frac{1}{2}$	$\frac{1}{2}$	0	0	0	0
I_z (isospin z-component)	$\frac{1}{2}$	$-\frac{1}{2}$	0	0	0	0
S (strangeness)	0	0	-1	0	0	0
C (charm)	0	0	0	+1	0	0
B (bottomness)	0	0	0	0	-1	0
T (topness)	0	0	0	0	0	+1
\mathcal{B} (baryon)	$\frac{1}{3}$	$\frac{1}{3}$	$\frac{1}{3}$	$\frac{1}{3}$	$\frac{1}{3}$	$\frac{1}{3}$

Quarks are added together to form mesons and baryons using SU(3) group, and mesons are bound states of quark-antiquark, while the baryons are bound states of three quarks. The properties of SU(3) tell us the number of the multiplets belonging to product of 3 by 3:

$$3 \otimes \bar{3} = 1 \oplus 8 \quad (1.3)$$

If a fourth quark such as charm c included, the SU(3) group can be extended to SU(4), and the sixteen mesons are grouped into a 15-plet and a singlet:

$$4 \otimes \bar{4} = 1 \oplus 15 \quad (1.4)$$

And this model can be extended with b included naturally.

The diagram of meson model is very clear and simple, and the similar picture can also be extended to baryons. The "ordinary" baryons are composed of u , d and s quarks, which can be processed in a similar manner to combine three triplets, namely three representations:

$$3 \otimes 3 \otimes 3 = 10_s \oplus 8_{M,S} \oplus 8_{M,A} \oplus 1_A \quad (1.5)$$

Here 10_s means symmetric states, $8_{M,S}$ and $8_{M,A}$ are mixed symmetry and anti-symmetry combinations respectively, and 1_A is a completely anti-symmetric three-quark system, where

the symmetries referred to are under the exchange of any two quarks.

1.1.2.2 QCD

The quark model successfully accommodates all these particles and resonances. A remarkable success of the $SU(3)_f$ was the prediction, including the mass of the $M(\Omega^-) = sss$ baryon^[48]. But the model has following problems. First, the most obvious problem is that no matter how hard physicists have tried, a free quark has never been observed. Is the quark a real particle or simply a mathematical construct that allows us to keep track to $SU(3)_f$ in an efficient manner. The second problem is the absence of anti-symmetric combinations of spin and of flavour representations in the baryon sector. This is not unrelated to a third problem, that of Fermi-Dirac statistics. Baryons, having an odd number of spin- $\frac{1}{2}$ components, should have totally anti-symmetric wave-functions. Since they have $L = 0$, their spatial wave-function is symmetric, and we have imposed that their spin and flavour wave-function factors be symmetric too. Therefore, the wave-functions are totally symmetric.

To solve the Fermi-Dirac statistic problem, Han and Nambu, Greenberg and Gell-Mann, independently proposed adding an additional quantum number to the quarks, which is named as "color"^[1]. The Lagrangian of QCD is given by:

$$\mathcal{L} = \sum_q \bar{\psi}_{q,a} (i\gamma^\mu \partial_\mu \delta_{ab} - g_s \gamma^\mu t_{ab}^C \mathcal{A}_\mu^C - m_q \delta_{ab}) \psi_{q,b} - \frac{1}{4} F_{\mu\nu}^A F^{A\mu\nu} \quad (1.6)$$

where the repeated indices are summed over. The γ^μ are the Dirac γ -matrixs. The $\psi_{q,a}$ are quark-field spinors for a quark of flavour q and mass m_q , with a color-index a that runs from 1 to 3. Quarks are said to be in the fundamental representation of the $SU(3)$ color group. The \mathcal{A}_μ^C is the gluon fields, with C running from 1 to 8, corresponding to eight kinds of gluon. The t_{ab}^C represents eight 3×3 matrixes and are the generators of $SU(3)$ group, which illuminates the fact that a gluon's interaction with quark rotates the quark's color in $SU(3)$ space. The quantity g_s is the QCD coupling constant. Neither quarks nor gluons are observed as free particles. Hadrons are color-singlet combination of quarks, anti-quarks, and gluons. From above formula, the fundamental parameters of QCD are the coupling g_s and the quark masses m_q .

Another interesting phenomenon in QCD is asymptotic freedom, which leads to a consequence that the strong coupling α_s is small enough, as sufficiently large momentum transfers, to allow application of perturbation theory in order to provide quantitative predictions of physical processes. The strong interaction coupling constant α_s is fundamentally different from the quantum electrodynamics coupling constant, as not only fermion loops are included in the

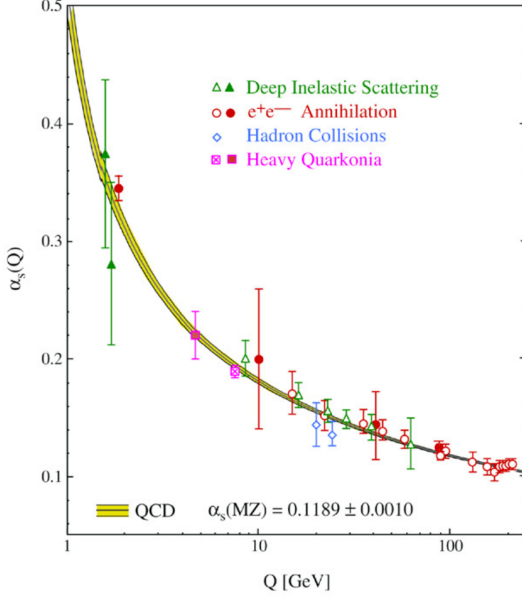


Figure 1.3 Summary of measurements of $\alpha_s(Q)$ as a function of the respective energy scale Q . Figure taken from Ref. 52

vertex expansion, but also gluon loops, owing to the fact that the gluons carry colour charges. And in QCD, the gluon-gluon interaction includes additional vacuum polarization diagrams that have virtual gluon loops. These gluon loops modify the QCD coupling strength α_s in a way that is opposite to QED: they cause α_s to decrease at short distances and increase at long distances, as shown in Figure 1.3

1.1.2.3 The QCD dilemma

In QCD, the component of the standard model of elementary processes that deal with strong interaction, the elementary particles are color-charged quarks and gluons. However, a consequence of confinement is that these particles cannot be seen in experiments. Although the QCD Lagrangian is expected, in principle, to completely describe the spectrum of hadrons and all of their properties, there is no rigorous first-principle translation of this into any useful mathematical expressions.

A fundamental process that can be computed with perturbative QCD is quark-quark elastic scattering at high-momentum transfer. This shows up in high-energy pp collider experiments as events with two high transverse momentum jets of hadrons that are nearly back to back in azimuth. The momentum distribution of quarks inside the proton is governed by long-distance QCD and approximated by universal parton distribution functions that are taken from fits to data obtained from hadron-collider measurements at low center of mass energies, deep inelastic lepton-proton scattering experiments, etc. The fundamental QCD $pp \rightarrow pp$ process cannot

be directly measured, instead, have to be inferred from the jets of hadrons that they produce. Thus, even processes that are perturbative QCD calculations involve significant long-distance QCD effects both in the initial and final states.

This nearly total disconnect between the hadrons observed in experiments and the quarks and gluons that appear in the theory is a problem of large proportions in particle physics. This is referred as "QCD dilemma". In addition to the intellectual dissatisfaction with a theory that is not directly applicable to the particles used and detected in experiments, there is also a practical problem in that many SM tests and searches for new physics (NP) with strong interacting hadrons involved in the initial and final states of the associated measurements. Even experiments without initial or final states that contain hadrons are still subject to their effects from virtual quantum fluctuations. As a result, the sensitivities of many NP searching experiments are ultimately limited by hadron-related theoretical uncertainties. Because of this, as the experimental sensitivities of NP searches improve, commensurate improvements of long-distance QCD become more and more important.

A possible way experiments might contribute to these improvements is by identifying patterns in hadron physics that may help guide the development of improved theoretical models, and the multi-quark states study offers an unique method to probe QCD.

1.1.3 Multiquark states

The concept of multiquark resonances came out accompanying with the quark model, as G. Zweig^[155] said: "*In general, we would expect that baryons are built not only from product of these aces, AAA, but also from $\bar{A}AAA$, $\bar{A}\bar{A}AAAA$, etc., where \bar{A} denotes an anti-ace.*" and M. Gell-Mann^[90] gave the similar expression: "*Baryons can now be constructed from quarks by using the combinations (qqq) , $(qqqq\bar{q})$, etc., while mesons are made of $(q\bar{q})$, $(qq\bar{q}\bar{q})$, etc.*". By then, many experiments tried to search tetraquark and pentaquark states, for example, LEPS Collaboration declared the observation of a narrow $\Theta^+(1540)$ particle, which is claimed as a pentaquark candidates, then this state became a hotspot at that time.^[123,154] However, this structure was not confirmed from high precise experiments^[112], and it is not deemed as a genuine resonance now^[120]. The research to $\Theta^+(1540)$ told us lessons but also brought us precious experience and opportunities, so we should not ignore the non-perturbative chromodynamics in spectroscopy study.

A bit of history is mentioned above, and current progress about heavy-flavour multiquark study will be reviewed from two perspectives, experimental evidences and theoretical models in next sections.

The observed status of the charmonium-like spectrum are listed in Figure. 1.4, which includes the standard charmonium, non-standard charmonium (tetraquark candidates) and pentaquark candidates. **Maybe to update later, to include $3P_c$, Z_{cs} , T_{cccc} and new X .**

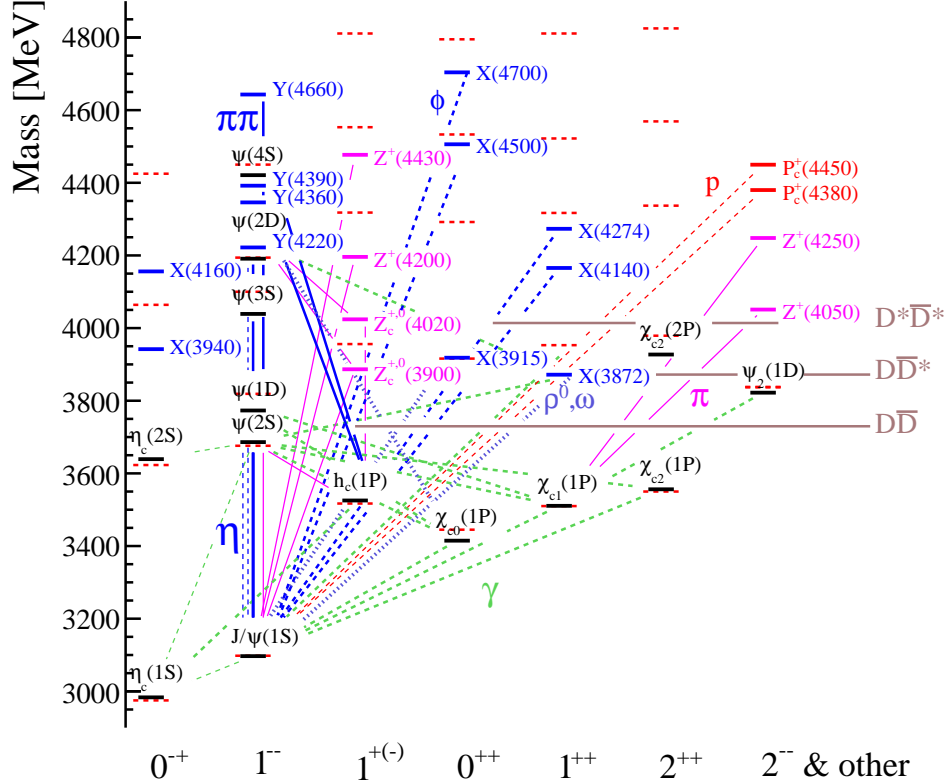


Figure 1.4 The level scheme of meson states containing a minimal quark content $c\bar{c}$. The name of a state is determined by its quantum number $I^G J^P C$. The arrows indicate the most dominate hadronic transitions. Taken from Ref. [127].

1.2 Experimental evidences of heavy-flavour multiquark candidates

1.2.1 Neutral X and Y multiquark candidates

1.2.1.1 First tetraquark candidate $\chi_{c1}(3872)$

The first multiquark candidate is $\chi_{c1}(3872)$, which was observed by Belle Collaboration as a narrow peak in the $\pi^+\pi^-J/\psi$ invariant mass distribution $B \rightarrow K\pi^+\pi^-J/\psi$ decays for in 2003^[71]. The invariant mass distribution of $B \rightarrow K\pi^+\pi^-J/\psi$ is shown in Figure. 1.5, this resonance is pretty narrow and close to the threshold of the $D\bar{D}^*$, it was popular to be assumed as molecular state, though the dynamic mechanism is under heated debate today. As this state

has been discovered more than 16 years, and confirmed in different experiments, the related studies are pretty fruitful in experimental and theoretical sectors, some comments about this particle will be given below.

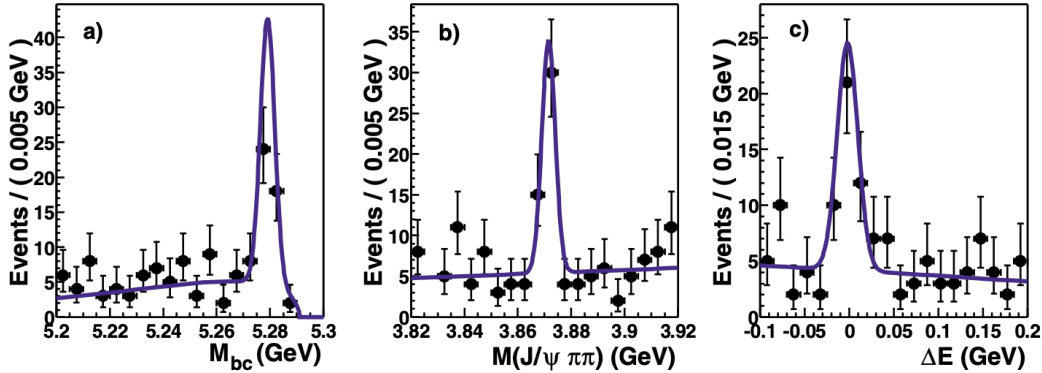


Figure 1.5 Signal-band projections of (a) M_{bc} , (b) $\Delta E_{c.m.}$, and (c) $M(\pi^+\pi^-J/\psi)$ distributions in signal region with the results of the unbinned fit^[71].

The spin and parity of this state were measured by LHCb Collaboration in 2013 with 3 fb^{-1} run-I data^[3]. 5D angular amplitude model was constructed to describe data, and likelihood ratio test is performed to discriminate between the 1^{++} and 2^{-+} assignment. Based on this technique, the quantum numbers of $\chi_{c1}(3872)$ are determined to be $J^{PC} = 1^{++}$, as shown in Figure. 1.6. By a toy simulation method, the statistical significance of this assignment can reach to 16σ .

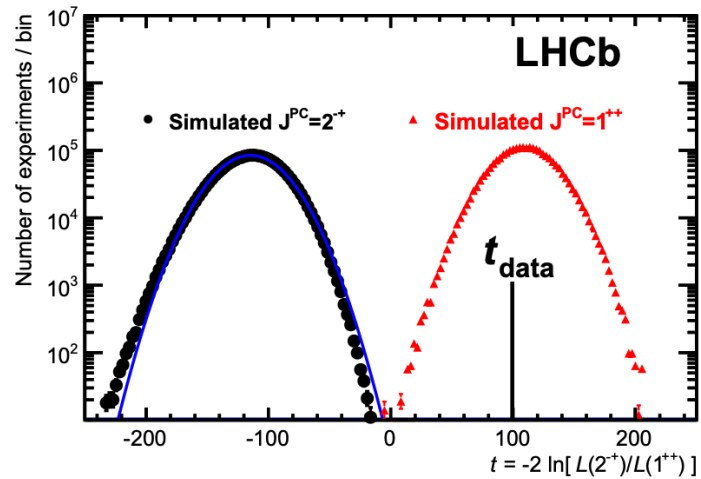


Figure 1.6 The log-likelihood ratio distribution between 1^{++} and 2^{-+} is shown above, a Gaussian fit to the 2^{-+} distribution is performed^[3].

As the spin and parity of $\chi_{c1}(3872)$ equal to 1^+ , this hadron is also expected as $2^3P_1 c\bar{c}$ state. However, there are still several reasons to classify it as exotic state^[128], and the apparent

evidence is isospin violation in its decay channel $\chi_{c1}(3872) \rightarrow \rho J/\psi$. Since the standard charmonium states contain no constituent u or d , their isospin number should be 0, as the ρ is isovector particle, the decay mode $\chi_{c1}(3872) \rightarrow \rho J/\psi$ should be strongly suppressed due to isospin violation, but branching fraction of this decay is nearly equal to the $\chi_{c1}(3872) \rightarrow \omega J/\psi$ mode. In consideration of a kinematic suppression to $\chi_{c1}(3872) \rightarrow \omega J/\psi$ by a factor of around 4, the $I = 0$ assignment is favored.

Many explorations to the nature of $\chi_{c1}(3872)$ were performed by different theoretical models^[114], and a good diagnosis to these predictions is to study the relative strength to the $\gamma\psi$ and $\gamma J/\psi$ decay modes. In the 1^{++} charmonium model, the χ_{c1}' and ψ' have the same radial wave function, and $\chi_{c1}' \rightarrow \gamma\psi'$ transition is more advantageous than that for $\gamma J/\psi$. In contrast, in the molecular hypothesis, the decay to $\gamma\psi'$ is much suppressed^[79,143,144]. The evidence for the decay mode $\chi_{c1}' \rightarrow \gamma\psi'$ was found in 2014, and the measured value agrees with expectations of charmonium for pure interpretation of the $\chi_{c1}(3872)$ state and mixture of charmonium interpretations, it does not support a pure $D\bar{D}^*$ molecular interpretation^[6].

Another experimental test to distinguish hypothesis is to measure the prompt production of $\chi_{c1}(3872)$ in high-energy hadron collisions. If the $\chi_{c1}(3872)$ is a $D\bar{D}^*$ state, its production in the hadron collisions would be more like those of known nuclei stuff, rather than those of the ψ' ^[53].

1.2.1.2 $X(3915)$

After the $\chi_{c1}(3872)$ was observed, Belle Collaboration studied $B \rightarrow K\omega J/\psi$ decay, and a prominent enhancement appeared in the $\omega J/\psi$ invariant mass distribution near the threshold, as shown in Figure. 1.7(a). Then, BaBar Collaboration confirmed this result with larger statistic sample, and the measured mass and width : $M = 3915 \pm 4$ MeV and $\Gamma = 31 \pm 11$ MeV, which are lower values comparing to Belle's measurement^[41]. Then, this state was also observed in the two-photon process $\gamma\gamma \rightarrow \omega J/\psi$, and the PDG table list the results from both channels^[156].

However, the spin-parity of this state has not been confirmed yet. With the $\gamma\gamma \rightarrow \omega J/\psi$ events, a spin-parity analysis was performed by BaBar, and their study demonstrated that $J^{PC} = 0^{++}$ quantum number assignment is favoured. And from this study, they thought the $X(3915)$ is a candidate for the 2^3P_0 charmonium state^[147]. This measured mass of $X(3915)$ is too high for the 2^3P_0 charmonium state, which is strongly contradicted with theoretical expectations^[82,111].

Besides, some people think the $J^{PC} = 2^{++}$ hypothesis cannot be ruled out by reanalyzing from the BaBar angular distributions^[153]. However, $X(3915) = \chi_{c2}'$ is not in accordance

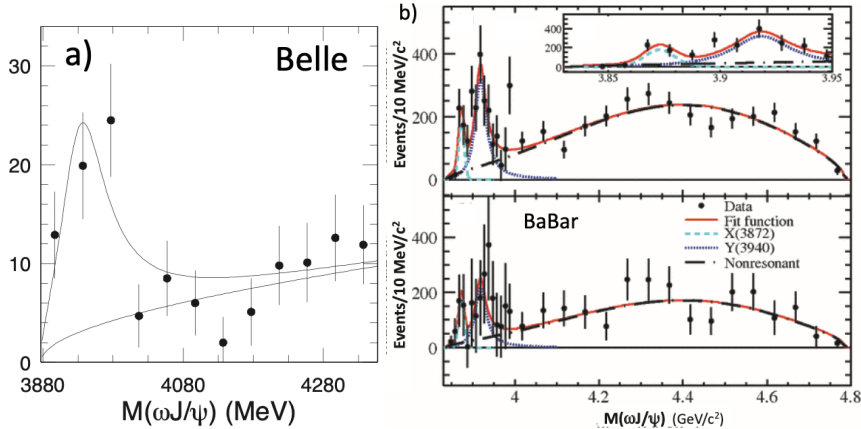


Figure 1.7 The decay $X(3915) \rightarrow \omega J/\psi$ states in $B \rightarrow K\omega J/\psi$ decay from Belle^[53] (left), and BaBar^[41] (right).

with the consequence of $X(3915)$ production in $B^+ \rightarrow K^+\omega J/\psi$ decay. Since that $\mathcal{B}(B^+ \rightarrow K^+\chi_{c2}(1P)) = (1.1 \pm 0.4) \times 10^{-5}$ is much smaller than the branching fraction of:

$$\mathcal{B}(B^+ \rightarrow K^+X(3915)) \times \mathcal{B}(X \rightarrow \omega J/\psi) = 3.0^{+0.9}_{-0.7} \times 10^{-5} \quad (1.7)$$

In the decay of B-meson to charmonium states, the decay widths are expected to be proportional to the square of the $c\bar{c}$ wave function at the origin, and decrease with increasing radial quantum number^[55]. The branching fraction measurement is contrary to this model obviously.

The mass of $X(3915)$ is 18.2 MeV below the $2m_{D_s^+}$ threshold, and this might mean that it consists of $c\bar{c}s\bar{s}$ component, or even in a $D_s^+D_s^-$ molecule-like situation. In the molecular picture, the $D\bar{D}$ decay would violate the OZI-rule^[51]. In the $c\bar{c}s\bar{s}$ configuration, the decay mode least affected by OZI-suppression is $X(3915) \rightarrow \eta\eta_c$ which could be expected to be a dominant decay mode. However, Belle saw no significant signal from previous study^[148]. The absence of an $\eta\eta_c$ model would be fatal for the $c\bar{c}s\bar{s}$ quark assignment if its partial width was shown to be definitely much smaller than that for $\omega J/\psi$ decays.

The $X(3915)$ is one of the most intriguing of the XYZ exotic meson candidates, however, its underlying nature is not fully understood, and larger data sample of this state is required in the future experiments. The J^P of this state is expected to be determined from Belle II, which have a good ability to reconstruct ω meson. Besides, LHCb experiment also has potential capacity to probe the $X(3915)$ quantum number, considering the ω has been detected in B^+ decay^[4].

1.2.1.3 $X(4140)$ and other $J/\psi\phi$ states

Among all known decays of b -hadrons, $B^+ \rightarrow J/\psi\phi K^+$ is unique, since conventional hadron contributions from kaon excitations (hereafter denoted as $K^{*+} \rightarrow \phi K^+$) are broad, and visible mass structures on the Dalitz plot are dominated by a number of relatively narrow $X \rightarrow J/\psi\phi$ states, which are candidates for tetraquarks with hidden-charm and hidden-strangeness. Contributions from these exotic hadron components approach half of the entire rate in this decay channel. The first evidence for the $J/\psi\phi$ state was observed by CDF^[24], as shown in the left of Figure 1.8. A very narrow ($\Gamma = 15.3_{-6.1}^{+10.4} \pm 2.5$ MeV), near-threshold ($M = 4143.4 \pm 3.0 \pm 0.6$ MeV) $X(4140)$ state was claimed. ⁽¹⁾ Such narrow structure was not confirmed by the Belle^[67], BaBar^[103], and early low-statistics LHCb^[2] data. However, the near-threshold state was observed by the CMS collaboration^[64]. There was also an evidence for it from the D0 experiment^[26], as shown in the right of Figure 1.9.

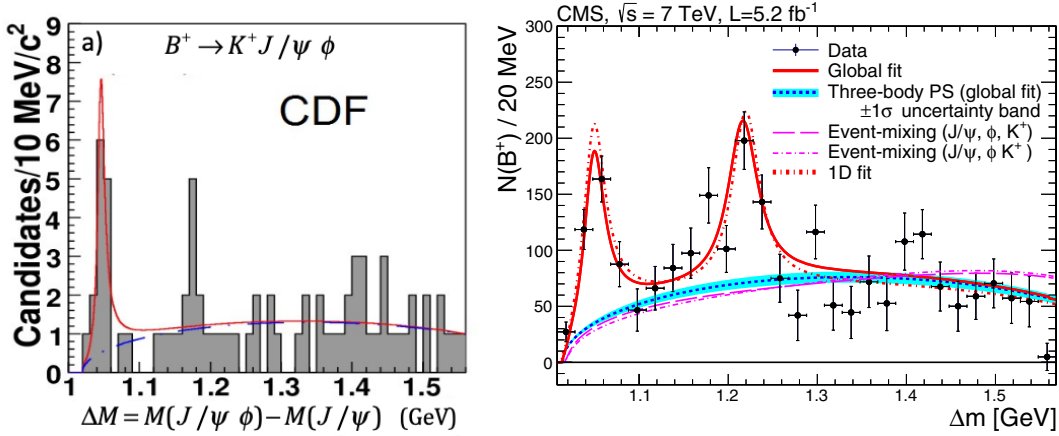


Figure 1.8 The $\Delta M = M(J/\psi\phi) - M(J/\psi)$ distribution of $B^+ \rightarrow J/\psi\phi K^+$ decays candidates from CDF experiment in left^[24]; The number of $B^+ \rightarrow J/\psi\phi K^+$ candidates as a function of $\Delta m = m(\mu^+\mu^- K^+ K^-) - m(\mu^+\mu^-)$ at CMS in right^[26].

An evidence for a second structure, $X(4274)$, in the CDF^[24] and CMS^[64] was observed. The $J/\psi\phi$ mass distribution among 2480 ± 160 $B^+ \rightarrow J/\psi\phi K^+$ events detected by CMS is shown in right of Figure 1.8, which was obtained after the subtraction of a very large combinatorial background. There is also hint of the second structure near 4274 MeV in the $J/\psi\phi$ mass distribution at D0, as shown in the left of Figure 1.9, with a small significance around 1.7σ . Besides, Belle reported a 3.2σ evidence of a narrow $J/\psi\phi$ peak around 4351 MeV, and the corresponding J^P assignment is 0^{++} or 2^{++} . However, there is no obvious $X(4140)$ evidence in the same sample^[136].

⁽¹⁾ The recent PDG^[156] naming convention calls this state $\chi_{c1}(4140)$. However, the generic X label for $J/\psi\phi$ states is used here, which is independent of their J^P assignments.

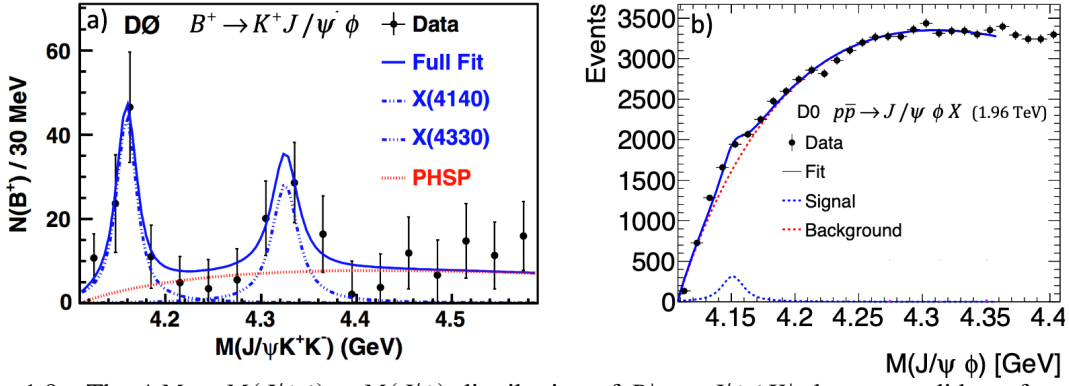


Figure 1.9 The $\Delta M = M(J/\psi\phi) - M(J/\psi)$ distribution of $B^+ \rightarrow J/\psi\phi K^+$ decays candidates from CDF experiment in left^[24]; The number of $B^+ \rightarrow J/\psi\phi K^+$ candidates as a function of $\Delta m = m(\mu^+\mu^-K^+K^-) - m(\mu^+\mu^-)$ at CMS in right^[26].

LHCb^[15,16] performed the first amplitude analysis of $B^+ \rightarrow J/\psi\phi K^+$ decays, by investigating the $J/\psi\phi$ structures in Run 1 data. The number of $B^+ \rightarrow J/\psi\phi K^+$ signal events was 4289 ± 141 with a background fraction of 23%. The data can be described by including seven $K^{*+} \rightarrow \phi K^+$ resonances, which are determined by the fit and consistent with either known or predicted states, besides, four $X \rightarrow J/\psi\phi$ structures and non-resonant ϕK^+ and $J/\psi\phi$ also contribute. The mass projections of ϕK^+ and $J/\psi\phi$ combinations are shown in Figure. 1.10. The four X structures and a non-resonant $J/\psi\phi$ contribution all had significance above 5σ . The existence of $X(4274)$ was established.

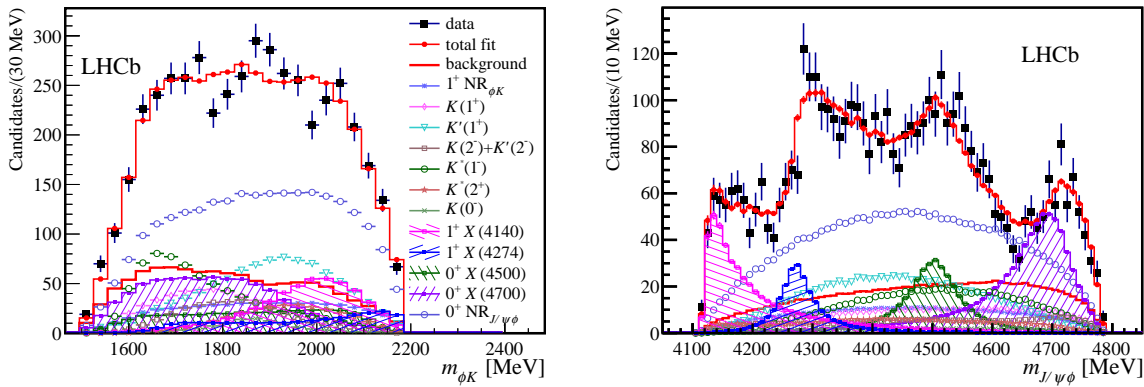


Figure 1.10 Distributions of ϕK^+ (left) and $J/\psi\phi$ (right) invariant masses for the $B^+ \rightarrow J/\psi\phi K^+$ candidates (black data points) compared with the results of the default amplitude fit to the Run 1 data^[16].

The J^P quantum numbers of $X(4140)$ are determined to be 1^{++} . Besides, the $X(4274)$ state were identified as 1^{++} at $> 5\sigma$ significance, while the $X(4500)$ and $X(4700)$ states as 0^{++} at $> 4\sigma$. Actually, the 1^{++} quantum number for $X(4140)$ and $X(4274)$ rule out the 0^{++} or 2^{++} $D_s^{*+}D_s^{*-}$ molecular models^[38,56,78,113,122,151]. Besides, some people suggested $X(4140)$ structure

is kinematically induced cusp^[100,142]. No proposed molecular bound-state or cusp model can account for these $X(4274)J^{PC}$ values. A hybrid charmonium state in this mass region would have $J^{PC} = 1^{-+}$ ^[117]. An exception is a tetraquark model implemented by Stancu^[140], states that not only correctly assigned 1^{++} to the $X(4140)$, but also predicted a second 1^{++} state at a mass that is not much higher than that of the $X(4274)$. The $X(4500)$ and the $X(4700)$ have been suggested as candidates for the $\chi_{c0}(4P)$ and $\chi_{c0}(5P)$ states, since they lie in the predicted mass and width ranges for these states^[116,129]. However, none of the J/ψ structures observed in B decays are consistent with the state seen in two-photon collisions by the Belle collaboration.^[136]

Notably, the $X(4140)$ width was substantially larger than previously determined, while the mass is consistent with the $X(4140)$ values from CDF and CMS. In the spectroscopy study, a one-dimensional fit to a mass distribution for a resonance peak might lead to biased mass and width. Besides, a one-dimensional fit might underestimate systematic error, due to the given assumption about the background shape and its incoherence^[127].

The experimental results about $J/\psi\phi$ structures are summarized in Table. 1.2 and Table. 1.3, which are updated from the tables shown in Ref. [128]. The lastest results based on LHCb Run 1 and Run 2 samples are also included, which are also partial conclusions in Chapter. 3 of this dissertation. It is possibly that the $J/\psi\phi$ structures are derived from molecular model or cusp effect, the mass thresholds of $D_s^+D_s^-$, with S-wave J^P values, are shown in Table 1.4. It is found that only the $X(4140)$ is close to the thresholds and have the S-wave J^P consistent with the determinations from the amplitude fit. Higher values of angular momentum are expected to be suppressed for threshold effects.

1.2.1.4 X states in e^+e^- collision

Three X states, $X^*(3860)$, $X(3940)$ and $X(4160)$, are introduced in this section, which are not observed in any B-meson decay channel. The first is $X(3940)$, which was first seen at Belle in 2007^[27]. According to the distribution of masses recoiling against a J/ψ in inclusive $e^+e^- \rightarrow J/\psi X$ annihilation, four peaks appear clearly, as shown in Figure. 1.11 above. The fourth peak is named as $X(3940)$, as is not associated with any known or expected charmonium. Besides, this peak was also observed in the $D\bar{D}^*$ invariant mass distribution for $e^+e^- \rightarrow J/\psi DX$ events^[130]. At the same energy point, Belle observed the $X(4160)$ structure in $D\bar{D}$ invariant mass distribution for exclusive $e^+e^- \rightarrow J/\psi D^*\bar{D}^*$ ^[130]. The J^P of $X(3940)$ and $X(4160)$ are 0^{-+} possibly according to these measurements by Belle. In consideration of the masses of these two states are far below expectations for the 0^{-+} charmonium, $X(3940)$ and $X(4160)$ are

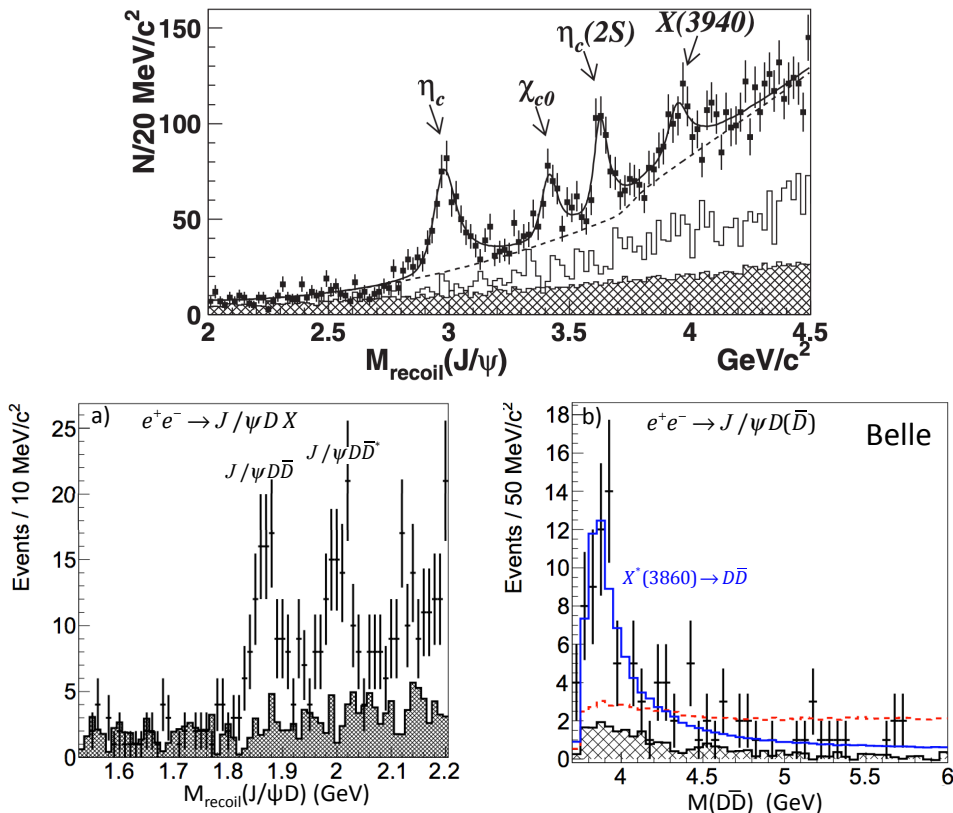


Figure 1.11 The distribution of masses recoiling from the J/ψ at Belle^[27] (above). The distribution of masses recoiling from a reconstructed J/ψ and D-meson in $e^+e^- \rightarrow J/\psi DX$ annihilation (bottom left) and $D\bar{D}$ invariant mass distribution (bottom right)^[130].

Table 1.2 Results related to the $X(4140) \rightarrow J/\psi\phi$ mass peak, first observed in $B^+ \rightarrow J/\psi\phi K^+$ decays. The first (second) significance quoted for Ref. [26] is for the non-prompt (prompt) production components (the mass and width were determined from the non-prompt sample). The last column gives a fraction of $B^+ \rightarrow J/\psi\phi K^+$ rate attributed to the $X(4140)$ structure, however, the CDF and D0 results were normalized to a $B^+ \rightarrow J/\psi\phi K^+$ rate that excluded the high $J/\psi\phi$ mass range.

$B \rightarrow J/\psi\phi K$	$X(4140)$ peak			
yield	Mass [MeV]	Width [MeV]	Significance	Fraction %
2008	CDF 2.7 fb ⁻¹ 23			
58 ± 10	$4143.0 \pm 2.9 \pm 1.2$	$11.7^{+8.3}_{-5.0} \pm 3.7$	3.8σ	
2009	<i>Belle</i> 59			
325 ± 21	4143.0 fixed	11.7 fixed	1.9σ	
2011	CDF 6.0 fb ⁻¹ 24			
115 ± 12	$4143.4^{+2.9}_{-3.0} \pm 0.6$	$15.3^{+10.4}_{-6.1} \pm 2.5$	5.0σ	$14.9 \pm 3.9 \pm 2.4$
2011	LHCb 0.37 fb ⁻¹ 2			
346 ± 20	4143.4 fixed	15.3 fixed	1.4σ	< 7 @ 90%CL
2013	CMS 5.2 fb ⁻¹ 64			
2480 ± 160	$4148.0 \pm 2.4 \pm 6.3$	$28^{+15}_{-11} \pm 19$	5.0σ	10 ± 3 (stat.)
2013	D0 10.4 fb ⁻¹ 25			
215 ± 37	$4159.0 \pm 4.3 \pm 6.6$	$19.9 \pm 12.6^{+1.0}_{-8.0}$	3.0σ	$21 \pm 8 \pm 4$
2014	BaBar 103			
189 ± 14	4143.4 fixed	15.3 fixed	1.6σ	< 13.3 @ 90%CL
2016	LHCb 3.0 fb ⁻¹ 15, 16			
4289 ± 151	$4146.5 \pm 4.5^{+4.6}_{-2.8}$	$83 \pm 21^{+21}_{-14}$	8.4σ	$13.0 \pm 3.2^{+4.8}_{-2.0}$
2021	LHCb 9.0 fb ⁻¹ Chapter. 3			
24220 ± 170	$4118 \pm 11^{+19}_{-36}$	$162 \pm 21^{+24}_{-49}$	13σ	$17 \pm 3^{+19}_{-6}$
2015	D0 10.4 fb ⁻¹ 26			
$p\bar{p} \rightarrow J/\psi\phi\dots$	$4152.5 \pm 1.7^{+6.2}_{-5.4}$	$16.3 \pm 5.6 \pm 11.4$	5.7σ (4.7σ)	

taken as tetraquark candidates. The bottom left plot of Figure. 1.11 shows the distribution of masses recoiling against a detected J/ψ and D meson in $e^+e^- \rightarrow J/\psi D^+X$ annihilation events collected in Belle^[69], while The bottom right plot of Figure. 1.11 shows $D\bar{D}$ invariant mass distribution for the exclusive $e^+e^- \rightarrow J/\psi D\bar{D}$ events. From an amplitude fit, $X(3862)$ structure is very significant and $J^{PC} = 0^{++}$ quantum number assignment gives the best fit. This state is considered as $\chi_{c0}(2P)$ charmonium state now.

Table 1.3 Results related to $J/\psi\phi$ mass structures heavier than the $X(4140)$ peak. The unpublished results are shown in italics. The last column gives a fraction of the total $B^+ \rightarrow J/\psi\phi K^+$ rate attributed to the given structure.

$B \rightarrow J/\psi\phi K$		$X(4274 - 4351)$ peaks(s)			Fraction [%]
yield	Mass [MeV]	Width [MeV]	Significance		
2011	<i>CDF</i> 6.0 fb^{-1}	24			
115 ± 12	$4274.4^{+8.4}_{-6.7} \pm 1.9$	$32.3^{+21.9}_{-15.3} \pm 7.6$	3.1σ		
2011	<i>LHCb</i> 0.37 fb^{-1}	2			
346 ± 20	4274.4 fixed	32.3 fixed			$< 8 @ 90\% \text{CL}$
2013	<i>CMS</i> 5.2 fb^{-1}	64			
2480 ± 160	$4313.8 \pm 5.3 \pm 7.3$	$38^{+30}_{-15} \pm 16$			
2013	<i>D0</i> 10.4 fb^{-1}	25			
215 ± 37	4328.5 ± 12.0	30 fixed			
2014	<i>BaBar</i> 103				
189 ± 14	4274.4 fixed	32.3 fixed	1.2σ		$< 18.1 @ 90\% \text{CL}$
2016	<i>LHCb</i> 3.0 fb^{-1}	15, 16			
4289 ± 151	$4273.3 \pm 8.3^{+17.2}_{-3.6}$	$56 \pm 11^{+8}_{-11}$	6.0σ	$7.1 \pm 2.5^{+3.5}_{-2.4}$	
	$4506 \pm 11^{+12}_{-15}$	$92 \pm 21^{+21}_{-20}$	6.1σ	$6.6 \pm 2.4^{+3.5}_{-2.3}$	
	$4704 \pm 10^{+14}_{-24}$	$120 \pm 31^{+42}_{-33}$	5.6σ	$12 \pm 5^{+9}_{-5}$	
2021	<i>LHCb</i> 9.0 fb^{-1}	Chapter. 3			
24220 ± 170	$4294 \pm 4^{+3}_{-6}$	$53 \pm 5 \pm 5$	18σ	$2.8 \pm 0.5^{+0.8}_{-0.4}$	
	$4474 \pm 3 \pm 3$	$77 \pm 6^{+10}_{-8}$	20σ	$5.6 \pm 0.7^{+2.4}_{-0.6}$	
	$4684 \pm 7^{+13}_{-16}$	$126 \pm 15^{+37}_{-41}$	15σ	$7.2 \pm 1.0^{+4.0}_{-2.0}$	
	4694^{+16}_{-3}	$87 \pm 8^{+16}_{-3}$	17σ	$8.9 \pm 1.2^{+4.9}_{-1.4}$	
2010	<i>Belle</i> 136				
$\gamma\gamma \rightarrow J/\psi\phi$	$4350.6^{+4.6}_{-5.1} \pm 0.7$	$13^{+18}_{-9} \pm 4$	3.2σ		

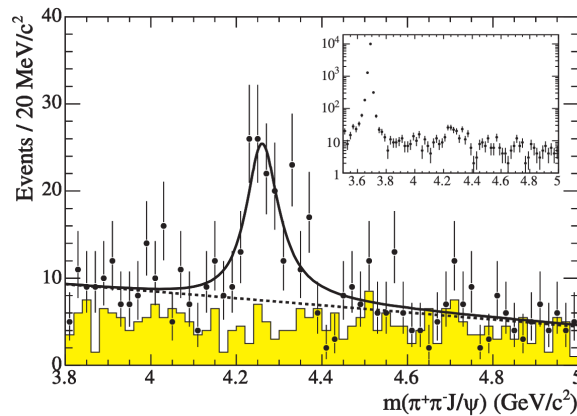


Figure 1.12 The $J/\psi\pi^+\pi^-$ invariant mass distribution in the process $e^+e^- \rightarrow \gamma\pi^+\pi^-J/\psi$ at BaBar^[47].

Table 1.4 Mass threshold and S-wave J^P of $D_s^+ D_s^-$ containing $c\bar{c} s\bar{s}$.

$L=0$	$0^- D_s^+$ (1968 MeV)	$1^- D_s^{*+}$ (2112 MeV)	$0^+ D_{s0}^{*+}$ (2318 MeV)	$1^+ D_{s1}^+$ (2460 MeV)	$1^+ D_{s1}^+$ (2536 MeV)	$2^+ D_{s2}^{*+}$ (2573 MeV)
$0^- D_s^-$ (1968 MeV)	0^+ (3926 MeV)	1^+ (4080 MeV)	0^- (4286 MeV)	1^- (4428 MeV)	1^- (4504 MeV)	2^- (4541 MeV)
$1^- D_s^{*-}$ (2112 MeV)	-	$(0, 1, 2)^+$ (4224 MeV)	1^- (4430 MeV)	$(0, 1, 2)^-$ (4572 MeV)	$(0, 1, 2)^-$ (4648 MeV)	$(1, 2, 3)^-$ (4685 MeV)
$0^+ D_{s0}^{*-}$ (2318 MeV)	-	-	0^+ (4636 MeV)	1^+ (4778 MeV)	1^+ (4854 MeV)	2^+ (4891 MeV)
$1^+ D_{s1}^-$ (2460 MeV)	-	-	-	$(0, 1, 2)^+$ (4920 MeV)	$(0, 1, 2)^+$ (4996 MeV)	$(1, 2, 3)^+$ (5033 MeV)
$1^+ D_{s1}^-$ (2536 MeV)	-	-	-	-	$(0, 1, 2)^+$ (5072 MeV)	1^+ (5109 MeV)
$2^+ D_{s2}^{*-}$ (2573 MeV)	-	-	-	-	-	$(0, 1, 2, 3, 4)^+$ (5146 MeV)

1.2.1.5 Y states with $J^{PC} = 1^{--}$

The BaBar group considered to search the possible 1^{--} state in the $e^+e^- \rightarrow \gamma\pi^+\pi^-J/\psi$ process after the $X(3872)$ was discovered in Belle. No structure around 3872 MeV appeared. However, an unexpected strong accumulation of events in $J/\psi\pi^+\pi^-$ invariant masses distribution have a peak near 4260 MeV^[47], as shown in Figure. 1.12. This observation is confirmed very quickly by CLEO^[74] and Belle^[152].

Afterwards, BaBar observed another peak around 4320 MeV^[46], as shown in the left of Figure. 1.13. Then, Belle confirmed this state with a larger data sample^[150], as shown in the right of Figure. 1.13. As the mass peak is near 4360 MeV, finally, it is named as $Y(4360)$. BESIII performed a data scan between $E_{cm} = 3882$ MeV and 4567 MeV later^[28], with "high luminosity" and "low luminosity" scans respectively, as shown in Figure. 1.14. It is obvious that the line shape cannot be well described by a single Breit-Wigner function, then the fit was performed using two BW amplitude by BESIII, and the corresponding masses of two resonances are 4222 ± 4 MeV and 4320 ± 13 MeV, which were explained as $Y(4260)$ and $Y(4360)$.

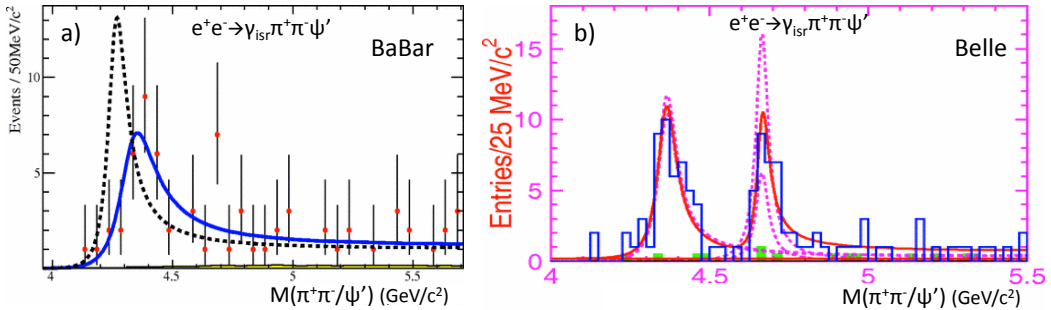


Figure 1.13 The $J/\psi\pi^+\pi^-$ invariant mass distribution in the process $e^+e^- \rightarrow \gamma\pi^+\pi^-J/\psi$ at BaBar^[47].

The J^{PC} of Y states is 1^{--} , which is as same as photon and J/ψ . This is a strong evidence

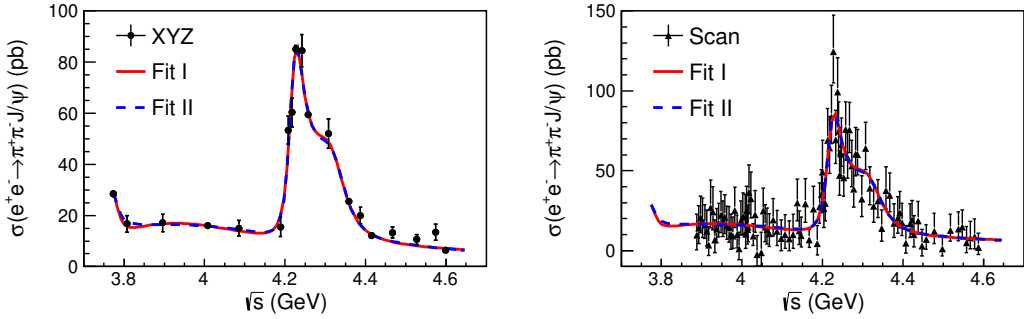


Figure 1.14 The cross section for $e^+e^- \rightarrow \gamma\pi^+\pi^-J/\psi$ at BESIII, right one for "high luminosity" scan,^[28] left one is "low luminosity" scan^[28].

that it contains $c\bar{c}$ quark pair. However, all of the $1^{--} c\bar{c}$ charmonium with mass below 4450 MeV have been seen in the e^+e^- collision between 2.6 and 4.6 GeV. In addition, there is no evidence it decaying to open-charmed mesons. Based on above considerations, many theorists infer that this state is multiquark meson or $c\bar{c}$ -gluon hybrid^[93,118].

The narrow $X(6900)$ was observed by LHCb in the J/ψ -pair mass spectrum recently^[PAPER-2020-011], which is the first four charm quarks candidate.

1.2.2 Charged multiquark candidates Z_c and Z_{cs}

1.2.2.1 Z_c in B decay

The first candidate of charged charmonium-like state is $Z(4430)$, which was observed at Belle in $\bar{B} \rightarrow \psi\pi^+K^-$ decay in 2007^[29], and in this plot the signal structure is shown in the left of Figure. 1.15. Then the existence of $Z(4430)$ was independently confirmed in 2014 at LHCb experiment^[8], which was studied based on a 4-dimensional amplitude analysis in the $\bar{B} \rightarrow \psi\pi^+K^-$ decay. According to these independent measurements, the average mass and width are determined to be $M = 4478^{+15}_{-81}$ MeV and $\Gamma = 181 \pm 31$ MeV for $Z_c(4430)$. Besides, the J^P assignment is ascertained to be 1^+ at 9.7σ level as well. The corresponding "Argand" plot is shown in the left of Figure. 1.16, revealing the character of Breit-Wigner resonances as a nearly circular in shape. In addition, a broad peak named as $Z_c(4240)$ is required for a satisfied fitting, and this additional structure appeared in $\psi\pi^+$ mass distribution as shown in right of Figure. 1.15.

Belle also performed an amplitude of $\bar{B} \rightarrow J/\psi\pi^+K^-$ decays^[70], and a new very broad 1^+ $Z_c(4200)$ state is required for a satisfactory fit. The measured mass and width of this state are $M = 4196^{+31}_{-29} \pm ^{+17}_{-13}$ MeV and $\Gamma = 370 \pm 70^{+70}_{-132}$ MeV. Besides, Belle also reported corresponding J^P is either 0^- or 1^+ , and "Argand" plot is shown in the right of Figure. 1.16, which displays a

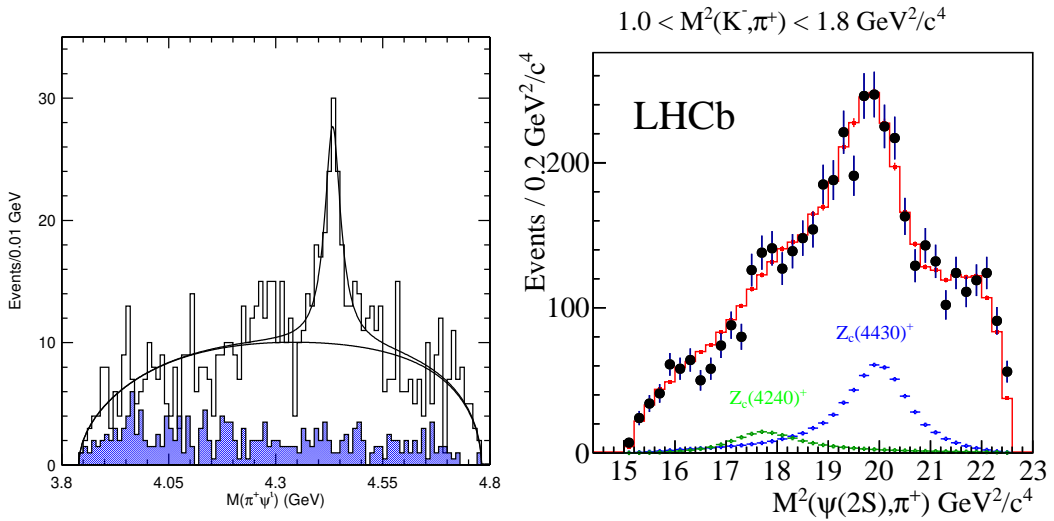


Figure 1.15 The $M(\psi\pi)$ distribution in $\bar{B} \rightarrow \psi\pi^+K^-$ decay at Belle^[29], the $M^2(\psi\pi)$ in $\bar{B} \rightarrow \psi\pi^+K^-$ from LHCb^[8].

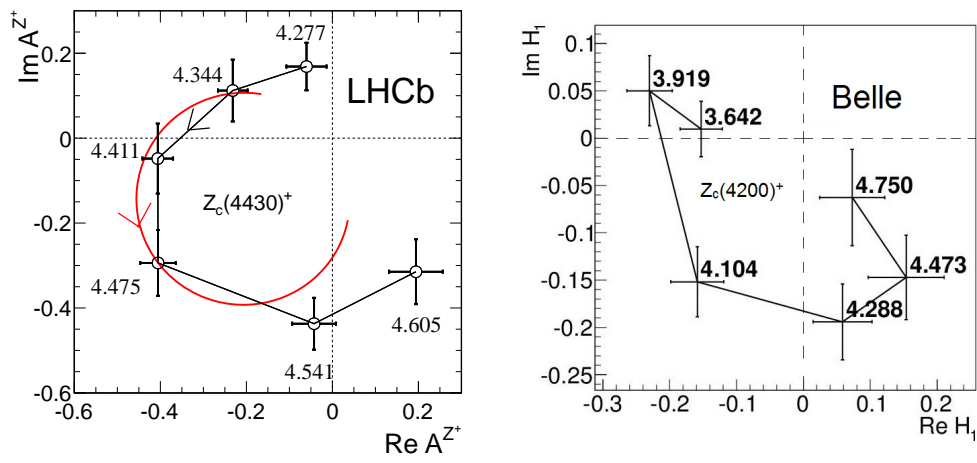


Figure 1.16 The real and imaginary parts of the amplitude for $Z_c(4430) \rightarrow \psi\pi^+$ decay at LHCb^[8], the $Z_c(4200) \rightarrow J/\psi\pi^+$ decay from Belle^[70].

nearly circular phase motion.

The charged Z_c states are pretty broad, and the interference effect is very obvious, which can distort the resonance line shape. For example, the original $Z_c(4430)$ results were based on a one dimensional Breit-Wigner line-shape fit, so they obtained lower values of mass and width than that from LHCb.

1.2.2.2 Z_c in e^+e^- collision

As mentioned in Section. 1.2.1.5, the $Y(4260)$ was observed at BaBar. This discovery prompted BESIII group to collect data at $E_{cm} = 4260$ MeV to search possible charged resonance in this channel. Then, the $Z_c(3900)$ was observed in $J/\psi\pi^+$ and $J/\psi\pi^-$ invariant mass distribution, using a 525 pb^{-1} BESIII data sample accumulatd at $E_{cm} = 4.26 \text{ GeV}$ ^[29], as shown in the left of Figure. 1.17. The measured mass is $3899.0 \pm 6.1 \text{ MeV}$ and the width is 46 ± 22 . Significantly, the mass of this state is around 24 MeV above the $m_{D^{*+}} + m_{\bar{D}^{*0}}$ threshold. The $Z_c(3900)$ was observed by Belle at about the same time^[115].

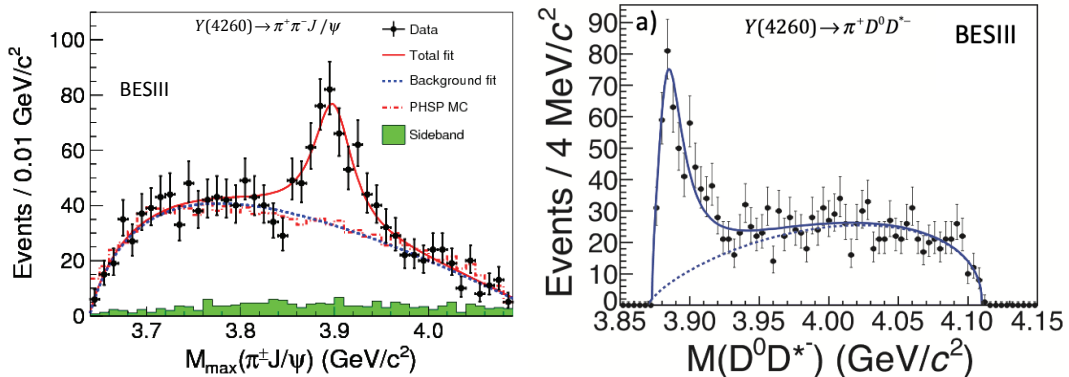


Figure 1.17 Distribution of the larger of two $J/\psi\pi^\pm$ masses in $e^+e^- \rightarrow J/\psi\pi^+\pi^-$ events collected in BESIII at $E_{cm} = 4260 \text{ MeV}$ ^[29] (left), The $D^0 D^{*-}$ invariant mass distribution in $e^+e^- \rightarrow D^0 D^{*-}\pi^+$ events collected in BESIII at $E_{cm} = 4260 \text{ MeV}$ ^[34] (right)

Subsequently, BESIII explored the $D^0 D^{*-}$ invariant mass distribution in $e^+e^- \rightarrow D^0 D^{*-}\pi^+$ events, and found the very strong near-threshold peak in this distribution, as shown in the right of Figure. 1.17. Then the mass and width are determined as $M = 3883.9 \pm 4.5 \text{ MeV}$ and $\Gamma = 24.8 \pm 12 \text{ MeV}$ from a one-dimentional fit, where the peak was discribed by a threshold-modified BW amplitude and background was repesented by a incoherent phase-space-like function^[34]. Thus, this state was named as $Z_c(2885)$ by BESIII collaboration. From the $Z_c(2885) \rightarrow D\bar{D}^*$ stong decay, BESIII also determined the J^P quantum number to be 1^+ , which is prefered than the 0^- or 1^- assignments. BESIII also reported the observation of

isospin partner of $Z_c(3900)$ in $e^+e^- \rightarrow J/\psi\pi^0\pi^0$ events^[31], as well as in $e^+e^- \rightarrow D^+D^{*-}\pi^0$ ^[34], with mass and width are consistent with the charged $Z_c(3900)$ state.

In addition to $Z_c(3900)$, BESIII collaboration observed the $Z_c(4020)$ in $h_c(1P)\pi^+\pi^-$ final states^[33], and the invariant mass distribution of $h_s\pi^\pm$ is shown in the left of Figure. 1.18. In this study, the mass of $Z_c(4020)$ was measured to be 4022.9 ± 2.8 MeV, which is about 5 MeV above $m_{D^{*+}} + m_{\bar{D}^{*0}}$. Similar to the neutral $Z_c(3900)$ study, the isospin partner of $Z_c(4020)$ was searched in $e^+e^- \rightarrow h_c\pi^0\pi^0$ events^[30], as shown in the right of Figure. 1.18. Afterwards, $Z_c(4020)$ and its isospin partner were searched in $e^+e^- \rightarrow D^{*+}D^{*0}\pi^-$ ^[35] and $e^+e^- \rightarrow D^*\bar{D}^{*0}\pi^0$ ^[32] events by BESIII. The measured mass and width from the double D invariant mass spectrum are agree with those measured for the $Z_c(4020) \rightarrow h_c\pi^+$ channel within errors.

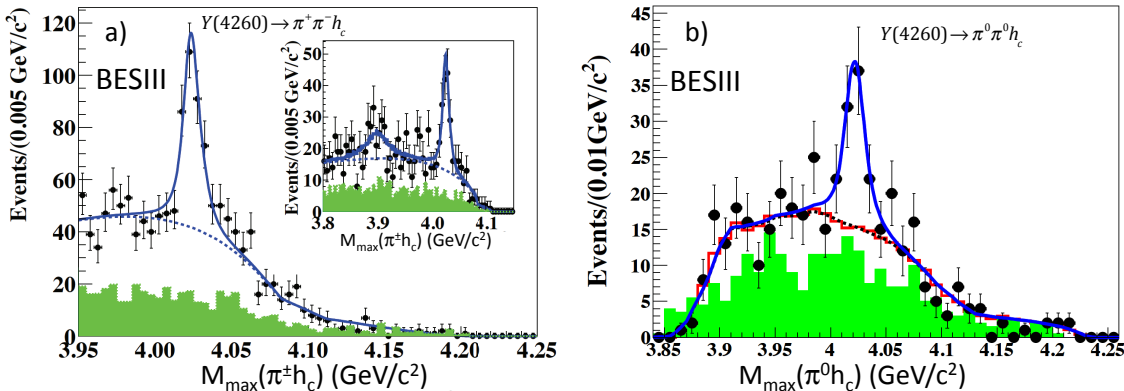


Figure 1.18 Distribution of the larger of two $h_c\pi^\pm$ masses in $e^+e^- \rightarrow h_c\pi^+\pi^-$ events collected in BESIII at $E_{cm} = 4260$ MeV and $E_{cm} = 4360$ MeV^[33] (left), The $h_c\pi^0$ invariant mass distribution in $e^+e^- \rightarrow h_c\pi^0\pi^0$ events collected in BESIII at BESIII^[30] (right)

The theoretical pictures of $Z_c(3900)$ and $Z_c(4020)$ are not very clear yet. For example, the mass of these two states are in agreement with the molecular interpretation, and both Z_c states should copiously decay to $h_c\pi$ in a purely molecular interpretation. But the $Z_c(4020)$ is not observed in $J/\psi\pi$ and $Z_c(3900)$ is not observed in $h_c\pi$.

1.2.2.3 Observation of Z_{cs} states

Recently, the BESIII experiment reported observation of the threshold structure in the $D_s^-D^{*0} + D_s^{*-}D^0$ mass distribution^[36]. This structure is interpreted as a resonance, and is named as $Z_{cs}(3985)^-$. The measured mass of this resonance is $3982.5^{+1.8}_{-2.6}$ (stat) ± 2.1 (syst) MeV and width is equal to $12.8^{+5.3}_{-4.4}$ (stat) ± 3.0 (syst) MeV, and the significance of this state is around 5.3σ . The corresponding K^+ recoil-mass distributions are shown in Figure. 1.19,

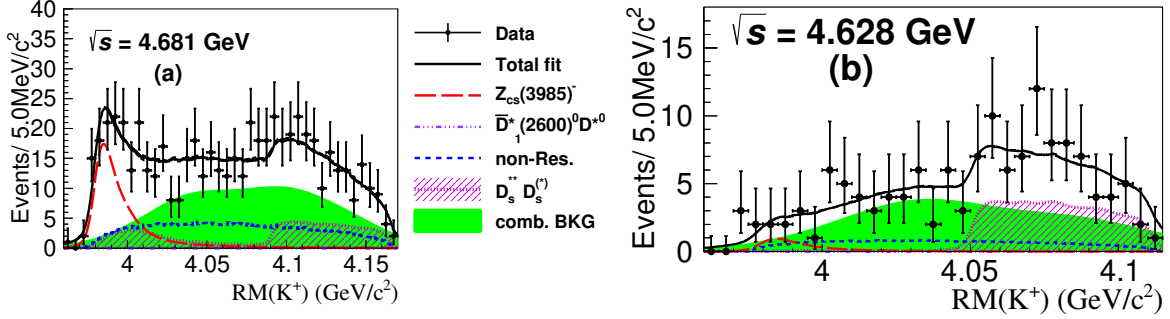


Figure 1.19 Simultaneous unbinned maximum likelihood fit to the K^+ recoil-mass spectra in data at 4.681 GeV (left) and 4.628 GeV (right)^[36].

Before the results from BESIII were reported, we had observed two Z_{cs} states, as well as several new X states, in $B^+ \rightarrow J/\psi \phi K^+$ decay based on a 6-dememtional amplitude analysis at LHCb. The detailed analysis procedure is introduced in Chapter. 3, and some main conclusions are illustrated here. Figure 1.20 shows the Dalitz plots for B^+ candidates in the signal region. The most apparent features are four bands in the $J/\psi \phi$ mass distribution, corresponding to the previously reported $X(4140)$, $X(4274)$, $X(4500)$ and $X(4700)$ states. There is also a distinct $J/\psi K^+$ band near 16 GeV^2 , which is the sign of $Z_{cs}(4000)$.

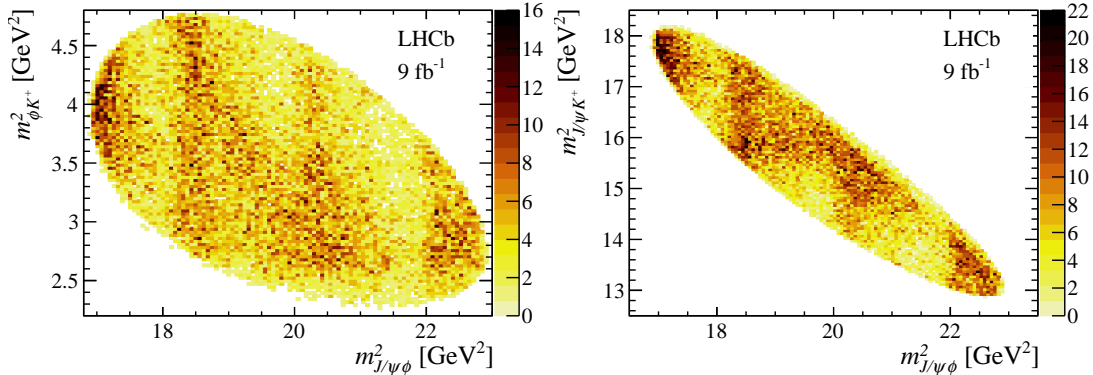


Figure 1.20 Dalitz plots for $B^+ \rightarrow J/\psi \phi K^+$ candidates in a region $\pm 15 \text{ MeV}$ around the B^+ mass peak.

The left two plots in Figure 1.21 shows the $m_{J/\psi K^+}$ distributions in two slices of $m_{J/\psi \phi}$, which illustrates the need for the narrower $Z_{cs}(4000)^+$ state. Beside, the spin and parity of $Z_{cs}(4000)$ is determined to be 1^+ . Further evidence for the resonant character of $Z_{cs}(4000)^+$ is observed in the right plot of Figure. 1.21, showing the evolution of the complex amplitude on the Argand diagram. The magnitude and phase exhibit approximately circular evolution with $m_{J/\psi K^+}$ in the counter-clockwise direction, as expected for a resonance.

We consider the $Z_{cs}(4000)$ observed at LHCb and $Z_{cs}(3985)$ claimed by BESIII are not same state. First, the width of these two states are pretty different. Second, we tried

to fix the mass or width of $Z_{cs}(3985)$ in $B^+ \rightarrow J/\psi \phi K^+$ amplitude model, but no significant likelihood improvement was obtained by this procedure. Considering the similar $Z_c(3900)$ and $Z_c(4020)$ have not been observed at any B meson decay channel, the production mechanism for $Z_{cs}(4000)$ and $Z_{cs}(3985)$ should be different.

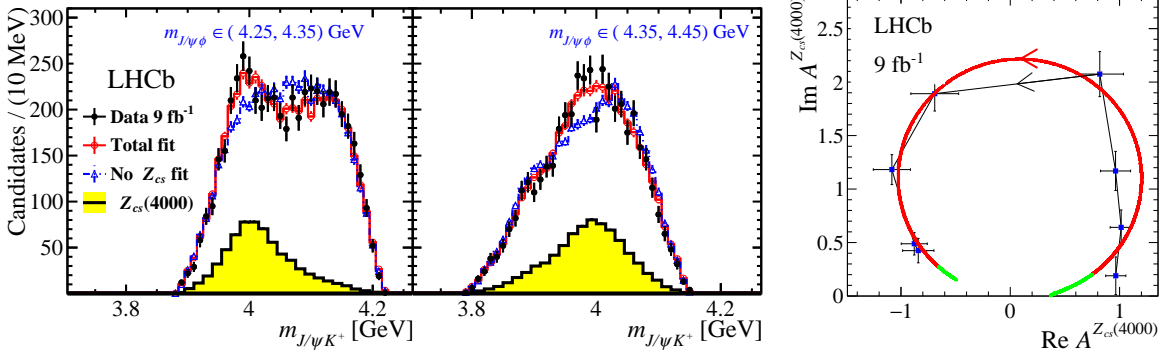


Figure 1.21 Fit projections onto $m_{J/\psi K^+}$ in two slices of $m_{J/\psi \phi}$ for the default model and the default model without the 1^+ Z_{cs} states (left and middle). Fitted values of the $Z_{cs}(4000)^+$ amplitude in eight $m_{J/\psi K^+}$ bins, shown on an Argand diagram (blue points). The red curve represents the expected Breit-Wigner behaviour between $-1.4\Gamma_0$ to $1.4\Gamma_0$ around the $Z_{cs}(4000)^+$ mass. The green curve is the same as the red curve but the mass is extended to the reachable range in the $B^+ \rightarrow J/\psi \phi K^+$ channel (right).

The mass thresholds of $D_s^+ \bar{D}^0$ excitations, with S-wave J^P values, are shown in Table 1.4 and 1.5. The $Z_{cs}(4000)$ and $Z_{cs}(3985)$ are close to the thresholds and the S-wave J^P are consistent to the results obtained from the amplitude fit. Higher values of angular momentum are expected to be suppressed for threshold effects.

Table 1.5 Mass threshold and S-wave J^P of $D_s^+ \bar{D}^0$ containing $c\bar{c}u\bar{s}$.

L=0	$0^- D_s^+$ (1968 MeV)	$1^- D_s^{*+}$ (2112 MeV)	$0^+ D_{s0}^{*+}$ (2318 MeV)
$0^- D^0$ (1870 MeV)	0^+ (3838 MeV)	1^+ (3982 MeV)	0^- (4188 MeV)
$1^- D^*$ (2007 MeV)	1^+ (3975 MeV)	0^+ (4119 MeV)	1^- (4325 MeV)
$0^+ D_0^*$ (2318 MeV)	0^- (4286 MeV)	1^- (4430 MeV)	0^+ (4636 MeV)

1.2.3 Pentaquark candidates

LHCb reported significant $J/\psi p$ mass structures in $\Lambda_b^0 \rightarrow J/\psi p K^-$ decays using Run 1 data sample, and the reflection from $\Lambda^* \rightarrow J/\psi K^-$ contributions have been excluded from full amplitude analysis^[12]. The Dalitz plot of $\Lambda_b^0 \rightarrow J/\psi p K^-$ is shown in the left of Figure 1.22 with Run 1 data. From the 6-dimentional amplitude analysis, the $P_c(4450)^+$ structure was determined to peak at $4449.8 \pm 1.7 \pm 2.5$ MeV, with a width of $39 \pm 5 \pm 19$ MeV. The

amplitude analysis also required a second broad $J/\psi p$ state for a reasonable description of the data, peaking at $4380 \pm 8 \pm 29$ MeV, with a width of $205 \pm 18 \pm 86$ MeV, even though it did not appear in the $m(J/\psi p)$ distribution. The fitting projection on $m_{J/\psi p}$ is shown in the left of Figure 1.23. The spins of these structures were not determined, and the data preferred spin combinations involving 3/2 and 5/2 in either order. The spin-parity preferences exhibited significant Λ^* model dependence. Investigation of the Argand diagrams for the $P_c(4450)^+$ and $P_c(4380)^+$ structures was inconclusive because of the large statistical errors. Then, cross check was performed in a nearly model independent way in Ref. [14], where it was shown that the $J/\psi p$ structure near 4450 MeV was too narrow to be accounted by a collection of pK contributions.

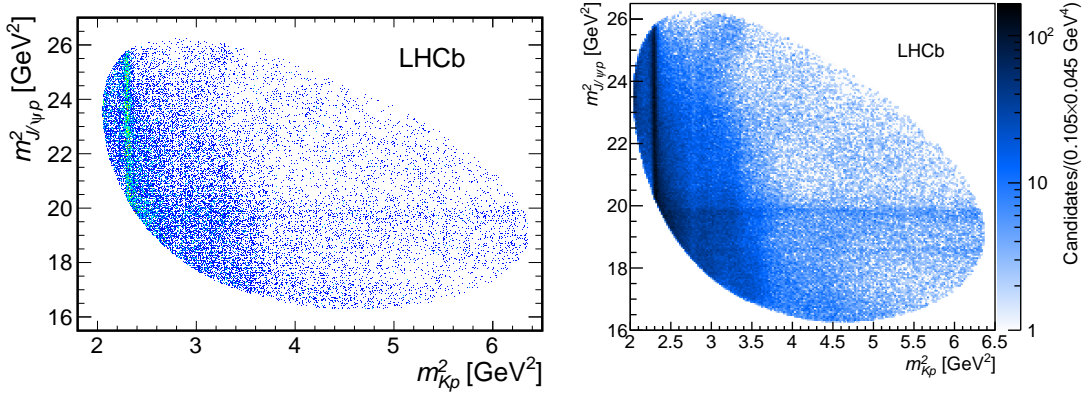


Figure 1.22 Dalitz plot of $\Lambda_b^0 \rightarrow J/\psi p K^-$ with Run 1 data sample (left)^[12], with Run 1 and Run 2 data sample together (right)^[19].

We then updated $\Lambda_b^0 \rightarrow J/\psi p K^-$ based on the combined data set collected by the LHCb collaboration in Run 1, with pp collision energies of 7 and 8 TeV corresponding to a total integral luminosity of 3 fb^{-1} , and the Run 2 samples with pp collision energies of 13 TeV corresponding to 6 fb^{-1} ^[19]. In this updated analysis, the selection procedure is optimized, which helps to improve the Λ_b^0 reconstruction efficiency by almost a factor of two and leaves the background level almost unchanged, details of selection procedure are introduced in Appendix. A. The invariant mass distributions are consistent to the previous study according to the Dalitz plots, as shown in Figure 1.22. Besides, performing a rigorous amplitude analysis of this new data sample is computationally challenging. Therefore, we applied binned fits to the 1-dimensional distribution $m_{J/\psi p}$ distribution, as shown in the right of Figure 1.23. Using the nine-fold increased Λ_b^0 sample, the previous reported $P_c(4450)^+$ peak is confirmed and resolved into two narrow states, $P_c(4440)^+$ and $P_c(4457)^+$. A narrow $P_c(4312)^+$ is discovered with 7.3σ significance.

Since all three states are narrow and below the $\Sigma_c^+ \bar{D}^0$ and $\Sigma_c^+ \bar{D}^{*0}$ thresholds within plausible hadron-hadron binding energies, they provide the strongest experimental evidence to date for the existence of bound states of a baryon and a meson. According to some theoretical models^[60,89,91,96,119], several other P_c^+ states should exist. We expect more structures will be observed at LHCb with a larger data sample.

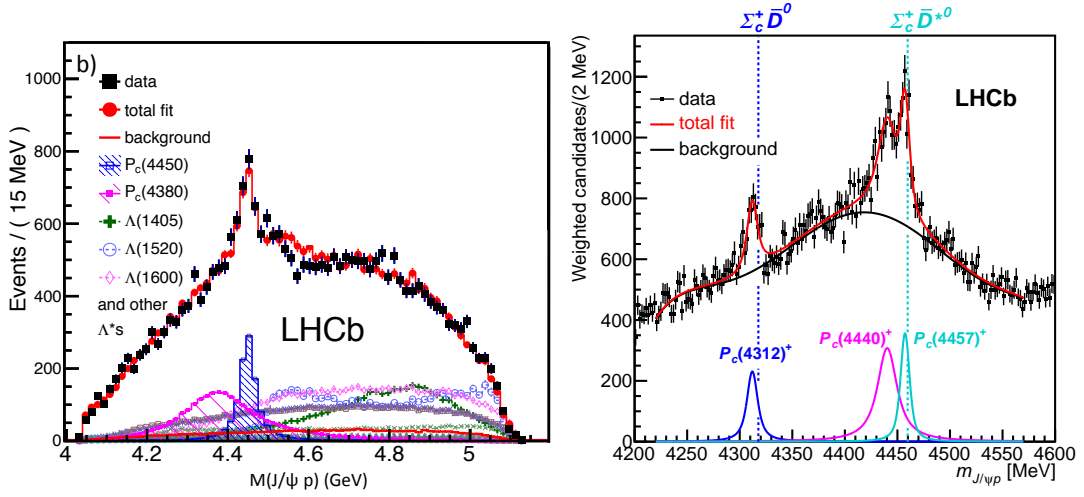


Figure 1.23 Fit projection for $m_{J/\psi p}$ with two P_c states (left)^[12]. Fit to $m_{J/\psi p}$ distribution with three BW described P_c states (right)^[19].

The Cabibbo-suppressed decay $\Lambda_b^0 \rightarrow J/\psi p\pi^-$ was also inspected at LHCb with Run 1 sample^[13]. From a 6-dimentional amplitude analysis, 3.1σ evidence for summed presence of $P_c(4380)^+$, $P_c(445)^+$ and $Z_c(4200)^-$ is obtained. The $m_{p\pi}$ and $m_{J/\psi p}$ projections of the fit are compared in Figure. 1.24. Due to the ambiguities between P_c^+ and Z_c^- terms, any individual exotic state cannot be confirmed from this study. Furthermore, the previous amplitude model should be updated, since three P_c^+ candidates are observed from the updated ananlysis at LHCb^[19]. We expect more significant conclusions can be obtained from the updated analysis of $\Lambda_b^0 \rightarrow J/\psi p\pi^-$. The selection optimization of this channel has been finished, and detailed progresses are introduced in Appendix. B.

The open-strange pentaquark states are searched in $\Xi_b^- \rightarrow J/\psi \Lambda_c^+ K^-$ decay at LHCb^[20], and its significance exceeded 3σ . The $P_{cs}(4459)^0$ state has a mass only about 19 MeV below the $\Xi_c^0 \bar{D}^{*0}$ threshold and a narrow width. Motivated by this fact, the hypothesis of two resonances contributing to the enhancement is tested. The data cannot confirm or refute the two-peak hypothesis.

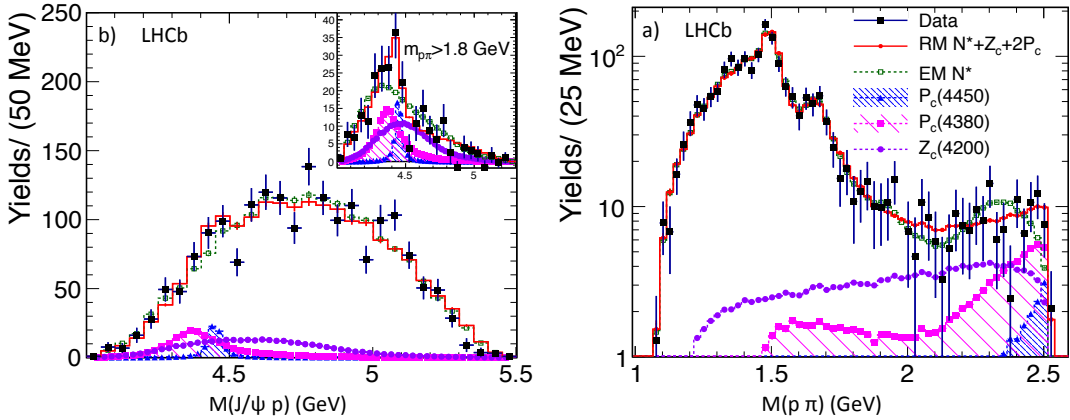


Figure 1.24 Projections of the amplitude fit onto $m_{p\pi}$ (left) and $m_{J/\psi p}$ data distribution for $\Lambda_b^0 \rightarrow J/\psi p\pi^-$ decay in LHCb^[13].

1.3 Theoretical models of multiquark states

Many theoretical models are constructed to explain the exotic hadrons observed in experiments^[114]. The first-principle strategy to treat these observations is lattice QCD, where the path integral is achieved by transcribing the relevant integrals to a lattice of discrete space-time points. This is a rigorous method to test the consistency between experimental discoveries and QCD principle, but the realistic lattice QCD computations require extreme computational resources, which makes it very hard to perform lattice QCD computing. Some simplified models are introduced below.

1.3.1 Multiquark states as molecules

The molecule model thinks the multiquark states are meson-meson or meson-baryon molecule-like systems that are bound via Yukawa-like nuclear forces, and bound states comprised of quarkonium cores surrounded by clouds of light quarks and gluons. Later, the coupled-channel effect, various hyperfine interactions and recoil corrections were introduced into the one-boson-exchange model step by step. Within this model, the hidden-charm molecular type pentaquarks were predicted. In 2019, LHCb collaboration updated their analysis with a ten times larger data sample, which strongly supports the molecular pentaquarks. At present, the idea with one boson exchanged between meson-meson or meson-baryon is an popular way to treat many exotic hadronic interactions. Nevertheless, this model sometimes lacks the definite predictive power as too many unknown parameters such as the coupling constants and cutoff parameter^[114].

1.3.2 Chromomagnetic interaction

In hadron spectroscopy, the hyperfine structure is from the spin-related interaction between quarks or between quarks and antiquarks. The one-gluon-exchange potential causes the mass splittings of the conventional hadrons, whose color configuration is unique. Then, the Hamiltonian of this model can be constructed with the quark masses included, which can be used to calculate the exotic hadrons' masses effectively. The chromomagnetic interaction models play an important role in understanding the multiquark systems, since this model do catch the basic features of spectra and the mass splittings of hadrons rely on the basic controlling symmetries of the quark world.

1.3.3 Hadrocharmonium

In hadrocharmonium picture, a compact color-singlet $Q\bar{Q}$ charmonium core state is treated as “blob” of light hadronic matter. These two components interact via QCD versions of the Van der Waals force, and the mutual forces in this configuration are strong enough to form bound states if the light hadronic matter is in a highly excited resonant state. In this model, decays to the hidden charmonium core state are enhanced to a level where they are competitive with the mode decaying to open-charm final particles^[80].

1.3.4 Rescattering-induced kinematic effects

While the classic signal for the presence of an unstable hadron resonance is a peak in the invariant mass distribution of its decay products, not all mass-spectrum peaks are genuine hadron states, since some peaks are produced by near-threshold kinematic effects. These include threshold cusps and anomalous triangle singularities^[127]. The threshold cusp may be observed when the intermediate two particles must rescatter into final states with a lower threshold. On the other hand, the triangle singularity appears in three-body decay, when the three virtual particles that form the triangle are all simultaneously on the mass shell^[92].

Chapter 2 LHC and LHCb

The data collected from proton-proton collisions is used in this dissertation, which is generated by the Large Hadron Collider(LHC) and collected in LHCb experiment, so a brief overview of LHC and LHCb during Run 1 and Run 2 will be given in this chapter. Currently, the LHCb sub-detectors are being upgraded for higher luminosity situation in the following Run 3 era, the Upgrade I scenario for each subdetector will also be mentioned. As this dissertation includes some ECAL simulation results for LHCb Upgrade II, more detailed description related to LHCb calorimeter system will be reviewed in this chapter.

2.1 The large hadron collider

LHC, an international project at the European Organization for Nuclear Research (CERN) laboratory in Geneva, Switzerland, is the most powerful particle accelerator ever constructed. It produces the highest energy particle beams ever created, making it the premier facility in the world for research in elementary particle physics. The LHC consists of a superconducting particle accelerator, approximately 27 kilometers in circumference, providing two counter-rotating proton beams with a design energy of 7 TeV per beam. It can also provide colliding beams of heavy ions, such as lead. During 2011 and 2012 (Run1) the LHC operated at 4 TeV per beam because of a limitation in the electrical connections between the superconducting magnets. After the connections were upgraded during a nearly two-year shutdown, Run2 began in mid-2015 and lasted to the end of 2018 at 6.5 TeV per beam, exploring a new energy region not accessible during Run1.

Actually, the LHC is the last element of accelerator complex at CERN, which is a succession of machines that accelerate particles to increasingly higher energies, as shown in Figure. 2.1. Each machine in the complex boosts the energy of a beam of particles, before injecting the beam into the next machine in the sequence. Most of the other accelerators in the chain have their own experimental halls where beams are used for experiments at lower energies.

The proton source comes from a simple bottle of hydrogen gas. Then, electric field is used to strip the electrons in hydrogen atoms to create protons. Linac 2, the first accelerator in the complex, accelerates the protons to the energy of 50 MeV. Subsequently, the beam is then injected into the Proton Synchrotron Booster (PSB), which accelerates the protons to 1.4 GeV,

CERN's Accelerator Complex

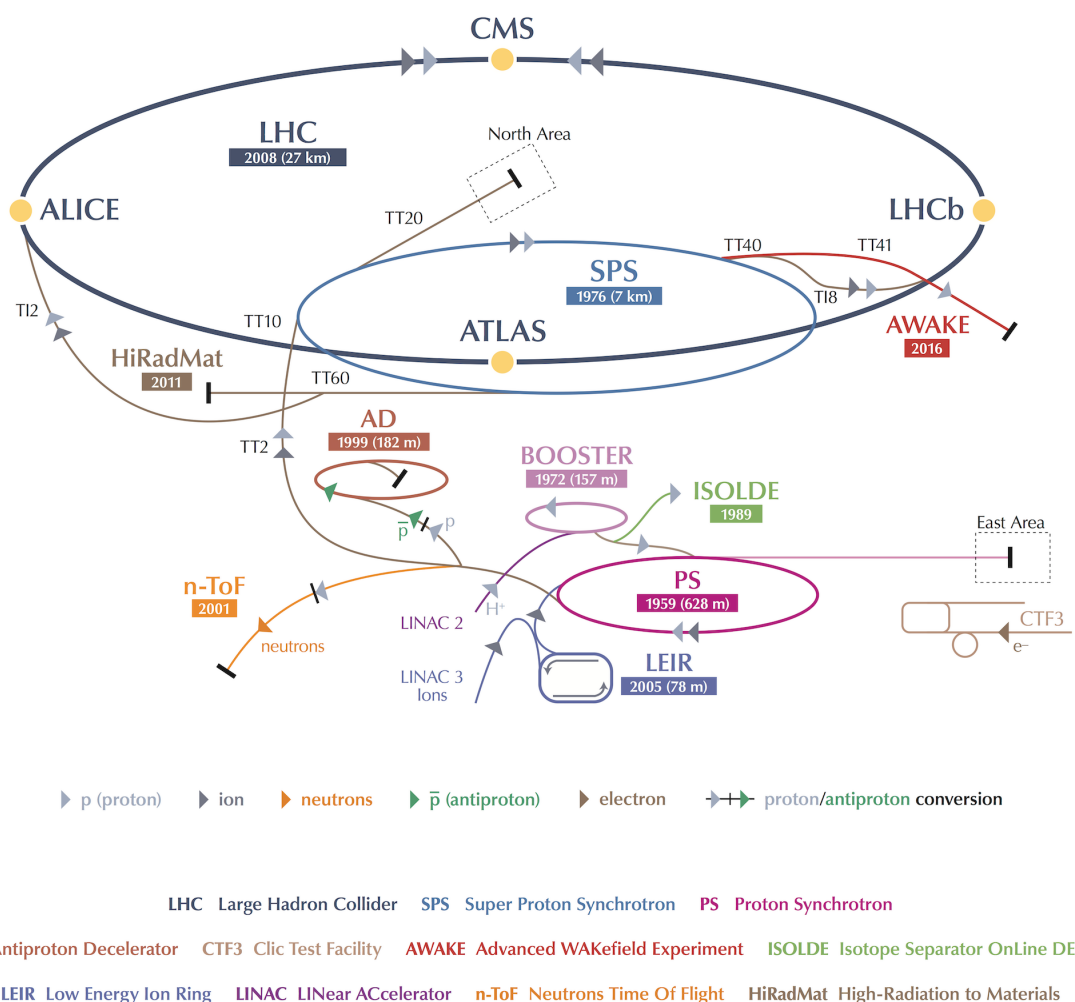


Figure 2.1 The CERN accelerator complex. The LHC is the last ring (dark grey line) in a complex chain of particle accelerators. The smaller machines are used in a chain to help boost the particles to their final energies and provide beams to a whole set of smaller experiments, which also aim to uncover the mysteries of the Universe^[94].

afterwards, the Proton Synchrotron (PS) pushes the beam to 25 GeV. Then, protons are sent to the Super Proton Synchrotron (SPS) which accelerates them to 450 GeV. Finally, the protons are transferred to the two beam pipes of the LHC. Two beams in LHC circulate clockwise or anticlockwise respectively. It takes around 4 minutes to fill each LHC ring, and 20 minutes for the protons to reach their maximum energy of 6.5 TeV. Beams run for several hours inside the LHC beam pipes under normal operating conditions. The two beams collide inside four detectors, ALICE, ATLAS, CMS and LHCb, in which the total energy at the collision point is equal to 13 TeV. The accelerator complex is the Antiproton Decelerator and the Online Isotope Mass Separator (ISOLDE) facility, and the Compact Linear Collider test area, as well as the neutron time-of-flight facility (nTOF). It also provides beams to Gran Sasso (CNGS) project for neutrino experiment. Besides, protons are not the only particles accelerated in the LHC, In addition to the protons, lead ions can be accelerated in LHC, which start from a source of vaporised lead and enter Linac 3 before being collected, they then follow the same route to maximum energy as the protons.

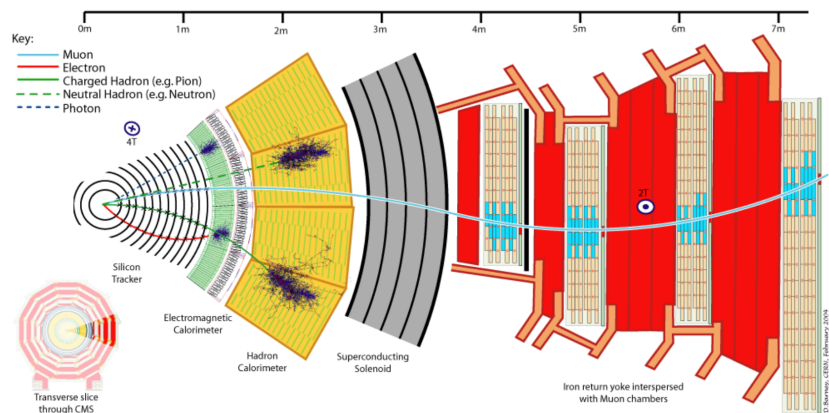


Figure 2.2 Transverse slice through the CMS detector, the particle type can be inferred by combining the detector response in the different subdetectors.^[125]

Four main experiments are placed at the LHC. Two of them are general purpose experiments, studying many aspects of particle productions and decays. These are ATLAS (A Toroidal LHC Apparatus) and CMS (Compact Muon Solenoid) experiments, each of them involves more than 3000 scientists and engineers, in order to search particles beyond standard model directly. The other experiments, each involving around 1000 scientists and engineers, and the physical destinations are more specialised: ALICE, (A Large Ion-Collider Experiment) is concerned with heavy-ion collisions, and LHCb (LHC b-hadron experiment) focuses more on the decays of hadrons containing the bottom quark.

These detectors have been constructed as a series of subdetectors, and all follow roughly

the same scheme, as shown in Figure. 2.2, where the CMS is taken as an example. Starting from the inner layers, which are positioned closest to the interaction region, each detector consists of: subdetectors to measure charged-particle trajectories; subdetectors to stop photons, electrons and hadrons, and measure their energies; subdetectors to record muons, the only charged particles that reach the detector’s outermost layers. The ALICE, ATLAS and CMS detectors are approximately cylindrical in shape, so as to be sensitive to particles emerging in all directions from an interaction. The majority of the particles of interest in LHCb are emitted at small angles, and so the experiment’s detector covers only a narrow cone around the direction of the incoming protons. In next section, the detailed structure of LHCb will be reviewed.

2.2 The LHCb detector

LHCb is a single-arm spectrometer with a forward angular coverage from approximately 10 mrad to 300 (250) mrad, corresponding to a pseudorapidity range of $1.8 < \eta < 4.9$. The layout of the LHCb spectrometer is shown in Figure. 2.3. The right-handed coordinate system adopted has the z axis along the beam, and the y axis along the vertical. This particular geometry of the detector was chosen as the production of b and \bar{b} quarks at LHC energies is such that their directions will tend to be along the beam line. The polar angles of the b and \bar{b} hadrons produced for $\sqrt{s} = 8$ TeV collisions are shown in Figure. 2.4, as predicted from PYTHIA 8 simulations^[137], and similar results apply for pp collisions with the centre-of-mass energy ranging from 7 TeV to 14 TeV.

The detector during Run1 and Run2 was designed to operate at a luminosity of $\mathcal{L} = 2 \times 10^{32} \text{ cm}^{-2}\text{s}^{-1}$, considering the LHC’s design maximum luminosity of $10^{34} \text{ cm}^{-2}\text{s}^{-1}$, a lower luminosity is applied to make for less “busy” events. Higher luminosities mean much larger number of interactions per bunch crossing, leading to more points where proton-proton collisions take place. A proton-proton collision point is also named as a primary vertex (PV), and the identification of primary vertices is essential in many analyses in order to accurately reconstruct the paths of decaying particles. A high number of primary vertices in an event makes it much more difficult to identify the primary vertex from which a particle originated. The higher track multiplicity events, which would result from more collisions, would also make event reconstruction more difficult. Moreover, operating at lower luminosities also limits the radiation damage and detector occupancy. A method referred to as “luminosity leveling” is used to achieve the lower luminosity. This is done by shifting the beams relative to each other, as the number of proton bunches goes down, the beams can be made to overlap more in small

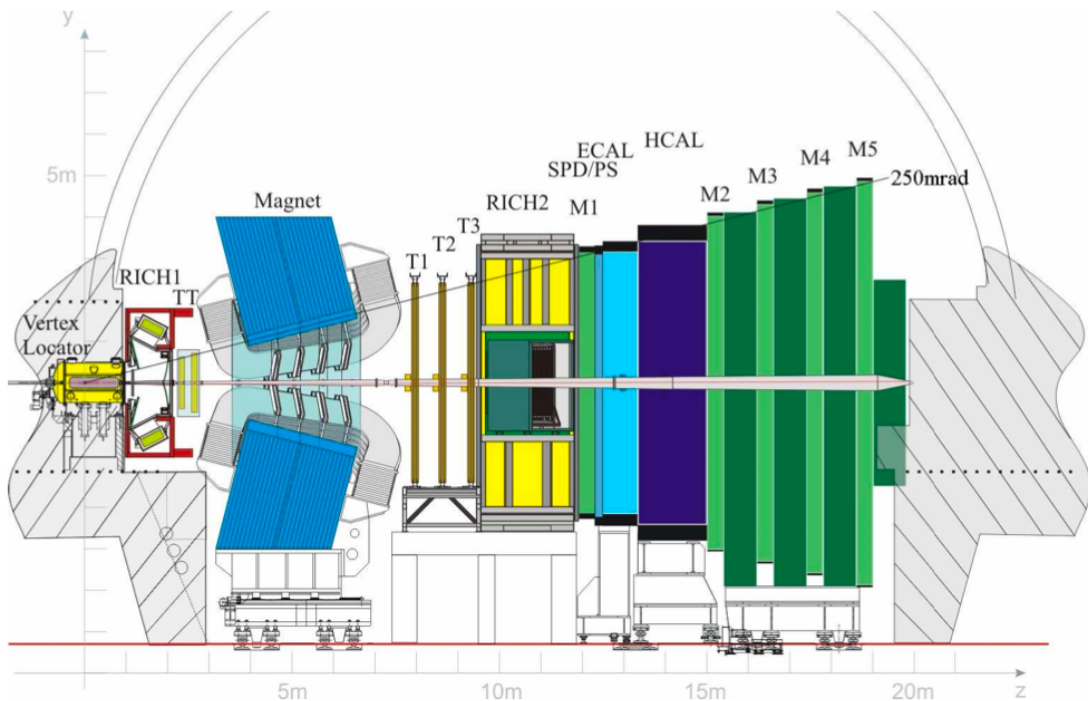


Figure 2.3 View of the LHCb detector^[39].

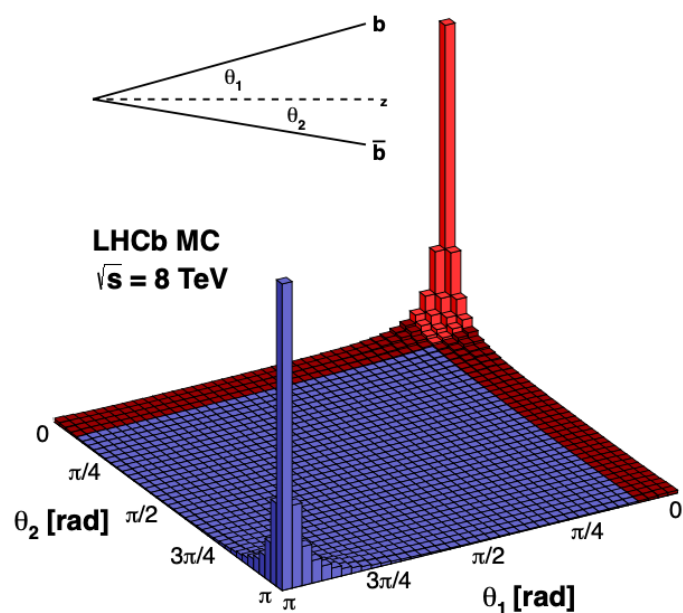


Figure 2.4 Display of $b\bar{b}$ production angles as simulated with PYTHIA 8. The LHCb acceptance is shown in red.

increments so that the luminosity is also kept constant.

After Upgrade I, the luminosity during LHC Run3 will be increased to $2 \times 10^{33} \text{ cm}^{-2} \text{s}^{-1}$, which is around 5 times larger than the value in Run2^[88]. After Upgrade II, the luminosity can reach to $1.5 \times 10^{34} \text{ cm}^{-2} \text{s}^{-1}$, total around 300 fb^{-1} of data will be recorded, which offer us an opportunity to take full advantage of the flavour-physics opportunities at the HL-LHC^[84,131]. More comments to Upgrade II and corresponding the challenge to detector upgrade will be discussed in Chapter 5, especially about ECAL.

2.2.1 Tracking

The tracking system are used to reconstruct charged particles, and the particles go through tracking subdetectors in proper sequence, which contains several parts at LHCb, the Vertex Locator (VELO), Dipole Magnets and four tracking stations, as shown in Figure. 2.5. When it comes to the four stations, one is set in the front of magnet field, referred as Tracker Turicensis (TT) and constructed using silicon microstrip sensors, and other three are located behind the magnet, known as T1, T2 and T3. These three stations are divided into inner and outer parts, the inner section is built by silicon microstrip, called as Inner Tracker (IT), while the outer part is a drift-time detector, referred to as Outer Tracker (OT). The following is some details about these sub-detectors.

2.2.1.1 Vertex Locator

The VELO is used to reconstruct the pp collision point, reconstruct the decay vertices of b and c hadrons and play an important role in second level trigger⁽¹⁾. For precise vertexing measurement, the VELO should be put as close as possible to the decay vertices, and make the material between the first measured point and the vertex as less as possible.

The current VELO is constructed by a series of silicon modules, each providing a measure of the r and ϕ coordinates and perpendicular to the beam direction, as shown in Figure. 2.6. The VELO includes 25 stations, and all of them silicon are placed in vacuum. Each station contains 2 modules, positioned on left and right, as shown in the bottom of Figure. 2.6. Every module has 2 silicon sensors, one is called ϕ -measuring sensor, provides information on the azimuthal coordinate around the beam, the other sensor, called the r -measuring sensor, provides information on the radial distance from the beam axis. The total number of strips for both sensor types is about 180000 channels.

⁽¹⁾ Details about the trigger at LHCb will be discussed in Section 2.2.3.

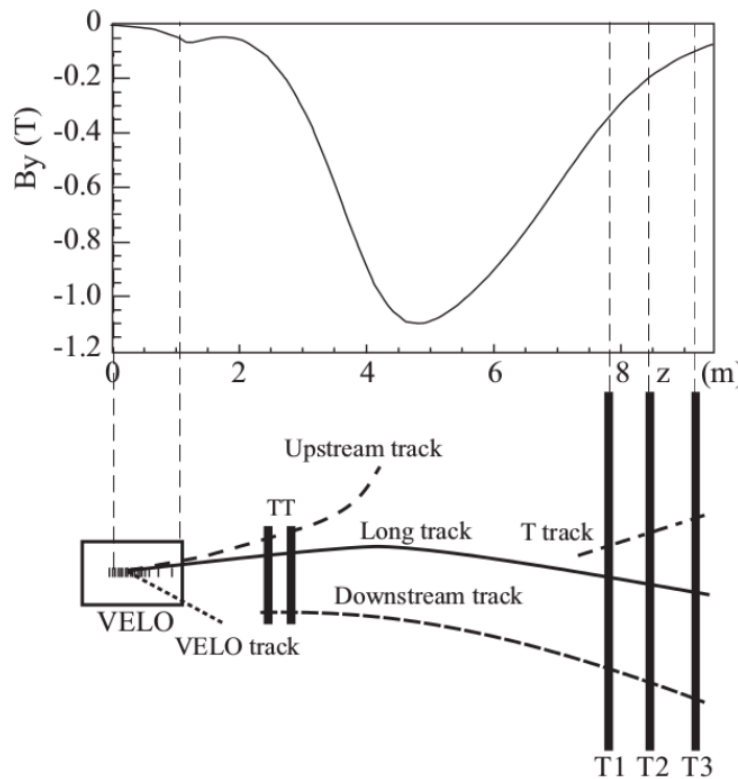


Figure 2.5 Schematic of the tracking components with different types of tracking definitions in the tracking reconstruction^[10]

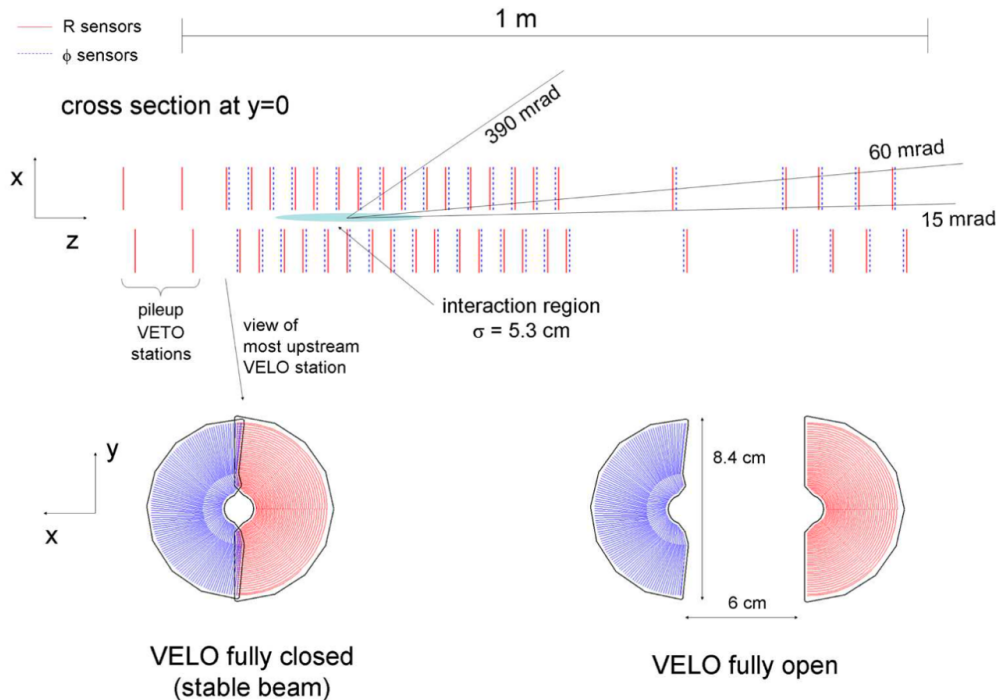


Figure 2.6 Overview of the VELO as seen in the (x, z) plane, at $y=0$, at top. The front face of the modules in the (x, y) plane, for both closed (left) and open (right) positions, at bottom^[39].

Many auxiliary system is designed to keep VELO running normally. As VELO dector is running in extreme radiation environment with strongly non-uniform fluences, the sensors are required to maintaining at a temperature between -10 and 0 °C to counteract the radiation effects. The cooling system use two-phase CO₂ to transfer heat by a conventional freon cooler, which is transferred via a 60 m long line. Besides, in order to reduce beam-induced effects, the dectors have to be operated under vaccum, actually, fully vacuum condition is not unrealizable, a vaccum around 10⁻⁴ mb is required. The dedicated valves and restrictions are used to maintain the vaccum situation, which are activated by membrane switches that react at the desired pressure difference. Another intersting system is known as movement system, which is used to adjust the distance between VELO and interaction points. Before the LHC ring is filled, VELO has to move away, when the pp clusters running stable, the VELO need to be placed into an optimized position, and this position is not exactly known beforehand.

Currently, LHCb Upgrade I is ongoing for Run3 with higher luminosity. The new pixel dector with pixel pitch of 55 μm will be utilized, and this kind of detector cannot lead to ghost tracks. Besides, totally new front-end electronics are included, a thin aluminium radio frequency foil is used to make the detector closer to the interaction points^[141].

2.2.1.2 Dipole Magnets

A dipole magnet is applied to measure the momentum of charged particles, which inlcudes two separate aluminum coils, shaped like a saddle and mounted symmmetrically in a window-frame magnetic yoke. Each coil has fifteen pancakes arranged in five triplets, and the conductor has a specific ohmic resistance below 28Ω m at 20 °C. An overview of the magnet can be seen in Figure. 2.7. The magnetic field is vertically in the y-direction, and covers the acceptance ±250 mrad vertically and ±300 mrad horizontally. The total magnetic field for tracks of 10 m in length is 4 Tm. In order to achieve a good momentum resolution, the integrated magnetic field must have a very precision value, which is on the order of 10⁴. This precision was achieved using arrays of hall probes, with which the components of the field were measured in a fine grid spanning from the interaction point to the RICH2 detector. In order to study the detector asymmetry, the polarity of the magnet is also able to be reversed.

2.2.1.3 Silicon Tracker

Silicon tracker are used in Tracker Turicensis (TT) and the Inner Tracker (IT), which are constructed by silicon microstrip sensors with a strip pitch of about 200 μm. The TT is a planar tracking station, which is located upstream of the LHCb dipole magnet and covers the

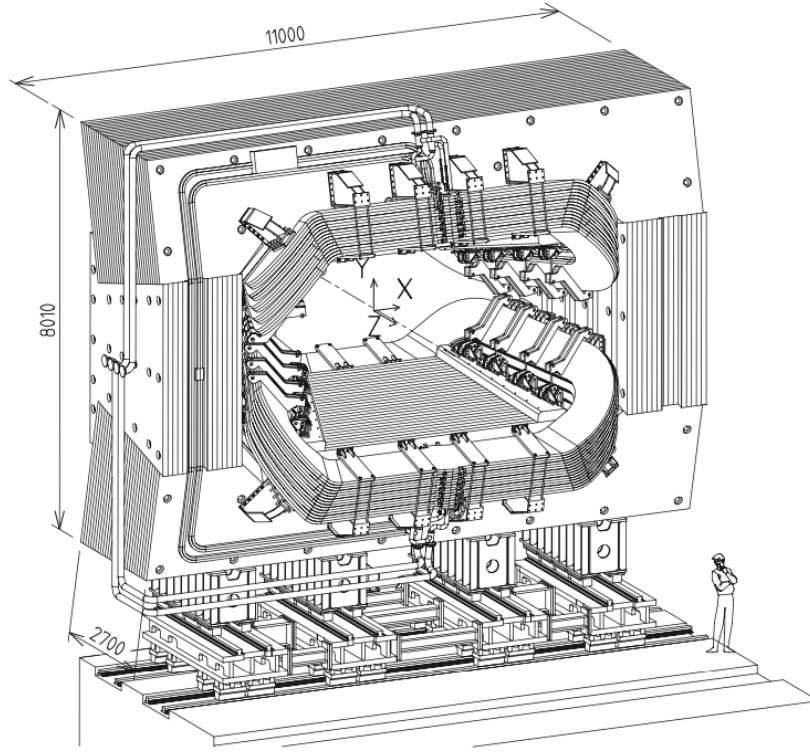


Figure 2.7 Perspective overview of dipole magnet(units in mm)^[39]

full acceptance of the experiment, as shown in the top of Figure. 2.8. The IT refers to the center region of the three tracking stations downstream of the magnet, which is 120 cm wide and 40 cm, as shown in the bottom of Figure. 2.8.

The basic building blocks of the TT layers are half modules, which cover half of the acceptance and are joined together end-to-end in order to create the full module. The half modules are made up of seven silicon sensors, which are organized into either two or three readout sectors, depending on the proximity to the beampipe. The read-out sectors have one, two, three, or four sensors bonded together, such that the sectors closer to the beampipe, which encounter the higher particle flux, have the lower number of sensors bonded together. The space above and below the beampipe are each covered by a half module, and the regions to the sides are covered by rows of seven full modules in the first two layers and eight full modules in the last two layers. To avoid acceptance gaps, adjacent modules are staggered by about 1 cm in z to allow overlap by a few millimeters in x. For the u and v layers, individual modules are rotated by the respective stereo angle.

The three IT stations consist of four detector boxes arranged around the beampipe. A detector box contains four detection layers which are arranged in the same ($x - u - v - x$) configuration as the TT. Each of the detection layers has seven silicon modules. Acceptance

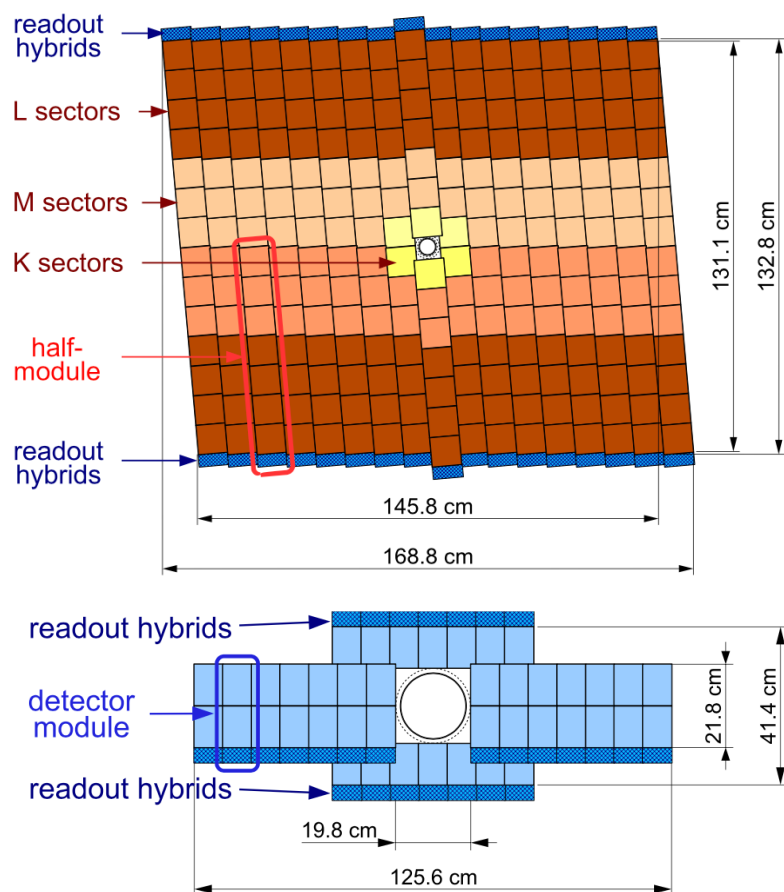


Figure 2.8 Overview of the TT (top) and IT (bottom)^[39]

gaps are avoided by having adjacent modules staggered by 4 mm in the z direction and an overlap by 3 mm in the x direction. The modules in the top and bottom boxes consist of a single silicon sensor, while the modules in the side boxes consist of two silicon sensors.

2.2.1.4 Outer Tracker

To keep the costs low, the IT is enclosed by the Outer Tracker (OT), which is a large area straw-tube detector, and detects about 70% of the charged particles tracks that are produced inside the LHCb acceptance. It has a lower granularity than the ST due to the lower activity in the outer regions. Same as the ST it consists of four layers in an (xuvx) arrangement. The OT provides excellent momentum resolution which is necessary for the precise determination of the invariant mass of the reconstructed b-hadrons. The front-end electronics measure drift times of ionisation clusters produced by charged particles traversing the straw tubes, which is translated into hit position. Figure. 2.9 shows the three OT stations which comprise two layers of circular straws with an inner diameter of 4.9 mm. The straws are filled with a mixture of Argon (70%), CO₂ (28.5%) and O₂ (1.5%) to ensure a fast drift time below 50 ns and a sufficient drift-coordinate resolution (200 μ m).

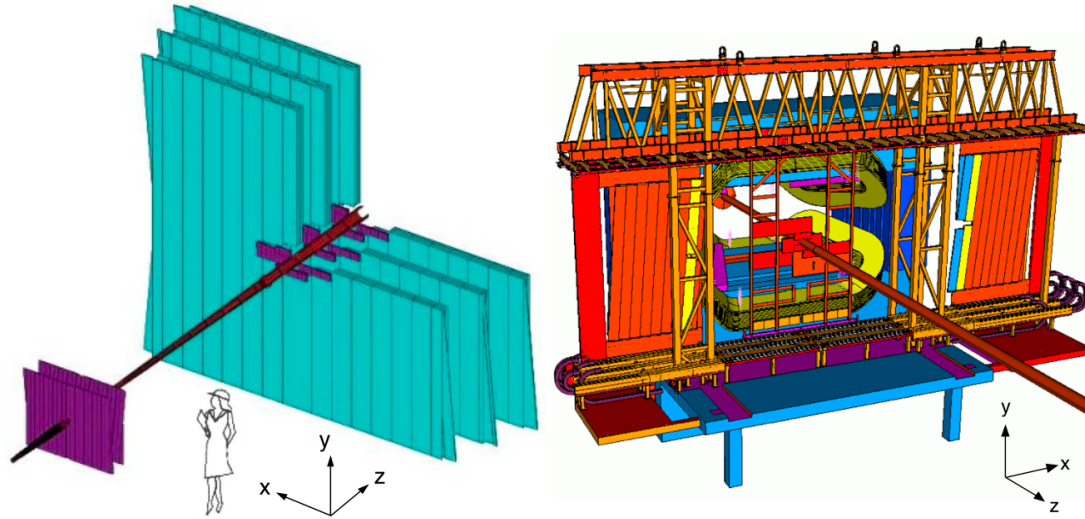


Figure 2.9 Left: The three OT stations surrounding the three IT stations (purple). Right: Overview of the OT bridge carrying the C-frames^[39]

All tracking detectors are being upgraded for Run 3. The upstream tracker (UT) will use silicon strip technology with improved segmentation and acceptance, and the total structure is similar to the current one. The sensors have finer granularity comparing to TT to cope with an increased particle density. Sensor strips are vertical to have precise measurement in the

horizontal direction, the direction that charged tracks bend in the dipole magnet. Each plane is constructed from 16 columnar structure called "staves", which most have 14 sensor modules, and mounted alternatively on the front and the back surfaces of its support structure^[106,132,134].

The tracking stations downstream of the magnet will be replaced with a scintillating fiber (SciFi) system during Upgrade I, which is a total different detector comparing to OT. The SciFi tracker consists of three stations each with four detection planes. The detector is built from individual modules ($0.5\text{ m} \times 4.8\text{ m}$), each comprising 8 fibre mats with a length of 2.4 m as active detector material. The fibre mats consist of 6 layers of densely packed blue-emitting scintillating fibres with a diameter of $250\text{ }\mu\text{m}$. The scintillation light is recorded with arrays of state-of-the-art multi-channel silicon photomultipliers (SiPMs). A custom ASIC is used to digitize the SiPM signals. Subsequent digital electronics performs clustering and data-compression before the data is sent via optical links to the DAQ system. To reduce the thermal noise of the SiPM, in particular after being exposed to a neutron fluence of up to $10^{12}n_{\text{eq}}/\text{cm}^2$, expected for the lifetime of the detector, the SiPM arrays are mounted in so called cold-boxes and cooled down by 3D-printed titanium cold-bars to -40°C ^[106,121].

2.2.2 Particle identification

The purpose of the particle identification (PID) system is to identify the different particle species that travel through the LHCb detector. In $p p$ collisions at the LHC predominantly pions are produced, hence it is crucial to distinguish them from the other particle types. Information from the Ring Imaging Cherenkov detectors is used to distinguish the charged final state hadrons - kaons, pions, and protons. The calorimeters provide information to identify and measure the energy of photons, electrons and hadrons. The muon detectors are employed to detect and measure muons.

2.2.2.1 RICH

The Ring Imaging CHerenkov (RICH) detectors at LHCb are based on the principle of Cherenkov radiation. Cherenkov radiation occurs when a charged particle travels through a medium faster than the speed of light in that medium. Cherenkov photons are emitted in a cone shape with opening angle θ_c with respect to the direction of the particles momentum as

$$\cos(\theta_c) = \frac{1}{n\beta} \quad (2.1)$$

where n is the refractive index of the medium and $\beta = v/c$, where v is the velocity of the particle and c is the speed of light in a vacuum.

The RICH detectors constains RICH1 and RICH2, amimg to identify charged tracks with low momentum and high momentum respectively. The RICH1 detector is positioned between the VELO and the TT. It covers the full angular momentum and provides PID for particles between $1 - 60 \text{ GeV}/c$. The photodetector planes are split into two halves, one above the beam line and one below the beam line. The RICH2 covers the full LHCb angular acceptance. The RICH2 sub-detector is placed between the third tracking station and the first muon station. It successfully distinguishes particles with momenta between 15 and $100 \text{ GeV}/c$. Since high momentum particles are less bent by the magnet, the RICH2 detector covers a smaller angular acceptance of 15 mrad up to 100 (120) mrad in the vertical (horizontal) plane. The RICH2 Rdetector plane is also made up of two sections, placed at either horizontal side of the beam line. The layout of the RICH detectors is given in Figure 2.10. The Cherenkov radiation is emitted and reflected out of the detector acceptance by a spherical mirror and a flat mirror. They are focused on detection planes, where the Cherenkov photons are detected using Hybrid Photon Detectors (HPDs). Each half of RICH1 (RICH2) is equipped with 98 (144) HPDs. The particles velocity is reconstructed by identifying rings of Cherenkov photons. In combination with the momentum information from the tracking stations, the mass is determined, and the particle can be identified.

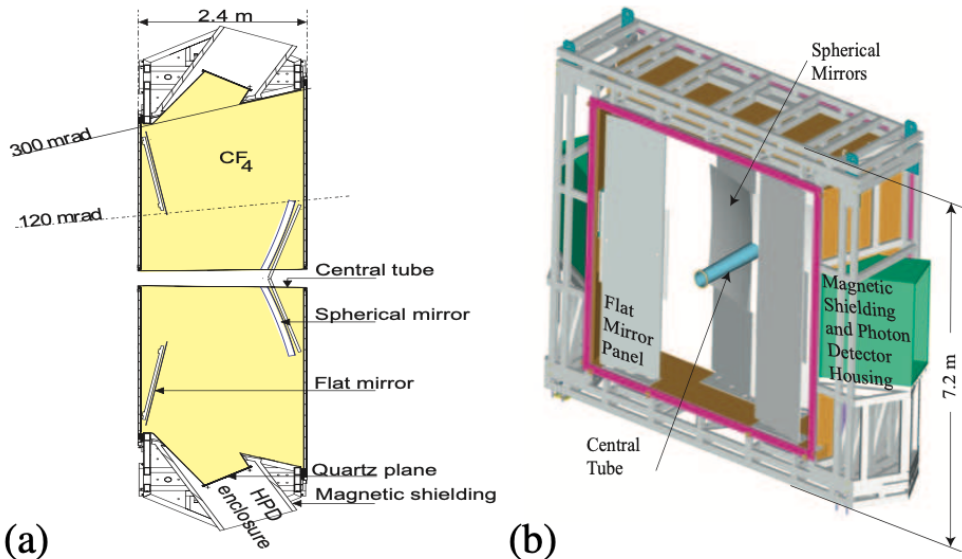


Figure 2.10 Sideview of the RICH1 detector (Left) and top view of the RICH2 detector^[39]

In order to allow operation of the RICH detector system at the upgrade luminosity, The RICH detectors is being upgraded by installing new single-photon detectors (multianode photomultiplier tubes in place of hybrid photo-detectors) read out by 40 MHz capable electronics, and by modifying the upstream RICH optics and mechanics. The RICH1 optical system has

been redesigned: in particular the focal length of the spherical mirrors is increased from 2.7 m to 3.7 m to reduce the hit occupancy on the photodetectors^[87,106].

2.2.2.2 Calorimeters

The main purpose of the calorimeter system is the identification of hadrons, electrons and photons, and the measurement of their energies and positions. It is important for calorimeters to enable the reconstruction of B -decay channels containing a prompt photon or π^0 . The requirement of a good background rejection and reasonable efficiency for these channels adds demanding conditions on the detector performance in terms of resolutions shower separation.

The general structure is that of an electromagnetic calorimeter (ECAL) followed by a hadron calorimeter (HCAL) as shown in Figure. 2.3. Besides, The scintillator pad detector (SPD) and preshower detector (PS) are set in the front of ECAL, the SPD is used to reduce the background for electron trigger, while the PS performs to reject the high background of charged particles in L0 trigger. The ECAL has three zones with different cell size, as shown in the left plot of Figure. 2.11. In the inner section, the cell size is designed to be close to the Moliere radius, which leads most of the energy of a shower deposited in one cell. The right plot of Figure. 2.11 shows the lateral segmentation of HCAL, which is divided into two zone according to the cell size. Some properties to the calorimeter sub-detector are summarized in Table. 2.1.

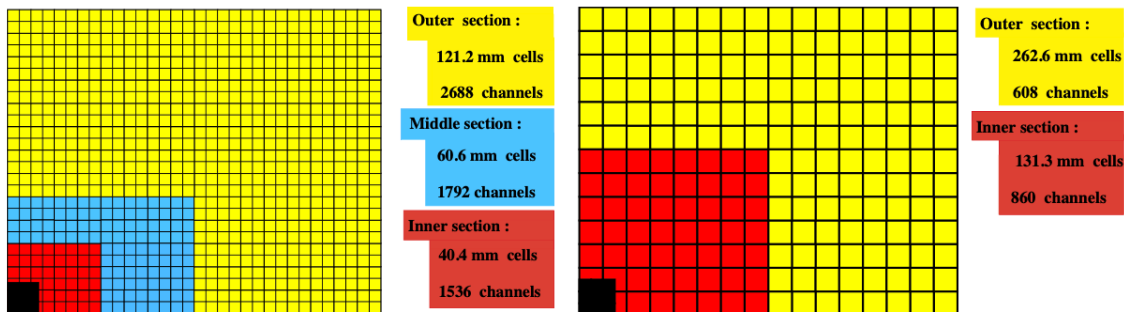


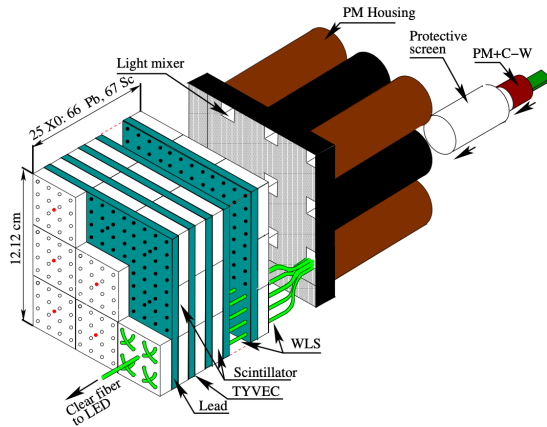
Figure 2.11 The lateral segmentation of the SPD /PS and ECAL (left) and the HCAL (right) for a quarter of the detector front^[39]

The basic principle for current four detectors is that the light generated in scintillator is used to measure the energy deposition, which is transmitted by wavelength shifting fibers, the ECAL will be taken as an example to give more details here.

Figure. 2.12 illustrate the construction of ECAL module used in the inner zone. To set up this sampling calorimeter module, total 66 lead plates and 67 scintillator are used, with the sampling ratio Pb:Sc is 2 : 4 (mm), stringed by the wavelength-shifting (WLS) fibers. The

Table 2.1 Properties of the calorimeter sub-detector.

sub-detectors	SPD /PS	ECAL	HCAL
number of channels	2×5952	5952	1468
overall lateral dimension in x,y	$6.2 \text{ m} \times 7.6 \text{ m}$	$6.3 \text{ m} \times 7.8 \text{ m}$	$6.8 \text{ m} \times 8.4 \text{ m}$
depth in z	$2X_0$	$25X_0$	$5.6\lambda_{\text{int}}$
basic requirements	20 – 30 photoelectrons per MIP	$\sigma(E)/E = 10\%/\sqrt{E} \oplus 1.5\%$	$\sigma(E)/E = 80\%/\sqrt{E} \oplus 10\%$
dynamic range	0 – 100 MIP	$0 - 10 \text{ GeV } E_T$	$0 - 10 \text{ GeV } E_T$


 Figure 2.12 Shashlik construction of ECAL in the inner zone^[42]

WLS is used to transported the light to the photomultipliers (PM), which can digitize the light signal. The digitized signal are processed at 40 MHz rate by the dead-timeless Front-End electronics. This kind of module is called as shashlik technology.

After the Upgrade I, the calorimeter system at LHCb will become very different. The present ECAL and HCAL will kept, while the PS and SPD will be removed as all trigger will perform in software level⁽²⁾. The ECAL and HCAL front-end electronics will be totally rebuilt, the PM gain will be reduced by factor of 5 to reduce the PM degradation^[105].

The HCAL will be removed after Upgrade II, and the ECAL will be rebuilt using a total new technology. The specific scheme of ECAL at LHCb is under consideration, and more details about this will discussed in Chapter. 5.

2.2.2.3 Muon system

The final part of the LHCb detector is the muon system which provides the identification of muons. The muon system is made of five stations (M1 to M5) covering an angular acceptance of

(2) More details will be discussed in Section. 2.2.3

± 300 mrad in the horizontal plane and ± 200 mrad in the vertical plane, as shown in Figure 2.13. This corresponds to a geometrical efficiency of approximately 46% for the detection of muons arising from B hadrons. The first muon station, M1, is placed before the calorimeters in order to avoid possible multiple scattering effects that could modify the particle trajectory. The remaining stations, M2 to M5, are placed after the calorimeter system, at the end of the LHCb detector, and are separated by iron planes 80 cm thick. Each muon station is divided into four regions (R1-R4) as shown in Fig. 2.19. The R1 region is the closest to the beam-pipe and has the most dense segmentation while the R4 region is the farther. The segmentation defined per region is such that the charged particle occupancy is expected to be approximately the same in each region. All the muon chambers are composed by Multi-Wire Proportional Chambers, except for the inner region of the M1 station, which exploits three gas electron multiplier foils sandwiched between anode and cathode planes (GEM detectors). In total, the muon system consist of 1368 MWPC and 12 GEM detectors.

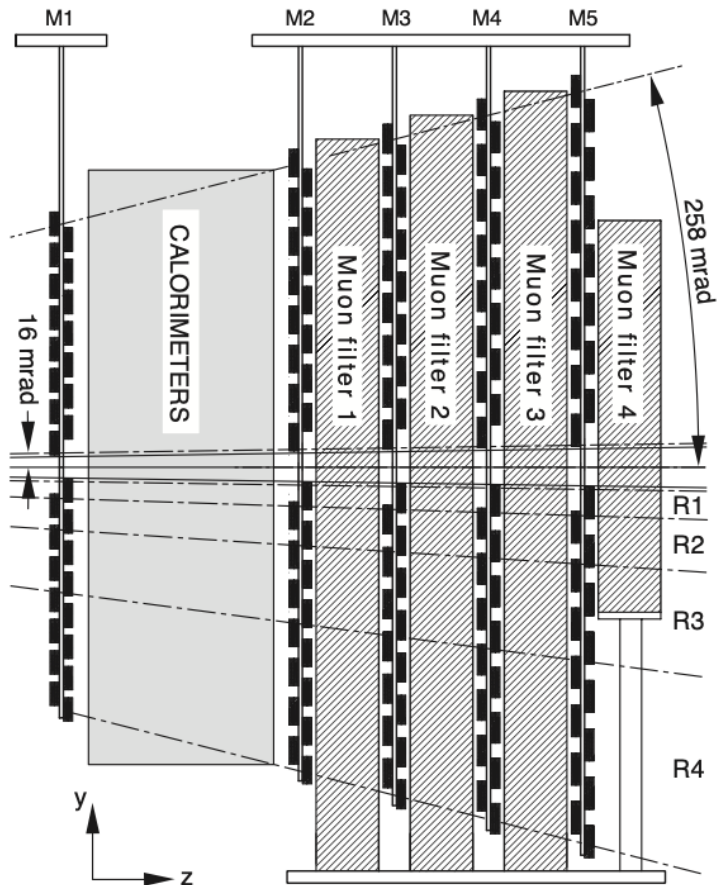


Figure 2.13 Sideview of the muon system^[39]

During Upgrade I, the muon off-detector readout electronics will be redesigned to allow

complete event readout at 40 MHz. Besides, the M1 before the calorimeter system will be removed^[63,106].

2.2.3 Trigger

The nominal instantaneous luminosity is around $2 \times 10^{32} \text{ cm}^{-2} \text{ s}^{-1}$ during Run 1 and Run 2, and the rate of events with collisions is roughly 10 MHz when produce at least two charged particles with enough VELO and tracking hits to allow for their reconstruction. In fact, the rate to storage is about 2-5 kHz, which is achieved by the trigger system to reduce the rate by selecting only interesting events. An intial reduction down to 1 MHz comes from the Level-0 (L0) hardware trigger, which uses custom electronics and runs synchronously with the 40 MHz bunch crossing frequency. High Level Trigger (HLT) follows the L0, which is a software-base trigger. The HLT is subdivided into two stage, which runs asynchronously on a processor farm and reduces the rate to the desired range. The LHCb trigger scheeme is shown in Figure. 2.14. More details will be given on each stage in the following sections.

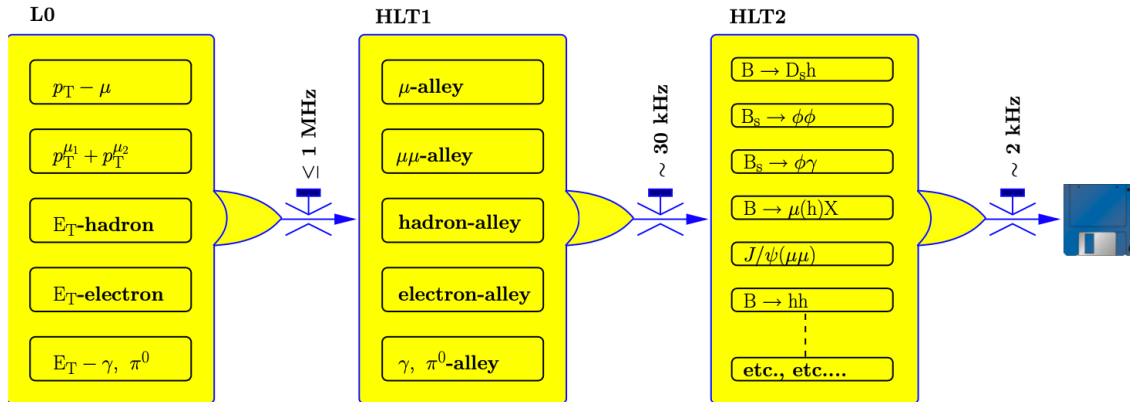


Figure 2.14 Flow-diagram of the different trigger sequences^[39].

2.2.3.1 L0 trigger

The L0 trigger contains three components: the pile-up system, the Level-0 calorimeter trigger and the Level-0 muon trigger. All components are connected to the Level-0 dicision unit (DU) which is used to evaluate the final dicision by collecting all the information obtained from the trigger system, as shown in Figure. 2.15.

The pile-up system is used to distinguish the crossings with single and multiple visible interactions, which is based on the silicon sensors in the VELO to measure the radial position of tracks. The pile-up system has two functions: to provide the position of the primary vertices

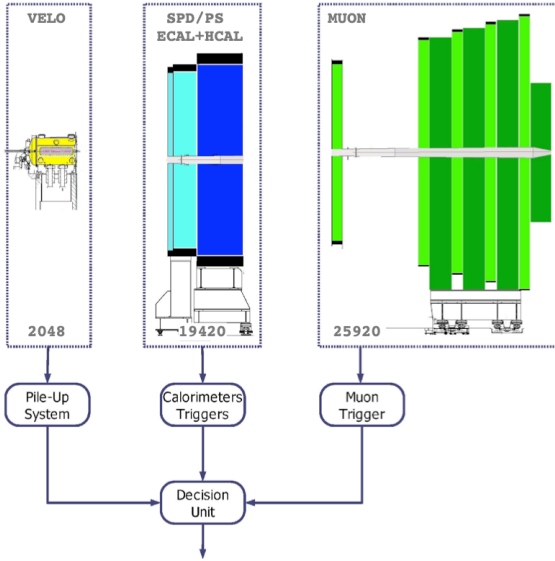


Figure 2.15 Overview of the L0 trigger^[39].

candidates along the beam-line and to measure of the total backward charged track multiplicity.

The calorimeter trigger is designed to search for high E_T particles by adding the E_T of 2×2 cells and selecting the clusters with the largest E_T , this step is performed on the Front-End card. Then the information from ECAL and PS&SPD are merged to identify the type of electromagnetic candidate, electron, γ or π^0 . Besides, the E_T of all HCAL cells is summed to reject crossings without visible interactions. The total number of SPD cells with a hit are counted to provide a measure of the charged track multiplicity in the crossing.

A L0 muon processor is used to search for the two muon tracks with the largest and second largest p_T , which is performed on the logical pads. This trigger can look for hits regarded as a straight line through the five muon stations and pointing to the interaction point. The track position in the first two stations allows the determination of its p_T . From this system, the p_T resolution of a reconstructed stand-alone muon can reach to 20%.

2.2.3.2 HLT1 trigger

The HLT1 trigger can reconstruct the trajectories of charged particles traversing full LHCb tracking system, besides, a precision primary vertex reconstruction is perform^[22] Most particle-identification algorithms cannot be executed in this stage excepting muon identification, due to a clean signature. At the same time, the electrons are identified by associating tracking to ECAL clusters, photon and neutral pion are also built from the clusters reconstructed in the L0 trigger.

The steps of HLT1 algorithms is shown in Figure. 2.16. Firstly, the VELO tracks are

reconstructed, as well as the finding of primary vertices. Then the VELO tracks are extrapolated to match the hits in the TT stations to form upstream tracks. By the way, this process can also reduce the number of fake VELO tracks. Finally, the long tracks are reconstructed by combining the information from downstream trackers, and the search window in the IT and OT is defined by the maximum possible function of charged particles with p_T larger than 500 MeV. The next step is to fit tracks with a Kalman filter to obtain the optimal parameter estimate, as well as the fake track rejection to removed the tracks with poor quality.

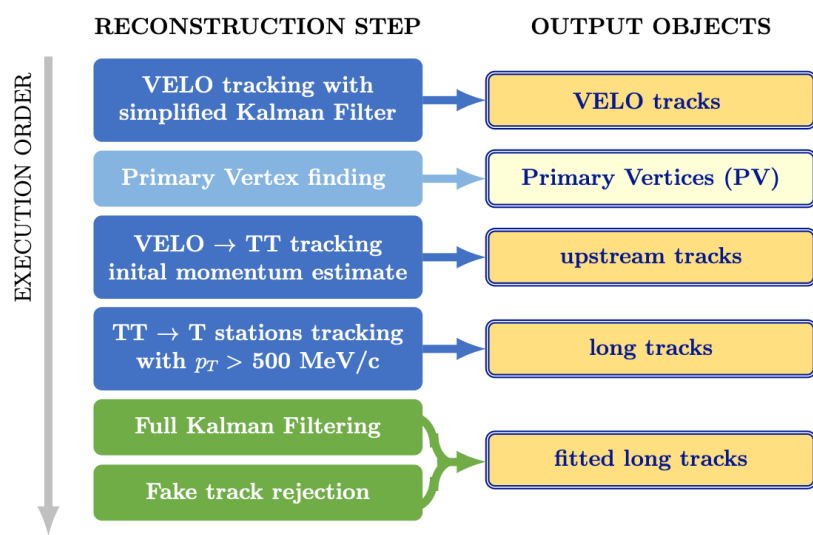


Figure 2.16 Track and vertex reconstruction in the HLT1 trigger^[22].

The muon identification in HLT1 with all fitted tracks. For the muon tracks, the corresponding hits are required in the four MUON stations, which is also used in HLT2 and offline.

2.2.3.3 HLT2 trigger

In the HLT2 stage, the full event reconstruction and identification is performed, including the charged track reconstruction, neutral particle reconstruction and particle identification with the information from PID detectors considered. The corresponding steps of track and vertex reconstruction are shown in Figure. 2.17.

In the charged particle reconstruction process, the HLT1 algorithm is repeated firstly, a second step is to reconstruct the lower-momentum tracks which is overlooked in HLT1. The track reconstruction becomes larger as low p_T tracks included and no TT hits required. Besides, the long-live particles that decay outside the VELO are reconstructed using T-station segments, which are extrapolated to the magnetic field and combined with hits in the TT. Next step

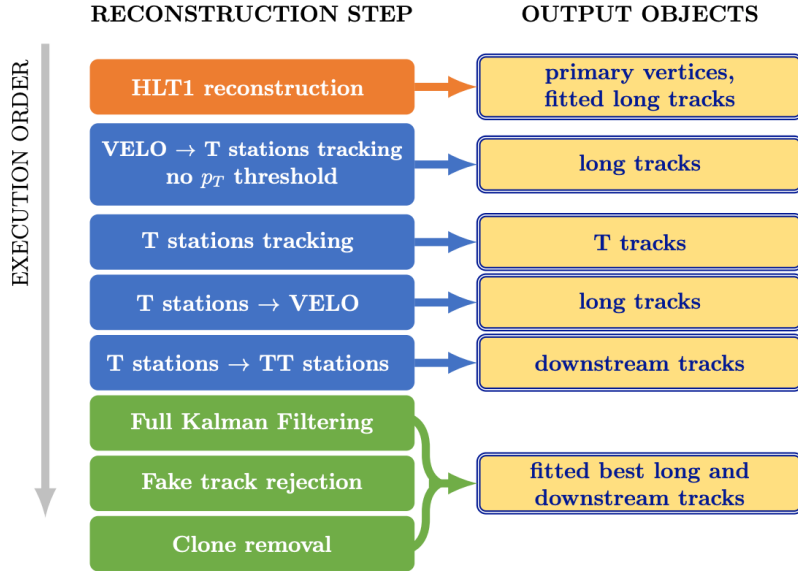


Figure 2.17 Track and vertex reconstruction in the HLT2 trigger^[22].

is to reject fake tracks from the random combination of hits or a mismatch with different tracks segments. This procedure is based on the Kalman filter and multi-variable analysis tool (TMVA). Then the remaining tracks are filtered to remove the clone tracks that share enough hits in each subdetector.

The RICH detectors provide the important discrimination between kaons, pions and protons, and this information can add likelihood for each mass hypothesis to the reconstructed tracks. The calorimeter system can offer PID information by matching between reconstructed tracks and calorimeter clusters, combining the information from MUON system, mature PID values are provided to the tracks.

2.2.3.4 Trigger system after Upgrade I

The most distinguishing feature of trigger after Upgrade I at LHCb is a full software scheme, which can offer unprecedented flexibility in designing selections, and in particular allows efficient triggering on low-momentum signatures which would normally be out of the reach for hadron collider. The dataflow after Upgrade I is illustrated in Figure. 2.18

As the L0 trigger is removed, all the trigger decisions are based on the HLT, which is split into two stages, as similar as the strategy in Run 2. This two stages are separated by a disk buffer that save data used for alignment and calibration. The HLT1 can reject events containing only poor interesting particles for any LHCb analysis, and HLT2 uses the full reconstruction and identification algorithms to obtain the high-level physics objects relevant to analysis for permanent storage. Many R&D projects are under way currently, and some algorithm

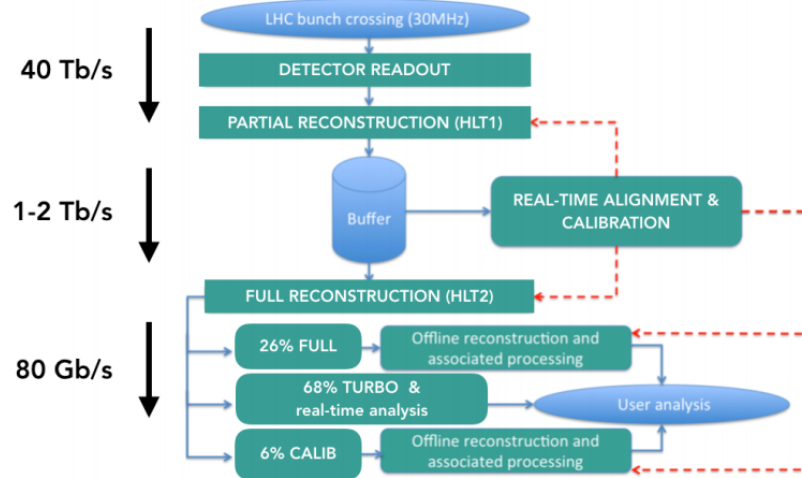


Figure 2.18 Dataflow in the upgraded LHCb detector^[108].

optimization and code migration tasks have made great advances^[75,107–109].

Chapter 3 Observation of Z_{cs} states in $B^+ \rightarrow J/\psi \phi K^+$ decay

3.1 Study motivation

Since the discovery of the $X(3872)$ state by the Belle experiment in 2003^[71], more than twenty non-conventional hadrons that contain $c\bar{c}$ or $b\bar{b}$ quarks have been found and studied^[156]. In contrast to the neutral states, charged states like $Z_c(3900)^+$ ^[29,115] and $Z_c(4430)^+$ ^[8,68,72] provide evidence for tetraquark exotic states, because light quarks are required to account for the non-zero electric charge in addition to the heavy quarkonium. ⁽¹⁾ Previously, only the u or d quarks were observed to constitute the light quark content of such charged exotic states, even though the existence of a Z_{cs} state as a strangeness-flavour partner of the $Z_c^+(3900)$ state has been predicted^[65,77,86,102,149]. Therefore, it is an important research topic to search the hidden charm tetraquark with strangeness in hadron spectroscopy field, the property of this type of states can help test different theoretical predictions to nonstandard hadron states.

3.1.1 Previous studies

In Run 1 analysis, $Z_{cs}^+ \rightarrow J/\psi K^+$ contributions were also tested. The results were mentioned in Ref. [15] and detailed in Thomas Britton's Ph.D. thesis^[58]. They are summarized in Table 3.2. The improvement for $J/\psi K^+$ mass distribution is shown in Figure. 3.1. About 3σ evidence for a Z_{cs}^+ was found, but deemed insufficient to claim discovery of an exotic state with a new quark content.

3.1.2 This analysis

In this analysis with full Run 1 and Run 2 data, and an improved selection, the B^+ signal yield is about 5.5 times of that found in the Run 1 analysis (20% more signal found in Run 1 data). At the same time background fraction is reduced to much smaller level (4%). The improved data sample offers better sensitivity to exotic hadron with smaller contributions. Therefore, in this analysis we focus on exploring $X \rightarrow J/\psi \phi$ sector in more detail, as well as on $Z_{cs}^+ \rightarrow J/\psi K^+$ states.

⁽¹⁾ Charge conjugation is implied throughout this thesis.

Table 3.1 Results from previous publication based on Run 1 data at LHCb^[16].

Contribution	Significance	Fit results		
		M_0 [MeV]	Γ_0 [MeV]	FF%
All K(1 ⁺)	8.0 σ			$42 \pm 8^{+5}_{-9}$
NR _{ϕK}				$16 \pm 13^{+35}_{-6}$
2^1P_1 K(1 ⁺)	7.6 σ	$1793 \pm 59^{+153}_{-101}$	$365 \pm 157^{+138}_{-215}$	$12 \pm 10^{+17}_{-6}$
2^3P_1 K'(1 ⁺)	1.9 σ	$1968 \pm 65^{+70}_{-172}$	$396 \pm 170^{+174}_{-178}$	$23 \pm 20^{+31}_{-29}$
All K(2 ⁻)	5.6 σ			$11 \pm 3^{+2}_{-5}$
1^1D_2 $K_2(1770)$	5.0 σ	$1777 \pm 35^{+122}_{-77}$	$217 \pm 116^{+221}_{-154}$	
1^3D_2 $K_2(1820)$	3.0 σ	$1853 \pm 27^{+18}_{-35}$	$167 \pm 58^{+83}_{-72}$	
$K(1^-)$				
1^3D_1 $K^*(1680)$	8.5 σ	$1722 \pm 20^{+33}_{-109}$	$354 \pm 75^{+140}_{-181}$	$6.7 \pm 1.9^{+3.2}_{-3.9}$
$K(2^+)$				
2^3P_2 $K_2^*(1980)$	5.4 σ	$2073 \pm 94^{+245}_{-240}$	$678 \pm 311^{+1153}_{-559}$	$2.9 \pm 0.8^{+1.7}_{-0.7}$
$K(0^-)$				
3^1S_0 $K(1830)$	3.5 σ	$1874 \pm 43^{+59}_{-115}$	$168 \pm 90^{+280}_{-104}$	$2.6 \pm 1.1^{+2.3}_{-1.8}$
All $X(1^+)$				$16 \pm 3^{+6}_{-2}$
$X(4140)$	8.4 σ	$4146.5 \pm 4.5^{+4.6}_{-2.8}$	$83 \pm 21^{+21}_{-14}$	$13.0 \pm 3.2^{+4.8}_{-2.0}$
$X(4274)$	6.0 σ	$4273.3 \pm 8.3^{+17.2}_{-3.6}$	$56 \pm 11^{+8}_{-11}$	$7.1 \pm 2.5^{+3.5}_{-2.4}$
All $X(0^+)$				$28 \pm 5 \pm 7$
NR _{$J/\psi\phi$}	6.4 σ			$46 \pm 11^{+11}_{-21}$
$X(4500)$	6.1 σ	$4506 \pm 11^{+12}_{-15}$	$92 \pm 21^{+21}_{-20}$	$6.6 \pm 2.4^{+3.5}_{-2.3}$
$X(4700)$	5.6 σ	$4704 \pm 10^{+14}_{-24}$	$120 \pm 31^{+42}_{-33}$	$12 \pm 5^{+9}_{-5}$

3.2 Selection

3.2.1 Dataset

This analysis uses all the pp collision data in Run 1 and Run 2 stages, corresponding to an integrated luminosity of 9 fb^{-1} . The simulation samples of the $B^+ \rightarrow J/\psi \phi K^+$ decay⁽²⁾ are generated by PYTHIA with pp collisions, with PYTHIA 8 generator. The Monte Carlo event type is 12145051, in which B^+ is forced to decay into the $J/\psi \phi K^+$ final state with the PHSP(phase space) model. The statistics and simulation version is show in Table 3.3

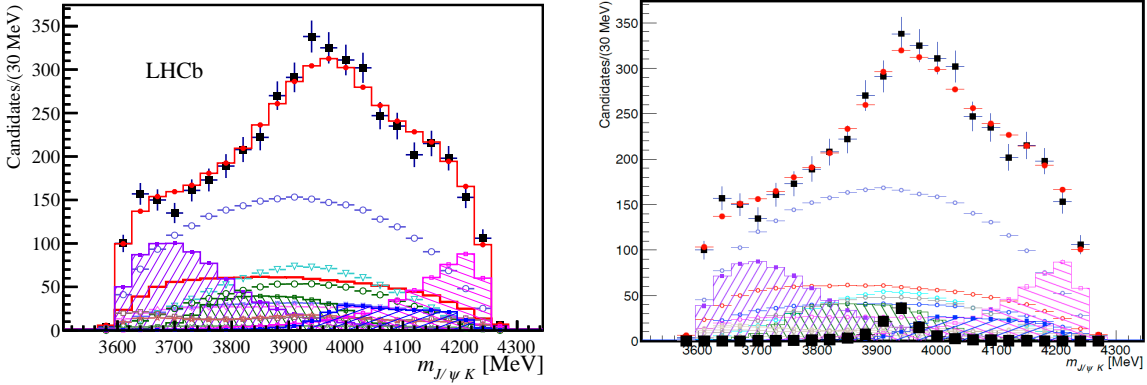
3.2.2 Reconstruction and pre-selection

In this analysis the reconstruction of the B^+ candidate starts from the stripping line FullDSTDIMuonJpsi2MuMuDetachedLine in the DiMuon stream. The stripping version of each dataset is listed in Table 3.4. The selection criteria in this stripping line did not vary in different years, and are summarized in Table B.1. The J/ψ candidate is formed by two oppositely charged tracks consistent with muon hypotheses (IsMuon) with $p_T > 500 \text{ MeV}$ and

⁽²⁾ Inclusion of charge conjugation is implied throughout this note.

Table 3.2 Z_{cs}^+ tests of LHCb Run 1 analysis^[58].

J^P	mass [MeV]	width [MeV]	fit fraction	significance
$2^+/0^-$	no inform	4-5	0.5-0.6%	$1.2\sigma/2.5\sigma$
$1^+/2^-$	(3937 ± 7)	$47/(51 \pm 15)$	1.9/2.5%	$2.5\sigma/3.1\sigma$
1^- (fit did not converge)	~ 4220	~ 500	$\sim 10\%$	


 Figure 3.1 Distributions of $J/\psi K^+$ invariant masses for the $B^+ \rightarrow J/\psi \phi K^+$ candidates (black data points) compared with the results of the default amplitude fit (left) and amplitude fit with a Z_{cs}^+ (right) in Run 1 analysis^[58]. The Z_{cs}^+ contribution is shown by large black square point.

good track fit quality $\chi^2/\text{ndf} < 4$. The J/ψ candidate is required to have an invariant mass within the ± 100 MeV window around the known J/ψ mass^[145], and to have a vertex fit quality $\chi^2_{\text{vtx}} < 20$. The J/ψ candidate is consistent with originating from b -hadron decays by requiring its decay length significance (DLS) to be greater than three.

To select good J/ψ candidates, vertex fit χ^2 is required to be less than 9, and the dimuon invariant mass window is reduced to $[-57, 43]$ MeV around the known J/ψ mass^[145]. The J/ψ mass resolution is around 13 MeV. The asymmetric window is used to take FSR of muons into account. To reconstruct the B^+ candidate, the J/ψ candidate is combined with two positively and one negatively charged tracks, all consistent with kaons. This is achieved by PID cuts on the ProbNN variables: $\text{ProbNN}_K(K) > 0.1$ (MC12TuneV3 for Run 1 and MC15TuneV1 for Run 2, respectively). The kaon candidate is required to have transverse momentum, $p_T > 250$ MeV, and detached from the primary vertex (PV) with impact parameter (IP) satisfying $\chi^2_{\text{IP}} > 4$. The three kaon candidates are required to come from the same vertex with good vertex-fit quality, $\chi^2 < 50$ for $\text{ndf} = 3$. The B^+ candidate is required to have a displaced decay vertex, with flight distance (FD) more than 1.5 mm and form a good vertex with fit quality, $\chi^2/\text{ndf} < 9$. It should be consistent with being produced from PV by requiring $\chi^2_{\text{IP}} < 20$ and cosine value of the angle

Table 3.3 The statistics and simulation version of MC. MU is magnet up, MD is magnet down.

year	statistics(MU/MD)	simulation version
2011	754500/766498	Sim08c
2012	1004812/1003052	Sim09b
2016	1147294/1013030	Sim09b
2017	1004122/1014701	Sim09f
2018	1008192/1000411	Sim09f

Table 3.4 stripping version

year	stripping version
2011	Stripping21r1
2012	Stripping21
2015	Stripping24r1
2016	Stripping28r1
2017	Stripping29r2
2018	Stripping34

with respect to PV, DIRA > 0.99. The B^+ candidates with mass $4.9 < M(J/\psi \phi K^+) < 5.7$ GeV are preselected. To reject clone tracks, any two tracks in B^+ candidate have an opening angle smaller than 0.5 mrad are removed.

The $B^+ \rightarrow J/\psi \phi K^+$ decay chain is refitted with two sequential constraints using the DecayTreeFitter to improve the mass resolution: A) the J/ψ candidate mass constrained to its known value^[145] and the B^+ candidate constrained to originating from the associated PV; B) the invariant mass of the B^+ candidate constrained to the known B^+ mass value^[145], with the momenta of the J/ψ and kaon daughters re-calculated according to this constraint. For amplitude fits discussed later, the updated daughter four-momenta are used to calculate invariant masses and angles.

Then, at least one of the two K^+K^- combined mass to be within ± 15 MeV of the known ϕ mass is required^[145]. and only one ϕ candidate is accepted for further analysis. To be more

Table 3.5 Stripping selections of J/ψ candidates in the line FullDSTDiMuonJpsi2MuMuDetachedLine.

Quantity	Selections
IsMuon(μ)	= TRUE
DLL $_{\mu\pi}$	> 0
$p_T(\mu)$	> 500 MeV
Track $\chi^2/\text{ndf}(\mu)$	< 3
$\Delta M(J/\psi)$	< 100 MeV
Vertex $\chi^2(J/\psi)$	< 20
DLS(J/ψ)	> 3

specific, candidates that have two K^+K^- combinations with mass falling into the ± 15 MeV window are abandoned. This reduces the sample by about 3%. To be consistent with quantities used in amplitude analysis, the ϕ candidate mass is recalculated with kaon four-momenta after all kinematic constraints. All the selection criteria are summarized in Table B.2.

It should be noted that the PID requirements on the hadron tracks are not applied when reconstructing the B^+ candidates in the simulation sample. The effect, instead, is reconsidered after correcting the PID distributions in simulation using the PID calibration (PIDCorr).

Events with B^+ candidates in both the simulation and the data samples are required to fire any level-zero trigger line and to be of TOS type with respect to at least one high level trigger lines listed in Table 3.6.

Table 3.6 Trigger requirements on B^+ candidates.

	Run 1	Run 2
L0	Global_DecDecision	
Hlt1 TOS	TrackMuon	
	DiMuonHighMass	
	TrackAllL0	TrackMVA
		TwoTrackMVA
Hlt2 TOS	TopoMu2,3,4Body	
	DiMuonDetachedJPsi	
	DiMuonDetachedHeavy	

3.2.3 Multivariate analysis

The multivariate analysis (MVA) is used to further suppress the backgrounds. The signal training sample is from the $B^+ \rightarrow J/\psi \phi K^+$ simulation using the PHSP model, while the background sample is from the invariant-mass sidebands of $B^+ \rightarrow J/\psi \phi K^+$ data sample, with $M(J/\psi \phi K^+) \in [5.229, 5.254] \cup [5.304, 5.329]$ GeV/ c^2 . These samples are randomly split into two halves, one for the training and the other one for the test.

The following variables are used in the MVA: the log of χ^2_{IP} of B; the log of minimum of ProbNNk among the three kaons; the DIRA of B; the χ^2_{vertex}/dof of B; the p_T of B; the p_T sum of three kaons; the χ^2_{FD} of B; the log minimum χ^2_{IP} of kaons. The distributions of these variables for the signal in the simulation sample and for the background in the data B^+ sidebands are shown in Figure. 3.2 (Run 1) and Figure. 3.3 (Run 2).

For Run 1, The ROC curves of the results of different training methods are given in the left plot of Figure. 3.4. The BDTG method is used as the default method, and the overtraining test for the BDTG method is given for Run 1 in the right plot of Figure. 3.4. The BDTG

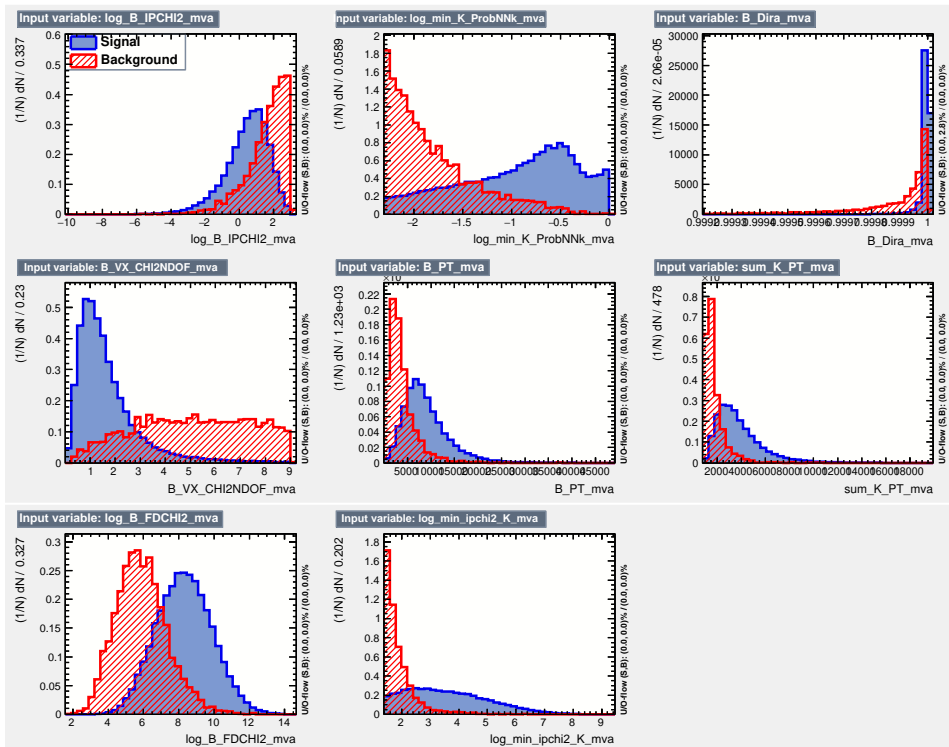


Figure 3.2 Discriminating variables used in the MVA training for Run 1

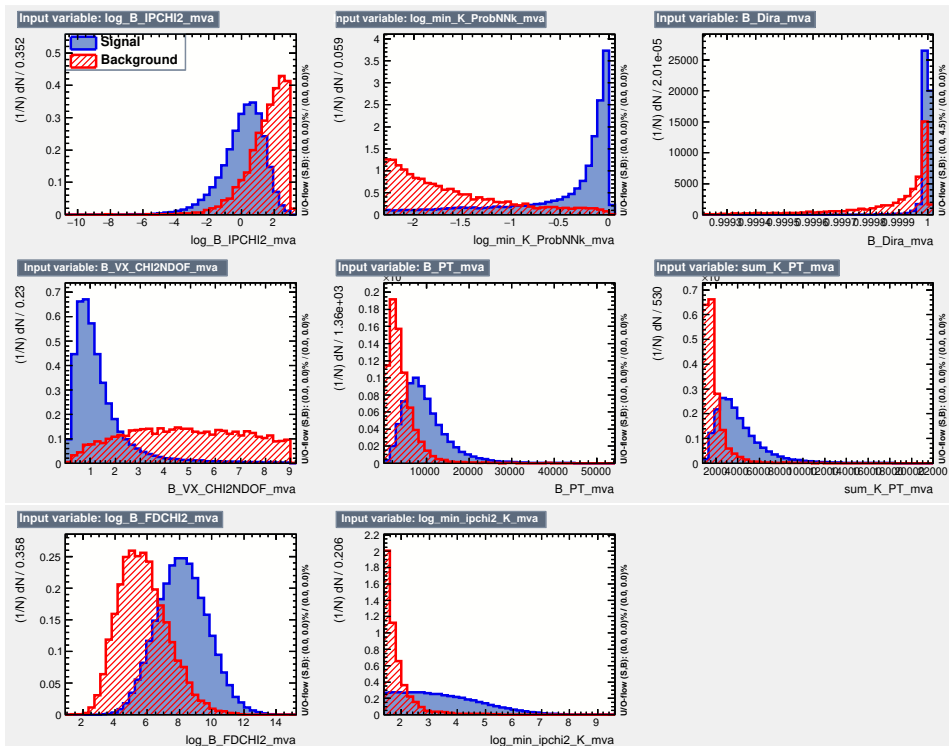


Figure 3.3 Discriminating variables used in the MVA training for Run 2

Table 3.7 All pre-selections of $B^+ \rightarrow J/\psi \phi K^+$ candidates including stripping and offline levels.

Candidate	Quantity	Selections
All tracks	Track fit χ^2/ndf	< 3
All tracks	Ghost prob	< 0.47
μ	IsMuon	= TRUE
μ	DLL $_{\mu\pi}$	> 0
μ	p_T	> 500 MeV
J/ψ	mass window	$\in (-57, 43)$ MeV
J/ψ	Vertex χ^2	< 9
J/ψ	DLS	> 3
K	ProbNNk	> 0.1
K	p_T	> 250 MeV
K	χ^2_{IP}	> 4
$3K$	Vertex χ^2/ndf	< 50/3
ϕ	mass window	± 15 MeV
B^+	Vertex χ^2	< 9
B^+	FD	> 1.5 mm
B^+	χ^2_{IP}	< 20
B^+	DIRA	> 0.99
B^+	M	$\in (4.9, 5.7)$ GeV
B^+	Opening angle of two tracks	> 0.5 mard
B^+	# of ϕ candidate	= 1

discriminant distributions for the training samples are consistent with those in the test samples. No effect of overtraining is observed. Similar results for Run 2 are given in Figure. 3.5.

A 2D scan of BDTG value and cut on track-ghost probability for the kaons is done to maximize the figure of merit (FoM) of the signal significance, defined as $\frac{S}{\sqrt{S+B}} \times \frac{S}{S+B}$. S (B) is the number of the signal (background) events in the $\pm 2.5\sigma$ region around the known B mass in the $J/\psi \phi K^+$ invariant mass distribution of the data. In Figure. 3.6 (Figure. 3.7), the distribution of the FoM as a function of the BDTG cut value and the track-ghost probability for kaons are given for Run 1 (Run 2). A BDTG cut value of > 0.15 (> -0.14) and the track-ghost probability for kaons of < 0.47 (< 0.40) are determined as the default working point for Run 1 (Run 2).

3.3 Invariant B mass fit and Dalitz plot distributions

3.3.1 Signal yields

After the selections, the sample of $B^+ \rightarrow J/\psi \phi K^+$ candidates consists of the signal and of the combinatorial background. Figure. 3.9 show the fitted invariant mass distribution of the $B^+ \rightarrow J/\psi \phi K^+$ candidates, for Run 1 and Run 2 separately. The signal shape is described by

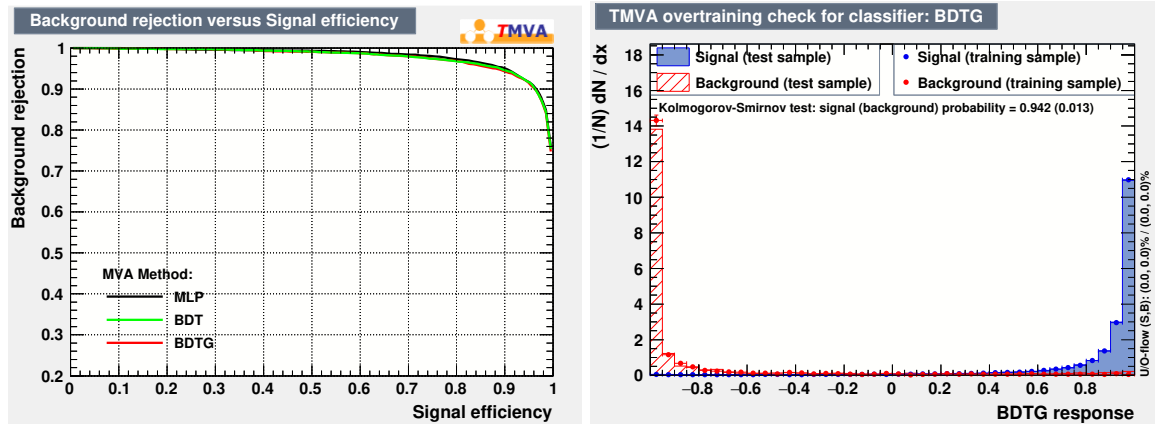


Figure 3.4 (left) ROC curves for different MVA methods and (right) the BDTG output distribution for signals and the background in the training sample and the test sample for Run 1.

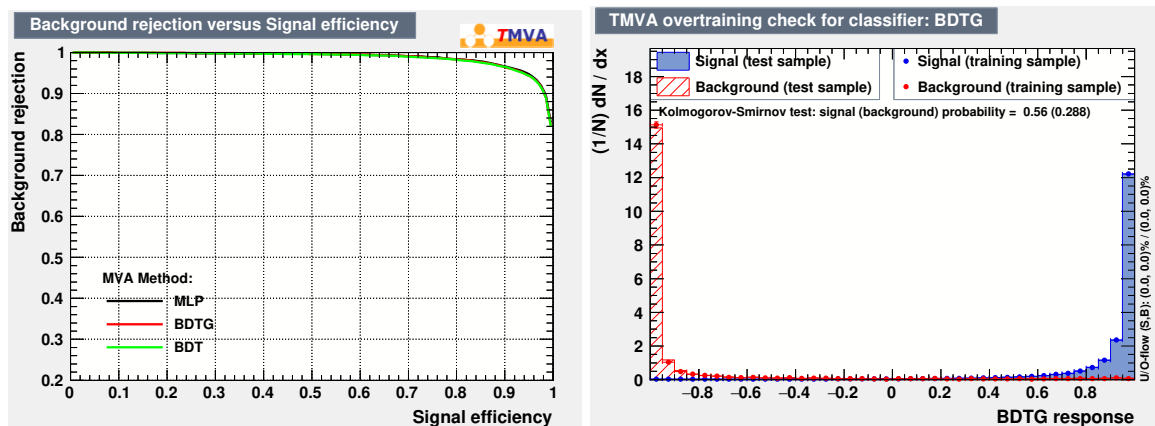


Figure 3.5 (left) ROC curves for different MVA methods and (right) the BDTG output distribution for signals and the background in the training sample and the test sample for Run 2.

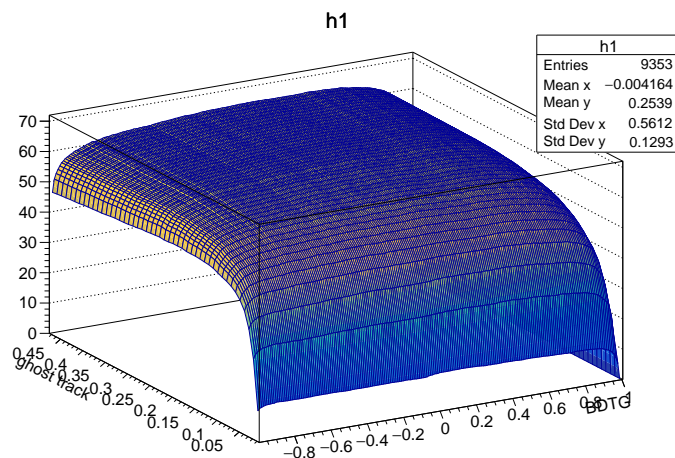


Figure 3.6 Signal significance (arbitrary units) for different cuts on BDTG and track-ghost probability for kaons for Run 1.

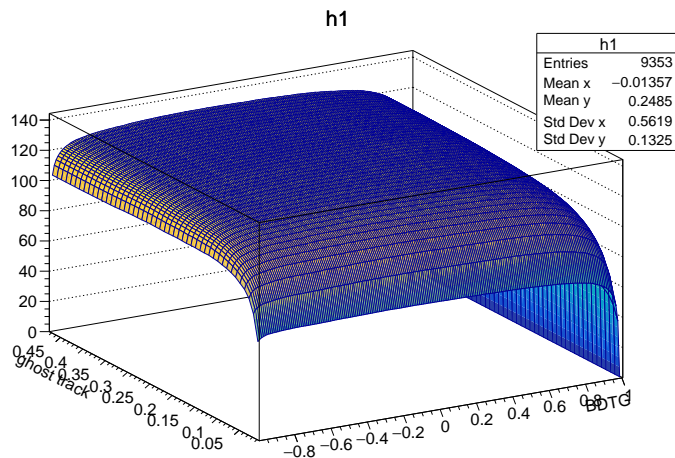


Figure 3.7 Signal significance (arbitrary units) for different cuts on BDTG and track-ghost probablity for kaons for Run 2.

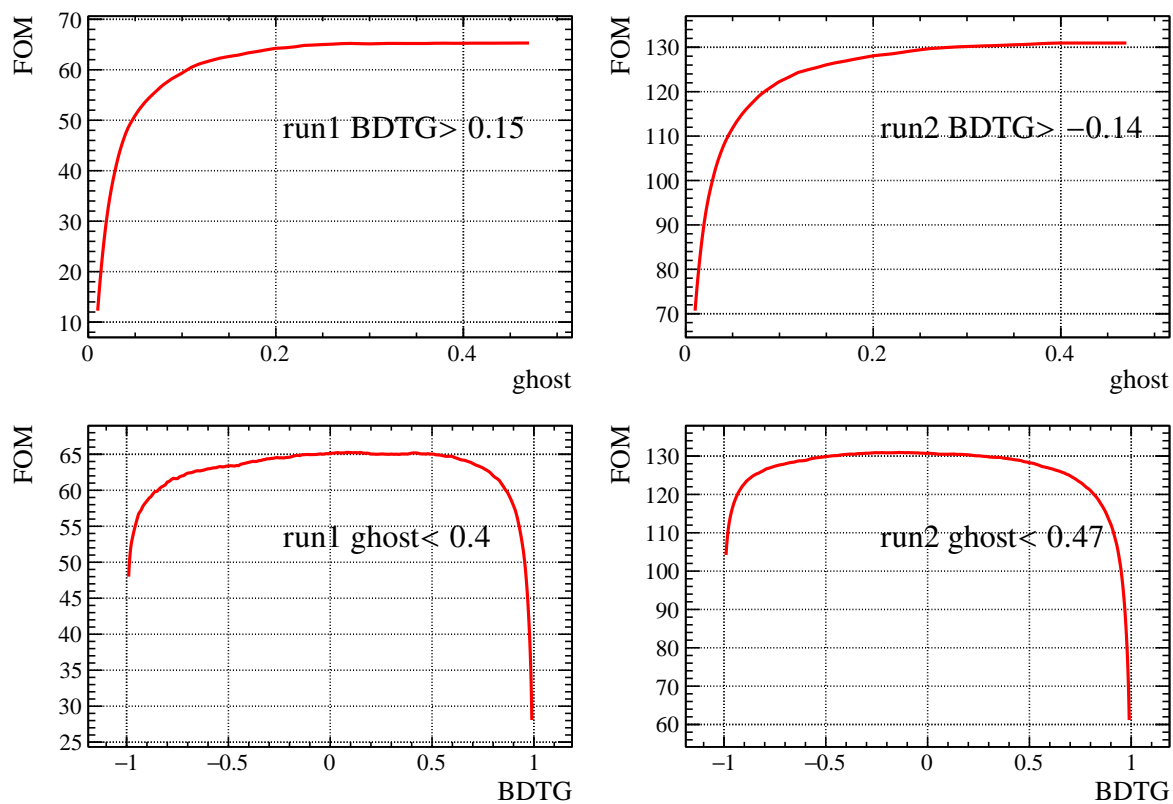


Figure 3.8 FOM versus BDTG, FOM versus ghost probability of kaons for run1 and run2

an Hypatia function. The shape of the combinatorial background is described by the second order Chebyshev polynomial function. In ± 15 MeV signal region around the B^+ peak, the signal yield is 5043 ± 77 (19176 ± 147), and the combinatorial background yield is 275 ± 10 (738 ± 17) for Run 1 (Run 2). Background fraction is 5.2% (3.7%) for Run 1 (Run 2), overall 4.0%. Due to loosen the χ^2_{IP} selection of the kaon candidates from > 9 to > 4 , 20% signal gain is achieved compared to the Run 1 publication. Also due to more input variables used in MVA (*e.g.* ProbNNk and χ^2_{FD}), the background fraction is significantly reduced from 27% to 5% (Run 1). The multiple candidate fraction is 0.9% in a B mass range of 5220-5360 MeV.

Figure. 3.11-3.13 show three Dalitz plot distributions, with the background subtracted by *sPlot* technique. The *sWeights* are determined by the fits displayed in Figure. 3.9. The log scale mass distribution is shown in Figure. 3.10. The most apparent features are four bands in $J/\psi\phi$ mass, corresponding to $X(4140)$, $X(4274)$, $X(4500)$ and $X(4700)$ claimed in the previous LHCb publication. No apparent structures in ϕK mass are seen, as many K^* resonances in this mass range are broad and overlapping. The increased data sample reveals clustering of events in the middle part of the Dalitz plots, best described as $J/\psi K$ mass band.

3.3.2 Non- ϕ background fraction

In this subsection, the non- ϕ background fraction in the total $B^+ \rightarrow J/\psi K^+ K^- K^+$ decays with $m_{K^+ K^-}$ in ± 15 MeV around the ϕ peak is estimated. To recover proper ϕ mass sideband, the one-phi selection requirement is removed. Later the efficiency of the one-phi cut using signal simulation is studied. A 2D fit to $m_{K^+ K^-}$ versus $m_{J/\psi K^+ K^- K^+}$ (2 entries per event) is done to Run 1 + Run 2 data sample. The fit result is shown in Figure.3.14.

The yields of different fit components are shown in Table.3.8. Without the one-phi cut, the non- ϕ contribution in $B^+ \rightarrow J/\psi K^+ K^- K^+$ decays is $1366/(22018 + 1366) = 5.8\%$ in the ± 15 MeV region around the ϕ and the B^+ mass peaks. According to the signal simulation, the real ϕ decays can generate combinatorial background in ± 15 MeV around the ϕ mass peak, via the second $K^+ K^-$ combination in the event, in a rate of 3.6 per 100 detected ϕ signal counts. This means $3.6/100 * 22018 = 793$ entries in the ϕ peak region are the reflections from ϕ signal. With the one-phi requirement, 94% of such non- ϕ combinations are rejected, with a ϕ signal efficiency of 97%. The remaining ϕ signal is $22018 * 97\% = 21357$, and the remaining non-phi background is $(1366 - 793) + (793 * 6\%) = 621$, thus $621/(621 + 21357) = 2.8\%$ is the non- ϕ component in the $B^+ \rightarrow J/\psi K^+ K^- K^+$ signal sample after the one-phi requirement. We have assumed above that the non-phi background efficiency is 100% for the one-phi requirement. Otherwise, the estimate is even lower than 2.8%.

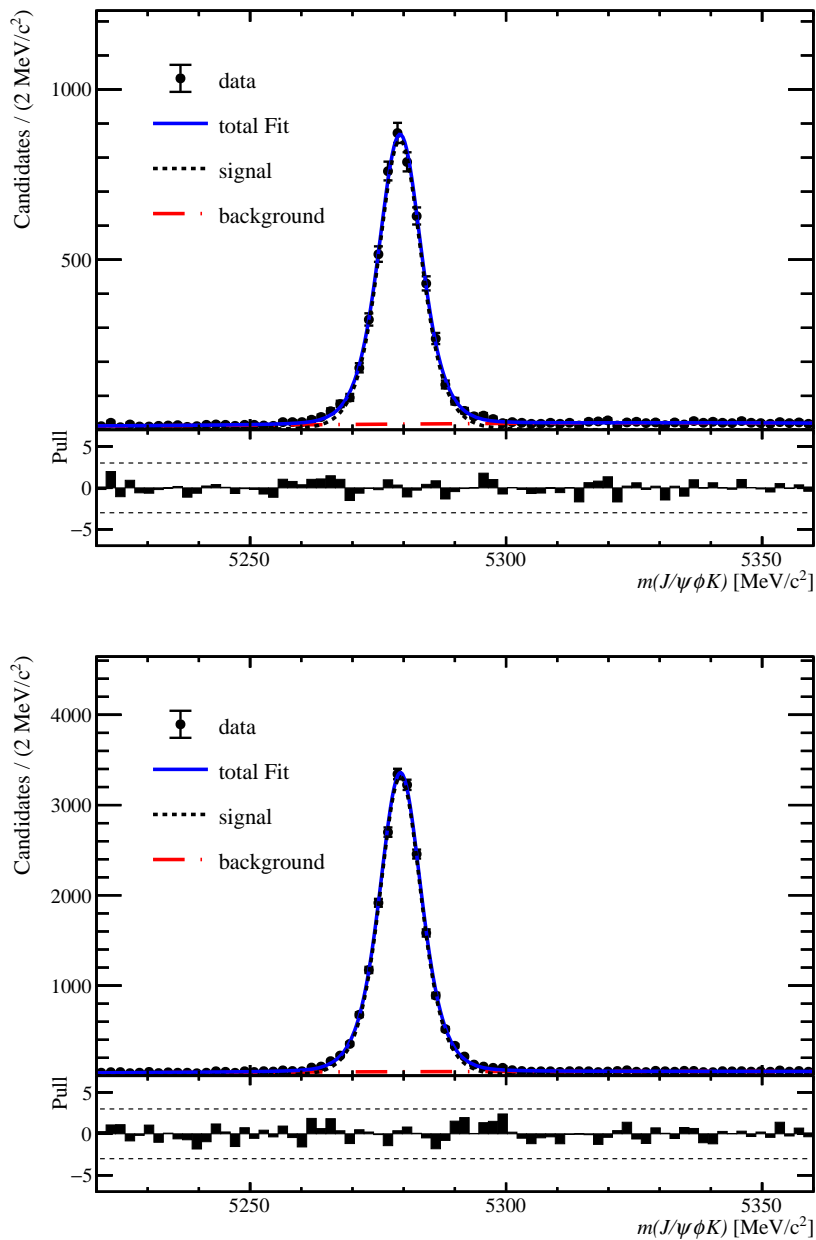


Figure 3.9 Invariant mass distribution of the $B^+ \rightarrow J/\psi \phi K^+$ decay and the fitted curve for Run 1 (top) and Run 2 (bottom).

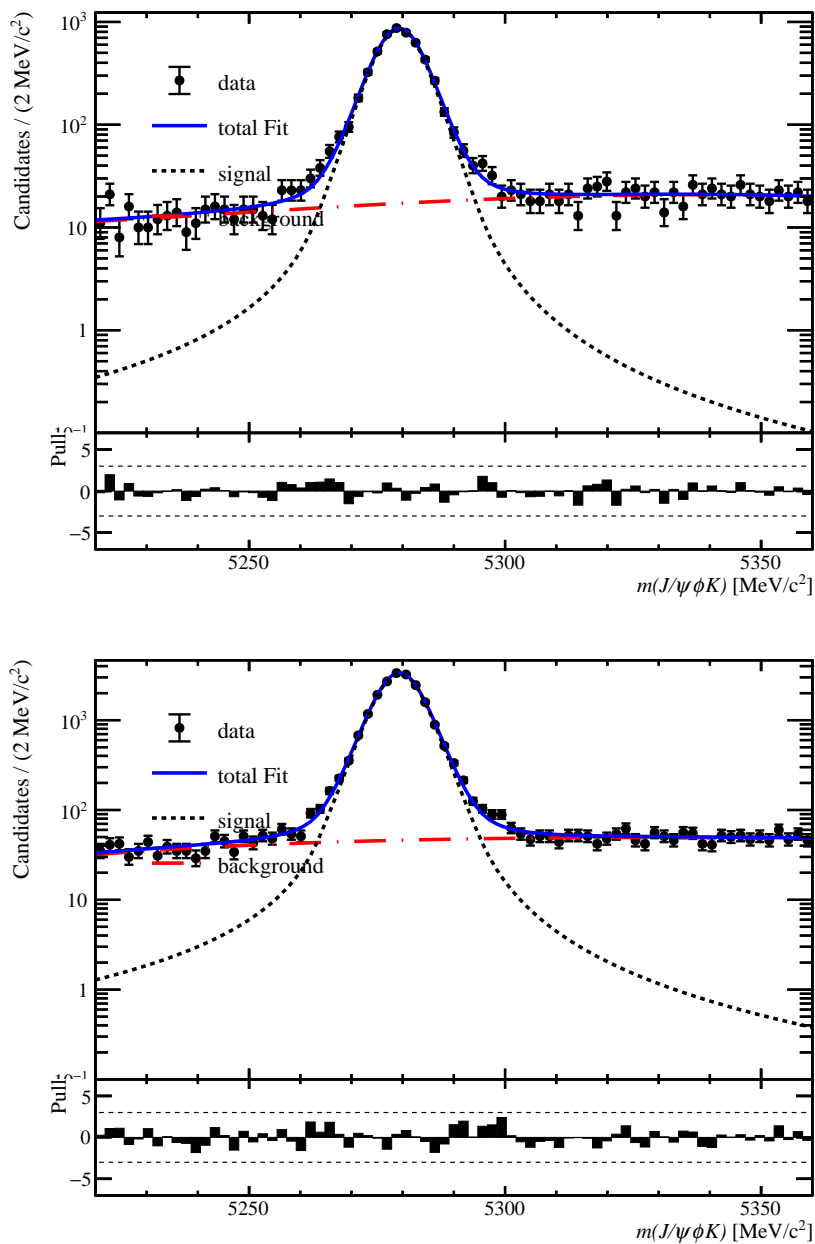


Figure 3.10 The log scale invariant mass distribution of the $B^+ \rightarrow J/\psi \phi K^+$ decay and the fitted curve for Run 1 (top) and Run 2 (bottom).

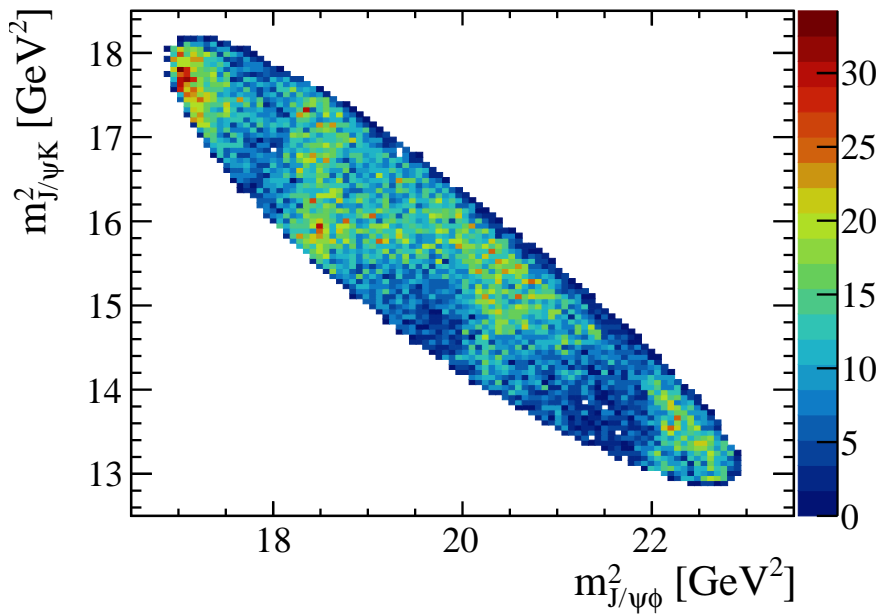


Figure 3.11 Dalitz-plot distribution of $J/\psi\phi$ vs $J/\psi K$, where the background is subtracted by *sPlot* technique.

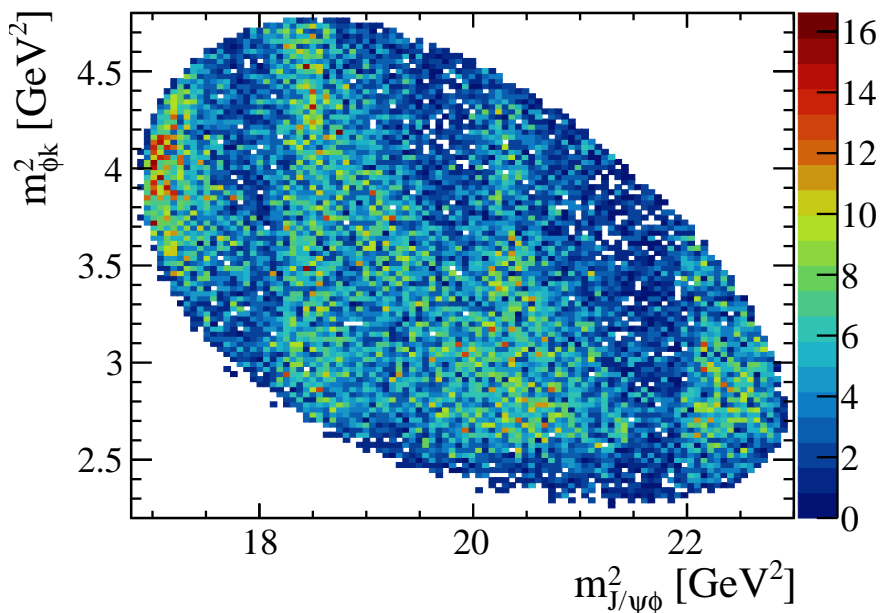


Figure 3.12 Dalitz-plot distribution of $J/\psi\phi$ vs ϕK , where the background is subtracted by *sPlot* technique.

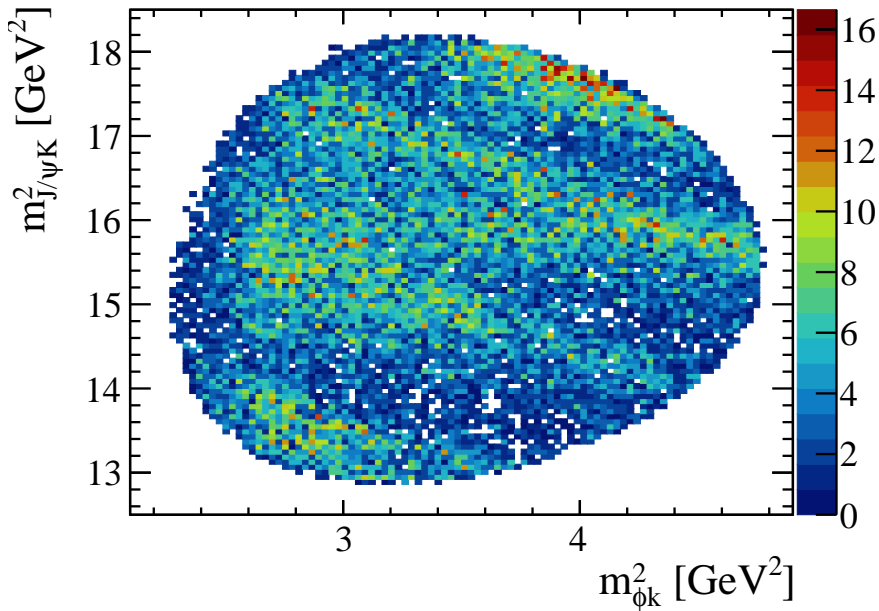


Figure 3.13 Dalitz-plot distribution of ϕK vs $J/\psi K$, where the background is subtracted by *sPlot* technique.

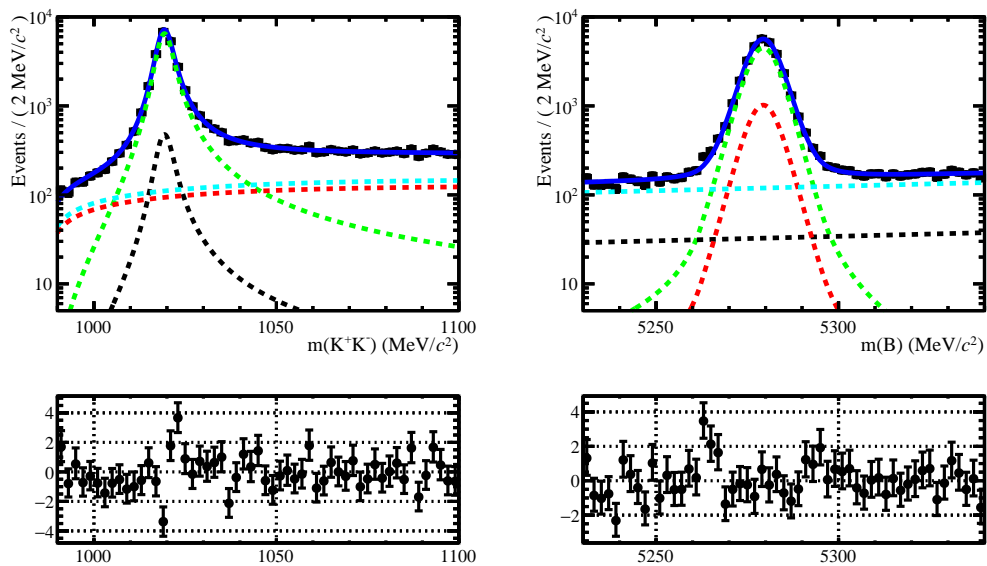


Figure 3.14 Projections of the 2D fit to m_ϕ vs. $m_{J/\psi K^+ K^-}$ (notice the log scale!). The deep blue line is the total pdf. The red line is the component where phi is background (modelled by phase-space) but B^\pm is signal (hypothia function). The green line is the component where phi is signal (Breit-Wigner) and B^\pm is signal as well. The black line is the component where phi is signal but B^\pm is background (linear polynomial). The light blue line is the component where phi and B^\pm are both background.

Table 3.8 The yields of 2D fit.

Yields	in fit region	in ± 15 MeV of both ϕ and B^+ signal region
$\phi_{signal} \otimes B_{signal}$	24826 ± 185	22018 ± 164
$\phi_{signal} \otimes B_{background}$	1823 ± 81	442 ± 20
$\phi_{background} \otimes B_{signal}$	5644 ± 124	1366 ± 30
$\phi_{background} \otimes B_{background}$	6670 ± 109	441 ± 7

3.4 The amplitude fitting formula

In this section, the general outline to construct helicity formula is introduced firstly, as well as the corresponding notation. Then, the matrix element for $B^+ \rightarrow J/\psi \phi K^-$, $J/\psi \rightarrow \mu^+ \mu^-$, $\phi \rightarrow K^+ K^-$ are described in sequence. Assuming the selected events of $K^+ K^-$ are all from ϕ decays, the mass-dependent term of $m_{K^- K^+}$ for ϕ lineshape is common for all decay chains, and omitted to save computation time. Subsequently, the method to combine all decay chains together is discussed. Besides, a possible reduction of number of helicity couplings to determine from the data by their relation to LS couplings is introduced. Finally, the method to subtract background contribution from the log-likelihood sum is shown, which is also named as "cFit".

3.4.1 Helicity formalism and notation

For each two-body decay $A \rightarrow BC$, a coordinate system is set up in the rest frame of A , with \hat{z} being the direction of quantization for its spin. We denote this coordinate system as $(x_0^{\{A\}}, y_0^{\{A\}}, z_0^{\{A\}})$, where the superscript " $\{A\}$ " means "in the rest frame of A ", while the subscript "0" means the initial coordinates. For the first particle in the decay chain, the choice of these coordinates is arbitrary. However, once defined, these coordinates must be used consistently between all decay sequences described by the matrix element. For subsequent decays, *e.g.* $B \rightarrow DE$, the choice of these coordinates is already fixed by the transformation from the A to the B rest frames, as discussed below. Helicity is defined as the projection of the spin of the particle onto the direction of its momentum. When the z axis coincides with the particle momentum, we denote its spin projection onto it (*i.e.* the m_z quantum number) as λ . To use the helicity formalism, the initial coordinate system must be rotated to align the z axis with the direction of the momentum of one of the daughter particles, *e.g.* the B . A generalized rotation operator can be formulated in three-dimensional space, $\mathcal{R}(\alpha, \beta, \gamma)$, that uses Euler angles. Applying this operator results in a sequence of rotations: first by the angle α about the \hat{z}_0 axis, followed by the angle β about the rotated \hat{y}_1 axis and then finally by the

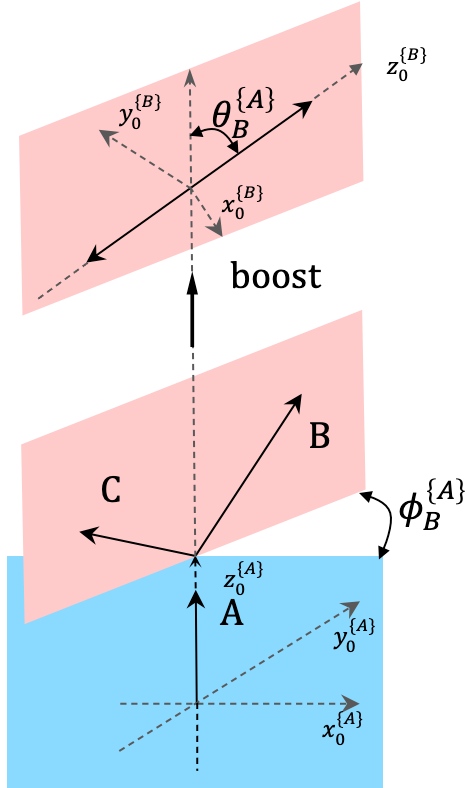


Figure 3.15 Coordinate axes for the spin quantization of particle A (bottom part), chosen to be the helicity frame of A ($\hat{z}_0 \parallel \vec{p}_A$ in the rest frame of its mother particle or in the laboratory frame), together with the polar ($\theta_B^{(A)}$) and azimuthal ($\phi_B^{(A)}$) angles of the momentum of its daughter B in the B rest frame (top part). Notice that the directions of these coordinate axes, denoted as $(x_0^{(A)}, y_0^{(A)}, z_0^{(A)})$, do not change when boosting from the helicity frame of A to its rest frame. After the Euler rotation $\mathcal{R}(\alpha = \phi_B^{(A)}, \beta = \theta_B^{(A)}, \gamma = 0)$ (see the text), the rotated z axis, $\hat{z}_2^{(A)}$, is aligned with the B momentum; thus the rotated coordinates become the helicity frame of B. If B has a sequential decay, then the same boost-rotation process is repeated to define the helicity frame for its daughters.

angle γ about the rotated \hat{z}_2 axis. We use a subscript denoting the axes, to specify the rotations which have been already performed on the coordinates. The spin eigenstates of particle A , $|J_A, m_A >$, in the $(x_0^{\{A\}}, y_0^{\{A\}}, z_0^{\{A\}})$ coordinate system can be expressed in the basis of its spin eigenstates, $|J_A, m'_A >$, in the rotated $(x_3^{\{A\}}, y_3^{\{A\}}, z_3^{\{A\}})$ coordinate system with the help of Wigner's Dmatrices,

$$|J_A, m_A > = \sum_{m'_A} D_{m_A, m'_A}^{J_A} (\alpha, \beta, \gamma)^* |J_A, m'_A > \quad (3.1)$$

where

$$d_{m_a, m'_a}^{j_a} (\alpha, \beta, \gamma)^* = < j, m | r(\alpha, \beta, \gamma) | j, m' >^* = e^{im\alpha} d_{m, m'}^j e^{im'\gamma} \quad (3.2)$$

and where the small-d Wigner matrix contains known functions of β that depend on J, m, m' . To achieve the rotation of the original $z_0^{\{A\}}$ axis on to the B momentum ($\vec{p}_B^{\{A\}}$), it is sufficient to rotate by $\alpha = \phi_B^{\{A\}}$, $\beta = \theta_B^{\{A\}}$, where $\phi_B^{\{A\}}$, $\theta_B^{\{A\}}$ are the azimuthal and polar angles of the B momentum vector in the original coordinates *i.e.* $(x_0^{\{A\}}, y_0^{\{A\}}, z_0^{\{A\}})$. which is depicted in Figure. 3.15. for the case when the quantization axis for the spin of A is its momentum in some other reference frame. Since the third rotation is not necessary, γ is equal to 0. The angle $\theta_B^{\{A\}}$ is usually called “the A helicity angle”, thus to simplify the B notation we will denote it as θ_A . For compact notation, $\phi_B^{\{A\}}$ is denoted as ϕ_B . These angles can be determined as,

$$\begin{aligned} \phi_B &= \text{atan2}\left(p_B^{\{A\}}_y, p_B^{\{A\}}_x\right) \\ &= \text{atan2}\left(\hat{y}_0^{\{A\}} \cdot \vec{p}_B^{\{A\}}, \hat{x}_0^{\{A\}} \cdot \vec{p}_B^{\{A\}}\right) \\ &= \text{atan2}\left((\hat{z}_0^{\{A\}} \times \hat{x}_0^{\{A\}}) \cdot \vec{p}_B^{\{A\}}, \hat{x}_0^{\{A\}} \cdot \vec{p}_B^{\{A\}}\right), \end{aligned} \quad (3.3)$$

$$\cos \theta_A = \hat{z}_0^{\{A\}} \cdot \hat{p}_B^{\{A\}}. \quad (3.4)$$

Angular momentum conservation requires $m'_A = m'_B + m'_C = \lambda_B - \lambda_C$ (since $\vec{p}_C^{\{A\}}$ points in the opposite direction to $\hat{z}_3^{\{A\}}$, $m'_C = -\lambda_C$). Each two-body decay adds a multiplicative term to the matrix element

$$\mathcal{H}_{\lambda_B, \lambda_C}^{A \rightarrow BC} D_{m_A, \lambda_B - \lambda_C}^{J_A} (\phi_B, \theta_A, 0)^*. \quad (3.5)$$

The helicity couplings $\mathcal{H}_{\lambda_B, \lambda_C}^{A \rightarrow BC}$ are complex constants. Their products from subsequent decays are to be determined by the fit to the data (they represent the decay dynamics). If the decay is strong or electromagnetic, it conserves parity which reduces the number of independent helicity couplings via the relation

$$\mathcal{H}_{-\lambda_B, -\lambda_C}^{A \rightarrow BC} = P_A P_B P_C (-1)^{J_B + J_C - J_A} \mathcal{H}_{\lambda_B, \lambda_C}^{A \rightarrow BC}, \quad (3.6)$$

where P stands for the intrinsic parity of a particle.

After multiplying terms given by Eq. (3.5) for all decays in the decay sequence, they must be summed up coherently over the helicity states of intermediate particles, and incoherently over the helicity states of the initial and final-state particles. Possible helicity values of B and C particles are constrained by $|\lambda_B| \leq J_B$, $|\lambda_C| \leq J_C$ and $|\lambda_B - \lambda_C| \leq J_A$.

When dealing with the subsequent decay of the daughter, $B \rightarrow D E$, four-vectors of all particles must be first Lorentz boosted to the rest frame of B , along the $\vec{p}_B^{\{A\}}$ i.e. $\hat{z}_3^{\{A\}}$ direction (this is the z axis in the rest frame of A after the Euler rotations; the subscript “3” is used for the number of rotations performed on the coordinates, and the $\gamma = 0$, these coordinates are the same as after the first two rotations). This is visualized in Figure. 3.15, with $B \rightarrow D E$ particle labels replaced by $A \rightarrow BC$ labels. This transformation does not change vectors that are perpendicular to the boost direction. The transformed coordinates become the initial coordinate system quantizing the spin of B in its rest frame,

$$\begin{aligned}\hat{x}_0^{\{B\}} &= \hat{x}_3^{\{A\}}, \\ \hat{y}_0^{\{B\}} &= \hat{y}_3^{\{A\}}, \\ \hat{z}_0^{\{B\}} &= \hat{z}_3^{\{A\}}.\end{aligned}\tag{3.7}$$

The processes of rotation and subsequent boosting can be repeated until the final-state particles are reached. In practice, there are two equivalent ways to determine the $\hat{z}_0^{\{B\}}$ direction. Using Eq. (3.7) can set it to the direction of the B momentum in the A rest frame

$$\hat{z}_0^{\{B\}} = \hat{z}_3^{\{A\}} = \hat{p}_B^{\{A\}}.\tag{3.8}$$

Alternatively, the fact that B and C are back-to-back in the rest frame of A can also be considered, $\vec{p}_C^{\{A\}} = -\vec{p}_B^{\{A\}}$. Since the momentum of C is antiparallel to the boost direction from the A to B rest frames, the C momentum in the B rest frame will be different, but it will still be antiparallel to this boost direction

$$\hat{z}_0^{\{B\}} = -\hat{p}_C^{\{B\}}.\tag{3.9}$$

To determine $\hat{x}_0^{\{B\}}$ from Eq. (3.7), the $\hat{x}_3^{\{A\}}$ should be calculated first. After the first rotation by ϕ_B about $\hat{z}_0^{\{A\}}$, the $\hat{x}_1^{\{A\}}$ axis is along the component of $\vec{p}_B^{\{A\}}$ which is perpendicular to the

$\hat{z}_0^{\{A\}}$ axis

$$\begin{aligned}\vec{a}_{B \perp z_0}^{\{A\}} &\equiv (\vec{p}_B^{\{A\}})_{\perp \hat{z}_0^{\{A\}}} = \vec{p}_B^{\{A\}} - (\vec{p}_B^{\{A\}})_{|| \hat{z}_0^{\{A\}}}, \\ &= \vec{p}_B^{\{A\}} - (\vec{p}_B^{\{A\}} \cdot \hat{z}_0^{\{A\}}) \hat{z}_0^{\{A\}}, \\ \hat{x}_1^{\{A\}} &= \hat{a}_{B \perp z_0}^{\{A\}} = \frac{\vec{a}_{B \perp z_0}^{\{A\}}}{|\vec{a}_{B \perp z_0}^{\{A\}}|}.\end{aligned}\quad (3.10)$$

After the second rotation by θ_A about $\hat{y}_1^{\{A\}}$, $\hat{z}_2^{\{A\}} \equiv \hat{z}_3^{\{A\}} = \hat{p}_B^{\{A\}}$, and $\hat{x}_2^{\{A\}} = \hat{x}_3^{\{A\}}$ is antiparallel to the component of the $\hat{z}_0^{\{A\}}$ vector that is perpendicular to the new z axis *i.e.* $\hat{p}_B^{\{A\}}$. Thus

$$\begin{aligned}\vec{a}_{z_0 \perp B}^{\{A\}} &\equiv (\hat{z}_0^{\{A\}})_{\perp \hat{p}_B^{\{A\}}} = \hat{z}_0^{\{A\}} - (\hat{z}_0^{\{A\}} \cdot \hat{p}_B^{\{A\}}) \hat{p}_B^{\{A\}}, \\ \hat{x}_0^{\{B\}} &= \hat{x}_3^{\{A\}} = -\hat{a}_{z_0 \perp B}^{\{A\}} = -\frac{\vec{a}_{z_0 \perp B}^{\{A\}}}{|\vec{a}_{z_0 \perp B}^{\{A\}}|}.\end{aligned}\quad (3.11)$$

Then obtain $\hat{y}_0^{\{B\}} = \hat{z}_0^{\{B\}} \times \hat{x}_0^{\{B\}}$.

If C also decays, $C \rightarrow F G$, then the coordinates for the quantization of C spin in the C rest frame are defined by

$$\hat{z}_0^{\{C\}} = -\hat{z}_3^{\{A\}} = \hat{p}_C^{\{A\}} = -\hat{p}_B^{\{C\}}, \quad (3.12)$$

$$\hat{x}_0^{\{C\}} = -\hat{x}_3^{\{A\}} = \hat{a}_{z_0 \perp B}^{\{A\}} = -\hat{a}_{z_0 \perp C}^{\{A\}}, \quad (3.13)$$

$$\hat{y}_0^{\{C\}} = \hat{y}_0^{\{B\}} = \hat{z}_0^{\{C\}} \times \hat{x}_0^{\{C\}}, \quad (3.14)$$

i.e. the z axis is reflected compared to the system used for the decay of particle B (it must point in the direction of C momentum in the A rest frame), but the y axis is kept the same, since particle B for the rotation used in Eq. (3.5) is chosen. This is to rotate 180 degree about the y axis.

3.4.2 Matrix element for the $K^{*+} \rightarrow \phi K^+$ decay chain

For the $B^+ \rightarrow \psi K_n^*$, $K_n^* \rightarrow \phi K$, $\phi \rightarrow K^+ K^-$, $\psi \rightarrow \mu^+ \mu^-$, this chain is described by one mass and 5 helicity angles.

The weak decay $B^+ \rightarrow \psi K_n^*$ is described only by helicity coupling $\mathcal{H}_{\lambda_\psi}^{B \rightarrow \psi K_n^*}$, with $\lambda_\psi = \lambda_{K^*}$, because B^+ has no spin.

The strong decay $K_n^* \rightarrow \phi K$ is described by helicity couplings, angular and mass terms, as

$$\mathcal{H}_{\lambda_\phi}^{K_n^*} D_{\lambda_{K^*}, \lambda_\phi}^{J_{K_n^*}}(\phi_\phi, \theta_{K^*}, 0)^* R_{K_n^*}(m_{\phi K}), \quad (3.15)$$

where the two helicity angles ϕ_ϕ , θ_{K^*} of K^* decays are defined by the particle ϕ . Wigner-D

function requires $|\lambda_\phi| \leq J_{K_n^*}$ and $|\lambda_\psi| \leq J_{K_n^*}$. Strong decay conserves parity, and gives the relation $\mathcal{H}_{-\lambda_\phi}^{K_n^*} = (-1)^{J_{K_n^*}} P_{K_n^*} \mathcal{H}_{\lambda_\phi}^{K_n^*}$, where $P_{K_n^*}$ is the parity of the K_n^* resonance.

The $\phi \rightarrow K^+ K^-$ decay provides one term

$$D_{\lambda_\phi, 0}^1(\phi_{K^+}, \theta_\phi, 0)^*, \quad (3.16)$$

where K^+ is used to define the two helicity angles of ϕ_{K^+} and θ_ϕ from ϕ decays. No independent helicity couplings are needed, as the daughters of ϕ are spineless.

The electromagnetic decay $\psi \rightarrow \mu^+ \mu^-$ is described by a term

$$D_{\lambda_\psi, \Delta\lambda_\mu}^1(\phi_\mu, \theta_\psi, 0)^*, \quad (3.17)$$

where $\Delta\lambda_\mu \equiv \lambda_{\mu^+} - \lambda_{\mu^-} = \pm 1$, and ϕ_μ, θ_ψ are the azimuthal and polar angles of μ^+ for B^+ in the ψ rest frame. There are no independent helicity couplings in Eq. (3.17), since they are all equal due to conservation of C and P parities. Therefore, this coupling can be set to unity as its magnitude and phase can be absorbed into the other helicity couplings which are left free in the fit.

Collecting all terms together, the matrix element is

$$\begin{aligned} \mathcal{M}_{\Delta\lambda_\mu}^{K_n^*}(\theta_{K_n^*}, \theta_\psi, \theta_\phi, \phi_{(\psi K^*)}) &\equiv \phi_\phi + \phi_\mu, \phi_{K^+}, m_{\phi K}) = \\ &\sum_{\lambda_\psi} e^{i\lambda_\psi \phi_{(\psi K^*)}} d_{\lambda_\psi, \Delta\lambda_\mu}^1(\theta_\psi) \sum_{\lambda_\phi} e^{i\lambda_\phi \phi_{K^+}} d_{\lambda_\phi, 0}^1(\theta_\phi) \sum_n \mathcal{H}_{\lambda_\psi}^{B \rightarrow \psi K_n^*} \mathcal{H}_{\lambda_\phi}^{K_n^*} d_{\lambda_\psi, \lambda_\phi}^{J_{K_n^*}}(\theta_{K_n^*}) R_{K_n^*}(m_{\phi K}) \end{aligned} \quad (3.18)$$

Here, $\phi_{(\psi K^*)} \equiv \phi_\phi + \phi_\mu$ is the azimuthal angle between the K^* and ψ decay angles (ϕ_ϕ and ϕ_μ cannot be independently probed). Here $\phi_{(\psi K^*)}$ is denoted as $\Delta\phi_{K_n^*, J/\psi}$ and ϕ_{K^+} is denoted as $\Delta\phi_{K_n^*, \phi}$ in the main text, respectively. The first two terms, summing over $\lambda_\psi = \pm 1, 0$ and $\lambda_\phi = \pm 1, 0$, are independent of the other terms, thus can be coded separately and cached. The last term depends on 3×3 matrix of λ_ψ and λ_ϕ values.

The term $R_{K_n^*}(m_{K\phi})$ describes the K_n^* resonance that appears in the invariant mass distribution of the $K\phi$ system,

$$R_{K_n^*}(m_{K\phi}) = B'_{L_B^{K_n^*}}(p, p_0, d) \left(\frac{p}{M_B} \right)^{L_B^{K_n^*}} \text{BW}(m_{K\phi} | M_0^{K_n^*}, \Gamma_0^{K_n^*}) B'_{L_{K_n^*}}(q, q_0, d) \left(\frac{q}{M_0^{K_n^*}} \right)^{L_{K_n^*}}. \quad (3.19)$$

Here, p is the K^* momentum in the B rest frame ($p = |\vec{p}_{K_n^*}^{\{B\}}|$). Similarly, q is the K momentum in the K^* rest frame ($q = |\vec{p}_K^{\{K^*\}}|$). The symbols p_0 and q_0 denote values of these quantities at the resonance peak ($m_{K\phi} = M_0^{K_n^*}$). The orbital angular momentum between the K^* and ψ particles in the B decay is denoted as $L_B^{K_n^*}$. Similarly, $L_{K_n^*}$ is the orbital angular momentum

between the K and ϕ in the K^* decay. For the orbital angular momentum barrier factors, $p^L B'_L(p, p_0, d)$, the Blatt-Weisskopf functions^[54] is used,

$$\begin{aligned}
 B'_0(p, p_0, d) &= 1, \\
 B'_1(p, p_0, d) &= \sqrt{\frac{1 + (p_0 d)^2}{1 + (p d)^2}}, \\
 B'_2(p, p_0, d) &= \sqrt{\frac{9 + 3(p_0 d)^2 + (p_0 d)^4}{9 + 3(p d)^2 + (p d)^4}}, \\
 B'_3(p, p_0, d) &= \sqrt{\frac{225 + 45(p_0 d)^2 + 6(p_0 d)^4 + (p_0 d)^6}{225 + 45(p d)^2 + 6(p d)^4 + (p d)^6}}, \\
 B'_4(p, p_0, d) &= \sqrt{\frac{11025 + 1575(p_0 d)^2 + 135(p_0 d)^4 + 10(p_0 d)^6 + (p_0 d)^8}{11025 + 1575(p d)^2 + 135(p d)^4 + 10(p d)^6 + (p d)^8}}, \\
 B'_5(p, p_0, d) &= \sqrt{\frac{893025 + 99225(p_0 d)^2 + 6300(p_0 d)^4 + 315(p_0 d)^6 + 15(p_0 d)^8 + (p_0 d)^{10}}{893025 + 99225(p d)^2 + 6300(p d)^4 + 315(p d)^6 + 15(p d)^8 + (p d)^{10}}},
 \end{aligned} \tag{3.20}$$

to account for the difficulty in creating the orbital angular momentum L , which depends on the momentum of the decay products p (in the rest frame of the decaying particle) and on the size of the decaying particle given by the constant d . We set $d = 3.0 \text{ GeV}^{-1} \sim 0.6 \text{ fm}$. The relativistic Breit-Wigner amplitude is given by

$$\text{BW}(m|M_0, \Gamma_0) = \frac{1}{M_0^2 - m^2 - iM_0\Gamma(m)}, \tag{3.21}$$

where

$$\Gamma(m) = \Gamma_0 \left(\frac{q}{q_0} \right)^{2L_{K^*}+1} \frac{M_0}{m} B'_{L_{K^*}}(q, q_0, d)^2. \tag{3.22}$$

The angles used here is calculated here and the sketch of angles is shown in Figure 3.16. The $z_0^{[K^*]}$ direction is defined by the boost direction from the B^+ rest frame, which coincides with the $-\hat{p}_\psi^{[K^*]}$ direction in this frame, details have been discussed in Section 3.4.1. Some expressions to calculate the angles are listed below. The axis of K^* rest frame is defined as:

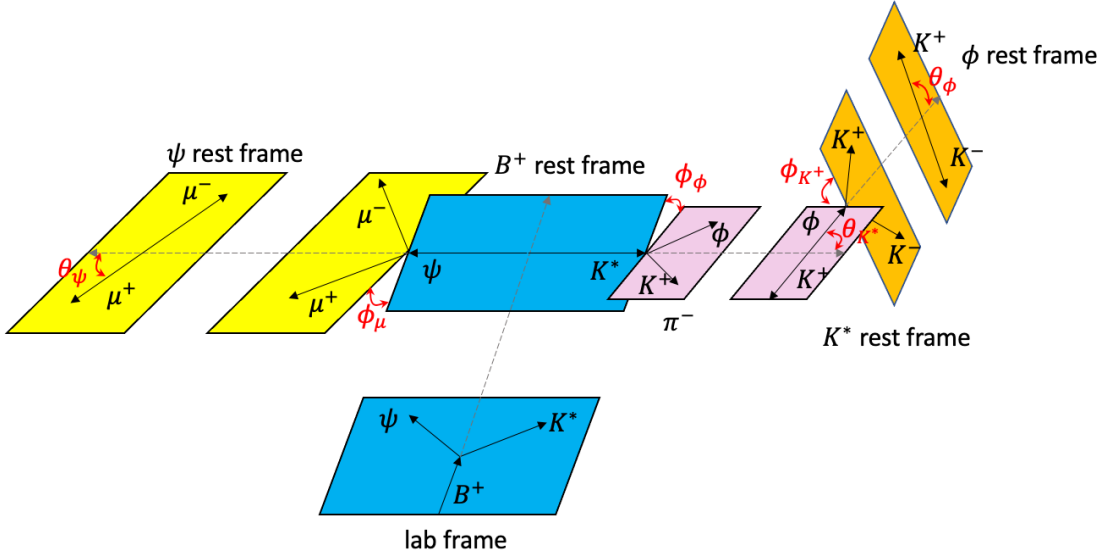
$$\hat{x}_0^{[K^*]} = -\frac{\hat{p}_{B^+}^{\{LAB\}} - (\hat{p}_{B^+}^{\{LAB\}} \cdot \hat{p}_{K^*}^{\{B^+\}}) \hat{p}_{K^*}^{\{B^+\}}}{\left| \hat{p}_{B^+}^{\{LAB\}} - (\hat{p}_{B^+}^{\{LAB\}} \cdot \hat{p}_{K^*}^{\{B^+\}}) \hat{p}_{K^*}^{\{B^+\}} \right|} \tag{3.23}$$

$$y_0^{[K^*]} = -\hat{p}_\psi^{[K^*]} \times x_0^{[K^*]} \tag{3.24}$$

$$z_0^{[K^*]} = -\hat{p}_\psi^{[K^*]} \tag{3.25}$$

with this choice, the polar angle of ϕ in K^* rest frame can be calculated:

$$\cos \theta_{K^*} = -\hat{p}_\psi^{[K^*]} \cdot \hat{p}_\phi^{[K^*]} \tag{3.26}$$


 Figure 3.16 Definaton of decay angles in the K^* chain.

and the azimuthal angle of ϕ in $K^*(\phi_\phi)$ rest frame can be determined from Equation. 3.3.

$$\phi_\phi = \text{atan}2 \left(\hat{y}_0^{\{K^*\}} \cdot \hat{p}_\phi^{\{K^*\}}, \hat{x}_0^{\{K^*\}} \cdot \hat{p}_\phi^{\{K^*\}} \right) \quad (3.27)$$

For the rest frame of ψ , the definition of axis:

$$\hat{x}_0^{\{\psi\}} = -\hat{x}_0^{\{K^*\}} \quad (3.28)$$

$$y_0^{\{\psi\}} = y_0^{\{K^*\}} \quad (3.29)$$

$$z_0^{\{\psi\}} = -z_0^{\{K^*\}} \quad (3.30)$$

The polar angle of μ^+ in ψ rest frame (θ_ψ):

$$\cos \theta_\psi = -\hat{p}_{K^*}^{\{\psi\}} \cdot \hat{p}_{\mu^+}^{\{\psi\}} \quad (3.31)$$

and the corresponding azimuthal angle of μ^+ in ψ rest frame:

$$\phi_\mu = \text{atan}2 \left(\hat{y}_0^{\{\psi\}} \cdot \hat{p}_{\mu^+}^{\{\psi\}}, \hat{x}_0^{\{\psi\}} \cdot \hat{p}_{\mu^+}^{\{\psi\}} \right) \quad (3.32)$$

The same calculation procedure is applied to $\phi \rightarrow K^+K^-$ channel, the polar angle of K^+ in ϕ rest frame is defined as:

$$\cos \theta_\phi = -\hat{p}_{K_S^0}^{\{K^*\}} \cdot \hat{p}_{K^+}^{\{\phi\}} \quad (3.33)$$

and azimuthal angle of K^+ in ϕ rest frame:

$$\phi_K = \text{atan}2 \left(\hat{y}_0^{\{\phi\}} \cdot \hat{p}_{K^+}^{\{\phi\}}, \hat{x}_0^{\{\phi\}} \cdot \hat{p}_{K^+}^{\{\phi\}} \right) \quad (3.34)$$

3.4.3 Matrix element for the $Z^+ \rightarrow \psi K^+$ chain

The chain of $B^+ \rightarrow Z_j^+ \phi$, $Z_j^+ \rightarrow \psi K^+$, $\phi \rightarrow K^+ K^-$, $\psi \rightarrow \mu^+ \mu^-$ also contains four terms. The $B_s^0 \rightarrow Z_j^+ \phi$ gives a term, $\mathcal{H}_{\lambda_\phi^Z}^{B \rightarrow Z_j \phi}$ and limits $\lambda_Z = \lambda_\phi^Z$. The superscript Z in λ_ϕ accounts for different helicity frame than that in the K^* chain.

The $Z_j^+ \rightarrow \psi K^+$ is described by one term

$$\mathcal{H}_{\lambda_\psi^Z}^{Z_j} D_{\lambda_Z, \lambda_\psi^Z}^{J_{Z_j}}(\phi_\psi^Z, \theta_Z, 0)^* R_{Z_j}(m_{\psi K}), \quad (3.35)$$

The helicity angles of Z decays ϕ_ψ^Z and θ_Z are defined by the ψ direction. The strong decay conserve parity, which gives the relation $\mathcal{H}_{-\lambda_\psi^Z}^{Z_j} = (-1)^{J_{Z_j}-1} P_{Z_j} \mathcal{H}_{\lambda_\psi^Z}^{Z_j}$.

The $\phi \rightarrow K^+ K^-$ provides one term

$$D_{\lambda_\phi^Z, 0}^1(\phi_{K^+}^Z, \theta_\phi^Z, 0)^*, \quad (3.36)$$

where K^+ is used to define the two helicity angles of $\phi_{K^+}^Z$ and θ_ϕ^Z from ϕ decays. We use the superscript Z to differentiate from the K^* chain.

The $\psi \rightarrow \mu^+ \mu^-$ decay is described by the term

$$D_{\lambda_\psi^Z, \Delta \lambda_\mu^Z}^1(\phi_\mu^Z, \theta_\psi^Z, 0)^*. \quad (3.37)$$

Since the muons are final-state particles, their helicity states in the Z decay chain, $|\lambda_\mu^Z\rangle$, need to be rotated to the muon helicity states in the f decay chain, $|\lambda_\mu\rangle$, before the Z matrix element terms can be coherently added to the f matrix element terms. The term aligning the muon helicity states between the two reference frames is given by

$$\sum_{\lambda_\mu^Z} D_{\lambda_\mu^Z, \lambda_\mu}^{J_\mu}(\alpha_\mu^Z, 0, 0)^* = \sum_{\lambda_\mu^Z} e^{i \lambda_\mu^Z \alpha_\mu^Z} \delta_{\lambda_\mu^Z, \lambda_\mu} = e^{i \lambda_\mu \alpha_\mu^Z}. \quad (3.38)$$

The transformation of μ^- states will be similar to that of the μ^+ states, except that since \hat{z}_ψ will have the opposite direction, $\alpha_{\mu^+}^Z = -\alpha_{\mu^-}^Z$. The transformation of $|\lambda_{\mu^+}^Z\rangle |\lambda_{\mu^-}^Z\rangle$ to $|\lambda_{\mu^+}\rangle |\lambda_{\mu^-}\rangle$ states will require multiplying the terms for the Z decay chain by

$$e^{i \lambda_\mu \alpha_\mu^Z} e^{i \lambda_{\bar{\mu}} \alpha_{\bar{\mu}}^Z} = e^{i (\lambda_\mu - \lambda_{\bar{\mu}}) \alpha_\mu^Z} = e^{i \Delta \lambda_\mu \alpha_\mu^Z}. \quad (3.39)$$

The total matrix element for the Z^+ chain from B^+ decay is

$$\begin{aligned} \mathcal{M}_{\Delta \lambda_\mu}^Z(\theta_Z, \theta_\psi^Z, \theta_\phi^Z, \phi_{(Z\phi)} \equiv \phi_{K^+}^Z + \phi_\psi^Z, \phi_\mu^Z, \alpha_\mu^Z, m_{\psi K}) &= e^{i \Delta \lambda_\mu \alpha_\mu^Z} \sum_{\lambda_\psi^Z} e^{i \lambda_\psi^Z \phi_\mu^Z} d_{\lambda_\psi^Z, \Delta \lambda_\mu}^1(\theta_\psi^Z) \\ &\times \sum_{\lambda_\phi^Z} e^{i \lambda_\phi^Z \phi_{(Z\phi)}} d_{\lambda_\phi^Z, 0}^1(\theta_\phi^Z) \sum_j \mathcal{H}_{\lambda_\phi^Z}^{B \rightarrow Z_j \phi} \mathcal{H}_{\lambda_\psi^Z}^{Z_j} d_{\lambda_\phi^Z, \lambda_\psi^Z}^{J_{Z_j}}(\theta_Z) R_{Z_j}(m_{\psi K}). \end{aligned} \quad (3.40)$$

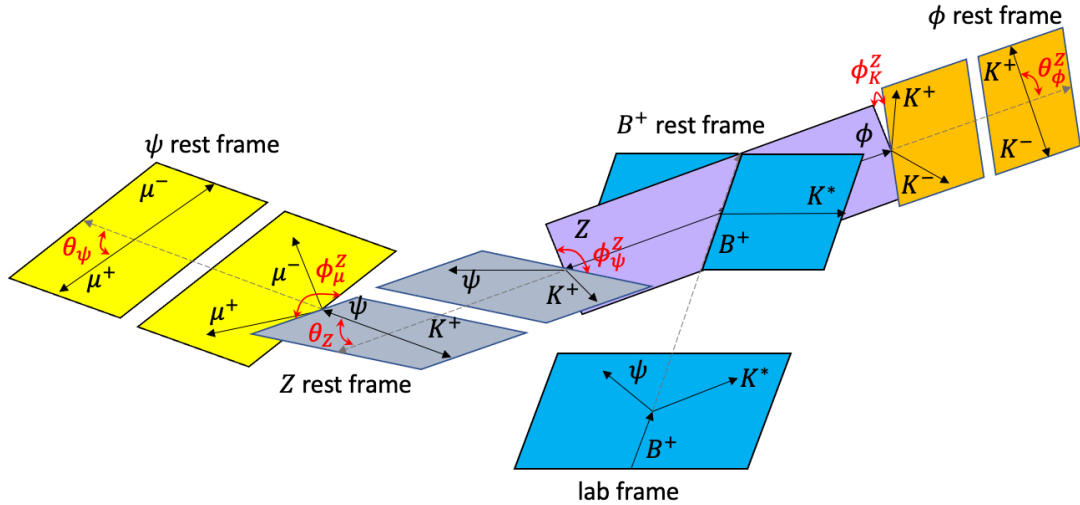


Figure 3.17 Defination of decay angles in the Z^+ chain.

The angles used in Z chain are defined in Figure 3.17. The polar angle of ϕ in Z rest frame can be calculated:

$$\cos \theta_Z = -\hat{p}_\phi^{\{Z\}} \cdot \hat{p}_\psi^{\{Z\}} \quad (3.41)$$

The axis of Z rest frame is defined as:

$$\hat{x}_0^{\{Z\}} = -\frac{\hat{p}_{B^0}^{\{LAB\}} - (\hat{p}_{B^0}^{\{LAB\}} \cdot \hat{p}_Z^{\{B^0\}}) \hat{p}_Z^{\{B^0\}}}{\left| \hat{p}_{B^0}^{\{LAB\}} - (\hat{p}_{B^0}^{\{LAB\}} \cdot \hat{p}_Z^{\{B^0\}}) \hat{p}_Z^{\{B^0\}} \right|} \quad (3.42)$$

$$\hat{y}_0^{\{Z\}} = -\hat{p}_\phi^{\{Z\}} \times \hat{x}_0^{\{Z\}} \quad (3.43)$$

$$\hat{z}_0^{\{Z\}} = -\hat{p}_\phi^{\{Z\}} \quad (3.44)$$

The azimuthal angle of ψ in Z rest frame can be determined from:

$$\phi_\psi^Z = \text{atan2} \left(\hat{y}_0^{\{Z\}} \cdot \hat{p}_\psi^{\{Z\}}, \hat{x}_0^{\{Z\}} \cdot \hat{p}_\psi^{\{Z\}} \right) \quad (3.45)$$

For the rest frame of ϕ , the definition of axis:

$$\hat{x}_0^{\{\phi\}Z} = -\hat{x}_0^{\{Z\}} \quad (3.46)$$

$$\hat{y}_0^{\{\phi\}Z} = \hat{y}_0^{\{Z\}} \quad (3.47)$$

$$\hat{z}_0^{\{\phi\}Z} = -\hat{z}_0^{\{Z\}} \quad (3.48)$$

The polar angle of K^+ in ϕ rest frame:

$$\cos \theta_\phi^Z = -\hat{p}_Z^{\{\phi\}Z} \cdot \hat{p}_{K^+}^{\{\phi\}Z} \quad (3.49)$$

The azimuthal angle of K^+ in ϕ rest frame:

$$\phi_K^Z = \text{atan}2\left(\hat{y}_0^{\{\phi\}Z} \cdot \hat{p}_{K^+}^{\{\phi\}Z}, \hat{x}_0^{\{\phi\}Z} \cdot \hat{p}_{K^+}^{\{\phi\}Z}\right) \quad (3.50)$$

The definition of axis of ψ rest frame is shown:

$$\hat{x}_0^{\{\psi\}Z} = -\frac{-\hat{p}_\phi^{\{Z\}} + (\hat{p}_\phi^{\{Z\}} \cdot \hat{p}_\psi^{\{Z\}}) \hat{p}_\psi^{\{Z\}}}{|\hat{p}_\phi^{\{Z\}} + (\hat{p}_\phi^{\{Z\}} \cdot \hat{p}_\psi^{\{Z\}}) \hat{p}_\psi^{\{Z\}}|} \quad (3.51)$$

$$\hat{y}_0^{\{\psi\}Z} = -\hat{p}_{K_S^0}^{\{\psi\}Z} \times \hat{x}_0^{\{\psi\}Z} \quad (3.52)$$

$$\hat{z}_0^{\{\psi\}Z} = -\hat{p}_{K_S^0}^{\{\psi\}Z} \quad (3.53)$$

The polar angle of μ^+ in ψ rest frame is defined as:

$$\cos \theta_\psi^Z = -\hat{p}_{K_S^0}^{\{\psi\}Z} \cdot \hat{p}_{\mu^+}^{\{\psi\}Z} \quad (3.54)$$

The azimuthal angle of μ^+ in ψ rest frame:

$$\phi_\mu^Z = \text{atan}2\left(\hat{y}_0^{\{\psi\}Z} \cdot \hat{p}_{\mu^+}^{\{\psi\}Z}, \hat{x}_0^{\{\psi\}Z} \cdot \hat{p}_{\mu^+}^{\{\psi\}Z}\right) \quad (3.55)$$

The angle α_μ^Z is defined as:

$$\alpha_\mu^Z = \text{atan}2\left((\hat{z}_0^{\{\mu^+\}Z} \times \hat{x}_0^{\{\mu^+\}Z}) \cdot \hat{x}_0^{\{\mu^+\}K^{*0}}, \hat{x}_0^{\{\mu^+\}Z} \cdot \hat{x}_0^{\{\mu^+\}K^{*0}}\right) \quad (3.56)$$

$\hat{z}_0^{\{\mu^+\}Z}$ means the z axis of μ^+ rest frame in the Z chain. Other symbols are similar. Here, $\hat{x}_0^{\{\mu^+\}K^{*0}}$, $\hat{x}_0^{\{\mu^+\}Z}$ and $\hat{x}_0^{\{\mu^+\}Z}$ are defined as:

$$\hat{x}_0^{\{\mu^+\}K^{*0}} = -\frac{-\hat{p}_{K^{*0}}^{\{\psi\}} + (\hat{p}_{K^{*0}}^{\{\psi\}} \cdot \hat{p}_{\mu^+}^{\{\psi\}}) \hat{p}_{\mu^+}^{\{\psi\}}}{|\hat{p}_{K^{*0}}^{\{\psi\}} + (\hat{p}_{K^{*0}}^{\{\psi\}} \cdot \hat{p}_{\mu^+}^{\{\psi\}}) \hat{p}_{\mu^+}^{\{\psi\}}|} \quad (3.57)$$

$$\hat{x}_0^{\{\mu^+\}Z} = -\frac{-\hat{p}_{K_S^0}^{\{\psi\}} + (\hat{p}_{K_S^0}^{\{\psi\}} \cdot \hat{p}_{\mu^+}^{\{\psi\}}) \hat{p}_{\mu^+}^{\{\psi\}}}{|\hat{p}_{K_S^0}^{\{\psi\}} + (\hat{p}_{K_S^0}^{\{\psi\}} \cdot \hat{p}_{\mu^+}^{\{\psi\}}) \hat{p}_{\mu^+}^{\{\psi\}}|} \quad (3.58)$$

$$\hat{z}_0^{\{\mu^+\}Z} = \hat{p}_{\mu^+}^{\{\psi\}} \quad (3.59)$$

Keep in mind that the axes have to be calculated in the same ψ rest frame.

3.4.4 Matrix element for the $X \rightarrow \psi \phi$ chain

The decay chain of $B^+ \rightarrow X_i K^+$, $X_i \rightarrow \psi \phi$, $\phi \rightarrow K^+ K^-$, $\psi \rightarrow \mu^+ \mu^-$ also contains four terms. The $B_s^0 \rightarrow X_i K^+$ gives a constant term $\mathcal{H}^{B^+ \rightarrow X_i K^+}$ and limits $\lambda_X = \lambda_K^X = 0$.

The $X_i \rightarrow \psi\phi$ is described by the term

$$\mathcal{H}_{\lambda_\psi^X, \lambda_\phi^X}^{X_i} D_{0, \lambda_\psi^X - \lambda_\phi^X}^{J_{X_i}}(\phi_\psi^X, \theta_X, 0)^* R_{X_i}(m_{\psi\phi}), \quad (3.60)$$

The helicity angles of X decays ϕ_ψ^X and θ_X are defined by the ψ direction. The strong decay conserves parity, which gives the relation $\mathcal{H}_{-\lambda_\psi^X, -\lambda_\phi^X}^X = (-1)^{J_X} P_{X_j} \mathcal{H}_{\lambda_\psi^X, \lambda_\phi^X}^X$.

The $\phi \rightarrow K^+K^-$ provides one term

$$D_{\lambda_\phi^X, 0}^1(\phi_{K^+}^X, \theta_\phi^X, 0)^*, \quad (3.61)$$

where K^+ is used to define the two helicity angles of $\phi_{K^+}^X$ and θ_ϕ^X from ϕ decays. We use the superscript X to differentiate from the other decay chains.

The $\psi \rightarrow \mu^+\mu^-$ decay is described by the term

$$D_{\lambda_\psi^X, \Delta\lambda_\mu^X}^1(\phi_\mu^X, \theta_\psi^X, 0)^*. \quad (3.62)$$

The muon helicity states are aligned by α_μ^X rotation.

The total matrix element for the X chain from B^+ decay is

$$\begin{aligned} \mathcal{M}_{\Delta\lambda_\mu}^X(\theta_X, \theta_\psi^X, \theta_\phi^X, \phi_{K^+}^X, \phi_\mu^X, \alpha_\mu^X, m_{\psi\phi}) &= e^{i\Delta\lambda_\mu\alpha_\mu^X} \sum_{\lambda_\psi^X} e^{i\lambda_\psi^X\phi_\mu^X} d_{\lambda_\psi^X, \Delta\lambda_\mu}^1(\theta_\psi^X) \\ &\times \sum_{\lambda_\phi^X} e^{i\lambda_\phi^X\phi_{K^+}^X} d_{\lambda_\phi^X, 0}^1(\theta_\phi^X) \sum_i \mathcal{H}^{B^+ \rightarrow X_i K^+} \mathcal{H}_{\lambda_\psi^X, \lambda_\phi^X}^{X_i} d_{0, \lambda_\psi^X - \lambda_\phi^X}^{J_{X_i}}(\theta_X) R_{X_i}(m_{\psi\phi}). \end{aligned} \quad (3.63)$$

The angles used in X chain are defined in Figure 3.18. The polar angle of ψ in X rest frame can be calculated:

$$\cos \theta_X = -\hat{p}_{K_S^0}^{\{X\}} \cdot \hat{p}_\psi^{\{X\}} \quad (3.64)$$

The axis of X rest frame is defined as:

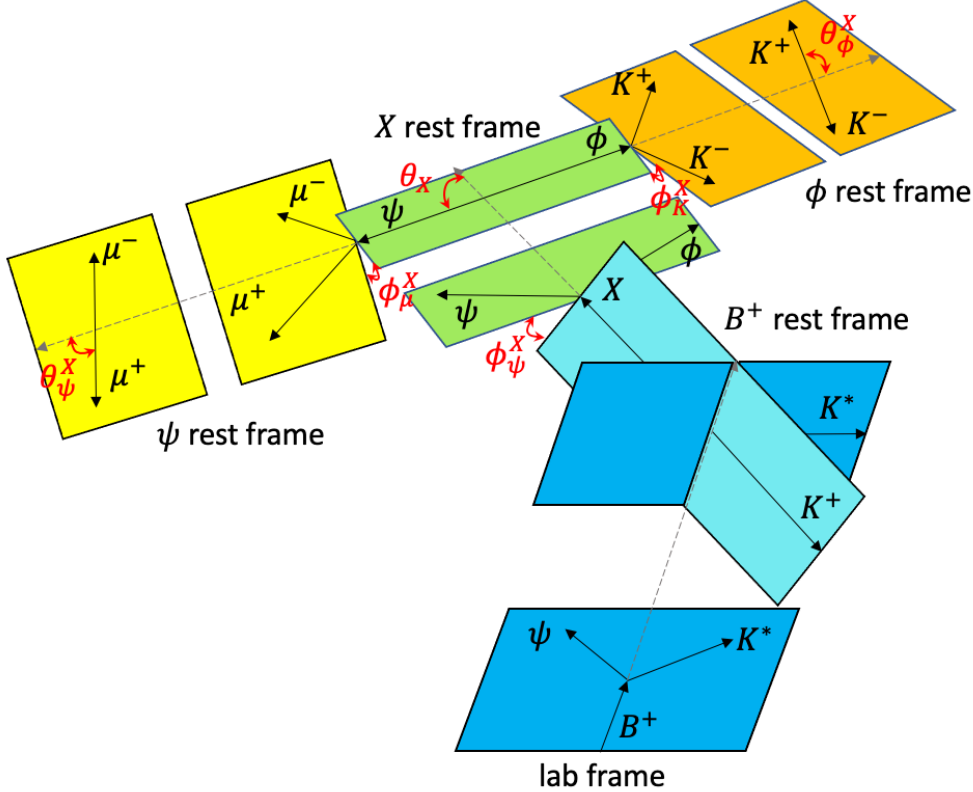
$$\hat{x}_0^{\{X\}} = -\frac{\hat{p}_{B^0}^{\{LAB\}} - (\hat{p}_{B^0}^{\{LAB\}} \cdot \hat{p}_X^{\{B^0\}}) \hat{p}_X^{\{B^0\}}}{\left| \hat{p}_{B^0}^{\{LAB\}} - (\hat{p}_{B^0}^{\{LAB\}} \cdot \hat{p}_X^{\{B^0\}}) \hat{p}_X^{\{B^0\}} \right|} \quad (3.65)$$

$$\hat{y}_0^{\{X\}} = -\hat{p}_{K_S^0}^{\{X\}} \times \hat{x}_0^{\{X\}} \quad (3.66)$$

$$\hat{z}_0^{\{X\}} = -\hat{p}_{K_S^0}^{\{X\}} \quad (3.67)$$

The azimuthal angle of ψ in X rest frame can be determined from:

$$\phi_\psi^X = \text{atan2}\left(\hat{y}_0^{\{X\}} \cdot \hat{p}_\psi^{\{X\}}, \hat{x}_0^{\{X\}} \cdot \hat{p}_\psi^{\{X\}}\right) \quad (3.68)$$


 Figure 3.18 Definaton of decay angles in the X chain.

The definition of axis of ψ rest frame is shown:

$$\hat{x}_0^{\{\psi\}X} = -\frac{-\hat{p}_{K_S^0}^{\{X\}} + (\hat{p}_{K_S^0}^{\{X\}} \cdot \hat{p}_\psi^{\{X\}}) \hat{p}_\psi^{\{X\}}}{|-\hat{p}_{K_S^0}^{\{X\}} + (\hat{p}_{K_S^0}^{\{X\}} \cdot \hat{p}_\psi^{\{X\}}) \hat{p}_\psi^{\{X\}}|} \quad (3.69)$$

$$\hat{y}_0^{\{\psi\}X} = -\hat{p}_\phi^{\{\psi\}X} \times \hat{x}_0^{\{\psi\}X} \quad (3.70)$$

$$\hat{z}_0^{\{\psi\}X} = -\hat{p}_\phi^{\{\psi\}X} \quad (3.71)$$

The polar angle of μ^+ in ψ rest frame is defined as:

$$\cos \theta_\psi^X = -\hat{p}_\phi^{\{\psi\}X} \cdot \hat{p}_{\mu^+}^{\{\psi\}X} \quad (3.72)$$

The azimuthal angle of μ^+ in ψ rest frame:

$$\phi_\mu^X = \text{atan2}\left(\hat{y}_0^{\{\psi\}} \cdot \hat{p}_{\mu^+}^{\{\psi\}}, \hat{x}_0^{\{\psi\}} \cdot \hat{p}_{\mu^+}^{\{\psi\}}\right) \quad (3.73)$$

The angle α_μ^X is defined as:

$$\alpha_\mu^X = \text{atan2}\left(\left(\hat{z}_0^{\{\mu^+\}X} \times \hat{x}_0^{\{\mu^+\}X}\right) \cdot \hat{x}_0^{\{\mu^+\}K^{*0}}, \hat{x}_0^{\{\mu^+\}X} \cdot \hat{x}_0^{\{\mu^+\}K^{*0}}\right) \quad (3.74)$$

$\hat{z}_0^{\{\mu^+\}X}$ means the z axis of μ^+ rest frame in the X chain. Other symbols are similar. Here,

$\hat{x}_0^{\{\mu^+\}K^0}$ is defined in Eq.3.57, $\hat{x}_0^{\{\mu^+\}X}$ and $\hat{x}_0^{\{\mu^+\}X}$ are defined as:

$$\hat{x}_0^{\{\mu^+\}X} = -\frac{-\hat{p}_\phi^{\{\psi\}} + (\hat{p}_\phi^{\{\psi\}} \cdot \hat{p}_{\mu^+}^{\{\psi\}}) \hat{p}_{\mu^+}^{\{\psi\}}}{|\hat{p}_\phi^{\{\psi\}} + (\hat{p}_\phi^{\{\psi\}} \cdot \hat{p}_{\mu^+}^{\{\psi\}}) \hat{p}_{\mu^+}^{\{\psi\}}|} \quad (3.75)$$

$$\hat{z}_0^{\{\mu^+\}X} = \hat{p}_{\mu^+}^{\{\psi\}} \quad (3.76)$$

For the rest frame of ϕ , the definition of axis:

$$\hat{x}_0^{\{\phi\}X} = -\hat{x}_0^{\{X\}} \quad (3.77)$$

$$\hat{y}_0^{\{\phi\}X} = \hat{y}_0^{\{X\}} \quad (3.78)$$

$$\hat{z}_0^{\{\phi\}X} = -\hat{z}_0^{\{X\}} \quad (3.79)$$

The polar angle of K^+ in ϕ rest frame:

$$\cos \theta_\phi^X = -\hat{p}_\psi^{\{\phi\}X} \cdot \hat{p}_{K^+}^{\{\phi\}X} \quad (3.80)$$

The azimuthal angle of K^+ in ϕ rest frame:

$$\phi_K^X = \text{atan2}\left(\hat{y}_0^{\{\phi\}X} \cdot \hat{p}_{K^+}^{\{\phi\}X}, \hat{x}_0^{\{\phi\}X} \cdot \hat{p}_{K^+}^{\{\phi\}X}\right) \quad (3.81)$$

Finally, total matrix element squared is given by

$$|\mathcal{M}|^2 = \sum_{\Delta\lambda_\mu=\pm 1} \left| \mathcal{M}_{\Delta\lambda_\mu}^{K^*} + \mathcal{M}_{\Delta\lambda_\mu}^Z + \mathcal{M}_{\Delta\lambda_\mu}^X \right|^2 \quad (3.82)$$

Assuming approximate CP symmetry, the helicity couplings for B^+ and B^- can be made equal, but the calculation of the angles requires some care, since parity (P) conservation does not change polar (i.e. helicity) angles, but does change azimuthal angles. Thus, not only must \vec{p}_{μ^-} be used instead of \vec{p}_{μ^+} for B^- candidates, as well as K^- instead of K^+ for the ϕ decay, but also all azimuthal angles must be reflected before entering the matrix element formula: all $\phi_i \rightarrow -\phi_i$, and two $\alpha_\mu \rightarrow -\alpha_\mu$ ^[68].

3.4.5 Usage of LS couplings

Since not all helicity couplings are independent because of parity conservation in strong decays, it is convenient to relate them to the LS couplings ($B_{L,S}$) using Clebsch-Gordan coefficients

$$\mathcal{H}_{\lambda_B, \lambda_C}^{A \rightarrow B C} = \sum_L \sum_S \sqrt{\frac{2L+1}{2J_A+1}} B_{L,S} \left(\begin{array}{cc} J_B & J_C \\ \lambda_B & -\lambda_C \end{array} \middle| \begin{array}{c} S \\ \lambda_B - \lambda_C \end{array} \right) \times \left(\begin{array}{cc} L & S \\ 0 & \lambda_B - \lambda_C \end{array} \middle| \begin{array}{c} J_A \\ \lambda_B - \lambda_C \end{array} \right). \quad (3.83)$$

Here L is the orbital angular momentum in the decay, and S is the total spin of the daughters, $\vec{S} = \vec{J}_B + \vec{J}_C$ ($|J_B - J_C| \leq S \leq J_B + J_C$). The LS couplings are all independent since they automatically satisfy the parity conservation relation in strong decays, by restricting L value to be odd or even using the selection $P_A = (-1)^L P_B \cdot P_C$, where P is parity of the particle.

Table 3.9 shows the allowed LS for various J^P of K excitations. The rule also applies to the $Z \rightarrow \psi K$ chain, because ψ and ϕ are vector particles, have the same $J^P = 1^-$. For $B^+ \rightarrow \psi K_n^*$ decays, $S = L_B^{K_n^*}$ can have up to three values, $J_{K_n^*} - 1$, $J_{K_n^*}$ and $J_{K_n^*} + 1$ (except for when $J_{K_n^*} = 0$, only one value $L_B^{K_n^*} = 1$ is possible), corresponding to three (or one) $B_{L,S}^{B^+ \rightarrow \psi K_n^*}$ couplings, respectively. For $K_n^* \rightarrow \phi K$ decay, $S = 1$, and $|J_{K_n^*} - 1| \leq L_{K_n^*} \leq J_{K_n^*} + 1$. Again when $J_{K_n^*} = 0$, $L_{K_n^*} = 1$. Parity conservation limits $L_{K_n^*}$ to be even or odd by $P_{K_n^*} = (-1)^{L_{K_n^*}}$, and natural parity ($1^-, 2^+, 0^+$ is forbidden) allows one $L_{K_n^*}$, while unnatural parity ($1^+, 2^- \dots$) allows two $L_{K_n^*}$. Since only the product of B^+ and K_n^* couplings can be determined, lowest L_{\min} coupling of K^* decay $B_{L_{\min},S}^{K_n^* \rightarrow \phi K}$ is defined as $(1, 0)$, which reduces one free coupling. To summarize whole K^* decay chain, $0^+ K_n^*$ is forbidden, 0^- is described by one coupling, $1^-, 2^+ \dots$ by three couplings, and $1^+, 2^- \dots$ by four couplings. The $0^- 2^1S_0$ is chosen as the reference channel, and the only one coupling of B decay is fixed to be $(1, 0)$. This is a very good choice to make fit stable, since the state has large and stable fit fraction about 10%, and only-one coupling is directly proportional to its fit fraction.

For $B^+ \rightarrow X_i K^+$ decays, only one coupling is needed, the coupling $B^{B^+ \rightarrow X_i K^+}$ is equal to $(1, 0)$, again because only the product of B^+ and X_i couplings can be determined. For $X_i \rightarrow \psi \phi$ decays, $S = 0, 1, 2$ and parity conservation relation $P_{X_i} = (-1)^{L_{X_i}}$ reduces L_{X_i} to about half. Table 3.10 shows the allowed LS for various J^P of X_i . Each LS combination requires one coupling that are determined by the fit.

Table 3.9 Allowed LS for various J^P in the $K_n^* \rightarrow \phi K$ decay chain.

J^P	$K_n^* \rightarrow \phi K$	$B \rightarrow J/\psi K_n^*$
0^+	forbidden	-
0^-	11	11
1^+	01, 21	00, 11, 22
1^-	11	00, 11, 22
2^+	21	11, 22, 33
2^-	11, 31	11, 22, 33

Table 3.10 Allowed LS for various J^P in the $X \rightarrow J/\psi\phi$ decay chain.

J^P	$X_i \rightarrow J/\psi\phi$	$B \rightarrow X_i K$
0^+	00, 22	00
0^-	11	00
1^+	01, 21, 22	11
1^-	10, 11, 12, 32	11
2^+	02, 20, 21, 22, 42	22
2^-	11, 12, 31, 32	22

3.4.6 cFit technique

We use *cFit* technique used in the previous publication^[16], which contains both signal and background PDFs. The signal PDF, \mathcal{P}_{sig} , is proportional to the matrix element squared, which is a function of six independent variables: $m_{\phi K}$ and the independent angular variables in the K^* decay chain Ω . The PDF also depends on the fit parameters, $\vec{\omega}$, which include the helicity couplings, and masses and widths of resonances. The two other invariant masses, $m_{\phi K}$ and $m_{J/\psi K}$, and the angular variables describing the X and Z_{cs}^+ decay chains depend on $m_{\phi K}$ and Ω , therefore they do not represent independent dimensions. The signal PDF is given by:

$$\frac{d\mathcal{P}}{dm_{\phi K} d\Omega} \equiv \mathcal{P}_{\text{sig}}(m_{\phi K}, \Omega | \vec{\omega}) = \frac{1}{I(\vec{\omega})} |\mathcal{M}(m_{\phi K}, \Omega | \vec{\omega})|^2 \Phi(m_{\phi K}) \epsilon(m_{\phi K}, \Omega), \quad (3.84)$$

where $\mathcal{M}(m_{\phi K}, \Omega | \vec{\omega})$ is the total matrix element given by Eq. (3.82) and discussed in detail in Appendix ???. $\Phi(m_{\phi K}) = p q$ is the phase space function, where p is the momentum of the ϕK^+ (*i.e.* K^*) system in the B^+ rest frame, and q is the K^+ momentum in the K^{*+} rest frame. The function $\epsilon(m_{\phi K}, \Omega)$ is the signal efficiency, and $I(\vec{\omega})$ is the normalization integral,

$$I(\vec{\omega}) \equiv \int \mathcal{P}_{\text{sig}}(m_{\phi K}, \Omega) dm_{\phi K} d\Omega \propto \frac{\sum_j w_j^{\text{MC}} |\mathcal{M}(m_{K^+ j}, \Omega_j | \vec{\omega})|^2}{\sum_j w_j^{\text{MC}}}, \quad (3.85)$$

where the sum is over simulated events, which are generated uniformly in B^+ decay phase space and passed through the detector simulation^[73] and data selection. In the simulation, pp collisions producing B^+ mesons are generated using PYTHIA^[138] with a specific LHCb configuration^[50]. The weights w_j^{MC} introduced in Eq. (3.85) contain corrections to the B^+ production kinematics and multiplicity in the generation and to the detector response to bring the simulations into better agreement with the data. The simulation sample contains 390 000 events reconstructed and selected, approximately 15 times the signal size in data. Run1 MC w_j^{MC} is multiplied by a constant scale (about 0.5) to let the sum of weights is proportional to the signal yield found in data, *i.e.* the ratio of MC sum weights is the same as the ratio of signal yields in Run 1 and Run 2 data. This procedure folds the detector response into the model

and allows a direct determination of the parameters of interest from the uncorrected data. The resulting log-likelihood sums over the data events (here for illustration, $\mathcal{P} = \mathcal{P}_{\text{sig}}$),

$$\begin{aligned}\ln L(\vec{\omega}) &= \sum_i \ln \mathcal{P}_{\text{sig}}(m_{\phi K_i}, \Omega_i | \vec{\omega}) \\ &= \sum_i \ln |\mathcal{M}(m_{\phi K_i}, \Omega_i | \vec{\omega})|^2 - N \ln I(\vec{\omega}) + \sum_i \ln [\Phi(m_{\phi K_i}) \epsilon(m_{\phi K_i}, \Omega_i)],\end{aligned}\quad (3.86)$$

where the last term does not depend on $\vec{\omega}$ and can be dropped (N is the total number of the events in the fit).

In addition to the signal PDF, $\mathcal{P}_{\text{sig}}(m_{\phi K}, \Omega | \vec{\omega})$, the background PDF, $\mathcal{P}_{\text{bkg}}(m_{\phi K}, \Omega)$ determined from the B^+ mass peak sidebands, is included. We minimize the negative log-likelihood defined as

$$\begin{aligned}-\ln L(\vec{\omega}) &= -\sum_i \ln [(1-\beta) \mathcal{P}_{\text{sig}}(m_{\phi K_i}, \Omega_i | \vec{\omega}) + \beta \mathcal{P}_{\text{bkg}}(m_{\phi K_i}, \Omega_i)] \\ &= -\sum_i \ln \left[(1-\beta) \frac{|\mathcal{M}(m_{\phi K_i}, \Omega_i | \vec{\omega})|^2 \Phi(m_{\phi K_i}) \epsilon(m_{\phi K_i}, \Omega_i)}{I(\vec{\omega})} + \beta \frac{\mathcal{P}_{\text{bkg}}^u(m_{\phi K_i}, \Omega_i)}{I_{\text{bkg}}} \right] \\ &= -\sum_i \ln \left[|\mathcal{M}(m_{\phi K_i}, \Omega_i | \vec{\omega})|^2 + \frac{\beta I(\vec{\omega})}{(1-\beta) I_{\text{bkg}}} \frac{\mathcal{P}_{\text{bkg}}^u(m_{\phi K_i}, \Omega_i)}{\Phi(m_{\phi K_i}) \epsilon(m_{\phi K_i}, \Omega_i)} \right] + N \ln I(\vec{\omega}) + \text{const.},\end{aligned}\quad (3.87)$$

where β is the background fraction in the peak region determined from the fit to the $m_{J/\psi \phi K}$ distribution (Figure 3.9), $\mathcal{P}_{\text{bkg}}^u(m_{\phi K}, \Omega)$ is the unnormalized background density proportional to the density of sideband events, with its normalization determined by^③

$$I_{\text{bkg}} \equiv \int \mathcal{P}_{\text{bkg}}^u(m_{\phi K}) dm_{\phi K} d\Omega \propto \frac{\sum_j w_j^{\text{MC}} \frac{\mathcal{P}_{\text{bkg}}^u(m_{\phi K_j}, \Omega_j)}{\Phi(m_{\phi K_j}) \epsilon(m_{\phi K_j}, \Omega_j)}}{\sum_j w_j^{\text{MC}}}. \quad (3.88)$$

The equation above implies that the background term is efficiency corrected, so it can be added to the efficiency-independent signal probability expressed by $|\mathcal{M}|^2$. This way the efficiency parameterization, $\epsilon(m_{\phi K}, \Omega)$, becomes a part of the background description which affects only a very small part of the total PDF.

The efficiency parameterization in the background term is assumed to factorize as

$$\begin{aligned}\epsilon(m_{\phi K}, \Omega) &= \epsilon_1(m_{\phi K}, \cos \theta_{K^*}) \epsilon_2(\cos \theta_\phi | m_{\phi K}) \times \\ &\quad \epsilon_3(\cos \theta_{J/\psi} | m_{\phi K}) \epsilon_4(\Delta \phi_{K^*, \phi} | m_{\phi K}) \epsilon_5(\Delta \phi_{K^*, J/\psi} | m_{\phi K}).\end{aligned}\quad (3.89)$$

The $\epsilon_1(m_{\phi K}, \cos \theta_{K^*})$ term is obtained by binning a two-dimensional (2D) histogram of the

^③ Notice that the distribution of MC events includes both the $\Phi(m_{\phi K})$ and $\epsilon(m_{\phi K}, \Omega)$ factors, which cancel their product in the numerator.

simulated signal events. Each event is given a $1/(p q)$ weight, since at the generator level the phase space is flat in $\cos \theta_{K^*}$ but has a $p q$ dependence on $m_{\phi K}$. A bi-cubic function is used to interpolate between bin centers. The $\epsilon_1(m_{\phi K}, \cos \theta_{K^*})$ efficiency and its visualization across the normal Dalitz plane are shown in Figure. 3.19. The other terms are again built from 2D histograms, but with each bin divided by the number of simulated events in the corresponding $m_{\phi K}$ slice to remove the dependence on this mass (Figure. 3.20).

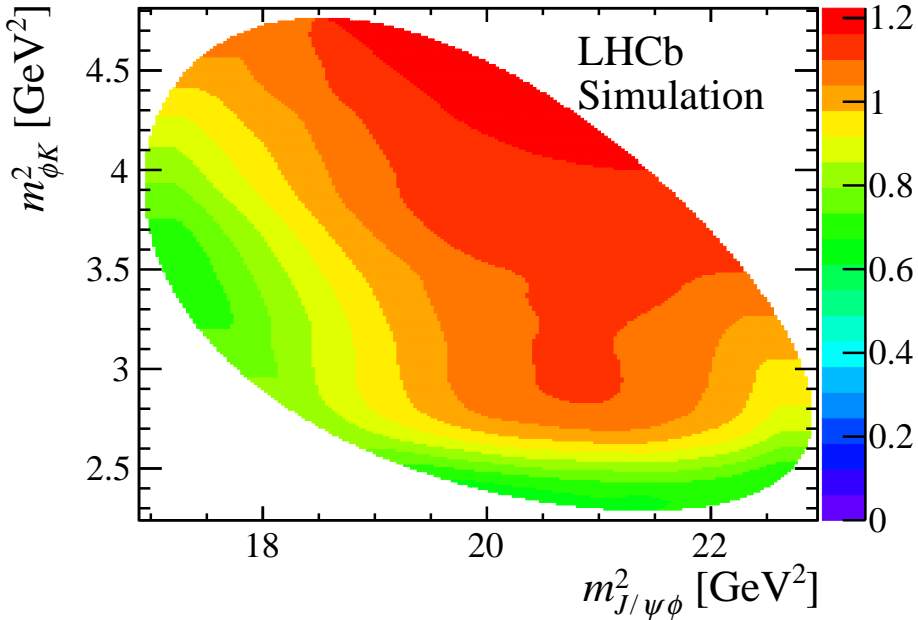


Figure 3.19 Parameterized efficiency representation in the Dalitz plane ($m_{J/\psi\phi}^2, m_{\phi K}^2$). Function values corresponding to the color encoding are given on the right. The normalization arbitrarily corresponds to unity when averaged over the phase space.

The background PDF, $\mathcal{P}_{\text{bkg}}^u(m_{\phi K}, \Omega)/\Phi(m_{\phi K})$, is built using the same approach,

$$\frac{\mathcal{P}_{\text{bkg}}^u(m_{\phi K}, \Omega)}{\Phi(m_{\phi K})} = P_{\text{bkg}_1}(m_{\phi K}, \cos \theta_{K^*}) P_{\text{bkg}_2}(\cos \theta_\phi | m_{\phi K}) \times \\ P_{\text{bkg}_3}(\cos \theta_{J/\psi} | m_{\phi K}) P_{\text{bkg}_4}(\Delta \phi_{K^*, \phi} | m_{\phi K}) P_{\text{bkg}_5}(\Delta \phi_{K^*, J/\psi} | m_{\phi K}). \quad (3.90)$$

The background function $P_{\text{bkg}_1}(m_{\phi K}, \cos \theta_{K^*})$ is shown in Figure. 3.21 and the other terms are shown in Figure. 3.22.

The fit fraction (FF) of any component R is defined as,

$$\text{FF} = \frac{\int |\mathcal{M}^R(m_{\phi K}, \Omega)|^2 \Phi(m_{\phi K}) dm_{\phi K} d\Omega}{\int |\mathcal{M}(m_{\phi K}, \Omega)|^2 \Phi(m_{\phi K}) dm_{\phi K} d\Omega}, \quad (3.91)$$

where in \mathcal{M}^R all terms except those associated with the R amplitude are set to zero.

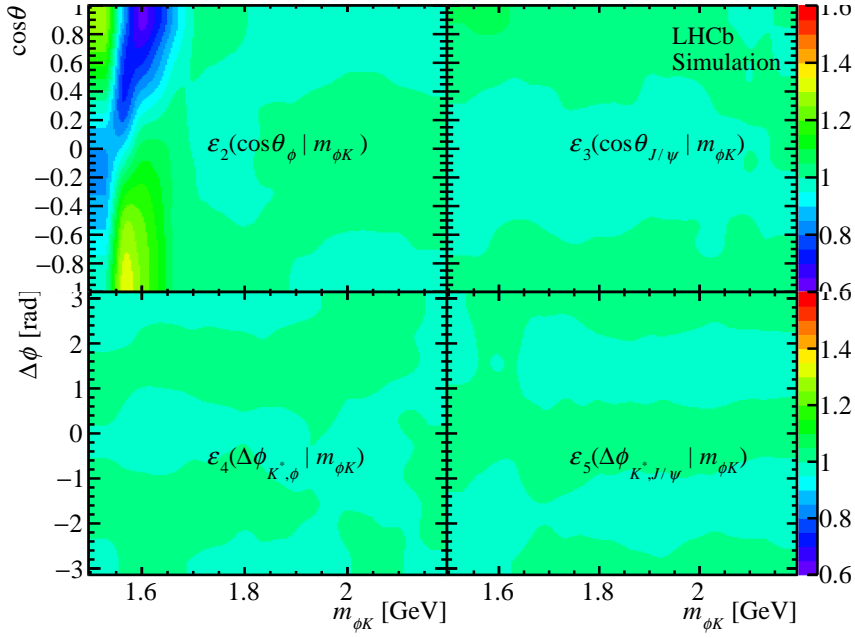


Figure 3.20 Parameterized efficiency $\epsilon_2(\cos \theta_\phi | m_{\phi K})$, $\epsilon_3(\cos \theta_{J/\psi} | m_{\phi K})$, $\epsilon_4(\Delta\phi_{K^*,\phi} | m_{\phi K})$, $\epsilon_5(\Delta\phi_{K^*,J/\psi} | m_{\phi K})$ functions. Function values corresponding to the color encoding are given on the right. By construction each function integrates to unity at each $m_{\phi K}$ value. The structure in $\epsilon_2(\cos \theta_\phi | m_{\phi K})$ present between 1500 and 1600 MeV is an artifact of removing $B^+ \rightarrow J/\psi K^+ K^- K^+$ events in which both $K^+ K^-$ combinations pass the ϕ mass selection window.

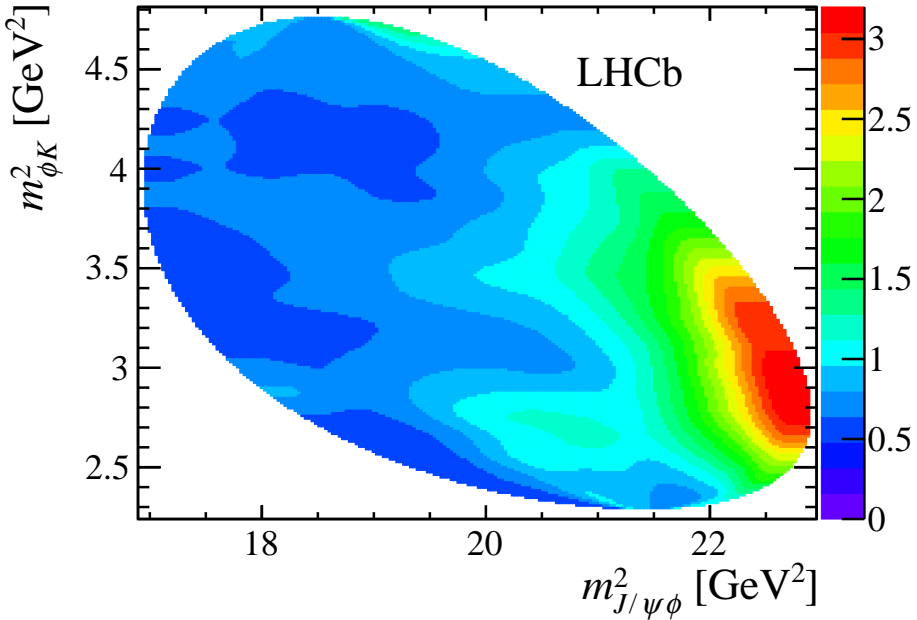


Figure 3.21 Parameterized background representation in the Dalitz plane ($m_{J/\psi\phi}^2, m_{\phi K}^2$). Function values corresponding to the color encoding are given on the right. The normalization arbitrarily corresponds to unity when averaged over the phase space.

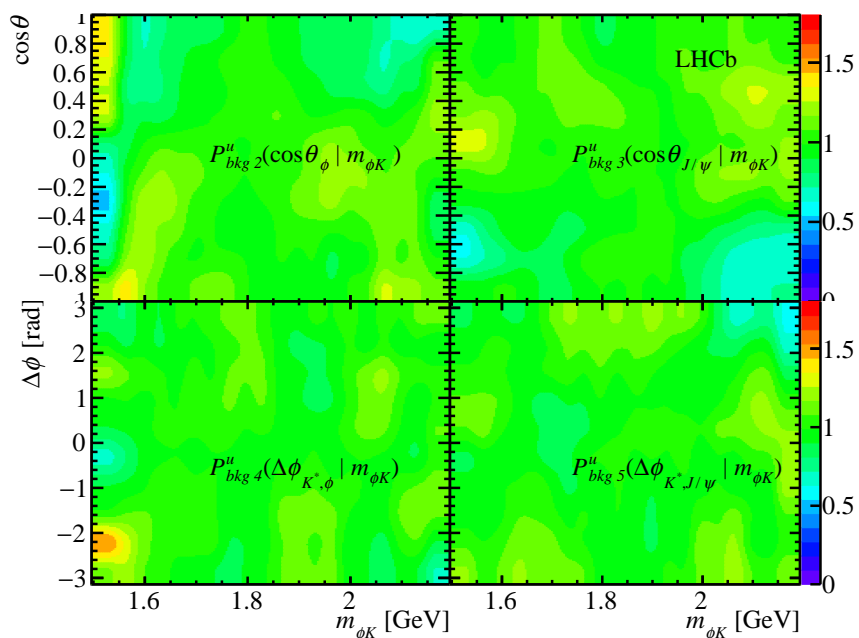


Figure 3.22 Parameterized background functions: $P_{\text{bkg},2}^u(\cos\theta_\phi | m_{\phi K})$, $P_{\text{bkg},3}^u(\cos\theta_{J/\psi} | m_{\phi K})$, $P_{\text{bkg},4}^u(\Delta\phi_{K^*,\phi} | m_{\phi K})$, $P_{\text{bkg},5}^u(\Delta\phi_{K^*,J/\psi} | m_{\phi K})$. Function values corresponding to the color encoding are given on the right. By construction each function integrates to unity at each $m_{\phi K}$ value.

3.5 The amplitude fitting results

We fit the events in ± 15 MeV around B^+ known mass^[145]. For the background, its fraction is fixed to 4.0% and its PDF is obtained from $\pm(25 - 50)$ MeV B sideband events as described in Section B.3.

3.5.1 Kaon excitations in $B^+ \rightarrow J/\psi \phi K^+$

The kaon mass spectrum as predicted in the relativistic potential model by Godfrey–Isgur^[Godfrey:1985xj] is shown in Figure. 3.23 together with the experimentally determined masses of both well-established and unconfirmed K^* resonances, with the status before our first amplitude analysis of $B^+ \rightarrow J/\psi \phi K^+$ ^[145]. Table 3.11 summarizes this status, with some more recent updates. Past experiments on K^* states decaying to ϕK ^[Armstrong:1982tw, Frame:1985ka, Kwon:1993xb] had limited precision, especially at high masses, gave somewhat inconsistent results, and provided evidence for only a few of the states expected from the quark model in the 1513–2182 MeV range probed in our data set. However, except for the $J^P = 0^+$ states which cannot decay to ϕK because of angular momentum and parity conservation, all other kaon excitations above the ϕK threshold are predicted to decay to this final state^[Kokoski:1985is]. In B^+ decays, production of high spin states, like the $K_3^*(1780)$ or $K_4^*(2045)$ resonances, is expected to be suppressed by the high orbital angular momentum required to produce them.

Like in our previous amplitude analysis, the predictions of the Godfrey–Isgur model as a guide to the number and J^P of the K^{*+} states are included in the model. We also consider several states that are below the mass threshold. We fix the masses and widths of well measured states to improve fit stability, and let the others vary.

3.5.2 Changes to the previous amplitude model

The model used in Run 1 publication^[15,16], listed in Table 3.1 is first tested. Many fits were done with random initial inputs to obtain the best solution ($\ln \mathcal{L} = 4367$). Figure 3.24 shows the fit projections onto the three masses. While gross mass peaking structures are reproduced, deficiencies in describing the $m_{J/\psi \phi}$ and $m_{J/\psi K}$ projections accurately are apparent. Therefore, improvements to the model are needed.

The fit results with the Run 1 model suggest several rather minor adjustments:

- $K(0^-)$: In Run 1 model, a candidate for 3^1S_0 state was found at $1874 \pm 43^{+59}_{-115}$ MeV with width of $168 \pm 90^{+280}_{-104}$ MeV, however, it was not very significant (3.5σ). In our fits, the width of such high mass 0^- state reaches to the upper limit set in the fits

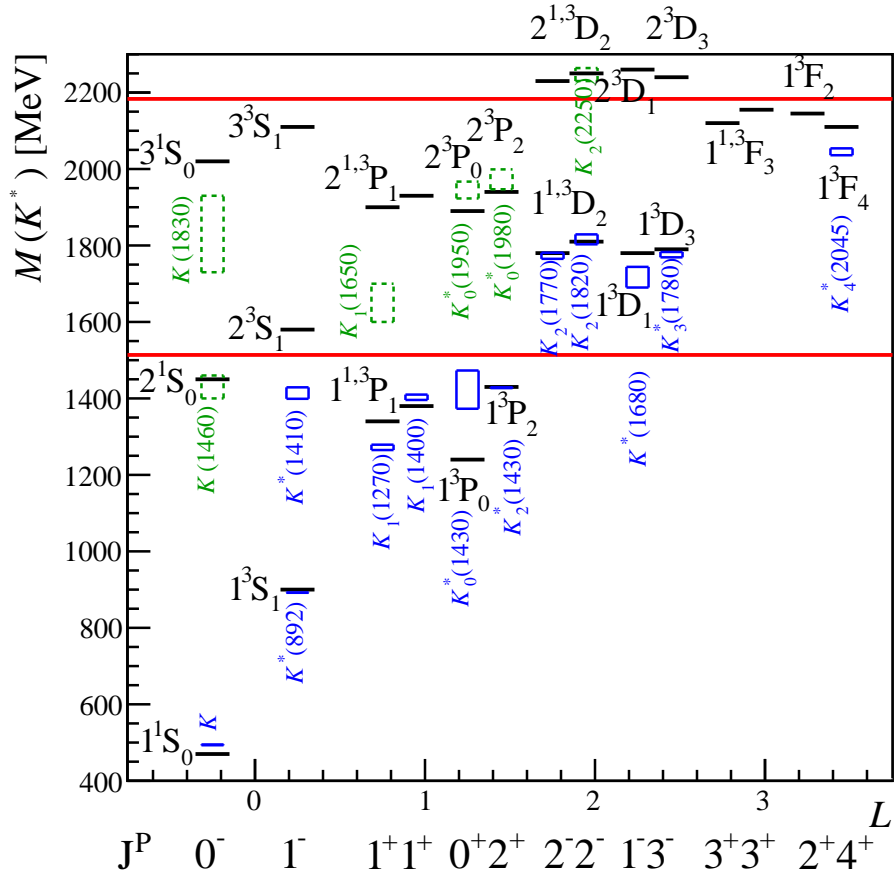


Figure 3.23 Kaon excitations predicted by Godfrey–Isgur^[Godfrey:1985xj] (horizontal black lines) labeled with their intrinsic quantum numbers: $n^{2S+1}L_J$ (see the text). Well established states are shown with narrower solid blue boxes extending to $\pm 1\sigma$ in mass and labeled with their PDG names^[126]. Unconfirmed states are shown with dashed green boxes. The long horizontal red lines indicate the ϕK mass range probed in $B^+ \rightarrow J/\psi \phi K^+$ decays.

Table 3.11 Possible contribution of kaon excitations to $B^+ \rightarrow J/\psi \phi K^+$ decays. For those states in bold, their masses and widths are fixed to listed values, in which 2014 PDG values to remove the contribution from the previous LHCb publication is used. That of the other states are varied in the fit.

States		M_0 [MeV]	Γ_0 [MeV]	Ref.
$K(0^-)$				
2^1S_0	$K(1460)$	1482.4 ± 15.6	335.6 ± 10.6	LHCb ^[18]
3^1S_0		Not observed		
$K(1^-)$				
2^3S_1	$K^*(1410)$	1414 ± 15	232 ± 21	PDG ^[145]
3^3S_1		Not observed		
1^3D_1	$K^*(1680)$	1717 ± 27	322 ± 110	PDG ^[126]
$K(1^+)$				
1^3P_1	$K_1(1400)$	1403 ± 7	174 ± 13	PDG ^[145]
2^1P_1	$K(1650)$	1672 ± 50	158 ± 50	PDG ^[145]
2^3P_1		Not observed		
$K(2^+)$				
2^3P_2	$K_2^*(1980)$	1942 ± 50	307^{+50}_{-31}	PDG ^[145]
1^3F_2		Not observed		
$K(2^-)$				
1^1D_2	$K_2(1770)$	1773 ± 8	186 ± 14	PDG ^[126]
1^3D_2	$K_2(1820)$	1816 ± 13	276 ± 35	PDG ^[126]
$K(3^-)$				
1^3D_3	$K_3^*(1780)$	1776 ± 7	159 ± 21	PDG ^[145]
$K(3^+)$				
1^1F_3		Not observed		
1^3F_3		Not observed		
$K(4^+)$				
1^3F_4	$K_4^*(2045)$	2048^{+8}_{-9}	199^{+27}_{-19}	PDG ^[145]

(2 GeV). Recently, LHCb established lower mass $2^1S_0 K(1460)$ state^[18], at larger mass (1482 ± 16 MeV) and width (336 ± 11 MeV) than previously measured. We include this state with the fixed mass and width, as its tail can clearly contribute. We explore adding a higher mass excitation to it later.

- $K(1^+)$: This major contribution to the total rate was described in Run 1 model as two resonances (roughly speaking mixed 2^3P_1 and 2^1P_1 states) and large non-resonant contribution. In the fit to the new data, such representation makes the higher mass state very broad (up to 1.2 GeV), therefore similar to non-resonant contribution, and they interfere profoundly (~84%). We obtain a better model by replacing the non-resonant contribution by the tail of the $1^3P_1 K_1(1400)$ resonance with the mass and width fixed to the previous measurements (see Table 3.11).
- $K(1^-)$: In addition to $1^3D_1 K^*(1680)$ state, a tail of $2^3S_1 K_1^*(1410)$ resonance is also included. Masses and widths are fixed to the values averaged over the previous measurements (Table 3.11).
- $K(2^-)$: The Run 1 model left the masses and widths of $K_2(1770)$ and $K_2(1820)$ free in the fit and demonstrated good consistency with the previous measurements, albeit with large errors. Since there are large interferences between these two close in mass and broad resonances, overall model stability by fixing them to the other measurements is improved.
- $X(4140)$: When fit with single-component mass-dependent width (eq. 3.22) we obtain $\Gamma_0 = 161 \pm 28$ MeV, which is about twice larger than Run 1 result (Table 3.1). Because M_0 is very close to the kinematic threshold, q_0 can be very small and strongly dependent on exact value of M_0 . This in turn, makes Γ_0 unstable too. Therefore, it is required to use of a constant width in the Breit-Wigner formula for $X(4140)$ ($\Gamma(m) = \Gamma_0$). As an alternative, two-component mass-dependent width formula is investigated later, in which $D_s^{*+} D_s^-$ is included as likely decay channel with the lower kinematic threshold (see Sec. 3.5.5).

To summarize these changes, fit quality and stability are improved by including a number of broad below-the-threshold K^* resonances (in Run 1 analysis such additional components were considered among systematic errors) and by fixing the masses and widths of several well established K^* resonances above the ϕK threshold to the other measurements. For K^* s which are below the ϕK decay threshold, and for X s that are close to the $J/\psi\phi$ threshold (*i.e.* $X(4140)$ and $X(4127)$ discussed later), a constant width in the Breit-Wigner formula is used. After these changes, with 9 K^* components (Run 1 model used 8) and 5 X components the likelihood

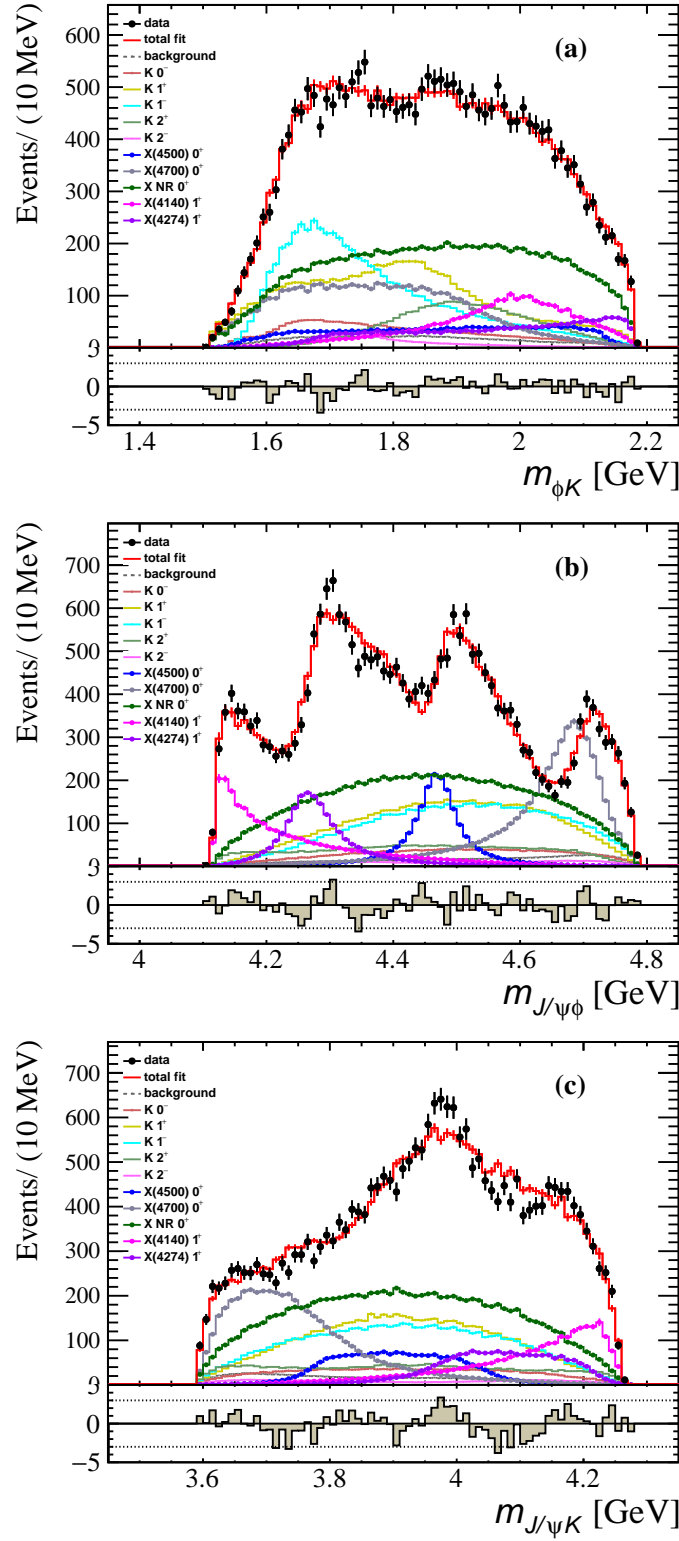


Figure 3.24 Fit projections of (a) $m_{\phi K}$, (b) $m_{J/\psi \phi}$, (c) $m_{J/\psi K}$ by fitting Run 1 model to the new Run 1+2 data sample.

is slightly improved to $\ln \mathcal{L} = 4424$ (i.e. $\Delta \ln \mathcal{L} = 56$), but the deficiencies in description of the mass projections persist.

Then, more drastic changes by adding new exotic hadron components are studied, X or Z_{cs} states of different J^P hypotheses. To ensure that such components are not reflections of inadequacy of our K^* model, besides, more predicted higher mass K^* resonances is also tried. The results from adding one component at a time are listed in Table 3.12, which shows two states giving the largest likelihood improvements first ($1^+ Z_{cs}$ and $1^+ X$), and then more check, if any further X or Z_{cs} state significantly improved the model, is applied. In the second iteration, several states give large improvements; 1^- and $1^+ Z_{cs}$ improve $\ln \mathcal{L}$ by 110 and 104, while 1^- and $2^- X$ by 100 and 69. Since the 1^+ and $1^- Z_{cs}$ are at about the same mass (4.2 GeV), they might be the same state. Therefore the two X states and one Z_{cs} state are chosen in the third iteration. In total, three more X and two Z components are added to the model. All new states have significances above 5σ , as evaluated by taking them out of the default model one-by-one. Further addition of an X state of any J^P gives components with significance below 5σ .

Larger improvement is from addition of the $3^3S_1 K$ candidate state, but the fit returns its mass at the upper kinematic limit and a width of more than 1 GeV. This state and $X(4140)$ state get very large fit fractions, each about 67%, and strong negative interference fraction between them of -93%. This is not physical, therefore, it is not considered in the nominal fit, but instead include it in extended K model.

Table 3.12 Improvement on $\ln \mathcal{L}$ by adding one X or Z or K with different J^P hypothesis.

J^P	0^+	0^-	1^+	1^-	2^+	2^-
X	25	25	133	98	64	81
Z_{cs}	forbidden	36	195	94	41	42
J^P	$3^1S_0(0^-)$	$1^3D_3(3^-)$	$1F_3(3^+)$	$1^3F_2(2^+)$	$3^3S_1(1^-)$	
K	5	18	5	37	70	

3.5.3 Nominal amplitude model

Based on the investigation described in the previous section, the nominal model is now built, which includes two Z_{cs} and three new X components in the fit, called $9K+5X+3X+2Z$ model. Since additional K^* resonances are not as significant, which are used to study systematic uncertainties. The second Z_{cs} with $J^P = 1^+$ or 1^- give similar fit likelihood. However the $1^- Z_{cs}$ fit is not very physical, because its interference fraction with $X(4140)$ state is -8.8%, but its FF is only 8.2%, and its mass is also at the high mass boundary. Instead, the $1^+ Z_{cs}$ looks more physical, therefore, the $1^+ Z$ fit for the nominal model is chosen, and use the other one as model variation used to evaluate systematic errors.

The nominal model gives $\ln \mathcal{L} = 5004$, about 580 improvement for 45 more free parameters with respect to the 9K+5X model which does not include new exotic hadron components. The improvement in $\ln \mathcal{L}$ is about equal to the sum of individual improvements in Table 3.12, illustrating that the added five exotic states are independent.

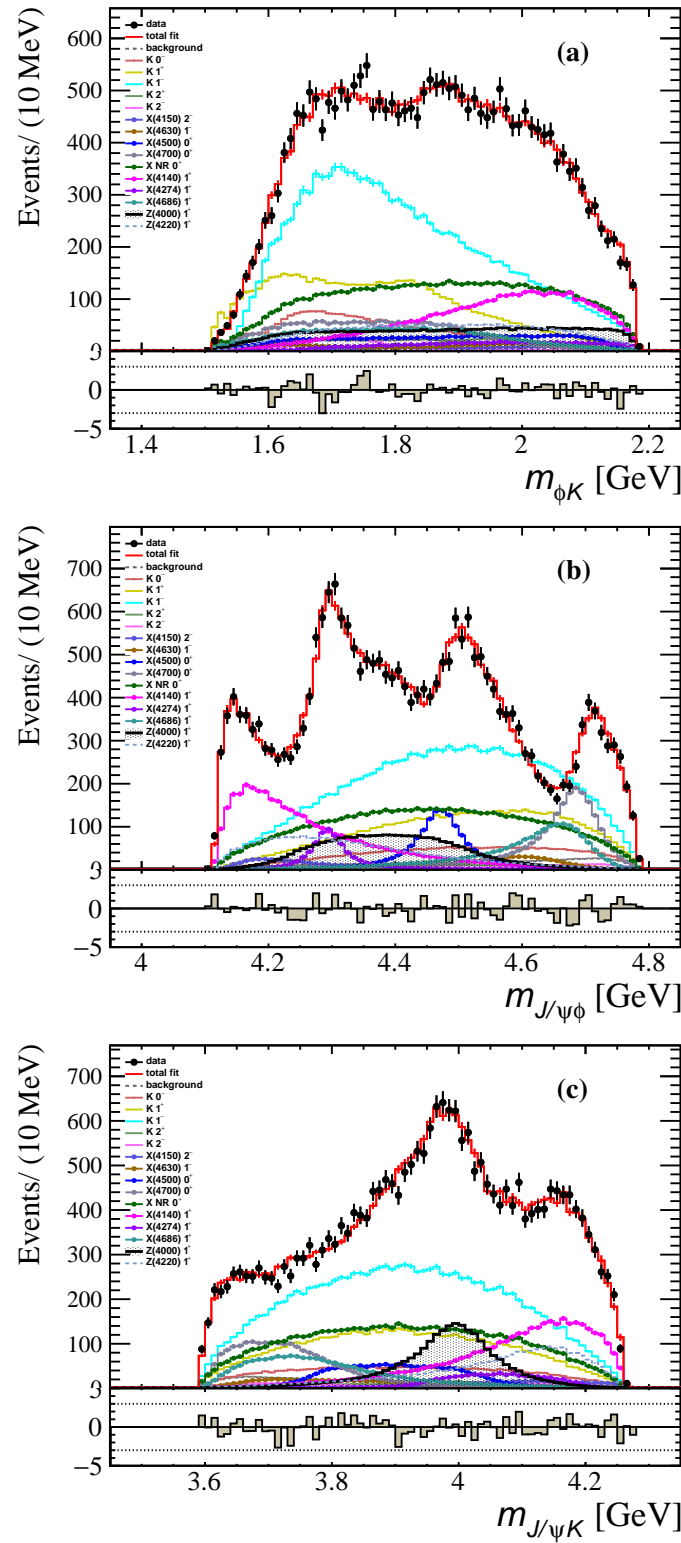
The mass projections are well modelled by the nominal fit as shown in Figure. 3.25. Two-dimensional Dalitz-plot distributions generated from the nominal amplitude model are shown Figure. 3.26. The data structures in Figures. 3.11-3.13 are well reproduced. Figure. 3.27 shows the $m_{J/\psi K}$ distributions in two slices of $m_{J/\psi \phi}$, as well as the overall $m_{J/\psi K}$ projection without the two $1^+ Z_{cs}$ states included in Figure. 3.28. The low mass $1^+ Z$ at about 4 GeV is evident. The angular distributions in ϕK decay chain are shown in Figure. 3.29. They are well described by the nominal fit.

Fit results are shown in Table 3.13, including masses, widths, fit fractions, and significance of each component. The significance of each component is evaluated by assuming that the change of $2 \ln \mathcal{L}$ between the default fit and the fit without this component, obeys the χ^2 distribution with number of degrees of freedom (ndf) equal to twice the reduction in number of free parameters, to take into account look elsewhere effect^[15]. The ndf is not multiplied by two for the K^* resonance whose mass and width are fixed. All the included states are above 5σ significant. The statistical significance for two Z_{cs} states are 16 and 8σ , respectively. Three new X states are 15, 8.7 and 5.7σ significant, respectively.

3.5.4 Extended K^* model

We add more K^* resonances to test the significance of each of components, and evaluate systematic uncertainties. Seven more K resonances are predicted in the allowed ϕK mass range by the relativistic potential model from Godfrey-Isgur^[Godfrey:1985xj]. They are $3^1S_0(0^-)$, $3^3S_1(1^-)$, $1^3D_3(3^-)$, $1^{1,3}F_3(3^+)$, $1^3F_2(2^+)$, and $1^3F_4(4^+)$. We add all of them except for the 4^+ resonance because $L_B = 3$ decays of B are expected to be much suppressed. We use only one BW to represent $1^{1,3}F_3(3^+)$ resonances to reduce possible large interference effects between these two states predicted to be very close in mass. The fit results are listed in Table 3.14. All the new exotic components preserve large significances of more than 5σ . Among additional K^* components, a candidate 3^3S_1 state is 4.4σ significant, and has large mass and width, as expected for such high radial excitation of triplet S -wave. A candidate for higher radial excitation of the singlet S -wave 3^1S_0 has a significance of 4.6σ , but very small fit fraction. Other states are even less significant. The mass projections of this fit are shown in Figure. 3.30.

In all the models, the two new X states around 4650 MeV are found to have significance of

Figure 3.25 Fit projections of (a) $m_{\phi K}$, (b) $m_{J/\psi \phi}$, (c) $m_{J/\psi K}$ from the $9K + 5X + 2X + 2Z$ model.

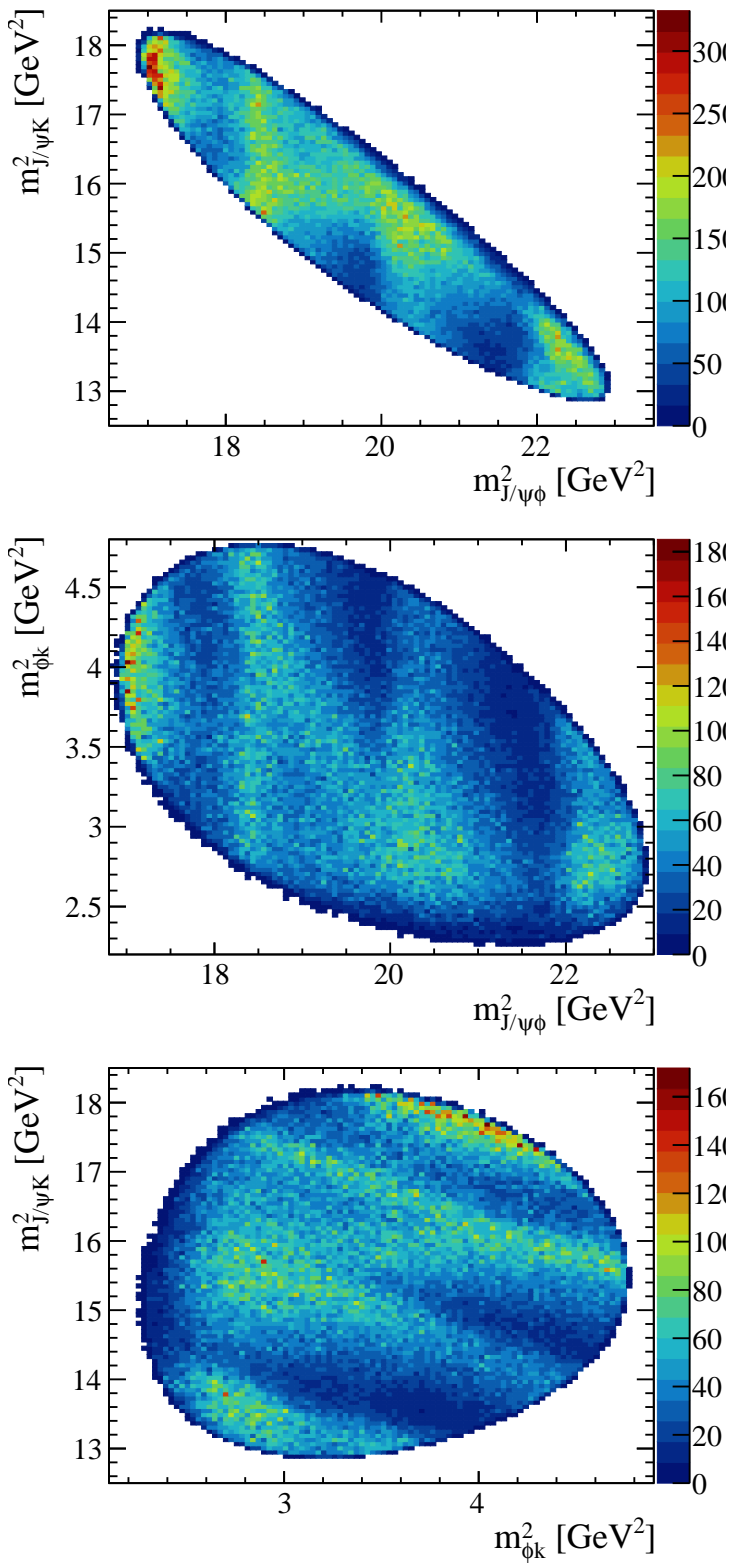


Figure 3.26 Dalitz-plot distributions of signal from the nominal fit model.

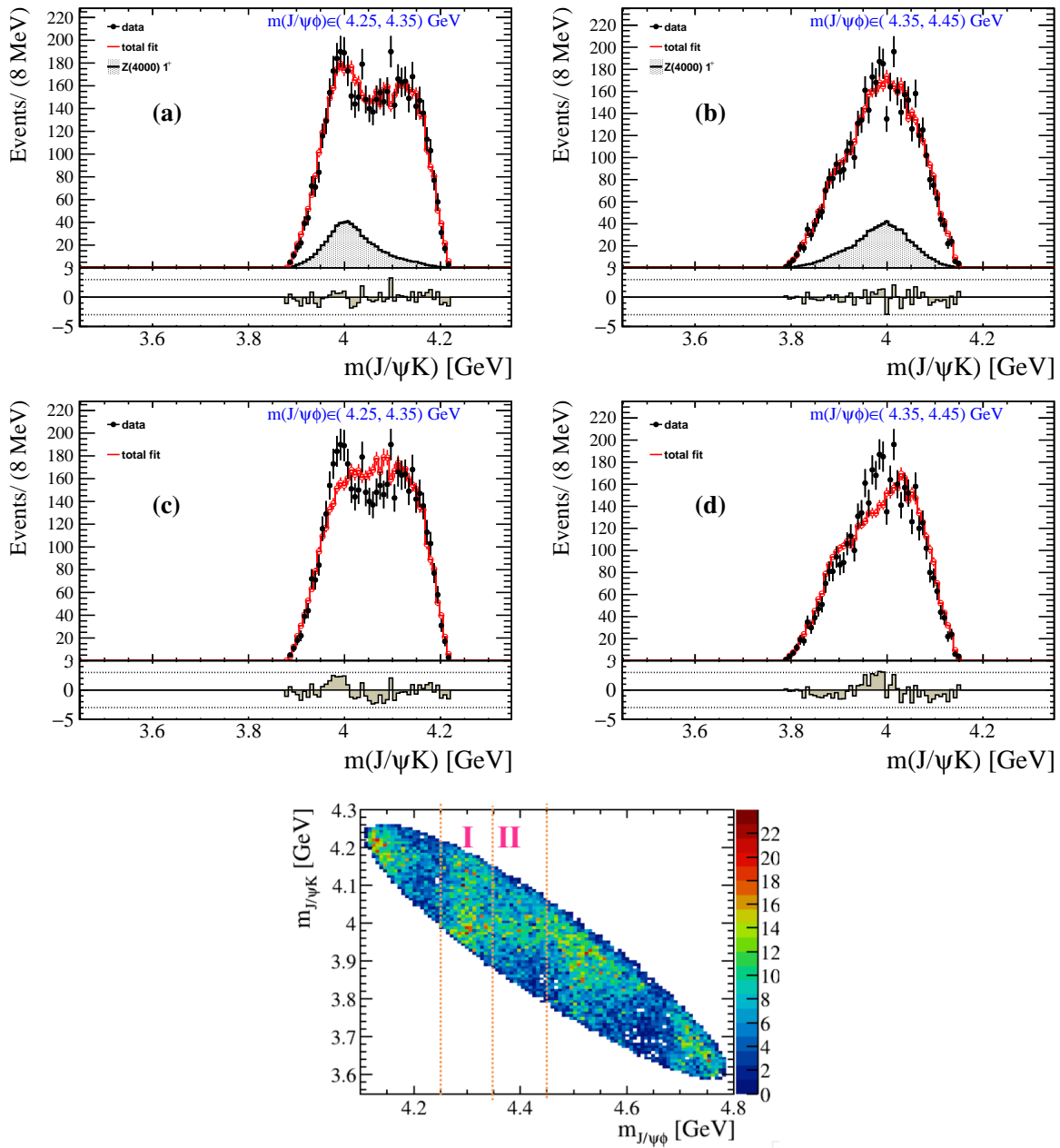


Figure 3.27 Fit projections of $m_{J/\psi K}$ in two slices of $m_{J/\psi \phi}$ from the nominal model (top) and the nominal model without $1^+ Z_{cs}$ (bottom). The narrow Z_{cs} is evident in the two $m_{J/\psi \phi}$ slices. Including $1^+ Z_{cs}$ improve the $\chi^2/n\text{bin}$ from 85/46 to 48/46 (left slice), and from 97/49 to 47/49 (right slice). Bottom figure shows the two slices of $m_{J/\psi \phi}$ regions.

Table 3.13 Fit results from the 9K+5X+3X+2Z model with $Z_{cs}(4220)$ $J^P = 1^+$. Significance is evaluated from the change of the $2 \ln \mathcal{L}$ assuming ndf to be **twice** the reduction in number of free parameters when removing the component in the fit. The ndf is not multiply by two for the K^* resonance whose mass and width are fixed.

Contribution	Significance	Fit results			
		M_0 [MeV]	Γ_0 [MeV]	FF%	
All $K(1^+)$		25.1 ± 3.6			
2^1P_1	$K(1^+)$	4.5σ	1861 ± 10	149 ± 41	
2^3P_1	$K'(1^+)$	4.5σ	1911 ± 37	276 ± 50	
1^3P_1	$K_1(1400)$	11σ			15.1 ± 2.7
All $K(2^-)$		2.1 ± 0.4			
1^1D_2	$K_2(1770)$	8.0σ			
1^3D_2	$K_2(1820)$	5.8σ			
All $K(1^-)$		50.3 ± 4.1			
1^3D_1	$K^*(1680)$	13σ			13.5 ± 2.3
2^3S_1	$K^*(1410)$	15σ			37.9 ± 5.2
$K(2^+)$					
2^3P_2	$K_2^*(1980)$	7.4σ	1988 ± 22	318 ± 82	2.3 ± 0.5
$K(0^-)$					
2^1S_0	$K(1460)$	13σ			10.2 ± 1.2
$X(2^-)$					
$X(4150)$	8.7σ	4146 ± 18	135 ± 28	2.0 ± 0.5	
$X(1^-)$					
$X(4630)$	5.7σ	4626 ± 16	174 ± 27	2.6 ± 0.5	
All $X(0^+)$		19.5 ± 4.8			
$X(4500)$	20σ	4474 ± 3	77 ± 6	5.6 ± 0.7	
$X(4700)$	18σ	4694 ± 4	87 ± 8	8.9 ± 1.2	
$NR_{J/\psi\phi}$	5.7σ				28.0 ± 7.5
All $X(1^+)$		26.0 ± 3.4			
$X(4140)$	16σ	4118 ± 11	162 ± 21	17.2 ± 2.9	
$X(4274)$	18σ	4294 ± 4	53 ± 5	2.8 ± 0.49	
$X(4685)$	15σ	4684 ± 7	126 ± 15	7.2 ± 1.0	
All $Z(1^+)$		25.0 ± 4.9			
$Z_{cs}(4000)$	16σ	4003 ± 6	131 ± 15	9.4 ± 2.1	
$Z_{cs}(4220)$	8.4σ	4216 ± 24	233 ± 52	10.3 ± 3.8	

Table 3.14 Fit results from Extended K+5X+3X+2Z model for $X(4220)$ with $J^P = 1^+$. Significance is evaluated from the change of the $2 \ln \mathcal{L}$ assuming ndf to be **twice** the reduction in number of free parameters when removing the component in the fit. The factor of two is not applied when mass and width are fixed. The two F K states have almost zero fit fractions and significances, therefore, their masses and widths from the fit are meaningless and not shown.

Contribution	Significance	Fit results				
		M_0 [MeV]	Γ_0 [MeV]	FF%		
All $K(1^+)$						23.2
2^1P_1	$K(1^+)$	4.9σ	1821 ± 15	372 ± 63		
2^3P_1	$K'(1^+)$	4.9σ	1871 ± 20	154 ± 28		
1^3P_1	$K_1(1400)$	9.2σ				15.0
All $K(2^-)$						2.1
1^1D_2	$K_2(1770)$	7.9σ				
1^3D_2	$K_2(1820)$	6.4σ				
All $K(1^-)$						52.5
1^3D_1	$K^*(1680)$	4.7σ				6.4
2^3S_1	$K^*(1410)$	7.7σ				34.2
3^3S_1		4.4σ	2128 ± 36	448 ± 132		4.5
All $K(2^+)$						1.6
2^3P_2	$K_2^*(1980)$	1.6σ	2182 ± 73	800 ± 230		2.4
1^3F_2		1.3σ	2076 ± 25	100 ± 74		0.4
All $K(0^-)$						10.0
2^1S_0	$K(1460)$	12σ				11.0
3^1S_0		4.6σ	2064 ± 15	108 ± 46		0.5
1^1F_3	$K(3^+)$	0.3σ				0.2
1^3D_3	$K(3^-)$	2.3σ				0.2
$X(2^-)$						
$X(4150)$		6.3σ	4117 ± 13	193 ± 81		2.8
$X(1^-)$						
$X(4630)$		5.5σ	4611 ± 28	193 ± 25		2.7
All $X(0^+)$						22.8
$X(4500)$		20σ	4476 ± 3	73 ± 6		5.6
$X(4700)$		17σ	4695 ± 4	89 ± 9		9.2
$NR_{J/\psi\phi}$		4.8σ				33.0
All $X(1^+)$						31.2
$X(4140)$		13σ	4107 ± 12	138 ± 22		21.1
$X(4274)$		18σ	4293 ± 3	53 ± 5		3.1
$X(4685)$		15σ	4681 ± 9	120 ± 17		6.3
All $Z(1^+)$						15.9
$Z_{cs}(4000)$		15σ	4001 ± 5	124 ± 19		8.2
$Z_{cs}(4220)$		5.9σ	4196 ± 22	176 ± 35		5.6

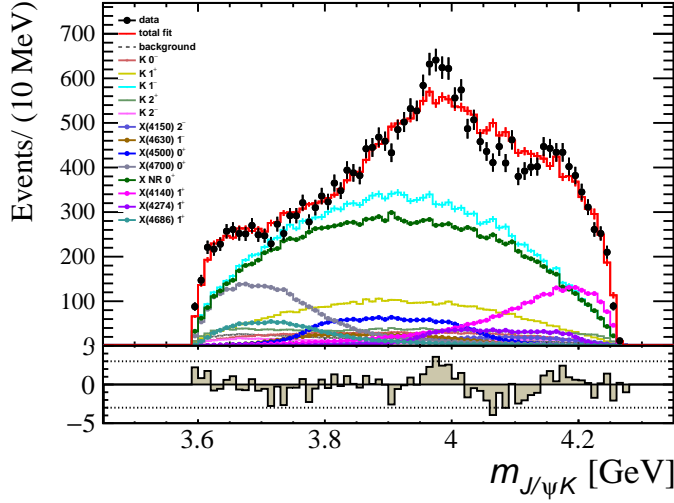


Figure 3.28 Fit projections of $m_{J/\psi K}$ from the nominal model without $1^+ Z_{cs}$.

more than 5σ , each. Together with the $X(4700)$ state, there are three X states around this mass region. We use χ^2 test on $m_{J/\psi \phi}^2$ vs. $m_{J/\psi K}^2$ plane to evaluate the fit quality in two-dimensions. The nominal model has $\chi^2_{2D}/\text{nbin} = 284.5/256$, while removing the two new X states gives $341.5/256$. The contributions to the χ^2_{2D} value for the nominal fit and for the fit without the two X states are compared in Figure. 3.31. The pull distributions are shown in Figure. 3.32.

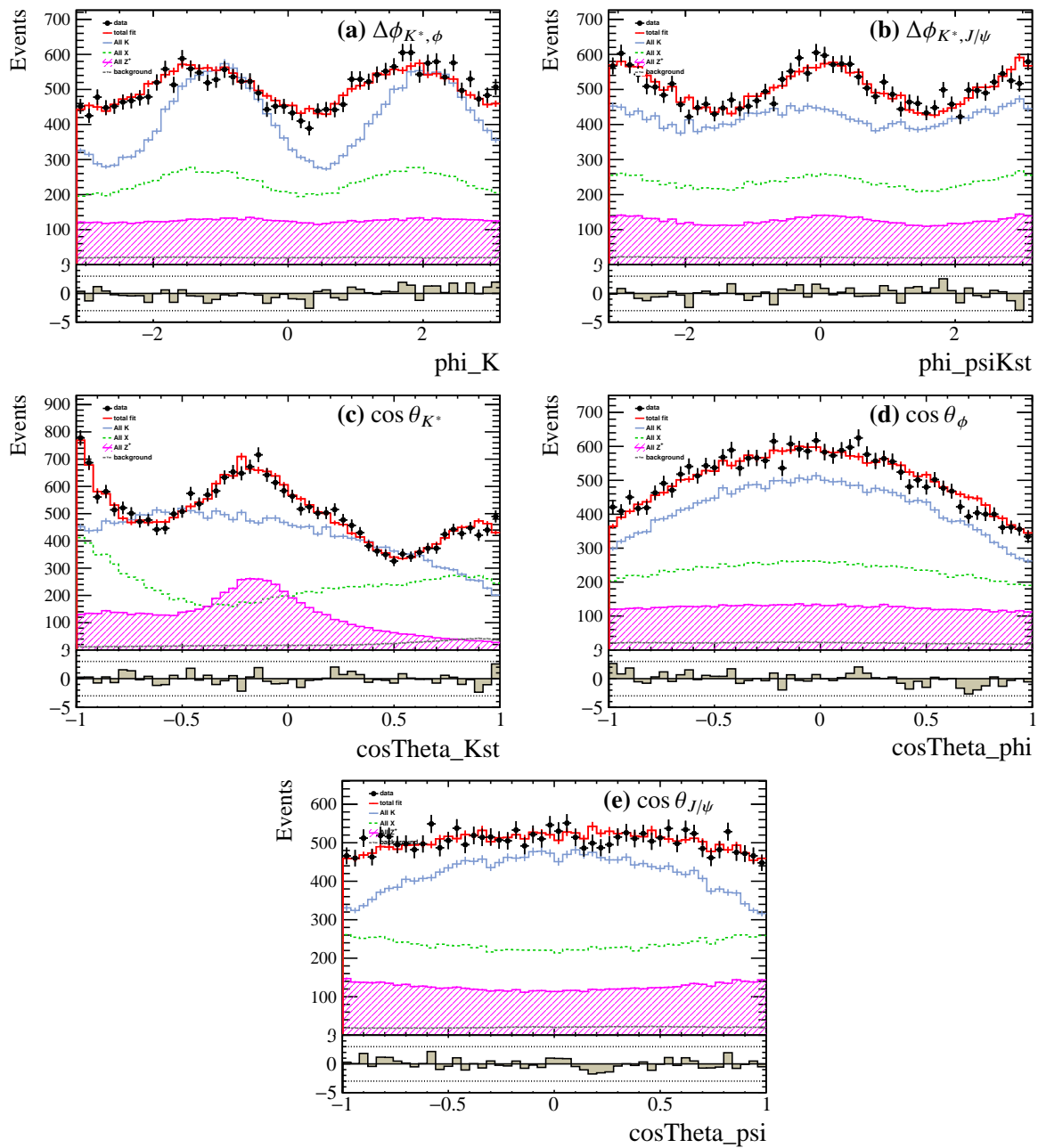
3.5.5 Flatté function for the $X(4140)$ and $Z_{cs}(4000)$ components

As demonstrated in Appendix ??, only $X(4140)$ and $Z_{cs}(4000)$ peak not far from the coupled-channel thresholds of right J^P values in S-wave (higher angular momenta are suppressed for threshold effects). In this section, possible impact of these thresholds is investigated.

Since $X(4140)$ peaks near the $J/\psi \phi$ kinematic threshold, decays to lighter particle combinations can have a significant impact on its line shape. As a 1^+ state $X(4140)$ should easily decay via S-wave to $D_s^{*\pm} D_s^\mp$ which has the lower mass threshold than $J/\psi \phi$. As an alternative to our nominal fit, in which mass dependence of $X(4140)$ width is neglected, in this section, mass-dependent width with both channels included is explored. The Breit-Wigner formula $BW(m)$ is replaced by the Flatté model:

$$\text{Flatte}_X(m|M_0, g_{J/\psi \phi}, g_{D_s^* D_s}) = \frac{1}{M_0^2 - m^2 - iM_0(g_{J/\psi \phi}\rho_{J/\psi \phi} + g_{D_s^* D_s}\rho_{D_s^* D_s})}, \quad (3.92)$$

where the parameters g_i are the $X(4140)$ coupling constants to channel i , the phase-space factors $\rho_i = 2p_i/m$ are dependent on $m \equiv m_{J/\psi \phi}$ and on momentum p_i of one of the daughters in channel i . The $m_{J/\psi \phi}$ mass projections of the fits with $X(4140)$ in the Flatté parameterizations for different models of the other components are shown in Figure. 3.33. The fit parameters are

Figure 3.29 Fit projections of angles in the ϕK decay chain.

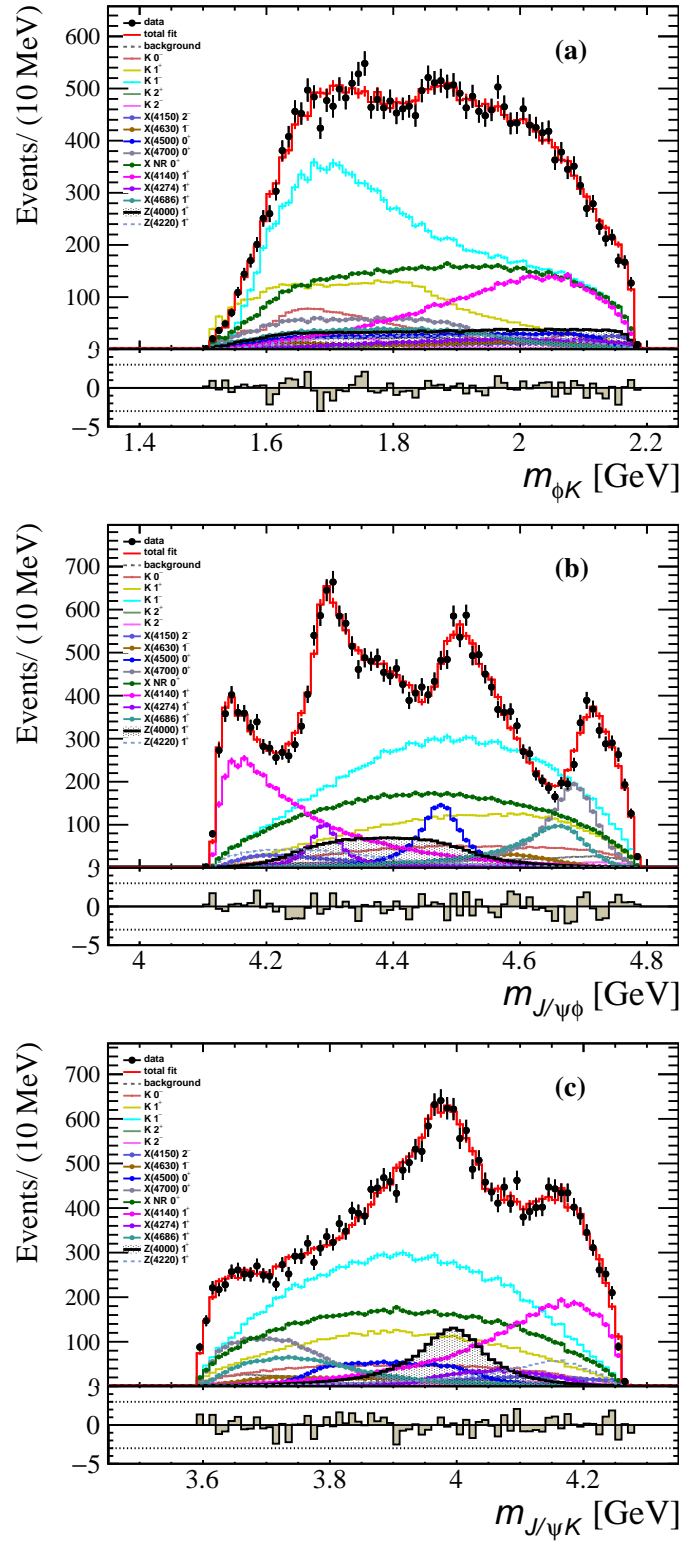


Figure 3.30 Fit projections of (a) $m_{\phi K}$, (b) $m_{J/\psi \phi}$, (c) $m_{J/\psi K}$ from the Extended $K+5X+2X+2Z$ model.

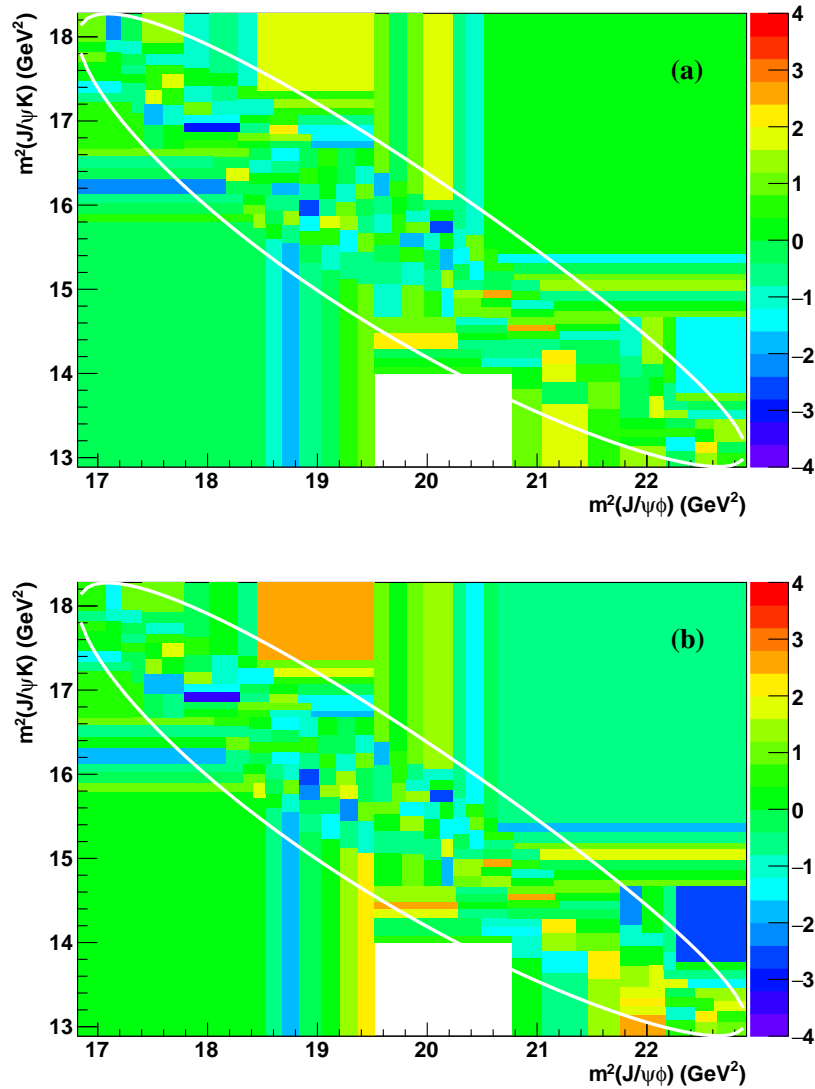


Figure 3.31 Comparison of the standard deviations between the data and the fit model, contributing to χ^2_{2D} value, for (a) the nominal fit, and (b) the fit without the two new X states. Some improvements are seen in (a) at $m^2(J/\psi\phi) = 22 \text{ GeV}^2$, as compared to (b).

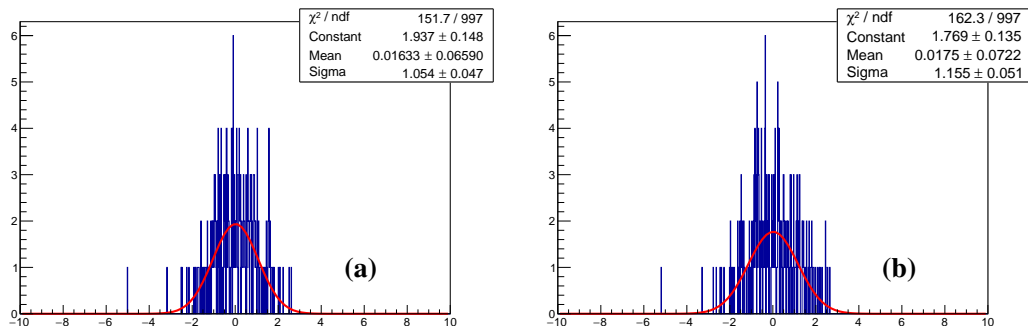


Figure 3.32 The pull distributions of χ^2_{2D} value in Figure. 3.31, The RMS of the pull distribution is smaller when additional X components are introduced.

given in Table 3.15. In term of fit likelihood, Flatté parameterization is better than the constant-width Breit-Wigner function by about $\Delta(2 \ln \mathcal{L}) \sim 20$ when the same resonance model is used. Since in the Flatté model p_i becomes imaginary below the kinematic threshold, the real part of the amplitude pole position is not necessarily equal to M_0 . The pole position $m_{\text{pole}} \equiv M_{\text{pole}} - i\Gamma_{\text{pole}}/2$ is obtained by solving the equation that the denominator in Equation. (3.92) becomes equal to zero when $m = m_{\text{pole}}$. The results are also reported in Table 3.15. The pole of Flatté fit corresponds to the 4th Riemann sheet. The $Z_{cs}(4220)$ with $J^P = 1^-$ and 1^+ hypotheses give similar fit likelihood and 2D χ^2 on Dalitz-plot $m_{J/\psi \phi}^2$ and $m_{J/\psi K}^2$ plane, and the fit results with $Z_{cs}(4220)$ in the 1^- hypothesis are also shown. In all Flatté fits, the coupling of $X(4140)$ to the coupled-channel is smaller than to the $J/\psi \phi$ and is insignificant.

Table 3.15 Comparison for $X(4140)$ resonance with Flatté and constant-width Breit-Wigner functions. The numbers between horizontal bands, the first (second), correspond to $Z(4220)$ with $J^P = 1^{-(+)}$. Also shown are the $\ln \mathcal{L}$ and 2D χ^2 of Dalitz-plot distribution in the $m_{J/\psi \phi}^2$ vs. $m_{J/\psi K}^2$ plane with 1018 adaptive bins.

Flatté	M_0 (MeV)	$g_{J/\psi \phi}$ (GeV)	$g_{D_s^* D_s}/g_{J/\psi \phi}$	Pole (MeV)	FF (%)	$\ln \mathcal{L}$	2D χ^2
Nominal	4202 ± 18	1.44 ± 0.36	$0.05^{+0.40}_{-0.05}$	$4092 - 90i$	19.1	5012.0	1022
Nominal	4223 ± 29	1.61 ± 0.48	$0.06^{+0.40}_{-0.06}$	$4082 - 113i$	17.7	5013.1	1039
Extended	4216 ± 23	1.46 ± 0.44	$0.10^{+0.40}_{-0.10}$	$4089 - 108i$	35.3	5080.1	1001
Extended	4187 ± 22	1.06 ± 0.49	$0.34^{+0.40}_{-0.28}$	$4084 - 83i$	21.0	5074.4	1027
BW	M_0 (MeV)	Γ (GeV)		Pole (MeV)	FF (%)	$\ln \mathcal{L}$	2D χ^2
Nominal	4116 ± 10	130 ± 21		$4116 - 65i$	18.0	5001.6	1028
Nominal	4118 ± 14	162 ± 22		$4118 - 81i$	17.4	5004.6	1044
Extended	4107 ± 12	168 ± 21		$4107 - 84i$	43.2	5070.4	1004
Extended	4108 ± 12	137 ± 22		$4108 - 69i$	21.0	5068.7	1029

The Flatté $X(4140)$ lineshapes, moduli of Eq. (3.92) squared, are compared in Figure. 3.34. Without the phase-space factor of $X \rightarrow J/\psi \phi$ decays, the lineshapes peak at the threshold. Similar results are obtained with the Breit-Wigner parameterization using constant width.

Using Flatté for $Z_{cs}(4000)^+$ is also investigated since it peaks close to the mass threshold of $D_s^+ \bar{D}^{*0}$ and $D_s^{*+} \bar{D}^0$, assuming the same couplings for the two open charm channels. Also note that when $m_{J/\psi K}$ is below the mass threshold of one of the coupled channels, the channel's phase space factor becomes imagery. The fit is slightly better, $\Delta(-2 \ln \mathcal{L}) = 2.8$, but the improvement is not significant given that there is one addition free parameter in this model. The fit results are $M_0^F = 4029 \pm 22$ MeV, $g_{J/\psi K^+} = 0.38 \pm 0.07$ GeV, $(g_{D_s^+ \bar{D}^{*0}} + g_{D_s^{*+} \bar{D}^0})/g_{J/\psi K^+} = 0.8 \pm 0.6$. While the coupling to $J/\psi \phi$ is significant, the coupling to the coupled-channels is not. However, within the large errors it is possible that the threshold plays an important role. A pole for $Z_{cs}(4000)^+$ in Flatté representation is found to be $M_0 - i\Gamma_0/2 = (4004 \pm 12 - i91 \pm 22)$ MeV.

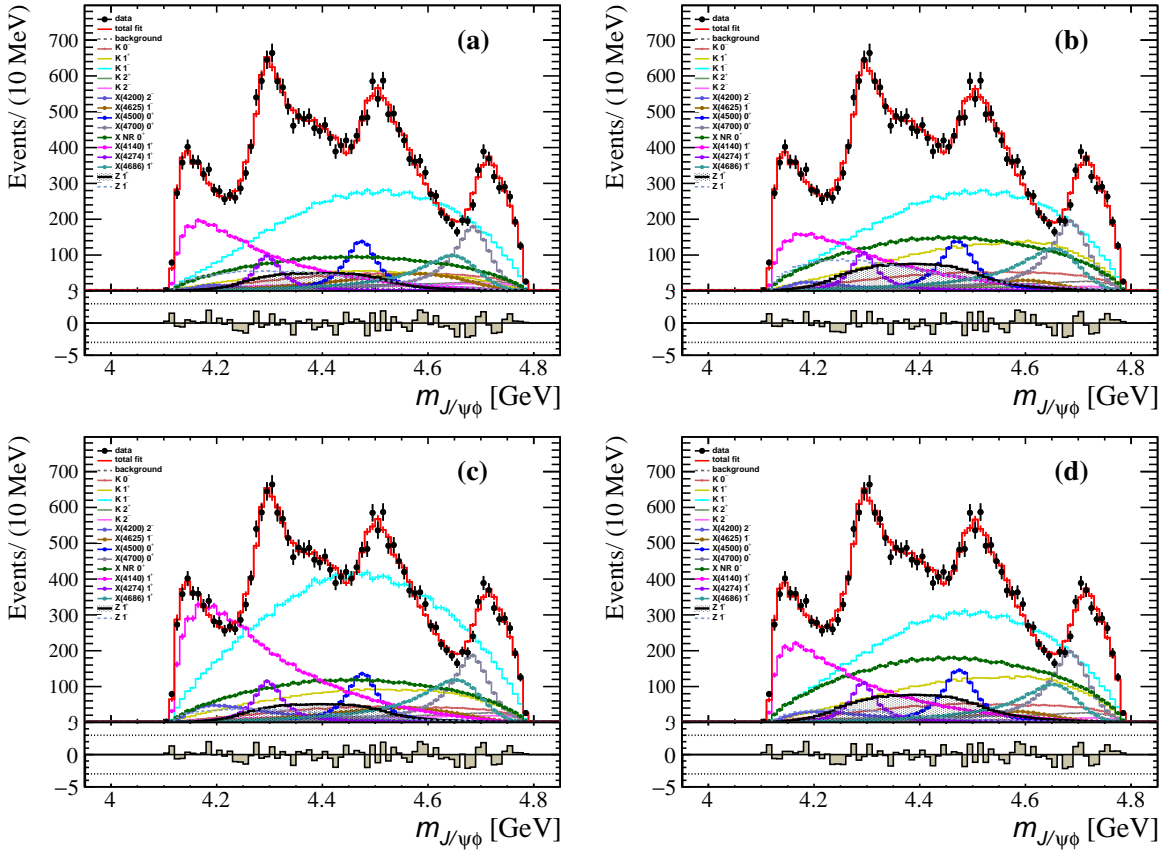
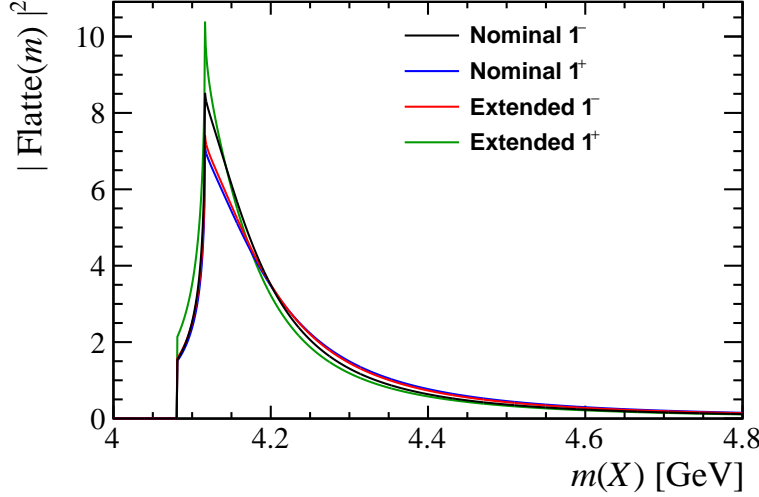
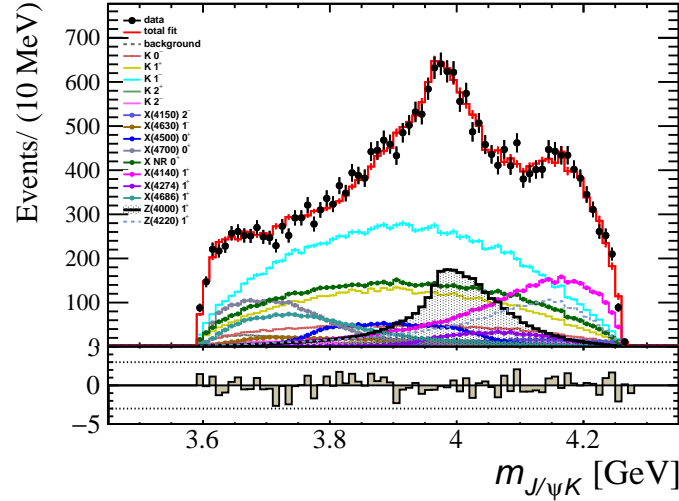


Figure 3.33 Projections of $m_{J/\psi\phi}$ from fits of Flatté function for describing $X(4140)$ in different resonance models (a) nominal K and $1^- Z(4220)$, (b) nominal K and $1^+ Z_{cs}(4220)$, (c) extended K and $1^- Z_{cs}(4220)$, (d) extended K and $1^+ Z(4220)$.

The statistical uncertainties are calculated by toy study where the correlations of the three parameters in Flatté function are taken into account. The projection of this fit onto $m_{J/\psi K}$ is shown in Figure. 3.35.

3.6 Spin and parity study

To determine the quantum numbers of each X and Z_{cs} state, fits are done under alternative J^P hypotheses. The likelihood-ratio test is used to quantify rejection of these hypotheses. Since different spin-parity assignments are represented by different functions in the angular part of the fit PDF, they represent separate hypotheses. For two models representing separate hypotheses, assuming a χ^2 distribution with one degree of freedom for $\Delta(-2 \ln \mathcal{L})$ under the disfavored J^P hypothesis gives a lower limit on the significance of its rejection^[8]. In practice, the significance for rejection of a J^P hypothesis is computed as $\sigma(J^P) = \sqrt{\Delta(-2 \ln \mathcal{L})}$, where $\Delta(-2 \ln \mathcal{L}) = 2 \ln \mathcal{L}(J^P) - 2 \ln \mathcal{L}(\text{preferred})$, *i.e.* the likelihood difference between the fits for given J^P hypothesis and for the preferred J^P for this state is used. The preferred J^P


 Figure 3.34 Lineshapes of Flatté parameterization of the $X(4140)$ resonance.

 Figure 3.35 Projections onto $m_{J/\psi K}$ from the fit with the Flatté function for describing $Z_{cs}(4000)^+$.

corresponds to the fit returning the smallest $-2 \ln \mathcal{L}$. In order to make sure the state is the same for different J^P hypotheses, mass and width are limited to be within $\pm 5\sigma$ range of the nominal fit results. The results for the default model are shown in Table 3.16, and for the extended- K^* model in Table 3.17. The J^P of previous reported four X states are confirmed to be correct. Two new exotic states $Z_{cs}(4000)$ and $X(4675)$ are determined to be both 1^+ for more than 15σ level. The J^P of the other new exotic states are not uniquely determined. The broad $Z_{cs}(4220)$ J^P hypothesis can be 1^+ or 1^- within about 2σ , therefore, both hypotheses for $Z_{cs}(4220)$ are used to test other states' J^P values. The $X(4175)$ state prefers 2^- by more than 4σ . The $X(4650)$ state prefers 1^- by 3σ over 2^- hypothesis. The other hypotheses are rejected by more than 5σ .

Table 3.16 Statistical significance of J^P preference for the X and Z_{cs} states in the default model. For the states with two lines, the upper (lower) row corresponds to the tests with $Z_{cs}(4220) J^P = 1^{(+/-)}$. The bold numbers highlight J^P values which cannot be ruled out with at least 5σ significance.

J^P	0^+	0^-	1^+	1^-	2^+	2^-
$X(4150)$	4.7σ	6.1σ	5.9σ	5.5σ	4.6σ	prefer
$X(4150)$	9.7σ	12σ	9.6σ	5.4σ	9.2σ	prefer
$X(4630)$	12σ	11σ	9.6σ	prefer	8.5σ	9.1σ
$X(4630)$	8.3σ	6.1σ	7.3σ	prefer	6.3σ	4.1σ
$X(4500)$	prefer	19σ	19σ	18σ	21σ	20σ
$X(4500)$	prefer	21σ	20σ	19σ	21σ	20σ
$X(4700)$	prefer	19σ	18σ	19σ	15σ	18σ
$X(4700)$	prefer	19σ	19σ	19σ	16σ	18σ
$X(4140)$	16σ	15σ	prefer	16σ	14σ	15σ
$X(4140)$	16σ	17σ	prefer	15σ	17σ	15σ
$X(4274)$	18σ	19σ	prefer	18σ	18σ	19σ
$X(4274)$	18σ	18σ	prefer	18σ	18σ	18σ
$X(4685)$	16σ	16σ	prefer	16σ	15σ	16σ
$X(4685)$	17σ	17σ	prefer	16σ	16σ	16σ
$Z_{cs}(4000)$	-	19σ	prefer	19σ	18σ	19σ
$Z_{cs}(4000)$	-	18σ	prefer	16σ	16σ	16σ
$Z_{cs}(4220)$	-	11σ	prefer	2.4σ	9.5σ	9.1σ

Table 3.17 Statistical significance of J^P preference for the X and Z_{cs} states in the extended model. For the states with two lines, the upper (lower) row corresponds to the tests with $Z_{cs}(4220) J^P = 1^{(+/-)}$. The bold numbers highlight J^P values which cannot be ruled out with at least 5σ significance.

J^P	0^+	0^-	1^+	1^-	2^+	2^-
$X(4150)$	6.7σ	7.4σ	7.4σ	5.8σ	4.2σ	prefer
$X(4150)$	6.6σ	9.1σ	7.7σ	6.6σ	6.7σ	prefer
$X(4630)$	12σ	11σ	10.0σ	prefer	10σ	8.8σ
$X(4630)$	6.7σ	5.3σ	5.8σ	prefer	5.9σ	3.0σ
$X(4500)$	prefer	19σ	20σ	18σ	20σ	19σ
$X(4500)$	prefer	18σ	18σ	18σ	18σ	18σ
$X(4700)$	prefer	19σ	19σ	19σ	16σ	19σ
$X(4700)$	prefer	18σ	19σ	18σ	14σ	17σ
$X(4140)$	14σ	15σ	prefer	20σ	13σ	15σ
$X(4140)$	14σ	15σ	prefer	14σ	13σ	14σ
$X(4274)$	18σ	19σ	prefer	18σ	18σ	19σ
$X(4274)$	18σ	18σ	prefer	18σ	18σ	19σ
$X(4685)$	17σ	17σ	prefer	17σ	17σ	15σ
$X(4685)$	16σ	16σ	prefer	15σ	16σ	15σ
$Z_{cs}(4000)$	-	18σ	prefer	18σ	17σ	17σ
$Z_{cs}(4000)$	-	17σ	prefer	17σ	15σ	16σ
$Z_{cs}(4220)$	-	8.6σ	2.0σ	prefer	4.9σ	5.7σ

We also show the nominal $K + 5X + 3X + 2Z$ model with a $1^- Z$ in Table 3.18 for completeness. The $1^- Z$ has large width and is at the high mass boundary allowed in the $B^+ \rightarrow J/\psi \phi K^+$ decay.

3.7 Argand diagrams

Further evidence for the resonant character of $Z_{cs}(4000)^+$ is shown in Figure 3.36 by demonstrating the evolution of the complex amplitude on the Argand diagram, obtained with the same method as previously reported for the $Z_c(4430)^-$ state^[8]. The magnitude and phase have approximately circular evolution with $m_{J/\psi K^+}$ in the counter-clockwise direction, as expected for a resonance.

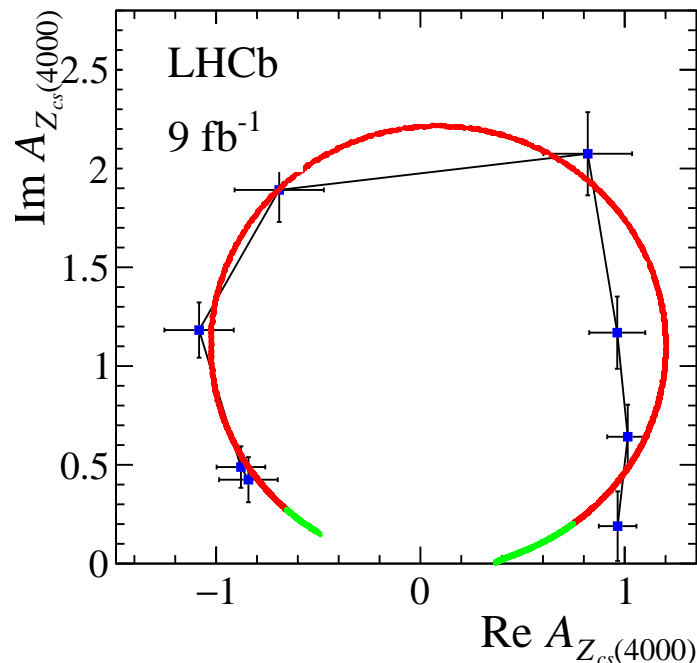


Figure 3.36 Fitted values of the $Z_{cs}(4000)^+$ amplitude in eight $m_{J/\psi K^+}$ bins, shown on an Argand diagram (blue points). The red line represents the expected Breit-Wigner behaviour in between $-1.4\Gamma_0$ to $1.4\Gamma_0$ around the $Z_{cs}(4000)^+$ mass. The green line is the reachable mass range in the $B^+ \rightarrow J/\psi \phi K^+$ channel.

3.8 Systematic uncertainties

Our main results are the properties and fit fractions of the resonances in the default model, as well as the significances of the resonances and of their J^P assignments. Systematic uncertainties are assessed for these quantities in our default model. For the significance values,

Table 3.18 Fit results from the 9K+5X+3X+2Z model with $Z_{cs}(4220)$ $J^P = 1^-$. Significance is evaluated from the change of the $2 \ln \mathcal{L}$ assuming ndf to be **twice** the reduction in number of free parameters when removing the component in the fit. The ndf is not multiply by two for the K^* resonance whose mass and width are fixed.

Contribution	Significance	Fit results			
		M_0 [MeV]	Γ_0 [MeV]	FF%	
All $K(1^+)$		10.8 ± 2.6			
2^1P_1	$K(1^+)$	6.4σ	1867 ± 10	147 ± 27	
2^3P_1	$K'(1^+)$	6.4σ	1918 ± 14	438 ± 74	
1^3P_1	$K_1(1400)$	6.9σ			12.8 ± 6.5
All $K(2^-)$		4.0 ± 0.4			
1^1D_2	$K_2(1770)$	13.0σ			
1^3D_2	$K_2(1820)$	12.0σ			
All $K(1^-)$		56.5 ± 3.3			
1^3D_1	$K^*(1680)$	9.5σ			6.2 ± 1.3
2^3S_1	$K^*(1410)$	11.7σ			35.8 ± 3.9
$K(2^+)$					
2^3P_2	$K_2^*(1980)$	7.3σ	1973 ± 18	301 ± 67	2.8 ± 0.5
$K(0^-)$					
2^1S_0	$K(1460)$	14.3σ			9.4 ± 0.9
$X(2^-)$					
$X(4150)$	4.8σ	4176 ± 14	112 ± 32	1.0 ± 0.3	
$X(1^-)$					
$X(4630)$	11.0σ	4650 ± 23	121 ± 15	5.5 ± 1.0	
All $X(0^+)$		24.6 ± 7.7			
$X(4500)$	18.0σ	4475 ± 3	70 ± 6	5.1 ± 0.5	
$X(4700)$	18.0σ	4693 ± 4	83 ± 8	7.8 ± 0.7	
$NR_{J/\psi\phi}$	6.9σ				18.7 ± 4.3
All $X(1^+)$		25.0 ± 3.6			
$X(4140)$	14.8σ	4116 ± 10	130 ± 21	18.0 ± 6.8	
$X(4274)$	17.3σ	4295 ± 4	53 ± 5	2.7 ± 0.6	
$X(4685)$	14.9σ	4675 ± 9	121 ± 15	5.7 ± 1.2	
$Z_{cs}(1^+)$					
$Z_{cs}(4000)$	18.2σ	3989 ± 4	109 ± 15	5.8 ± 0.4	
$Z_{cs}(1^-)$					
$Z_{cs}(4220)$	9.2σ	4263 ± 39	468 ± 126	8.1 ± 3.4	

smallest one among these systematic studies is used for the final result. We consider the following systematic sources:

- Uncertainties due to the fixed masses and widths of known K^* resonances. To evaluate them we perform fit with these masses and widths as free parameters but with Gaussian constraints on them to the values listed in Table 3.11. Labelled as “Fixed M&Q”.
- MC efficiency. The BDT training variables are compared between weighted MC and sWeighted data. The variable χ^2_{IP} of B is not well modelled, thus we smear it in MC to match the data, and repeat the default fit. This variation is labelled “ $\chi^2_{\text{IP}} \text{ smear}$ ” in the tables of the systematic variations.
- We explore uncertainty in the background model by varying the B^+ mass sidebands used to derive the background PDF. (Label “sideband”).
- The systematic uncertainty in the background fraction (β) is estimated by varying the background shape in the B mass fit, from the second order polynomial function to an exponential function: $\beta = 4.02 \pm 0.08 \pm 0.22\%$. We then vary it in the amplitude fit within its total uncertainty. (Label “ $\beta =$ ”).
- Change the L0 trigger requirement from L0 Global Decision to TOS on L0 Muon or Dimuon Decision. (Label “L0 Trigger”).
- Calibrate ProbNNk from PIDGen package, while the nominal calibration is performed using PIDcorr package. (Label “PID corr”).
- Below are amplitude modelling systematic uncertainties, in which we take the largest variation as final uncertainties.
- Hadron-size parameter in the Blatt-Weisskopf barrier factor (d) is 3 GeV^{-1} in the default fit. We vary it between 1.5 and 4.5 GeV^{-1} to evaluate systematic errors. (Label “BW d”).
- Uncertainty in selection of amplitude components is considered as follows: 1) the difference between the default and extended K^* models, Labelled as “Extended”; 2) different parameterizations of the $X(4140)$ state, labelled as “Flatte”; 3) addition of one extra X state of different J from 0 to 2 into the extended model, labelled as "Additional X". None of them has significance of more than 5σ . The most significant one is a $2^- X$ with the mass of 4530 MeV and the width of 70 MeV , giving the largest $\ln \mathcal{L}$ improvement, corresponding to a significance of 4.3σ . 4) $Z(4420) 1^-$ hypothesis. (Label “ $1^- Z$ ”).
- Uncertainty due to choice of NR component in the X sector. We use one NR component for 0^+ , which is set to constant with Blatt-Weisskopf barrier factors. Alternative

parameterization is tried, such as 1st order polynomial in $m_{J/\psi\phi}^2$. The improvement is small. The other NR S-wave contributions in X decays, *i.e.* 1^+ or 2^+ , are tried. Their significances are less than 5σ . We take them as systematic uncertainty in modeling of the amplitude. (Label that containing “ XNR ”).

- The smallest allowed orbital angular momentum L is used in Eq. 3.19. As an alternative, we associate the L dependent terms in the numerator (Blatt-Weisskopf factors, p^L, q^L) with each LS coupling and use its corresponding L value. The width term of Breit-Wigner function in Eq. 3.22, still uses the lowest allowed L value, because the width is expected to be dominated by it. From the fit, the higher L contribution(s) are less than 5% in most cases of the X and Z resonances. (Label as “ L vars”).
- The default ϕ mass selection window is ± 15 MeV. We remove candidates in which more than one K^+K^- pair fall within this window, which removes 3.2% of the events. After these cuts non- ϕ fraction of the selected $B^+ \rightarrow J/\psi K^+K^-K^+$ events is 2.1% from the previous publication^[15,16]. In our amplitude fits, we neglect this component. To evaluate systematics of this approximation we narrow down the ϕ mass selection window to ± 7 MeV, which reduces the ϕ signal yield by 13%, while decreasing the non- ϕ fraction by a factor of 2. We repeat the fit with the default amplitude model. Labelled as “ ϕ win”. Alternately, we fit K^+K^- mass distribution for a range below 1050 with ϕ and no ϕ components, and generate sWeights to subtract no ϕ contribution. The amplitude fit is reperformed, difference between this fit and the nominal fit is taken as systematic uncertainty. Labelled “non ϕ ”.
- We also consider modification of the width in the denominator of the BW function for the K^* resonances. In fact, all K^* states are expected to have sizable widths to the other decay modes, $K\pi$, $K\rho$, $K(892)\pi$, etc. Since ratios of these partial widths to the ϕK partial width are unknown, it is not possible to implement such formulation exactly. However, as a systematic check we have performed a fit in which mass dependence of the width is driven by the lightest decay mode possible, which is $K\pi$ for natural spin-parity resonances, and $K\omega$ for the others. This also changes L_{K^*} value. (Label “ K BW”).
- K-Matrix model for overlapping K^* components, instead of the BW sum (See Appendix C.4) (Label “K-Matrix”).
- Change the BW model to Flatte model to describe $Z_{cs}(4000)$ in order to investigate possible $D_s D^*0$ threshold effects. (Label “ $Z(4000)$ Flatte”).
- As an alternative to the nominal background parameterization in the fit, which assumes

the factorization in six-dimensions, we use approach of the multidimensional moments described in details in Appendix C.5. (Label ‘‘BKG factorization’’).

Table 3.19 Summary of the systematic errors on the parameters of the $K^{*+} \rightarrow \phi K^+$ states with $J^P = 1^+$. All numbers for masses and width are in MeV and fit fraction in %.

Systematic	$K(1^+)$	$K(2^1\text{P}_1)$		$K(2^3\text{P}_1)$		$K_1(1400)$
	FF	M_0	Γ_0	M_0	Γ_0	FF
Fixed M&W	0.59	0.56	-3.10	-0.31	5.54	0.53
$\chi^2_{\text{IP}} \text{smear}$	-0.08	1.06	2.62	0.90	-2.80	0.01
Right sideband	-0.86	-0.14	-0.60	-1.92	4.14	-0.67
Left sideband	0.89	-1.31	6.29	2.42	-0.60	0.68
$\beta = 0.043$	-0.05	-0.38	0.75	0.15	-0.07	0.01
$\beta = 0.037$	0.09	-0.85	1.32	-0.06	1.83	0.00
L0 Trigger	0.54	0.59	-2.10	-3.10	0.08	0.63
PID corr	-2.59	-2.36	-10.44	6.44	16.02	-1.36
ϕ win 7	-5.19	-8.73	54.82	73.12	99.12	-3.96
non ϕ	-4.70	-2.24	51.09	63.94	118.36	-2.51
Poly $m(XNR)$	-2.29	-13.82	68.40	122.19	317.14	0.21
$XNR(1^+)$	-4.51	-9.56	49.29	-43.49	-84.37	0.74
$XNR(2^+)$	5.14	11.37	23.26	-33.74	51.54	0.50
BW d=1.5	2.87	1.24	18.21	-10.98	14.26	1.16
BW d=4.5	-1.42	-1.50	1.76	4.21	4.64	-0.77
L vars	-4.18	5.12	78.89	71.30	148.42	-0.87
Flatte	-0.27	-6.16	-0.33	10.02	6.83	0.47
Extended	-2.13	-45.36	230.20	-29.18	-118.00	-0.29
Additional X	-1.12	-4.67	4.32	11.51	3.43	-0.48
1^-Z	-14.50	1.72	4.73	18.76	165.40	-10.77
K^*BW	0.01	-10.69	-9.48	5.49	17.41	-1.15
K-Matrix	-6.45	14.53	30.27	80.71	-155.88	-7.33
Z(4000) Flatte	0.14	-6.02	4.81	10.16	-1.97	0.14
BKG factorization	-0.31	-7.27	2.42	8.91	-0.01	-0.08
Total Sys.	(-14.80 , +5.99)	(-45.47 , +14.86)	(-16.17 , +230.57)	(-44.19 , +122.44)	(-156.89 , +317.6)	(-10.93 , +2.19)

3.9 Conclusions

By combining Run 1 and Run 2 data sample, and improving the data selection, we gained a factor of 5.5 in the $B^+ \rightarrow J/\psi \phi K^+$ signal statistics relatively to the previous amplitude analysis of these decays, while obtaining 5.8 smaller fractional non- B^+ background at the same time. The increased statistical power of the data revealed some inadequacies of the amplitude model developed to describe the previous Run 1 data sample.

The two 1^{++} ($X(4140)$ and $X(4274)$) and two 0^{++} ($X(4500)$ and $X(4700)$) states decaying to $J/\psi \phi$ are confirmed together with their quantum number assignments. The new mass and width determination supersede our previously published values.

An additional 1^{++} $X(4685)$ state is observed with relatively narrow width ($\Gamma = 126 \pm 15^{+37}_{-41}$ MeV) at more than 15σ . New partial $J/\psi \phi$ wave $X(4630)$ state is required with at least 6σ significance with 1^{-+} 3σ better than the 2^{-+} hypothesis. Other J^{PC} hypotheses are rejected for more than 5σ .

Table 3.20 Summary of the systematic errors on the parameters of the $K^{*+} \rightarrow \phi K^+$ states with $J^P = 1^-$ and $J^P = 2^-$. All numbers for masses and width are in MeV and fit fraction in %.

Systematic	$K(1^-)$ FF	$K^*(1680)$ FF	$K^*(1410)$ FF	$K(2^-)$ FF
Fixed M&W	4.69	2.70	1.62	0.16
$\chi_{\text{IP}}^2/\text{smear}$	0.07	-0.08	0.85	0.00
Right sideband	0.30	0.08	0.72	-0.03
Left sideband	-0.34	-0.17	-0.63	-0.58
$\beta = 0.043$	-0.13	-0.08	-0.24	0.01
$\beta = 0.037$	-0.03	-0.06	0.04	-0.04
L0 Trigger	-0.38	0.26	0.29	-0.04
PID corr	0.10	-0.26	0.39	0.10
ϕ win 7	0.77	-1.31	-3.80	-0.63
non ϕ	-6.70	-3.37	-9.67	-0.46
Poly $m(XNR)$	0.70	0.28	1.60	-0.44
$XNR(1^+)$	-18.79	-1.79	-14.20	-0.77
$XNR(2^+)$	0.48	-1.46	2.02	0.29
BW d=1.5	6.15	-4.10	10.68	-0.26
BW d=4.5	-2.75	4.54	-6.65	0.19
L vars	-2.24	-2.88	-2.56	-0.17
Flatte	-1.35	0.49	-0.98	-0.01
Extended	2.12 0	-7.34	-4.23	-0.02
1^-Z	-1.11	-5.82	-2.70	1.94
K^*BW	-3.36	1.50	-16.69	0.56
K-Matrix	8.27	34.35	-16.95	-0.91
Z(4000) Flatte	0.09	-0.11	-0.65	0.08
BKG factorization	-0.62	0.19	-1.70	0.01
Total Sys.	(-19.37, +9.53)	(-7.83 , +34.46)	(-17.08, +10.89)	(-1.10 , +2.03)

Table 3.21 Summary of the systematic errors on the parameters of the $K^{*+} \rightarrow \phi K^+$ states with $J^P = 2^+$ and $J^P = 0^-$. All numbers for masses and width are in MeV and fit fraction in %.

Systematic	$K_2^*(1980)$		$K(1460)$
	M_0	Γ_0	FF
Fixed M&W	-1.09	20.69	0.06
$\chi_{\text{IP}}^2/\text{smear}$	0.61	-2.50	-0.14
Right sideband	0.67	13.72	0.06
Left sideband	-0.05	-16.17	-0.08
$\beta = 0.043$	0.10	1.16	0.00
$\beta = 0.037$	0.69	-1.09	-0.01
L0 Trigger	-2.33	-7.87	-0.22
PID corr	-3.89	21.26	0.00
ϕ win 7	-14.94	-16.39	0.14
non ϕ	-29.18	-93.12	0.01
Poly $m(XNR)$	-11.65	40.03	0.39
$XNR(1^+)$	-11.50	277.98	-0.51
$XNR(2^+)$	18.72	3.83	-0.47
BW d=1.5	55.25	196.17	0.01
BW d=4.5	-21.89	-43.92	0.30
L vars	9.73	133.00	0.05
Flatte	1.55	-21.41	-0.19
Extended	193.57	477.92	0.12
Additional X	-2.02	3.22	-0.02
1^-Z	-15.04	-21.18	0.56
K^*BW	-65.44	-9.86	1.01
K-Matrix	-25.84	5.03	0.11
Z(4000) Flatte	-3.06	1.68	0.04
BKG factorization	-3.34	-3.33	0.02
Total Sys.	(-29.57, +193.63)	(-100.35, +479.38)	(-0.58 , +0.63)
			(-3.75 , +0.89)

Table 3.22 Summary of the systematic errors on the parameters of the $X \rightarrow J/\psi \phi$ states with $J^P = 0^+$. All numbers for masses and width are in MeV and fit fraction in %.

Systematic	$X(0^+)$		$X(4500)$		$X(4700)$		$NR_{J/\psi \phi}$ FF	
	M_0	Γ_0	M_0	Γ_0	FF			
Fixed M&W	2.42	0.15	-0.03	0.05	-0.39	-0.60	-0.13	3.65
$\chi^2_{IP} smear$	-0.05	0.27	0.35	0.08	0.12	1.33	0.22	-0.15
Right sideband	-0.59	0.09	0.28	0.03	0.34	0.86	0.13	-0.85
Left sideband	0.71	-0.04	-0.15	0.00	-0.20	-0.98	-0.16	1.09
$\beta = 0.043$	0.18	0.08	0.02	0.04	0.20	-0.02	0.00	0.29
$\beta = 0.037$	-0.11	-0.03	-0.07	-0.04	-0.20	-0.23	-0.06	-0.19
L0 Trigger	-0.17	0.15	-1.83	-0.05	-0.88	-1.73	-0.47	-0.78
PID corr	0.91	-0.10	0.64	0.11	0.65	0.45	0.27	1.60
ϕ win 7	-2.33	0.91	4.77	1.27	8.49	5.96	2.56	-2.43
non ϕ	0.55	1.33	9.23	2.41	15.86	15.44	4.85	4.05
Poly $m(XNR)$	-3.79	-2.91	2.37	0.61	2.38	10.70	4.52	-1.59
$XNR(1^+)$	13.00	2.70	6.91	1.75	4.03	7.68	2.69	17.70
$XNR(2^+)$	-3.11	0.95	-1.06	0.26	-1.08	-0.30	-0.36	-4.63
BW d=1.5	-0.20	0.90	0.48	0.08	0.40	1.17	0.69	-0.53
BW d=4.5	-0.61	-0.62	0.30	0.04	0.68	-0.00	-0.27	-0.51
L vars	-1.03	0.38	3.53	1.22	7.89	12.24	4.18	-1.84
Flatte	0.51	-0.44	0.18	0.04	-0.18	0.26	0.25	0.66
Extended	3.38	2.50	-3.81	0.07	0.47	1.64	0.32	5.15
Additional X	1.10	-1.77	-2.18	-0.06	0.06	1.89	0.52	2.83
1^-Z	-5.43	1.41	-6.70	-0.49	-1.21	-4.52	-1.09	-9.09
$K^* BW$	0.76	0.40	-2.03	-0.17	-1.70	1.59	0.11	0.87
K-Matrix	-3.27	0.14	9.84	1.58	5.80	11.23	3.65	-4.03
Z(4000) Flatte	0.32	-0.14	-0.31	-0.07	-0.05	-0.01	0.06	0.37
BKG factorization	0.28	0.61	1.13	0.08	0.63	-2.06	-0.25	0.29
Total Sys.	(-6.09 , +13.29)	(-2.93 , +2.72)	(-6.99 , +10.04)	(-0.52 , +2.42)	(-2.10, +15.91)	(-5.27 , +15.67)	(-1.26 , +4.89)	(-10.06 , +18.22)

Table 3.23 Summary of the systematic errors on the parameters of the $X \rightarrow J/\psi \phi$ states with $J^P = 1^+$. All numbers for masses and width are in MeV and fit fraction in %.

Systematic	$X(1^+)$		$X(4140)$		$X(4274)$		$X(4685)$			
	FF	M_0	Γ_0	FF	M_0	Γ_0	FF	M_0	Γ_0	FF
Fixed M&W	2.02	0.12	5.76	1.64	0.26	0.03	0.03	-0.14	2.72	0.25
$\chi^2_{IP} smear$	0.13	2.05	-0.12	0.06	0.76	0.65	0.00	-0.53	1.11	0.12
Right sideband	-0.09	0.14	1.07	0.19	-0.13	-0.01	0.00	-0.13	1.07	-0.13
Left sideband	-0.02	-0.45	-3.51	-0.42	-0.01	-0.17	-0.01	-0.09	-2.21	0.09
$\beta = 0.043$	-0.16	-0.12	-1.45	-0.12	-0.11	-0.10	0.01	0.01	-0.70	-0.09
$\beta = 0.037$	0.00	-0.02	-0.24	-0.07	0.03	0.03	-0.01	-0.33	0.21	0.03
L0 Trigger	0.25	3.40	-3.78	0.01	0.66	0.18	0.04	-0.58	1.12	0.11
PID corr	-1.86	9.65	-5.07	-1.57	0.52	0.83	0.02	-0.82	-4.42	-0.26
ϕ win 7	-3.65	0.30	-22.51	-3.05	-2.07	-2.83	-0.11	8.60	-26.60	-1.17
non ϕ	-6.93	1.94	-45.90	-5.75	-5.18	-3.77	-0.22	12.40	-39.80	-1.80
Poly $m(XNR)$	-4.03	6.31	-10.17	-2.53	-2.06	-2.45	-0.27	4.26	-22.07	-1.28
$XNR(1^+)$	-9.51	-33.65	-3.63	18.32	0.15	4.36	0.78	-15.72	35.54	3.84
$XNR(2^+)$	3.31	-0.90	-6.99	2.43	0.75	-0.02	0.08	1.88	-6.87	-0.03
BW d=1.5	6.12	-5.67	16.37	3.55	1.06	1.51	0.14	0.29	1.55	2.14
BW d=4.5	-3.02	6.10	1.30	-1.05	-0.05	-0.46	-0.08	0.06	-3.53	-1.06
L vars	-3.79	0.30	-38.61	-3.00	-4.03	-3.38	-0.19	2.45	-24.33	-1.48
Flatte	-2.30			0.22	0.25	4.26	0.61	-3.77	15.14	1.37
Extended	5.15	-10.87	-26.02	3.55	-1.94	-0.15	0.20	-3.61	-6.53	-0.94
Additional X	-0.66	-0.64	-4.77	-0.74	-1.12	-0.07	-0.06	0.74	-3.11	-0.18
1^-Z	-0.48	-1.84	-33.39	0.50	0.63	0.48	-0.24	-9.41	-5.60	-1.52
$K^* BW$	-5.72	14.57	2.72	-3.30	-0.31	-1.44	-0.16	-0.06	-8.09	-0.82
K-Matrix	0.17	8.69	-7.91	-0.23	0.06	-3.07	-0.25	4.10	-11.95	-0.06
Z(4000) Flatte	0.03	1.27	3.82	0.19	0.09	0.29	0.00	-0.85	2.79	0.18
BKG factorization	-0.76	1.08	1.48	-0.26	-0.18	0.14	0.01	-1.04	-1.72	-0.15
Total Sys.	(-9.90 , +7.46)	(-35.23 , +17.93)	(-46.86 , +18.89)	(-6.20 , +18.47)	(-5.31 , +1.58)	(-3.92 , +4.49)	(-0.28 , +0.78)	(-15.77 , +12.46)	(-40.25 , +36.04)	(-1.85 , +3.86)

Table 3.24 Summary of the systematic errors on the parameters of the $X \rightarrow J/\psi\phi$ states with $J^P = 1^-$ and $J^P = 2^-$. All numbers for masses and width are in MeV and fit fraction in %.

Systematic	$X(4630)$			$X(4150)$		
	M_0	Γ_0	FF	M_0	Γ_0	FF
Fixed M&W	0.72	-1.38	0.06	1.10	5.49	0.10
$\chi_{\text{IP}}^2 \text{smear}$	1.38	-0.25	-0.06	-3.86	2.81	0.09
Right sideband	-6.71	6.88	0.03	1.92	0.64	0.02
Left sideband	6.97	-11.30	-0.08	-2.95	-0.96	-0.02
$\beta = 0.043$	-0.62	0.62	0.00	-0.52	-0.04	0.00
$\beta = 0.037$	1.37	-1.79	0.00	-0.20	-0.24	-0.01
L0 Trigger	5.29	-11.86	-0.03	-10.69	15.05	0.14
PID corr	-8.33	6.88	0.08	5.87	-6.66	-0.10
ϕ win 7	-97.98	-49.06	-0.95	8.65	-9.15	-0.36
non ϕ	-101.91	-48.19	-0.66	-6.87	8.03	-0.28
Poly $m(XNR)$	-104.91	-63.91	-1.23	21.50	-12.76	-0.41
$XNR(1^+)$	-93.58	-33.65	-1.45	14.79	2.62	-0.05
$XNR(2^+)$	11.71	22.79	0.24	-20.93	47.18	0.34
BW d=1.5	11.47	-9.22	-0.46	-20.75	9.62	0.42
BW d=4.5	-10.96	4.57	0.24	19.55	-10.57	-0.32
L min sys	-108.92	-62.51	-1.29	-17.99	8.94	-0.04
Flatte	0.59	0.31	-0.15	10.54	-18.08	-0.29
Extended	-14.84	18.05	0.10	-30.11	56.48	0.81
Additional X	-3.75	2.36	-0.07	-0.83	-1.03	-0.02
1^-Z	24.01	132.82	2.94	29.42	-23.92	-0.97
K^*BW	0.15	17.14	0.28	27.38	-22.18	-0.63
K-Matrix	-104.00	-70.16	-1.29	-11.93	28.62	0.71
Z(4000) Flatte	-4.27	4.03	0.08	2.85	-1.41	-0.05
BKG factorization	-11.67	6.63	-0.23	3.70	-2.77	-0.14
Tot.	(-109.81, +18.23)	(-72.74, +134.20)	(-1.46 , +2.94)	(-32.93, +32.30)	(-29.71, +59.16)	(-0.99 , +0.84)

Table 3.25 Summary of the systematic errors on the parameters of the $Z \rightarrow J/\psi K^+$ states with $J^P = 1^+$. All numbers for masses and width are in MeV and fit fraction in %.

Systematic	$Z(1^+)$	$Z(4000)$			$Z(4220)$		
	FF	M_0	Γ_0	FF	M_0	Γ_0	FF
Fixed M&W	-3.34	-0.22	-3.60	-0.83	-2.28	-15.58	-1.67
$\chi_{\text{IP}}^2 \text{smear}$	1.71	0.21	1.01	0.09	5.15	4.49	1.05
Right sideband	-0.48	0.01	0.58	0.11	-2.25	-3.10	-0.28
Left sideband	0.41	-0.30	-1.16	-0.24	3.56	3.22	0.23
$\beta = 0.043$	-0.37	-0.06	-0.00	0.01	-1.14	-2.22	-0.25
$\beta = 0.037$	0.13	-0.02	0.26	0.02	0.41	0.96	0.05
L0 Trigger	1.77	0.45	0.58	0.19	0.64	13.05	1.20
PID corr	-2.75	-1.06	-1.82	-0.69	2.10	4.93	-1.67
ϕ win	-7.57	-4.71	-23.91	-2.75	6.10	-24.54	-3.38
non ϕ	-8.43	-2.87	-18.39	-1.79	-12.51	-25.80	-4.51
Poly $m(XNR)$	-3.66	-4.24	-16.36	-2.56	16.25	-5.14	-0.74
$XNR(1^+)$	10.10	1.49	-21.25	-2.53	38.13	89.32	9.20
$XNR(2^+)$	5.47	2.16	3.09	1.26	-2.85	62.58	5.16
BW d=1.5	2.22	-0.29	-5.27	-0.58	7.60	18.83	1.85
BW d=4.5	-1.07	0.08	1.81	0.04	-1.46	-8.52	-0.50
L vars	-2.47	2.75	-3.19	-1.18	-2.71	-55.64	-1.31
Flatte	2.29	0.52	-2.80	-0.45	11.99	33.00	2.01
Extended	-9.92	-2.35	-6.66	-1.16	-22.73	-61.76	-5.33
Additional X	-1.54	-0.68	2.07	0.30	-4.79	-11.37	-1.28
1^-Z	-14.00	-21.09	-3.46				
K^*BW	-5.98	0.08	-0.66	-0.32	-13.37	-29.68	-2.82
K-Matrix	-2.83	-3.75	-20.80	-2.85	8.10	-8.14	-0.46
Z(4000) Flatte	-0.78	0.18	51.91	2.83	-17.81	-10.97	1.00
BKG factorization	-0.46	0.10	-0.32	-0.12	-0.91	0.36	-0.27
Tot.	(-11.11 , +11.28)	(-14.05 , +3.12)	(-24.31 , +52.10)	(-3.07 , +3.05)	(-23.92 , +38.85)	(-65.55 , +91.98)	(-6.06 , +9.64)

Table 3.26 Fit results from the 9K+5X+3X+2Z model with $Z(4220)$ $J^P = 1^+$. Significance is evaluated from the change of the $2 \ln \mathcal{L}$ assuming ndf to be **twice** the reduction in number of free parameters when removing the component in the fit. The ndf is not multiply by two for the K^* resonance whose mass and width are fixed.

Contribution	Significance	Fit results		
		M_0 [MeV]	Γ_0 [MeV]	FF%
All $K(1^+)$				$25.1 \pm 3.6^{+6.0}_{-14.8}$
2^1P_1	$K(1^+)$	4.5σ	$1861 \pm 10^{+14.9}_{-45.5}$	$149 \pm 41^{+230.6}_{-16.2}$
2^3P_1	$K'(1^+)$	4.5σ	$1911 \pm 37^{+122.4}_{-44.2}$	$276 \pm 50^{+317.6}_{-156.9}$
1^3P_1	$K_1(1400)$	9.2σ		$15.1 \pm 2.7^{+2.2}_{-10.9}$
All $K(2^-)$				$2.1 \pm 0.4^{+2.0}_{-1.1}$
1^1D_2	$K_2(1770)$	7.9σ		
1^3D_2	$K_2(1820)$	5.8σ		
All $K(1^-)$				$50.3 \pm 4.1^{+9.5}_{-19.4}$
1^3D_1	$K^*(1680)$	4.7σ		$13.5 \pm 2.3^{+34.5}_{-7.8}$
2^3S_1	$K^*(1410)$	7.7σ		$37.9 \pm 5.2^{+10.9}_{-17.1}$
$K(2^+)$				
2^3P_2	$K_2^*(1980)$	1.6σ	$1988 \pm 22^{+193.6}_{-29.6}$	$318 \pm 82^{+479.4}_{-100.4}$
$K(0^-)$				
2^1S_0	$K(1460)$	12σ		$10.2 \pm 1.2^{+0.9}_{-3.8}$
$X(2^-)$				
$X(4150)$	4.8σ	$4146 \pm 18^{+32.3}_{-32.9}$	$135 \pm 28^{+59.2}_{-29.7}$	$2.0 \pm 0.5^{+0.8}_{-1.0}$
$X(1^-)$				
$X(4630)$	5.5σ	$4626 \pm 16^{+18.2}_{-109.8}$	$174 \pm 27^{+134.2}_{-72.7}$	$2.6 \pm 0.5^{+2.9}_{-1.5}$
All $X(0^+)$				$19.5 \pm 4.8^{+13.3}_{-6.1}$
$X(4500)$	20σ	$4474 \pm 3^{+2.7}_{-2.9}$	$77 \pm 6^{+10.0}_{-7.0}$	$5.6 \pm 0.7^{+2.4}_{-0.5}$
$X(4700)$	17σ	$4694 \pm 4^{+15.9}_{-2.1}$	$87 \pm 8^{+15.7}_{-5.3}$	$8.9 \pm 1.2^{+4.9}_{-1.3}$
$NR_{J/\psi\phi}$	4.8σ			$28.0 \pm 7.5^{+18.2}_{-10.1}$
All $X(1^+)$				$26.0 \pm 3.4^{+7.5}_{-9.9}$
$X(4140)$	13σ	$4118 \pm 11^{+17.9}_{-35.2}$	$162 \pm 21^{+18.9}_{-46.9}$	$17.2 \pm 2.9^{+18.5}_{-6.2}$
$X(4274)$	18σ	$4294 \pm 4^{+1.6}_{-5.3}$	$53 \pm 5^{+4.5}_{-3.9}$	$2.8 \pm 0.49^{+0.8}_{-0.3}$
$X(4685)$	15σ	$4684 \pm 7^{+12.5}_{-15.8}$	$126 \pm 15^{+36.0}_{-40.3}$	$7.2 \pm 1.0^{+3.9}_{-1.9}$
All $Z_{cs}(1^+)$				$25.0 \pm 4.9^{+11.3}_{-11.1}$
$Z_{cs}(4000)$	15σ	$4003 \pm 6^{+3.1}_{-14.1}$	$131 \pm 15^{+52.1}_{-24.3}$	$9.4 \pm 2.1^{+3.1}_{-3.1}$
$Z_{cs}(4220)$	5.9σ	$4216 \pm 24^{+38.9}_{-23.9}$	$233 \pm 52^{+92.0}_{-65.6}$	$10.3 \pm 3.8^{+9.6}_{-6.1}$

Pattern of masses and quantum numbers is not the one aligning with the expectations for pure charmonium states, thus tetraquark $c\bar{c}s\bar{s}$ structures are likely contributing to the mass spectrum. Direct color binding is more likely to be responsible than meson-meson interactions, because of the rich spectrum of quantum numbers and the decay widths larger than for the narrow $c\bar{c}u\bar{d}$ and $c\bar{c}uud$ states observed near the constituent hadron-hadron mass thresholds.

While broader $c\bar{c}u\bar{d}$ states decaying to $J/\psi\pi^+$ or $\psi'\pi^+$ were observed in $B \rightarrow \psi\pi^+K$ decays, our data requires for the first time $c\bar{c}u\bar{s}$ states decaying to $J/\psi K^+$. A relatively narrow, $\Gamma = 131 \pm 15^{+26}_{-26}$ MeV, $1^+ Z_{cs}(4000)^+ \rightarrow J/\psi K^+$ state is observed at $4003 \pm 6^{+4}_{-14}$ MeV, with a significance of more than 15σ . A broad $1^+ Z_{cs}(4220)^+$ state is also needed at 6σ significance.

Chapter 4 Open-charm pentaquark search in $\Lambda_b^0 \rightarrow \Lambda_c^+ K^+ K^- \pi^-$ decay

4.1 Study motivation

Over the last two decades, a wealth of information has been accumulated on the decays of b -hadrons. Measurements of their decays have been used to test the CKM mechanism 61 for describing weak decay phenomena in the Standard Model, as well as provide measurements against which various theoretical approaches, such as heavy quark effective theory 81 and the factorization hypothesis, can be compared. While many decays have been measured, a large number remain either unobserved or poorly measured, most notably decays of Λ_b^0 baryons. LHCb has observed many new Λ_b^0 decays to open charm modes, such as $\Lambda_b^0 \rightarrow \Lambda_c^+ \pi^- \pi^+ \pi^-$ 1, $\Lambda_b^0 \rightarrow \Lambda_c^+ \pi^- p\bar{p}$ 17, and $\Lambda_b^0 \rightarrow \Lambda_c^+ D_{(s)}^-$ 9. We report the discovery of the $\Lambda_b^0 \rightarrow \Lambda_c^+ K^+ K^- \pi^-$ decay in this note, where the Λ_c^+ decays to $pK^- \pi^+$. ^①

Besides, the $\Lambda_b^0 \rightarrow \Lambda_c^+ K^+ K^- \pi^-$ decay also provides an opportunity to search for possible single charmed pentaquarks ($c\bar{s}uud$) that could decay strongly to $\Lambda_c^+ K^+$. The LHCb experiment observed two pentaquark states using $\Lambda_b^0 \rightarrow J/\psi pK^-$ decays in 2015 12. This discovery motivates us to search for more pentaquark states. Recently Belle reported an observation of a new $\Xi_c(2930)^0$ resonance decay to $\Lambda_c^+ K^-$ in $B^+ \rightarrow \Lambda_c^+ \bar{\Lambda}_c^- K^+$ decays **Li:2017uvv**, and we can also examine the decays of resonances e.g. $\Xi_c^0 \rightarrow \Lambda_c^+ K^-$.

In the analysis of $\Lambda_b^0 \rightarrow \Lambda_c^+ p\bar{p}\pi^-$, the decay of $\Lambda_b^0 \rightarrow \Lambda_c^+ K^+ K^- \pi^-$ has been shown as a background. Figure 4.1 shows possible contributing Feynman diagrams to the $\Lambda_b^0 \rightarrow \Lambda_c^+ K^+ K^- \pi^-$ decay. As the knowledge about this channel is poor, the first step is the measurement of the branching ratio.

The branching fraction of the $\Lambda_b^0 \rightarrow \Lambda_c^+ K^+ K^- \pi^-$ decay with respect to that of the $\Lambda_b^0 \rightarrow \Lambda_c^+ D_s^-$ decay (with $D_s^- \rightarrow K^+ K^- \pi^-$), defined as

$$R \equiv \frac{\mathcal{B}(\Lambda_b^0 \rightarrow \Lambda_c^+ K^+ K^- \pi^-)}{\mathcal{B}(\Lambda_b^0 \rightarrow \Lambda_c^+ D_s^-; D_s^- \rightarrow K^+ K^- \pi^-)} \quad (4.1)$$

is measured in this analysis. The $\Lambda_b^0 \rightarrow \Lambda_c^+ D_s^-$ ($D_s^- \rightarrow K^+ K^- \pi^-$) decay channel is taken as a normalization channel, which has identical final states as that of the signal channel to cancel

^① Charge conjugate final states are implied throughout.

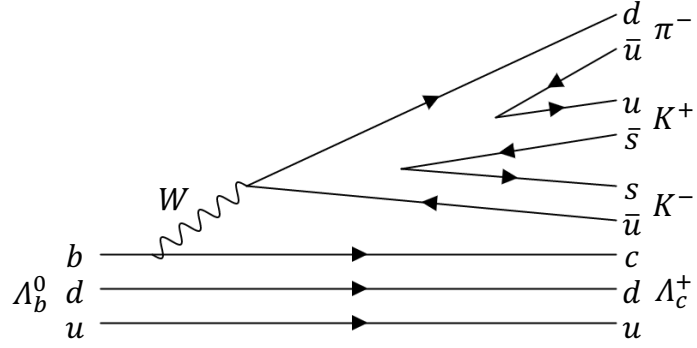


Figure 4.1 Possible Feynman diagrams contributing to the decay of $\Lambda_b^0 \rightarrow \Lambda_c^+ K^- K^+ \pi^-$.

large systematic uncertainties. The ratio is determined as

$$\begin{aligned} R &= \frac{\mathcal{B}(\Lambda_b^0 \rightarrow \Lambda_c^+ K^+ K^- \pi^-)}{\mathcal{B}(\Lambda_b^0 \rightarrow \Lambda_c^+ D_s^-; D_s^- \rightarrow K^+ K^- \pi^-)} \\ &= \frac{N(\Lambda_b^0 \rightarrow \Lambda_c^+ K^+ K^- \pi^-)}{N(\Lambda_b^0 \rightarrow \Lambda_c^+ D_s^-; D_s^- \rightarrow K^+ K^- \pi^-)} \frac{\epsilon(\Lambda_b^0 \rightarrow \Lambda_c^+ D_s^-; D_s^- \rightarrow K^+ K^- \pi^-)}{\epsilon(\Lambda_b^0 \rightarrow \Lambda_c^+ K^+ K^- \pi^-)}, \end{aligned} \quad (4.2)$$

by measuring the numbers (N) of candidates from signal and normalization modes and the relative efficiency (ϵ) between the $\Lambda_b^0 \rightarrow \Lambda_c^+ K^+ K^- \pi^-$ and $\Lambda_b^0 \rightarrow \Lambda_c^+ D_s^- (D_s^- \rightarrow K^+ K^- \pi^-)$ decays.

4.2 Selection

4.2.1 Dataset

In this analysis, the dataset with an integrated luminosity of 3.0 fb^{-1} collected by the LHCb experiment 10, 40 in 2011 and 2012 is used. The processes of $\Lambda_b^0 \rightarrow \Lambda_c^+ K^+ K^- \pi^-$ and $\Lambda_b^0 \rightarrow \Lambda_c^+ D_s^-$ are reconstructed with software versions of Reco14 Stripping21(r1) and DaVinci v42r6p1 for 2012(2011) data. In the reconstruction, the momentum scale calibration is used. In both data and MC, we use a decay tree fitter to constrain the Λ_b^0 to originate from the primary vertex, and the invariant mass to the known value for each open charm candidate 145. For the study of the relevant resonance structures, further constraint of the mass of Λ_b^0 to the PDG value is also applied. The resulting four momenta of final states are used to compute the invariant masses of the intermediate resonances in $\Lambda_b^0 \rightarrow \Lambda_c^+ K^+ K^- \pi^-$ decays.

For the Monte Carlo (MC) study, 2.2 million events for $\Lambda_b^0 \rightarrow \Lambda_c^+ K^+ K^- \pi^-$ and 0.7 million for $\Lambda_b^0 \rightarrow \Lambda_c^+ D_s^- (D_s^- \rightarrow K^+ K^- \pi^-)$ are generated in the simulated pp collisions at $\sqrt{s} = 7 \text{ TeV}$ and 8 TeV . Besides, the $\Lambda_b^0 \rightarrow \Lambda_c^+ K^+ K^- \pi^-$ channel is also generated via intermediate states: 1.4

million with $K(892)^{*0} \rightarrow K^+ \pi^-$ resonance and 1.4 million with also $a_1(1260)^+ \rightarrow K(892)^{*0} K^-$ resonance.

The fragmentation and hadronization are simulated by PYTHIA 8, the decay by EvtGEN and the detector response by GEANT4. For the reconstruction, the same software versions are adopted as used for data.

4.2.2 Preselection

The adopted trigger lines for $\Lambda_b^0 \rightarrow \Lambda_c^+ K^+ K^- \pi^-$ and $\Lambda_b^0 \rightarrow \Lambda_c^+ D_s^-$ are the same and listed in Table 4.1. The L0 trigger is chosen so that the systematic uncertainty of L0 efficiency could cancel a lot in the normalization ratio. And the 4-body topological line is also used considering the possible resonance state. In those two decays, the Λ_c^+ is reconstructed as a combination of $pK^-\pi^+$. Then Λ_c^+ is combined with D_s^- or $K^+K^-\pi^-$ for the reconstruction of Λ_b^0 . Those decays through $\Lambda_b^0 \rightarrow \Lambda_c^+ K^+ K^- \pi^-$ pass the `Lb2LcKKPiLc2PKPiBeauty2CharmLine` stripping line, while the $\Lambda_b^0 \rightarrow \Lambda_c^+ D_s^-$ candidates pass the `Lb2LcDD2HHHPIDBeauty2CharmLine`.

The selection criteria for Λ_c^+ and Λ_b^0 candidates are identical in the stripping, while some difference is used to select the $K^+K^-\pi^+$ candidates directly from the Λ_b^0 or the D_s^+ decays. The comparison of stripping selection for the two decay channels is shown in Table 4.2. In addition to the stripping selection, additional preselection criteria for both channels are used to suppress the background, that are given in Table 4.3. The proton candidates are required to have a large momentum to aim for a better particle identification. The Λ_b^0 particles come from the primary vertex, and decay after a short while, so the Λ_b^0 candidates are required to have a relatively large flight distance significance (χ_{FD}^2) and a small impact parameter significance (χ_{IP}^2). The reconstructed Λ_b^0 momentum should point back to the primary vertex, which leads to a small value of pointing angle θ_p . The Λ_c^+ particles decay after flying a short distance from Λ_b^0 decay vertex, so the z position of the decay vertex of Λ_c^+ should be larger than that of Λ_b^0 , however $z_{\text{endvtx}}(\Lambda_c^+) - z_{\text{endvtx}}(\Lambda_b^0)$ could also be slightly smaller than zero due to the resolution, thus $z(\Lambda_c^+) - z(\Lambda_b^0) > -1\text{mm}$ is required. The same PID requirements in stripping as $\Lambda_b^0 \rightarrow \Lambda_c^+ K^+ K^- \pi^-$ are required to the preselections of $\Lambda_b^0 \rightarrow \Lambda_c^+ D_s^-$ candidates. Besides, momentum and pseudorapidity cuts on final state particles are applied in the preselection

Table 4.1 Trigger lines for the $\Lambda_b^0 \rightarrow \Lambda_c^+ K^+ K^- \pi^-$ and $\Lambda_b^0 \rightarrow \Lambda_c^+ D_s^-$ candidates.

L0	Λ_b^0 L0HadronDecision(TOS)
Hlt1	Λ_b^0 TrackAllL0Decision(TOS)
Hlt2	Λ_b^0 Topo2(3,4)BodyBBDTDecision(TOS)

Table 4.2 Stripping selections on the $\Lambda_b^0 \rightarrow \Lambda_c^+ K^- \pi^-$ and $\Lambda_b^0 \rightarrow \Lambda_c^+ D_s^-$ candidates.

#	Selection variable	$\Lambda_b^0 \rightarrow \Lambda_c^+ K^- \pi^-$	$\Lambda_b^0 \rightarrow \Lambda_c^+ D_s^-$
all basic particles			
1	χ_{trk}^2/ndof		< 3
2	$P(\text{ghost})$		< 0.4
3	p_T		> 100 MeV/c
4	p		> 1000 MeV/c
5	χ_{IP}^2		> 4
Λ_c^+ selection			
6	$p_T(K) + p_T(p) + p_T(\pi)$		> 1800 MeV/c
7	χ_{vtx}^2/ndof		< 10
8	χ_{FD}^2		> 36
9	$ M_{rec} - M_{pdg} $		< 100 MeV/c ²
10	one track with	$p_T > 500 \text{ MeV}/c, p > 5000 \text{ MeV}/c$	
11	$PIDp(p)$		> -10
12	$PIDK(K^-)$		> -10
13	$PIDK(\pi^+)$		< 20
K^+, K^-, π^- from Λ_b^0 or D_s^+			
14	p	$> 2000 \text{ MeV}/c$	$> 1000 \text{ MeV}/c$
15	$PIDK(K^+, K^-)$	> -2	> -10
16	$PIDK(\pi^-)$	< 10	< 20
$K^+ K^- \pi^-$ vertex cut			
17	χ_{vtx}^2/ndof	< 8	< 10
18	χ_{FD}^2	> 16	> 36
19	$BPVcos(\theta_p)$	> 0.98	> 0
20	$BPVVDRHO$	> 0.1mm	—
21	$BPVVDZ$	> 2.0mm	—
22	$p_T(\text{daughtersum})$	> 1250 MeV/c	> 1800 MeV/c
23	invariant mass	< 3000 MeV/c ²	(1769.62, 2068.49) MeV/c ²
24	two track with	$p_T > 300 \text{ MeV}/c$	—
25	one track with	$p_T > 500 \text{ MeV}/c, p > 5000 \text{ MeV}/c$	
Λ_b^0 selections			
26	χ_{vtx}^2/ndof		< 10
27	τ		> 0.2 ps
28	χ_{IP}^2		< 25
29	$BPVcos(\theta_p)$		> 0.999
30	one track with	$p_T > 1.7 \text{ GeV}/c, p > 10 \text{ GeV}/c, \chi_{minIP}^2 > 16, \text{minIP} > 0.1 \text{ mm}$	
31	$p_T(\text{daughtersum})$		> 5 GeV/c

because of the coverage of the tracking efficiency calibration provided by tracking group.

Several vetoes are employed to remove cross-feed from charged D mesons and B mesons.

The vetoes are as follows:

- $B_s^0 \rightarrow D_s^+ X, D_s^+ \rightarrow K^+ K^- \pi^+$ with $X = K^+ K^- \pi^-$ or D_s^- : The proton in Λ_c^+ is set to

Table 4.3 The shared preselections on the $\Lambda_b^0 \rightarrow \Lambda_c^+ K^+ K^- \pi^-$ and $\Lambda_b^0 \rightarrow \Lambda_c^+ D_s^-$ candidates.

#	Selection variable	requirements
1	$p(p)$	$> 10 \text{ GeV}/c$
2	$ M_{rec}(\Lambda_c^+) - M_{pdg}(\Lambda_c^+) $	$< 15 \text{ MeV}/c^2$
3	$ProbNNp(p \text{ from } \Lambda_c^+)$	> 0.1
4	$PIDp(p \text{ from } \Lambda_c^+)$	> -10
5	$ProbNNK(K \text{ from } \Lambda_c^+)$	> 0.1
6	$PIDK(K \text{ from } \Lambda_c^+)$	> -10
7	$PIDK(\pi \text{ from } \Lambda_c^+)$	< 20
8	$PIDK(\pi \text{ from } \Lambda_b^0 \text{ or } D_s^+)$	< 10
9	$PIDK(K \text{ from } \Lambda_b^0 \text{ or } D_s^+)$	> -2
10	$\chi_{vtx}^2(\Lambda_b^0)/ndf$	< 10
11	$\chi_{FD}^2(\Lambda_b^0)$	> 64
12	$\chi_{IP}^2(\Lambda_b^0)$	< 20
13	$\cos \theta_p$	> 0.99994
14	$z_{endvtx}(\Lambda_c^+) - z_{endvtx}(\Lambda_b^0)$	$> -1 \text{ mm}$
15	All tracks η	[1.9, 4.9]
16	All tracks p	[5, 201] GeV/c

kaon hypothesis. We require the mass of Λ_c^+ candidate with this alternative hypothesis is more than $15 \text{ MeV}/c^2$ away from the known D_s^+ mass for both $\Lambda_b^0 \rightarrow \Lambda_c^+ K^+ K^- \pi^-$ and $\Lambda_b^0 \rightarrow \Lambda_c^+ D_s^-$, or the mass of the beauty particle is more than $25 \text{ MeV}/c^2$ from the B_s^0 mass for $\Lambda_b^0 \rightarrow \Lambda_c^+ K^+ K^- \pi^-$ ($\Lambda_b^0 \rightarrow \Lambda_c^+ D_s^-$) candidates. For the B hadron mass calculation, the mass of charm hadrons are constrained to the known D_s^+ mass from PDG. This process removes about 750 candidates in $\Lambda_b^0 \rightarrow \Lambda_c^+ K^+ K^- \pi^-$ sample and 260 candidates for $\Lambda_b^0 \rightarrow \Lambda_c^+ D_s^-$ sample.

- $B^0 \rightarrow D^+ X, D^+ \rightarrow K^+ K^- \pi^+$ with $X = K^+ K^- \pi^-$ or D_s^- : The proton in Λ_c^+ is set to kaon hypothesis. We require the mass of Λ_c^+ candidate with this alternative hypothesis is more than $15 \text{ MeV}/c^2$ away from the known D^+ mass for both $\Lambda_b^0 \rightarrow \Lambda_c^+ K^+ K^- \pi^-$ and $\Lambda_b^0 \rightarrow \Lambda_c^+ D_s^-$, or the mass of the beauty particle is more than $25 \text{ MeV}/c^2$ from the B^0 mass for $\Lambda_b^0 \rightarrow \Lambda_c^+ K^+ K^- \pi^-$ ($\Lambda_b^0 \rightarrow \Lambda_c^+ D_s^-$) candidates. For the B hadron mass calculation, the mass of charm hadrons are constrained to the known D^+ mass from PDG. This process removes about 2000 candidates in $\Lambda_b^0 \rightarrow \Lambda_c^+ K^+ K^- \pi^-$ sample and 540 candidates for $\Lambda_b^0 \rightarrow \Lambda_c^+ D_s^-$ sample.
- $B^0 \rightarrow D^+ K^+ K^- \pi^-, D^+ \rightarrow K^- \pi^+ \pi^+$ with $X = K^+ K^- \pi^-$ or D_s^- : The proton in Λ_c^+ is set to pion hypothesis. We require the mass of Λ_c^+ candidate with this alternative hypothesis is more than $15 \text{ MeV}/c^2$ from the known D^+ mass for both $\Lambda_b^0 \rightarrow \Lambda_c^+ K^+ K^- \pi^-$ and $\Lambda_b^0 \rightarrow \Lambda_c^+ D_s^-$, or the mass of the beauty particle is more than $25 \text{ MeV}/c^2$ from the

B^0 mass for $\Lambda_b^0 \rightarrow \Lambda_c^+ K^+ K^- \pi^-$ ($\Lambda_b^0 \rightarrow \Lambda_c^+ D_s^-$) candidates. For the B hadron mass calculation, the mass of charm hadrons are constrained to the known D^+ mass from PDG. This process removes about 480 candidates in $\Lambda_b^0 \rightarrow \Lambda_c^+ K^+ K^- \pi^-$ sample and 150 candidates for $\Lambda_b^0 \rightarrow \Lambda_c^+ D_s^-$ sample.

All the rejected fraction are also listed by vetos showed above, which is estimated from simulation sample. And the results are given in Table 4.4.

Table 4.4 The rejected fraction by vetos for the signal and normalization channels.

#	$\Lambda_b^0 \rightarrow \Lambda_c^+ K^+ K^- \pi^-$	$\Lambda_b^0 \rightarrow \Lambda_c^+ D_s^-$
$B_s^0 \rightarrow D_s^+ X, D_s^+ \rightarrow K^+ K^- \pi^+$	2.3%	1.9%
$B^0 \rightarrow D^+ X, D^+ \rightarrow K^+ K^- \pi^+$	1.0%	0.6%
$B^0 \rightarrow D^+ K^+ K^- \pi^-, D^+ \rightarrow K^- \pi^+ \pi^+$	0.9%	0.8%

In the channel $\Lambda_b^0 \rightarrow \Lambda_c^+ K^+ K^- \pi^-$, there is a peak from D_s^- in the invariant mass spectrum of $K^+ K^- \pi^-$ that are directly produced from the Λ_b^0 particle, shown in Figure. 4.2. They are the $\Lambda_b^0 \rightarrow \Lambda_c^+ D_s^-$ decays, which are not our signal, thus are vetoed by applying a $\pm 30 \text{ MeV}/c^2$ veto mass window. Besides, we apply a veto on $K^+ \pi^-$ mass spectrum on D^0 mass window ($\pm 30 \text{ MeV}/c^2$). A $\pm 40 \text{ MeV}$ D_s^- mass window cut is applied for the normalization channel, which can help remove many background.

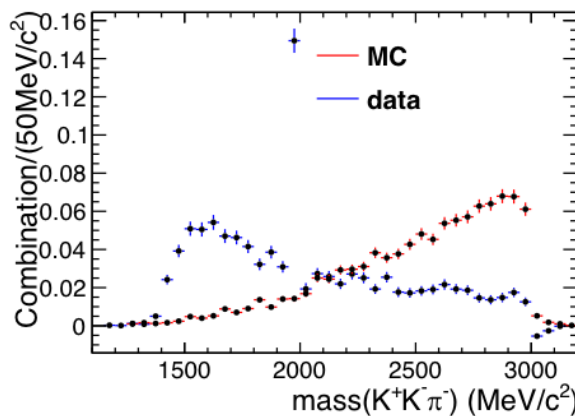


Figure 4.2 The mass distribution of $K^+ K^- \pi^-$ in the background subtracted data and MC

4.2.3 Removal of internal track clone candidates

As used in the previous analysis of $\Lambda_b^0 \rightarrow \Lambda_c^+ p \bar{p} \pi^-$, there is a special case of background: among the six tracks that are used to reconstruct $\Lambda_b^0 \rightarrow \Lambda_c^+ K^+ K^- \pi^-$ and $\Lambda_b^0 \rightarrow \Lambda_c^+ D_s^-$ ($D_s^- \rightarrow K^+ K^- \pi^-$), at least one pair of the tracks that have the same charge are clones to each other,

identified by the angle between the two tracks. The distribution of the angle between a clone track pair accumulates around zero, while non-clone track pair has wider angle distribution. By requiring all pairs of tracks with the same charge that are in one Λ_b^0 candidate to have an opening angle larger than 0.5 mrad, these background contributions are removed, which can be seen in Figure 4.3. This procedure is made with the data sample after all the event selections above, and it removes around 2.5% candidates for signal channel and around 2.5% candidates for normalization channel.

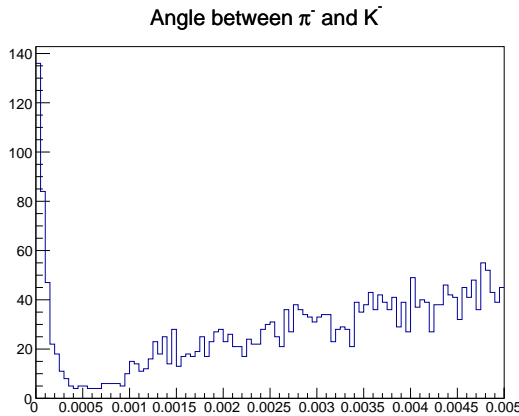


Figure 4.3 The distribution of the angle between K^- and π^- from the $\Lambda_b^0 \rightarrow \Lambda_c^+ K^+ K^- \pi^-$ decays. The unit of X-axis is rad. The peak near zero is generated from the clone track pairs, most of which has an angle less than 0.5 mrad.

4.2.4 Multiple candidates

Some of the multiple candidates are generated due to clone tracks, and in this situation, we keep one of the candidate in the event randomly. There are multiple candidates in the $\Lambda_b^0 \rightarrow \Lambda_c^+ K^+ K^- \pi^-$ and $\Lambda_b^0 \rightarrow \Lambda_c^+ D_s^-$ decays due to the exchange between the Kaon from Λ_c^+ and the Kaon directly from the Λ_b^0 decays or from the D_s^- for normalization channel, and in this situation, we also keep one of the candidate in the event randomly. This procedure is made with the data sample after all the event selections above, and it removes around 0.56% candidates for signal channel. The same process is applied to the normalization channel, though the removed number is negligible. We also check using MC sample, and this kind of background does not appear in simulation.

4.2.5 Multivariate Analysis

The $\Lambda_b^0 \rightarrow \Lambda_c^+ K^+ K^- \pi^-$ events satisfying these preselections are then further filtered using a multivariate analyzer. Gradient Boosted Decision Tree (BDTG) and Multilayer perceptron

Table 4.5 BDTG training variables.

Particle	Variables
Λ_c^+ daughters	χ_{IPmin}^2 , sum p_T
π^- from Λ_b^0	χ_{IP}^2, p_T
K^+, K^- from Λ_b^0	Min p_T , Min χ_{IP}^2
Λ_c^+	χ_{endvtx}^2
K^+, K^-, π^- from Λ_b^0	sum p_T
Λ_b^0 and Λ_c^+	$z_{\text{endvtx}}(\Lambda_c^+) - z_{\text{endvtx}}(\Lambda_b^0)$
Λ_b^0	$\chi_{\text{IP}}^2, \chi_{\text{FD}}^2, \cos \theta_p, \chi_{\text{vtx}}^2$

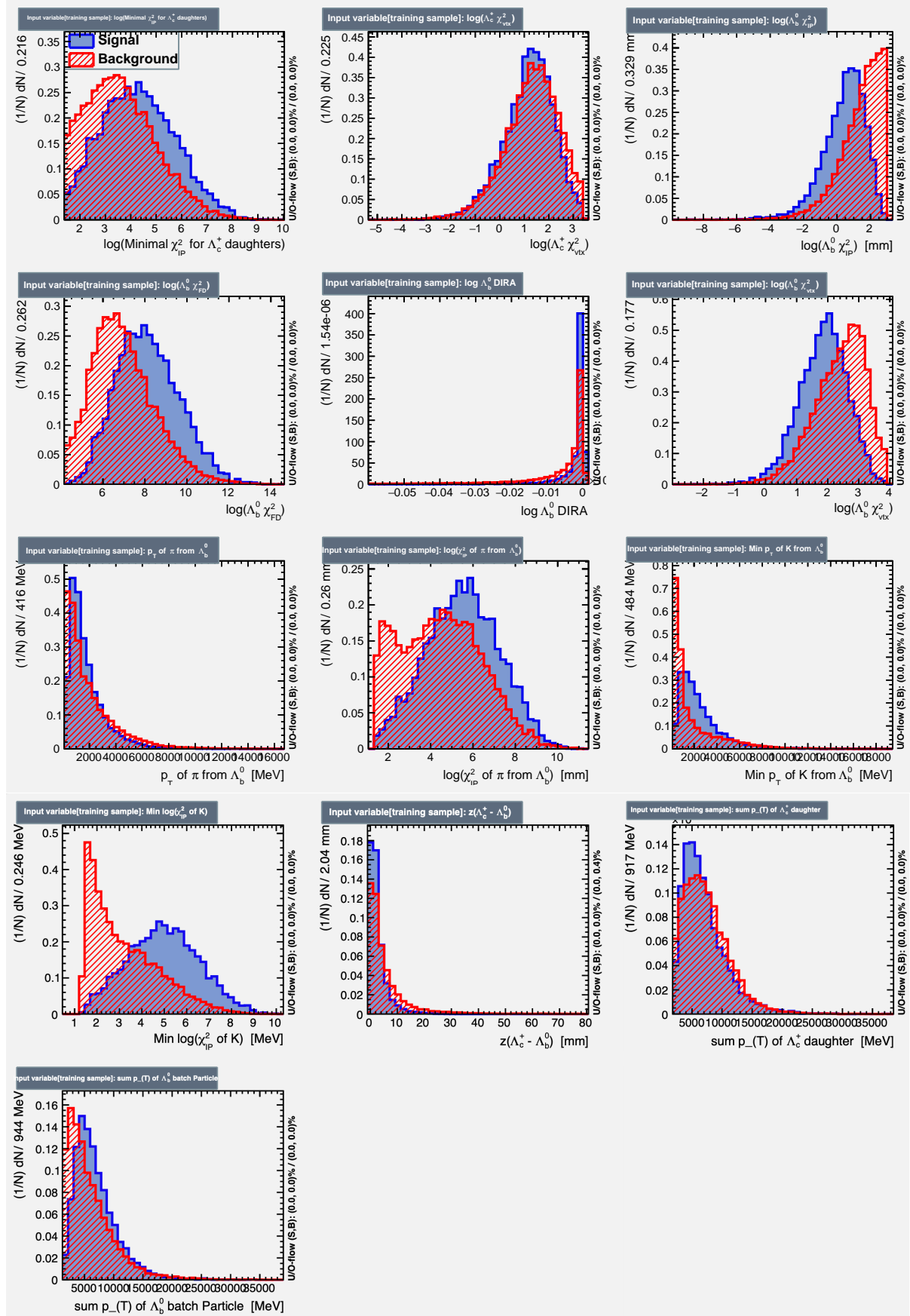
(MLP) techniques are compared. We optimise the choice of discriminating variables and use thirteen variables, that are listed in Table 4.5: the sum p_T of the Λ_c^+ daughters, the minimum χ_{IP}^2 among the Λ_c^+ daughters; the minimum p_T and the minimum χ_{IP}^2 among the K^+K^- directly from Λ_b^0 ; the p_T and χ_{IP}^2 of the bachelor π^- ; the χ_{endvtx}^2 of Λ_c^+ ; the $\chi_{\text{IP}}^2, \chi_{\text{FD}}^2, \cos \theta_p$ and χ_{endvtx}^2 of Λ_b^0 ; sum p_T of the bachelor particles; and the z position difference between the Λ_c^+ and Λ_b^0 decay vertices.

The BDTG and MLP techniques both involve a “training” procedure for event selection. A simulated signal MC and sideband (Λ_b^0 mass is larger than 5750 MeV) data background samples, both after preselection, are used to train the selection. Then separate samples are used to test the performance. The training and testing samples have almost equal event number, randomly divided from the total samples. Both the signal samples and the background samples are from the $\Lambda_b^0 \rightarrow \Lambda_c^+ K^+ K^- \pi^-$ decays.

The background sample contains the candidates with their Λ_b^0 mass larger than 5750 MeV/ c^2 . There are in total 40082 candidates in background sample and 10459 candidates in signal sample. Signal and background distributions for each of the variables used in the BDTG are shown in Fig. 4.4. There is discrimination power between signal and background in all of these variables. Figure 4.5 shows the correlation of used variables, and no large correlation for any two variables is found.

The distributions of the BDTG and MLP classifier for signal and background are shown in Figure. 4.6. Both MVA classifiers don’t have obvious overtraining and using MLP technique can get more consistent distributions between the training and test samples.

An optimal cut point on the BDTG and MLP response is determined by maximizing the signal significance, $S/\sqrt{S+B}$, where S (B) is the expected signal (background) yield in signal region, which is $\pm 3\sigma$ (± 30 MeV) of the known Λ_b^0 mass 145. The initial yield for signal and background, S_0 and B_0 , are estimated by using the mass spectrum of Λ_b^0 without BDTG or MLP


 Figure 4.4 Distributions of variables used in BDTG for $\Lambda_b^0 \rightarrow \Lambda_c^+ K^+ K^- \pi^-$ decays.

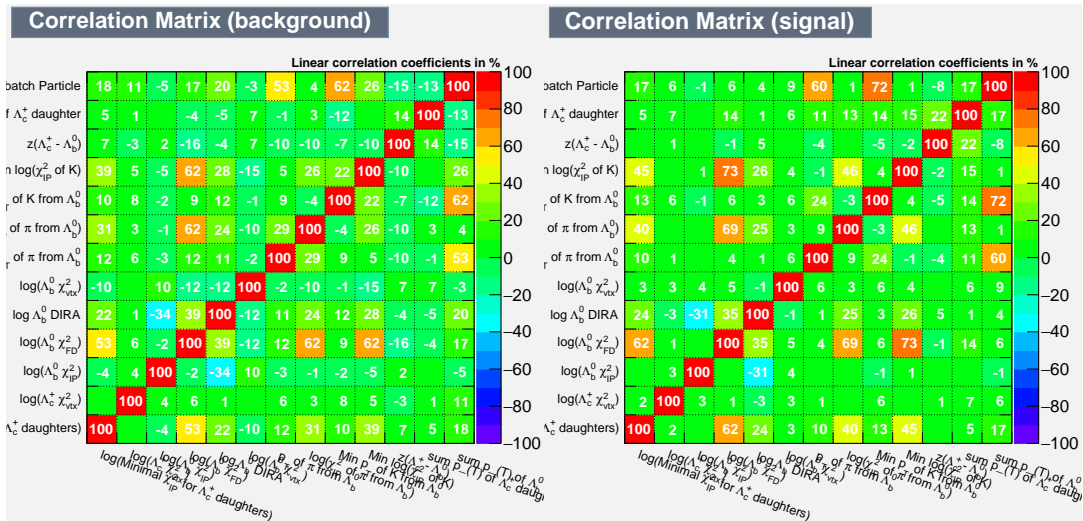


Figure 4.5 Correlation matrix of the training variables with TMVA toolkit for $\Lambda_b^0 \rightarrow \Lambda_c^+ K^+ K^- \pi^-$ decays for the background (left) and the signal (right).

Table 4.6 Rank of MLP trained variables

Rank	variable	Importance
1	Min p_T of K from Λ_b^0	0.0980
2	Sum p_T of Λ_b^0 batch particles	0.0955
3	p_T of batch π^-	0.0881
4	Min $\log(\chi_{IP}^2)$ of K	0.0856
5	$\log(\Lambda_b^0 \chi_{vtx}^2)$	0.0794
6	$\log(\Lambda_b^0 \chi_{IP}^2)$	0.0777
7	Min $\log(\Lambda_c^+ \text{ daughter } \chi_{IP}^2)$	0.0765
8	Sum p_T of Λ_c^+ daughter	0.0762
9	$\log(\Lambda_b^0 \chi_{FD}^2)$	0.0748
10	$\log(\chi_{IP}^2 \text{ of } \pi^- \text{ from } \Lambda_b^0)$	0.0777
11	$\log(\Lambda_c^+ \chi_{vtx}^2)$	0.0709
12	$\log(\Lambda_b^0 \text{ DIRA})$	0.0573
13	$z(\Lambda_c^+) - z(\Lambda_b^0)$	0.0472

requirements. The initial signal yield is estimated by fitting the Λ_b^0 mass in signal region($5490 \text{ MeV}/c^2 < m(\Lambda_b^0) < 5750$) with a DSCB(double-sided crystal ball) function for signal and a exponential function for background. With the these initial yields and the efficiencies of BDTG or MLP response of signal (MC) and background (sideband) samples in Figure. 4.6, we can derive the relation between BDTG or MLP cut threshold and the signal significance, which is shown in Figure. 4.7. Using MLP technique, we can get larger significance.

To maximize the signal significance, the BDTG and MLP working points are evaluated independently. The ROC curves of the results of different training methods are given in the Figure 4.8. We find the MLP method is more powerful to discriminate the background and

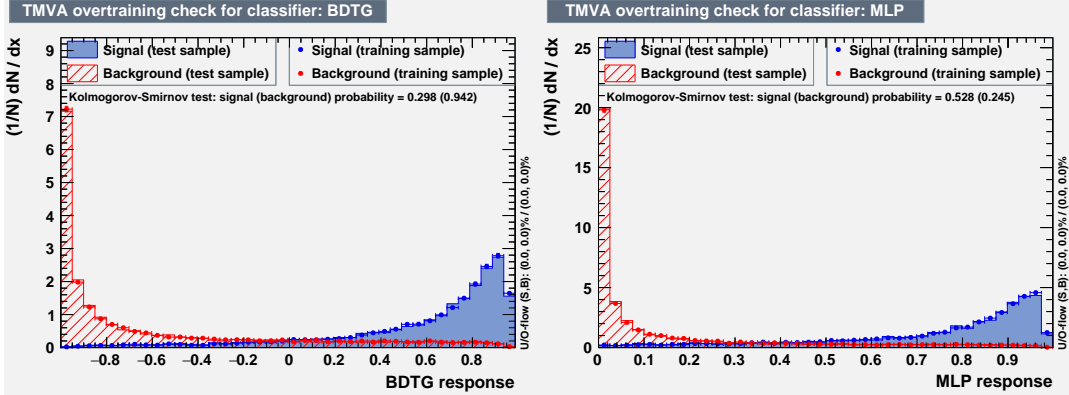


Figure 4.6 BDTG (left) and MLP (right) distributions for the signal and background for $\Lambda_b^0 \rightarrow \Lambda_c^+ K^- \pi^-$ decays.

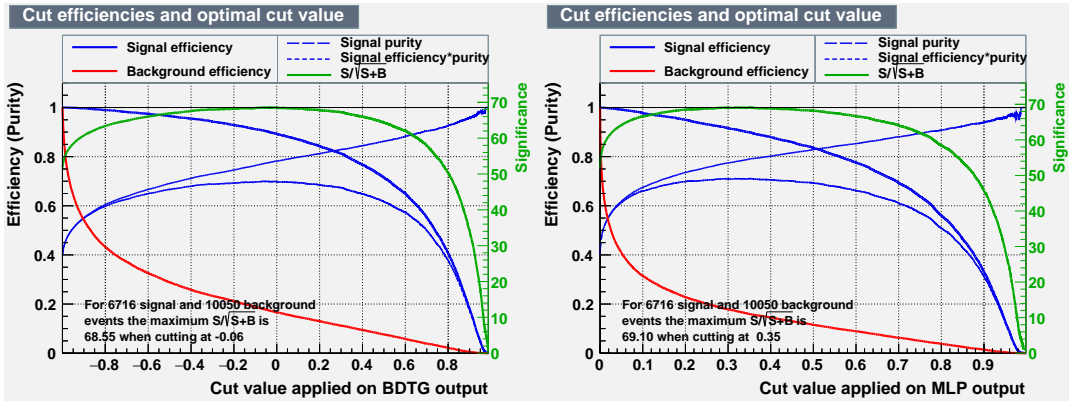


Figure 4.7 Curves showing the signal and background efficiencies as a function of the BDTG (left) and MLP (right) cut value for signal channel.

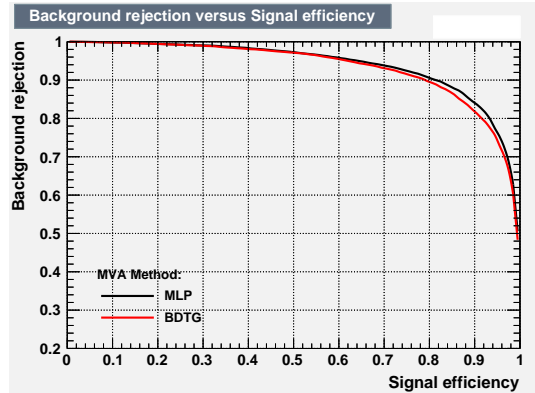


Figure 4.8 ROC curves for different MVA methods for signal channel.

signal, with a larger significance and less overtraining effect and hence we use the MLP as the default method. And a value of 0.35 is determined as the default working point with a significance about 69.10 using MLP method.

For the normalization channel $\Lambda_b^0 \rightarrow \Lambda_c^+ D_s^-$, the BDTG and MLP weights obtained in

the signal mode are used to evaluate the MVA outputs. To take into account the difference of nodf between the signal mode and $\Lambda_b^0 \rightarrow \Lambda_c^+ D_s^-$, this variable is adjusted to distribute as χ^2 with nodf=5. Signal and background with the process like $\Lambda_b^0 \rightarrow \Lambda_c^+ K^+ K^- \pi^-$ is estimated and determined as 0.09 for MLP cut.

4.2.6 Potential Resonances

Resonant contributions are expected in the signal decay $\Lambda_b^0 \rightarrow \Lambda_c^+ K^+ K^- \pi^-$, which are studied by the two body invariant mass distributions. In Figure. 4.9, the 2-dimensional distributions are shown, and $K^+ \pi^-$ decays are identified in the $K^* \rightarrow K^+ \pi^-$ mass spectrum, and the Λ_b^0 mass window in ± 30 MeV is applied.

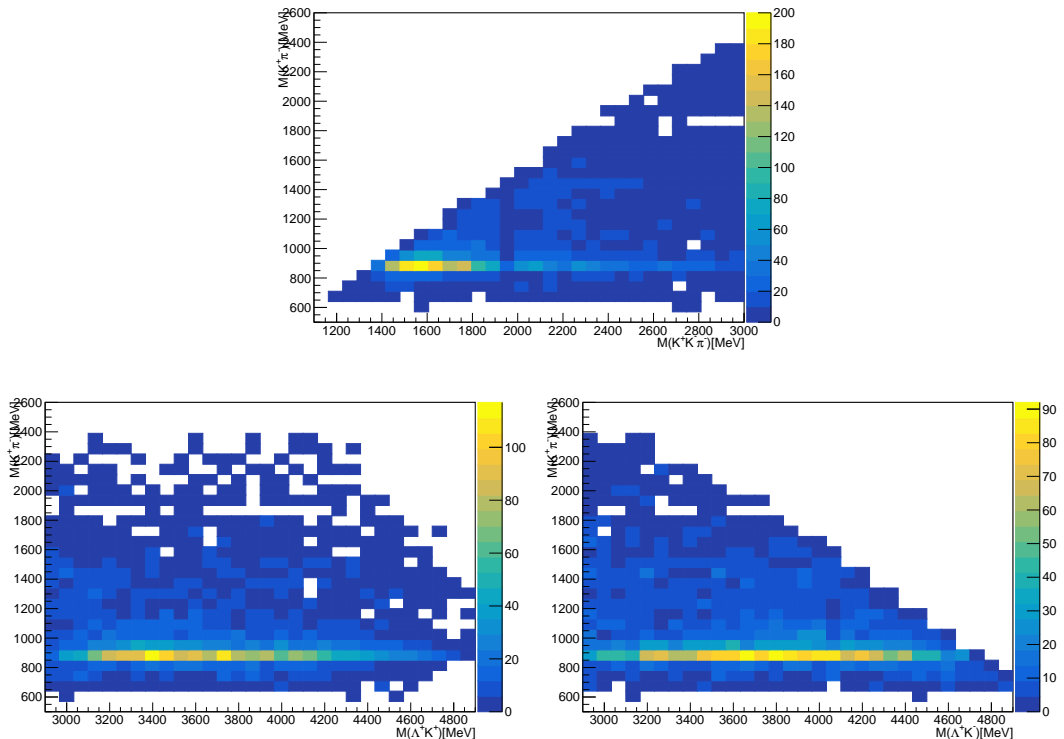


Figure 4.9 2-D distribution of combined invariant mass.

4.3 Signal extraction

4.3.1 Fit description

The signal yields of $\Lambda_b^0 \rightarrow \Lambda_c^+ K^+ K^- \pi^-$ and $\Lambda_b^0 \rightarrow \Lambda_c^+ D_s^- (D_s^- \rightarrow K^+ K^- \pi^-)$ are extracted using unbinned extended maximum likelihood fits to the distributions of the PV-constrained and Λ_c^+ mass constrained invariant mass (m) and D_s^+ mass is not constrained to the known

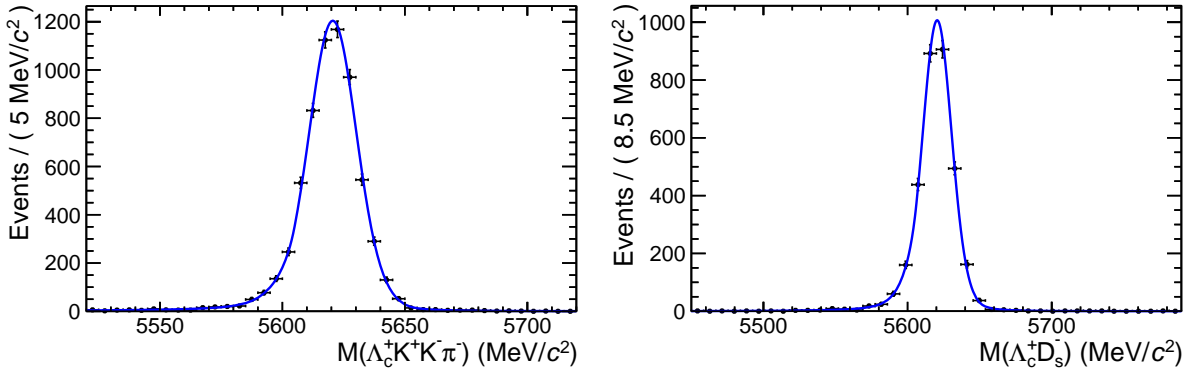


Figure 4.10 Signal shape for $\Lambda_b^0 \rightarrow \Lambda_c^+ K^+ K^- \pi^-$ (left) and $\Lambda_b^0 \rightarrow \Lambda_c^+ D_s^-$ (right) in the simulated events.

value. For the signal channel the likelihood has the form

$$\mathcal{L} = \frac{e^{-(N_S + \sum_j N_{B_j})}}{N!} \times \prod_{i=1}^N [N_S P_S(m_i) + \sum_j N_{B_j} P_{B_j}(m_i)] \quad (4.3)$$

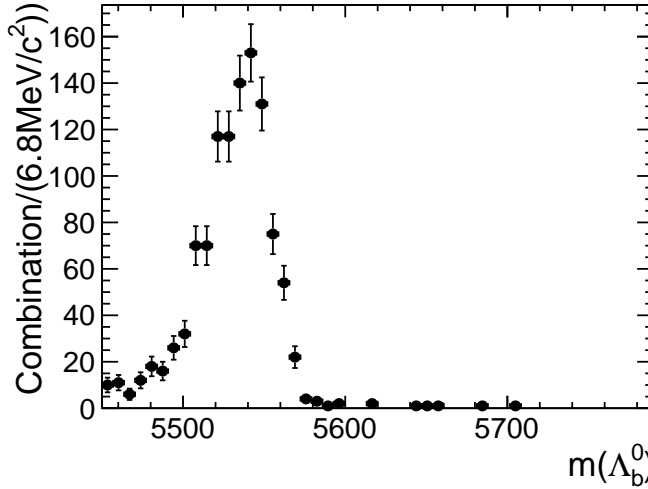
where N is the total number of events, index i run over all candidates. N_k ($P_k(m)$) is the yield (probability density function) for the category k as signal (S) and background (B_j) respectively. In addition to the combinatorial background, there is also physics background, thus index j accounts for different background sources.

4.3.2 Signal shape

The signal shape for both channels is each modeled by the sum of two Crystal Ball (CB) functions 139. The pair of CB functions for each signal have a common mean. The general form of the signal shapes is:

$$f_{sig} = f_{low} \times CB_-(m_0, \sigma_-, \alpha_-, n) + (1 - f_{low}) CB_+(m_0, \sigma_+, \alpha_+, n) \quad (4.4)$$

where m_0 is the shared mean value of the CB functions, σ_\pm are the width of the CB functions, α_\pm and n are parameters to describe the shape corresponding to the energy loss due to bremsstrahlung. And plus and minus signs suggest that the two CB have tails on opposite sides. With all parameters free, there are large correlations between the parameters. Fewer independent parameters are actually needed to describe the signal shapes well. α_\pm and n are determined using the simulated signal decays that pass all the selection as used for real data as well as the correct TRUEID information. The fitted shapes are shown in Figure. 4.10, and the fit parameters are shown in Table 4.7, and these parameters will be fixed when we fit the data.

Figure 4.11 Shape for $\Lambda_b^0 \rightarrow \Lambda_c^+ D_s^*$ reconstructed as $\Lambda_b^0 \rightarrow \Lambda_c^+ D_s^-$.

4.3.3 Physics background

4.3.3.1 Background from $\Lambda_b^0 \rightarrow \Lambda_c^+ D_s^*$ in normalization channel

The decay channel $\Lambda_b^0 \rightarrow \Lambda_c^+ D_s^*$ may emit a photon and be reconstructed as $\Lambda_b^0 \rightarrow \Lambda_c^+ D_s^-$, the shape of this background is obtained from $\Lambda_b^0 \rightarrow \Lambda_c^+ D_s^*$ simulated decays. The fitted shapes are shown in Figure 4.11, and this histogram will be used when we fit the data sample.

4.3.3.2 $\Lambda_b^0 \rightarrow \Lambda_c^+ K^+ K^- \pi^-$ background in normalization channel

For $\Lambda_b^0 \rightarrow \Lambda_c^+ D_s^-$ channel, there is a clear presence of $\Lambda_b^0 \rightarrow \Lambda_c^+ K^+ K^- \pi^-$ in D_s^- sideband, where the sideband the value of $|m(K^+ K^- \pi^-) - m(D_s^+)|$ changed from 40 to 80 MeV.(as shown in Figure. 4.12) The width of this sideband is same to the D_s^- mass window of ± 40 MeV, in order to gain the number of this background. This charmless background sizes and shapes will fixed in the mass fit. We also check this distribution in different sideband region and different D_s^+ life time regionse. More plots are in Appendix. ??

Table 4.7 Fit result of simulated $\Lambda_b^0 \rightarrow \Lambda_c^+ K^+ K^- \pi^-$, $\Lambda_b^0 \rightarrow \Lambda_c^+ D_s^- (D_s^- \rightarrow K^+ K^- \pi^-)$ mass spectrum

Parameter	$\Lambda_b^0 \rightarrow \Lambda_c^+ K^+ K^- \pi^-$	$\Lambda_b^0 \rightarrow \Lambda_c^+ D_s^- (D_s^- \rightarrow K^+ K^- \pi^-)$
α_+	1.8893 ± 0.13594	1.5740 ± 0.26813
α_-	-2.37242 ± 0.16725	-2.11783 ± 0.31333
n	1.2957 ± 0.22705	2.4483 ± 0.61617

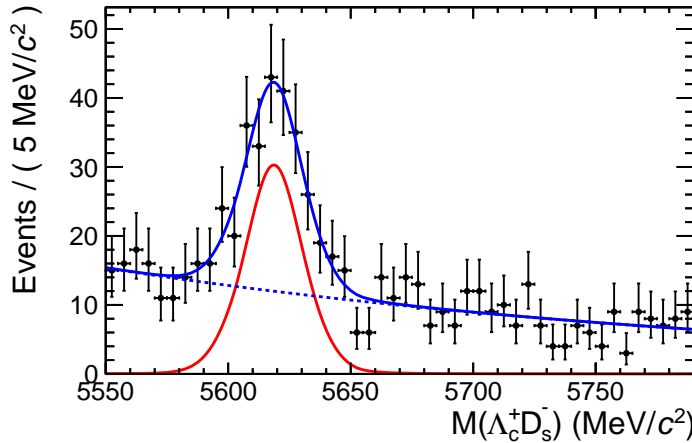


Figure 4.12 $\Lambda_b^0 \rightarrow \Lambda_c^+ K^+ K^- \pi^-$ where the $KK\pi$ mass is in the sideband of the D_s^- . The blue line is full fit, the blue dashed line is the combinatorial background, and the red line is the signal shape.

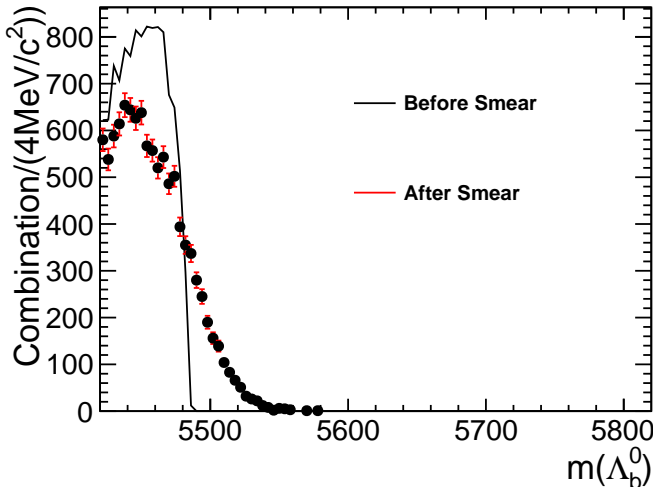


Figure 4.13 The distribution gained from $\Lambda_b^0 \rightarrow \Sigma_c K^+ K^- \pi^-$ MC sample.

4.3.3.3 $\Lambda_b^0 \rightarrow \Sigma_c K^+ K^- \pi^-$ background in signal channel

For signal channel, there is a clear presence of $\Lambda_b^0 \rightarrow \Sigma_c K^+ K^- \pi^-$ in $\Lambda_b^0 \rightarrow \Lambda_c^+ K^+ K^- \pi^-$ low sideband. The shape of this background is obtained from generator level simulated sample. Considering the mass resolution, we smear the Λ_b^0 candidate mass in the MC sample with $27.4 \text{ MeV}/c^2$, which is the signal mass resolution estimated by fitting data sample. This background distribution is shown in Figure. 4.13.

4.3.4 Combinatorial background

The combinatorial background shape is described by an exponential function, with a shape parameter that is freely varied in the fit.

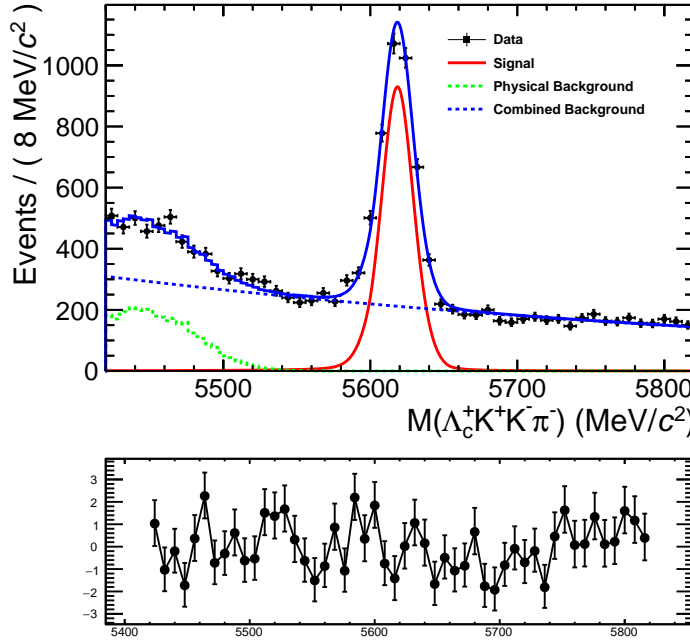


Figure 4.14 Reconstructed mass distribution for $\Lambda_b^0 \rightarrow \Lambda_c^+ K^+ K^- \pi^-$ candidates. A fit is overlaid, as described in the text. The blue line is full fit, the blue dashed line is the combinatorial background, the green dashed line is $\Lambda_b^0 \rightarrow \Sigma_c K^+ K^- \pi^-$ background and the red dashed line is the signal shape.

Table 4.8 Fit result of $\Lambda_b^0 \rightarrow \Lambda_c^+ K^+ K^- \pi^-$ mass spectrum in data sample.

Parameter	Value
m_0 (MeV/ c^2)	5618.5 ± 0.3
n_{sig}	3411.0 ± 75.5
n_{phybkg}	1672.4 ± 26.3

Table 4.9 Fit result of $\Lambda_b^0 \rightarrow \Lambda_c^+ D_s^-$ mass spectrum in data sample.

Parameter	Value
m_0 (MeV/ c^2)	5618.8 ± 0.3
n_{sig}	2546.2 ± 57.1
n_{phybkg}	477.7 ± 14.8

4.3.5 Fit results

Unbinned maximum likelihood fits to the $\Lambda_c^+ K^+ K^- \pi^-$ and $\Lambda_c^+ D_s^-$ mass spectra, with some parameters are fixed to the value obtained from Monte Carlo. The fit results for $\Lambda_b^0 \rightarrow \Lambda_c^+ K^+ K^- \pi^-$ are shown in Figure 4.14 and Table 4.8. The fit results for $\Lambda_b^0 \rightarrow \Lambda_c^+ D_s^-$ is shown in Figure 4.15 and Table 4.9. To reduce the number of free parameters, the ratio of σ^+ and σ_- in $\Lambda_b^0 \rightarrow \Lambda_c^+ D_s^-$ signal shape is fixed to the value obtained from the simulation.

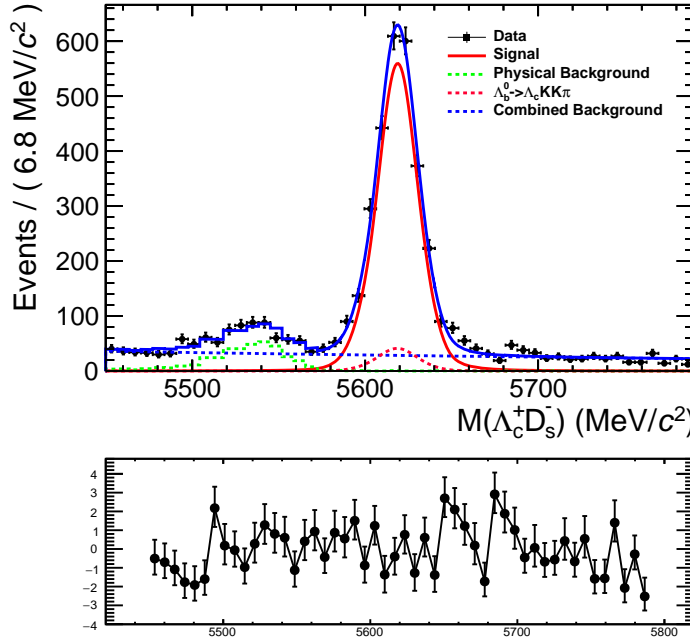


Figure 4.15 Reconstructed mass distributions for $\Lambda_b^0 \rightarrow \Lambda_c^+ D_s^-$ candidates. A fit is overlaid, as described in the text. The blue line is full fit, the blue dashed line is the combinatorial background, the green dashed line is the physical background, the red line is the signal shape, the pink dash line is $\Lambda_b^0 \rightarrow \Lambda_c^+ K^+ K^- \pi^-$ background.

4.4 Tuning MC sample

To have a better estimation of the signal efficiency, the MC is tuned to match the data.

4.4.1 IP smearing

The χ_{IP}^2 of the final state tracks and Λ_b^0 is different in the background subtracted data and signal MC in $\Lambda_b^0 \rightarrow \Lambda_c^+ D_s^-$ and in $\Lambda_b^0 \rightarrow \Lambda_c^+ K^+ K^- \pi^-$ (as shown in Figure. 4.16). We smeared the distributions of these variables and the distribution after smearing are listed in the right of Figure. 4.16, and generating gaussian random numbers to get χ^2 distributed variables. As for $\Lambda_b^0 \rightarrow \Lambda_c^+ K^+ K^- \pi^-$, the same smearing are applied to the MC sample.

The distribution of variables used in TMVA, χ_{IP}^2 of the final tracks need to be tuned. And other variables that are used in the cut have consistent distributions between data and MC.

4.4.2 p_T , y , nTracks reweight

In order to take into account data-MC difference, especially the initial kinematic of the mother particle Λ_b^0 , the MC samples need to be reweighted.

The p_T , rapidity y and nTracks weight is obtained from the normalization channel $\Lambda_b^0 \rightarrow \Lambda_c^+ D_s^-$ with Λ_b^0 Global(TOS) requirement and apply the weights to both $\Lambda_b^0 \rightarrow \Lambda_c^+ K^+ K^- \pi^-$

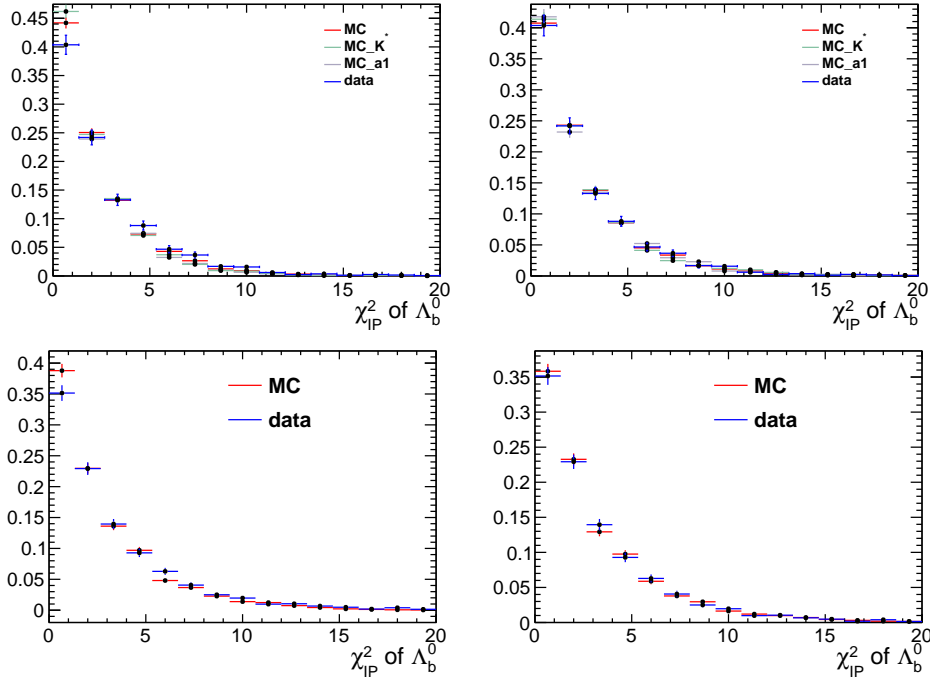


Figure 4.16 The comparison of background subtracted data and signal MC for and $\Lambda_b^0 \rightarrow \Lambda_c^+ K^+ K^- \pi^-$ (top) and $\Lambda_b^0 \rightarrow \Lambda_c^+ D_s^-$ (bottom), and the s-plot method is used to get the background subtracted data. The red line is the MC signal and blue is data. Left is the distribution before smearing and Right is after smearing.

and $\Lambda_b^0 \rightarrow \Lambda_c^+ D_s^-$ samples. As the p_T and y are properties of Λ_b^0 which is the same mother particle for signal channel and normalization channel, it should be fine to apply the weight obtained from the normalization channel to the signal channel. The nTracks representing the multiplicity of the event, and don't have large difference between the signal channel and normalization channel. Beside, we have considered the track correction, trigger, PID efficiency in the Monta Carlo sample before applying p_T , y weight.

We weight the $p_{T,y}$ at the same time, and then apply a nTracks weight, because the statistics is limited to use a 3-D weight. The transverse momentum and rapidity of Λ_b^0 are compared between the data sample after background with the sPlot technique and the MC sample. The ratio between data and MC distribution in the two dimensions is taken as weights, as shown in Figure. 4.17.

There's some difference between the distribution of multiplicity in background subtracted data and signal MC. And when estimating the PID efficiencies, the nTracks are used. We reweighted the distribution of MC to be the same as real data. We generate the weight tables of signal channel and normalization channel using $\Lambda_b^0 \rightarrow \Lambda_c^+ D_s^-$ sample.

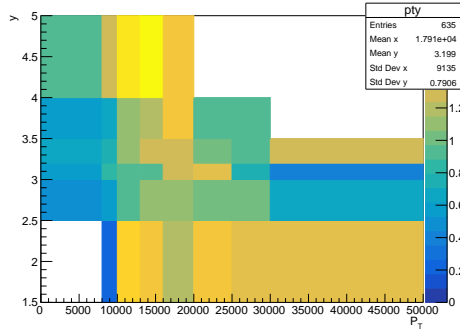


Figure 4.17 Relative yields between background-subtracted data and signal MC of $\Lambda_b^0 \rightarrow \Lambda_c^+ \pi^-$ as function of p_T and y of Λ_b^0 baryons. The relative yield in each bin is shown with the color sized Z axis, and it's larger when it goes yellow.

4.4.3 Λ_c^+ Dalitz reweight

The description of Λ_c^+ decays in simulated events can be different from the real situation. Since the MC have different Λ_c^+ decays in the signal and normalization channels, separate weights are obtained. For normalization channel, the statistics of data and MC are both large, so we apply a 2-D Dalitz reweight so that the MC distribution is consistent with data. The comparison between MC and data for normalization channel is shown in Figure. 4.18.

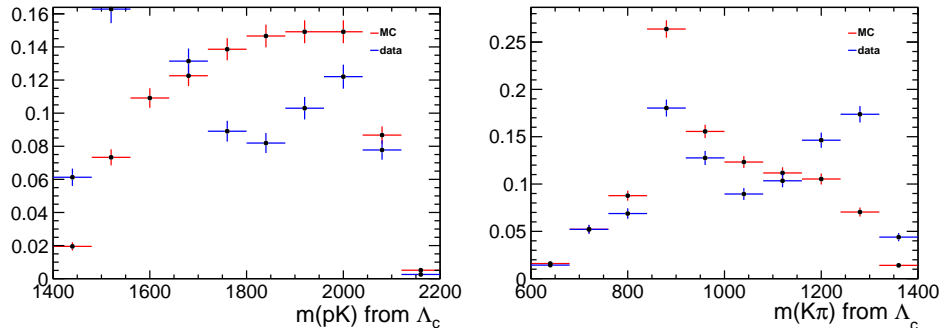


Figure 4.18 The distribution of invariant mass of combination of Λ_c^+ daughters in $\Lambda_b^0 \rightarrow \Lambda_c^+ D_s^-$ channel

For the signal channel, the same method is used. Because the statistics of the data is limited for signal channel, the bin width is larger than that used in the normalization channel. Figure 4.19 shows the comparison between data and MC for invariant mass distributions of pK and πK . The weights for these two channels are shown in Figure. 4.20. Then these weights are applied to our MC samples both in reconstruction and generator level.

4.4.4 Λ_c^+ polarization

The polarization of Λ_b^0 is consistent with no-polarization, which is discussed in LHCb-ANA-2017-009, however, Λ_c^+ could polarized because of weak decay of Λ_b^0 . The MC simulation

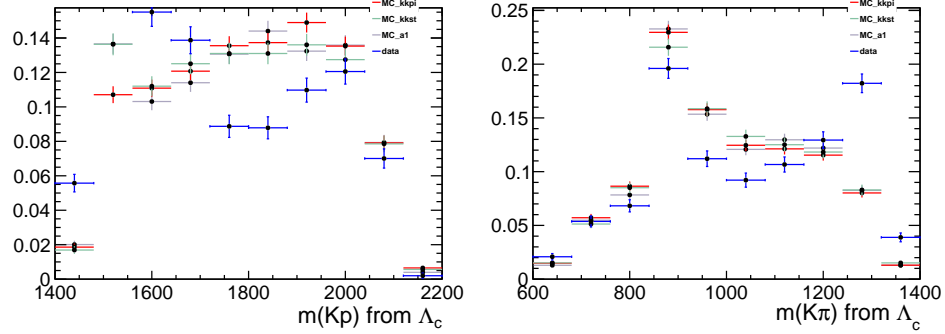


Figure 4.19 The distribution of invariant mass of combination of Λ_c^+ daughters in $\Lambda_b^0 \rightarrow \Lambda_c^+ K^+ K^- \pi^-$ channel

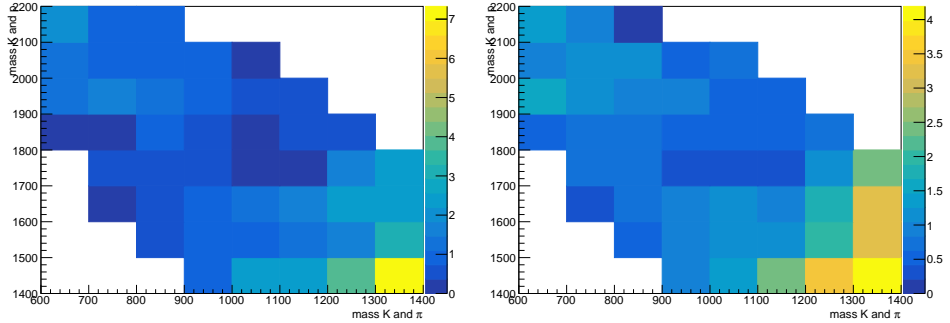


Figure 4.20 The distribution of combination invariable mass of Λ_c^+ daughters in $\Lambda_b^0 \rightarrow \Lambda_c^+ D_s^-$ channel (left) and $\Lambda_b^0 \rightarrow \Lambda_c^+ K^+ K^- \pi^-$ channel (right)

assumes no-polarization for both Λ_b^0 and Λ_c^+ . This assumption may lead to a different angular distribution from the Λ_c^+ decay in data and MC. As the polarization of Λ_c^+ in $\Lambda_b^0 \rightarrow \Lambda_c^+ D_s^-$ and $\Lambda_b^0 \rightarrow \Lambda_c^+ K^+ K^- \pi^-$ may not be the same, so the signal channel and normalization channel are handled separately.

We compare the distribution of $\theta_{\pi}^{\Lambda_c^+}$, $\phi_{\pi}^{\Lambda_c^+}$, θ_p^{pK} and ϕ_p^{pK} in data and MC of both signal channel and normalization channel, and the MC distribution are after all weight mentioned before. Here $\theta_{\pi}^{\Lambda_c^+}$, $\phi_{\pi}^{\Lambda_c^+}$ correspond to the polar angle and azimuthal angle, respectively, of the π in the Λ_c^+ rest frame. And θ_p^{pK} and ϕ_p^{pK} correspond to the polar and azimuthal angle, respectively, of the proton in the pK rest frame. The method to obtain these decay angles are discussed in 12.

The result of this comparison is shown in Figure. 4.21 for normalization channel and Fig. 4.22 for signal channel. There are not obvious inconformities for these distribution, we don't reweight for these distributions.

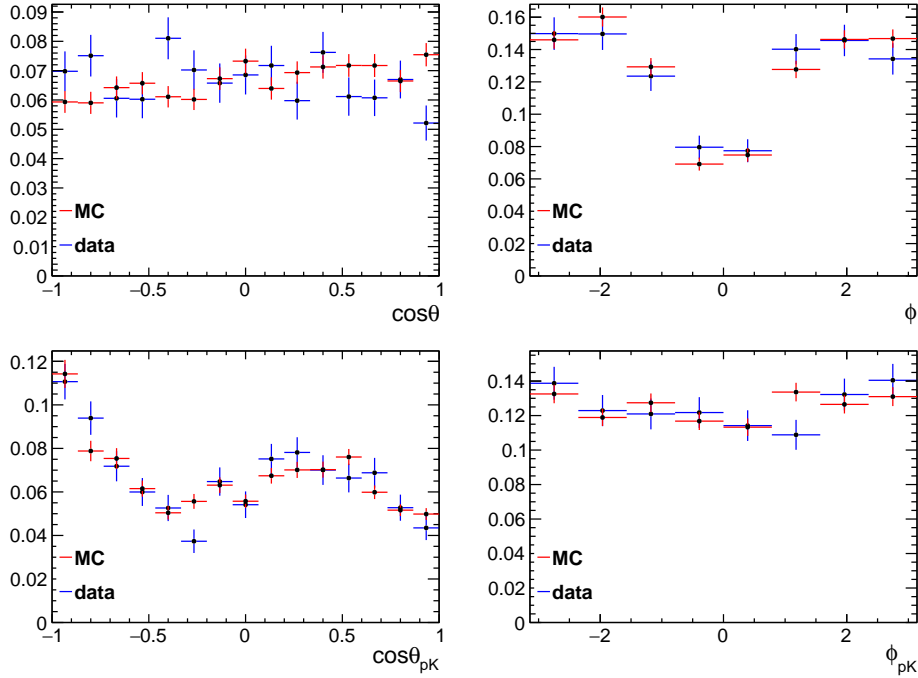


Figure 4.21 The distribution of some polarization angle in normalization channel

 Table 4.10 Fit result of $\Lambda_b^0 \rightarrow \Lambda_c^+ K^+ K^- \pi^-$ using MC samples.

Parameter	Number
$n_{nonresonance}$	824.1 ± 36.7
n_{K^*}	275.2 ± 49.2
$n_{a_1(1260)^-}$	2059.8 ± 61.4

4.4.5 Resonances in $\Lambda_b^0 \rightarrow \Lambda_c^+ K^+ K^- \pi^-$

The description of the intermediate states in the signal Λ_b^0 decays in simulated events can be different from the real situation, many resonances are found in the $\Lambda_b^0 \rightarrow \Lambda_c^+ K^+ K^- \pi^-$ from the data sample while PHSP model is used in the MC sample. To estimate the components of data sample, we fit it using three MC samples – PHSP $K^+ K^- \pi^-$ sample, with $K^*(892)^0 K^-$, and with $a_1(1260)^- \rightarrow K^*(892)^0 K^-$ resonance.

Comparing the invariant mass distribution of two body combination or three body combination, we find the invariant mass of $K^+ \pi^-$ and $K^+ K^- \pi^-$ have large differences. The three MC samples with floating yields are used to fit the background subtracted data distributions of two dimensional invariant masses of $K^+ \pi^-$ and $K^+ K^- \pi^-$, the projected distributions are shown in Figure. 4.23.

The fitting fractions are used to construct a blended MC sample to better describe data. The fitting results are listed in Table 4.10.

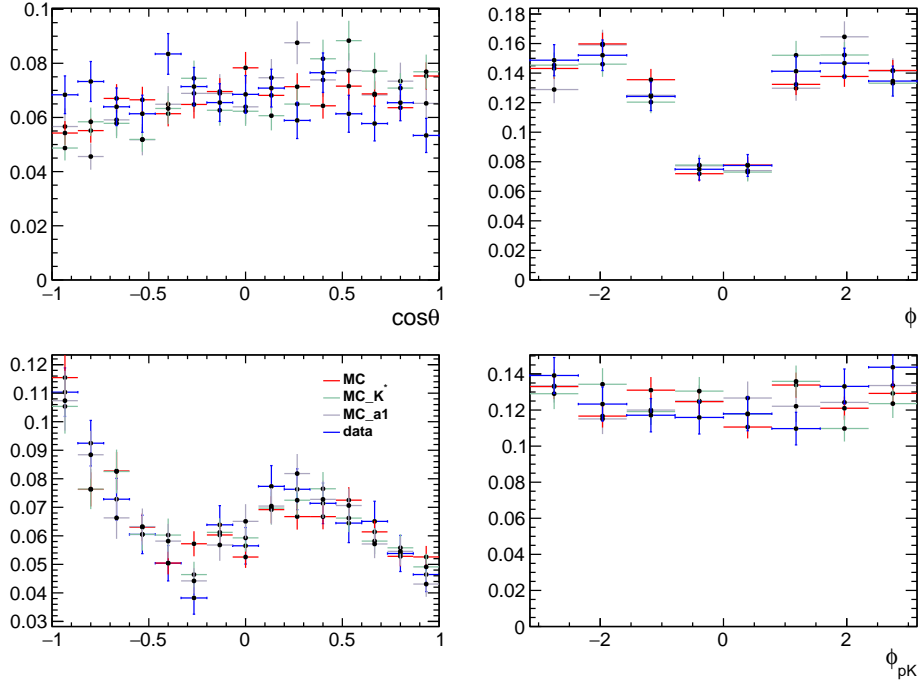


Figure 4.22 The distribution of polarization angle in signal channel

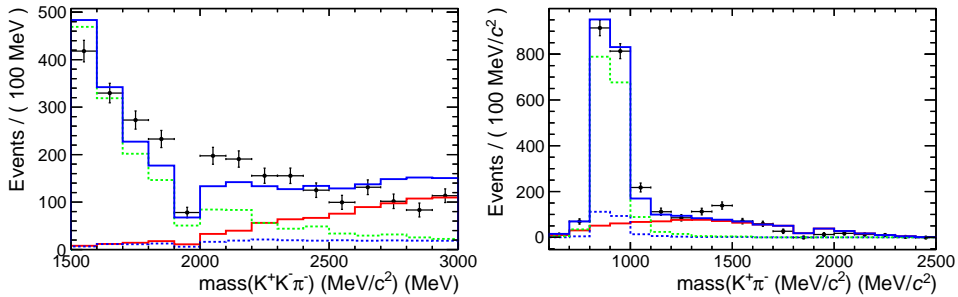
Figure 4.23 The projection from two dimensions fit, the black points are data, red line is PHSP sample, blue dash line is MC sample with K^* , green dash line is MC sample with a_1 and blue line is full fit result.

Figure 4.24 and Figure 4.25 show the combinations distribution between the data sample and blended MC sample. As we have employed some vetoes in mass spectrum of $K^+\pi^-$ and $K^+K^-\pi^-$, the bin's size used in the resonance weight is larger than the size of veto mass window, in this way, we can avoid the divide-by-zero errors.

From the bottom left plot shown in the Figure 4.24, a clear peak of Σ_c appears in the mass spectrum of $\Lambda_c^+\pi^-$, this disagreement might cause a deviate for the estimation of efficiency, so we considered this effect in the systematic uncertainty calculation.

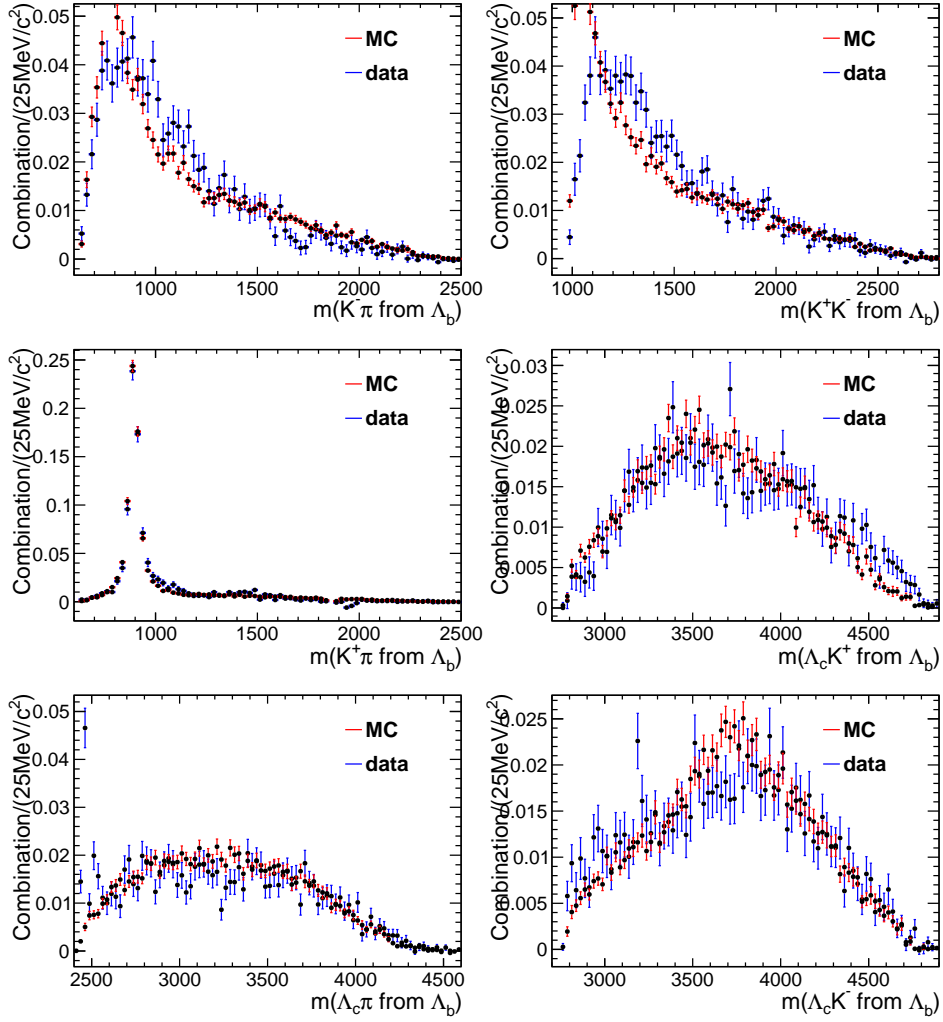


Figure 4.24 The invariant mass distribution of two body combination for $\Lambda_b^0 \rightarrow \Lambda_c^+ K^+ K^- \pi^-$ in the background subtracted data and MC.

4.4.6 Check the Reweight

We applied the p_T , y weight, nTracks weight, Λ_c^+ dalitz weight and mass weight sequentially, with a weighting procedure performed on top of the previous weighting. In this case, we need to make sure the distributions weighted previously is not changed significantly by a later reweighting. So we need to check the distribution especially the first few weights. Some distributions after all weight are shown in Figure. 4.26 and Figure. 4.27. All variables are consistent with each to a certain extent.

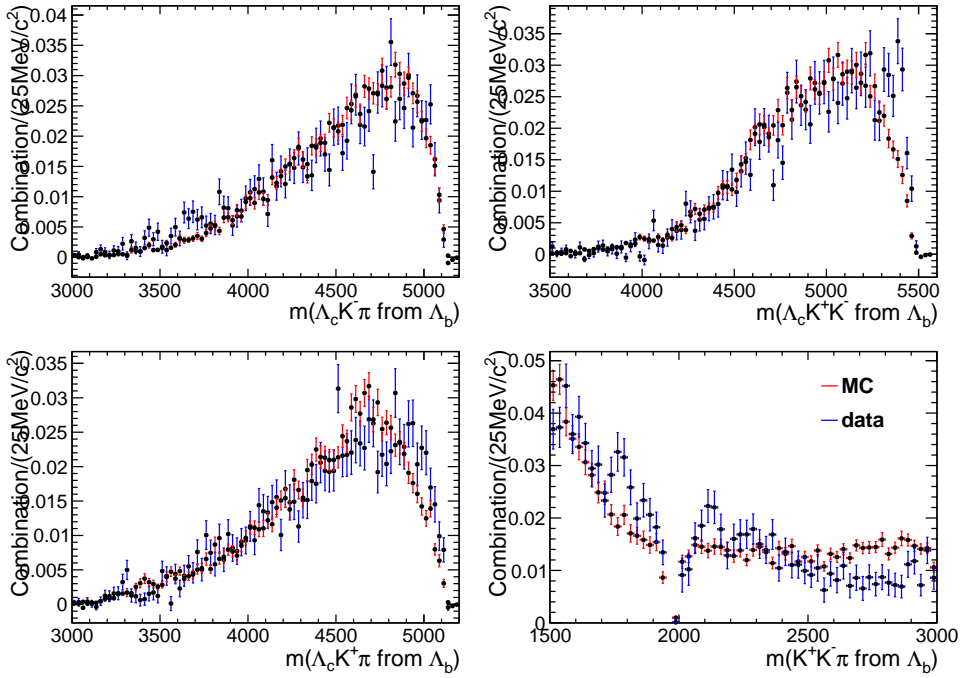


Figure 4.25 The invariant mass distribution of three body combination for $\Lambda_b^0 \rightarrow \Lambda_c^+ K^+ K^- \pi^-$ in the background subtracted data and MC.

4.5 Efficiency

The total efficiency for $\Lambda_b^0 \rightarrow \Lambda_c^+ K^+ K^- \pi^-$ and $\Lambda_b^0 \rightarrow \Lambda_c^+ D_s^-$ decays is defined as

$$\epsilon_{\text{tot}} = \epsilon_{\text{acc}} \cdot \epsilon_{\text{rec\&sel\&hlt|acc}} \cdot \epsilon_{\text{L0trig|sel\&hlt}}, \quad (4.5)$$

where ϵ_{acc} is the geometrical acceptance of the LHCb detector, $\epsilon_{\text{rec\&sel|acc}}$ stands for the reconstruction and selection efficiency, $\epsilon_{\text{trig|sel}}$ is the trigger efficiency. The summary of efficiencies is shown in Table 4.11.

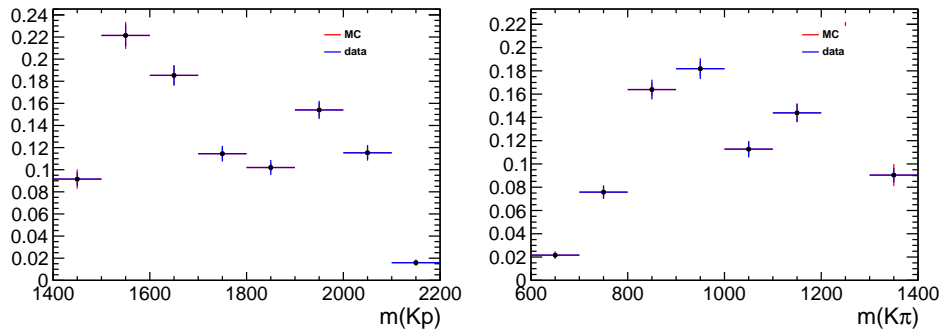


Figure 4.26 Comparison of variables between background subtracted data and weighted MC in the $\Lambda_b^0 \rightarrow \Lambda_c^+ D_s^-$ channel.

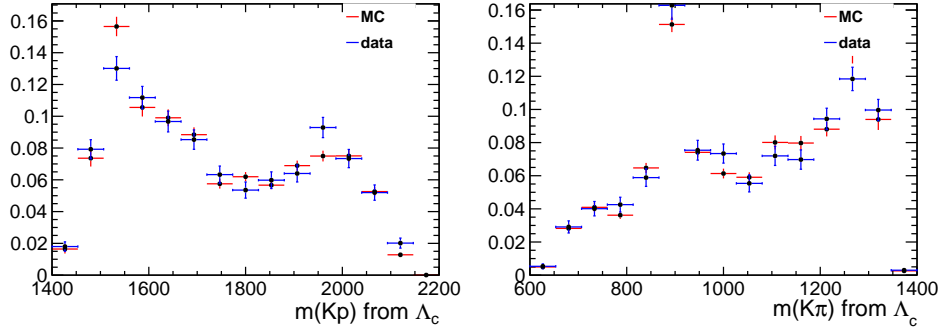


Figure 4.27 Comparison of variables between background subtracted data and weighted MC in the $\Lambda_b^0 \rightarrow \Lambda_c^+ K^+ K^- \pi^-$ channel.

Table 4.11 Relative efficiency values. Uncertainties listed are due to finite MC statistic, and are discussed in detail in Sec. 4.7

$\frac{\epsilon(\Lambda_b^0 \rightarrow \Lambda_c^+ K^+ K^- \pi^-)}{\epsilon(\Lambda_b^0 \rightarrow \Lambda_c^+ D_s^-; D_s^- \rightarrow K^+ K^- \pi^-)}$	value
Acceptance	0.9947 ± 0.0061
Rec. Sel.and Hlt (No PID)	0.8286 ± 0.0128
Tracking Correction	1.0003 ± 0.0031
PID	1.0032 ± 0.0064
L0 Trigger	0.9458 ± 0.0168
Total	0.7822 ± 0.0198

4.5.1 Geometrical acceptance

The geometrical acceptance requires all final state particles in $\Lambda_b^0 \rightarrow \Lambda_c^+ K^+ K^- \pi^-$ ($\Lambda_b^0 \rightarrow \Lambda_c^+ D_s^-$) decays to be within a polar angle θ from 10 to 400 mrad. It is studied with generator level MC events for both $\Lambda_b^0 \rightarrow \Lambda_c^+ K^+ K^- \pi^-$ and $\Lambda_b^0 \rightarrow \Lambda_c^+ D_s^-$ decays respectively, generated without the daughter in LHCb acceptance requirement. Then the requirement is applied to the MC samples, and the acceptance efficiency is calculated as $\epsilon_{\text{acc}} = N_{\text{acc}}/N_{\text{GL}}$, where N_{acc} is the number of events after the LHCb acceptance cuts and N_{GL} is the number of events with only the requirement of the fiducial cuts.

4.5.2 Reconstruction, selection and HLT efficiency

The reconstruction and selection efficiency is defined as $\epsilon_{\text{rec\&sel|acc}} = N_{\text{rec\&sel\&hlt}}/N_{\text{acc}}$, where $N_{\text{rec\&sel\&hlt}}$ is the signal yield of the full simulation sample after event selection and passing HLT1 and 2 requirements (without PID requirement) and N_{acc} is the corresponding number of generated events in the LHCb acceptance. The efficiency is estimated by candidate-by-candidate method using weighted Monte Carlo samples, while HLT and MVA are also included.

4.5.3 Tracking efficiency

The tracking efficiency is estimated from simulation, and calibrated with data by introduction factor of the MC efficiencies. The correction of MC efficiency is taken as a function of the momentum and pseudorapidity of the track, and the event-by-event correction factor is taken as the product of the correction factors of each final tracks. After the correction, we calculated the ratio tracking efficiencies with the weight.

4.5.4 L0 Trigger efficiency

The trigger efficiency tables are taken from calibration data, with 2011 and 2012 separately. These tables are used to compute L0 Hadron TOS decision, in bins of their real ET when arriving to the HCAL surface, and separately for the inner and outer regions of the calorimeter. We reweight our MC sample using these tables and the trigger efficiency on event is computed by combining the efficiencies corresponding to each one of the final tracks, assuming Λ_b^0 fires the L0 trigger if at least one track triggers it. Details see the link.

4.5.5 PID selection efficiency

It is known that the PID variables are not well described by the simulation, therefore a data-driven method is used instead. The PID efficiencies for the $p, \bar{p}, \pi^\pm, K^\pm$ are applied using the PIDCALIB package, which gives 3-D histograms that shows the efficiency of a certain PID requirement of a track as a function of the momentum and pseudorapidity of the track, and the multiplicity of the event. The single event efficiency are taken from this method, and the total PID efficiency of $\Lambda_b^0 \rightarrow \Lambda_c^+ K^- \pi^-$ ($\Lambda_b^0 \rightarrow \Lambda_c^+ D_s^-$) is derived by averaging the single event efficiencies of the candidates in the full simulated signal samples that pass all the event selections (except for PID cut).

For the calibration of proton PID efficiencies, we use the calibration samples from Λ_c^+ decays to cover the similar kinematic space as the protons from our decay modes.

4.6 Branching fraction

The branching fraction is calculated using this function:

$$\frac{N(\Lambda_b^0 \rightarrow \Lambda_c^+ K^- \pi^-)}{N(\Lambda_b^0 \rightarrow \Lambda_c^+ D_s^-; D_s^- \rightarrow K^+ K^- \pi^-)} = R \times \frac{\epsilon(\Lambda_b^0 \rightarrow \Lambda_c^+ K^- \pi^-)}{\epsilon(\Lambda_b^0 \rightarrow \Lambda_c^+ D_s^-; D_s^- \rightarrow K^+ K^- \pi^-)}, \quad (4.6)$$

where $N(\Lambda_b^0 \rightarrow \Lambda_c^+ K^- \pi^-)$ and $N(\Lambda_b^0 \rightarrow \Lambda_c^+ D_s^-; D_s^- \rightarrow K^+ K^- \pi^-)$ are the yields for signal and normalization channels, R is the relative branching fraction, $\epsilon(\Lambda_b^0 \rightarrow \Lambda_c^+ K^- \pi^-)$ and

$\epsilon(\Lambda_b^0 \rightarrow \Lambda_c^+ D_s^-; D_s^- \rightarrow K^+ K^- \pi^-)$ are the efficiencies for signal and normalization channels. The relative branching fraction obtained is 1.7127 ± 0.0692 , which only includes statistical error from data, for the MC sample statistical error will be considered in the systematic uncertainty.

4.7 Systematic

Table 4.12 lists sources of systematic uncertainties that come from the relative yield and efficiency.

Table 4.12 Summary of systematic uncertainties, and for the relative branching fraction ratio in unit of %.

Source	BF Uncertainty (%)
Background fit model	0.93
Signal fit model	0.48
MC statistics	2.48
Trigger efficiency	0.09
PID efficiency	0.40
p_T, y reweight	0.78
nTracks reweight	0.84
Dalitz reweight	1.37
$\Lambda_c^+ \pi$ mass distribution	1.33
$\Lambda_c^+ K^+ K^-$ and $K^+ K^-$ mass distribution	2.62
Λ_b^0 IP smearing	0.09
Physical background	0.26
$\Lambda_b^0 \rightarrow \Lambda_c^+ K^+ K^- \pi^-$ in normalization channel	0.77
MC fraction estimation	0.17
Total	4.46

4.7.1 Background model

The choice of combinatorial background is motivated by the background shape in the high mass sideband. The second order polynomial function is used as an alternative model to study the systematic uncertainty due to the background model. We take the difference of the relative branching fraction as the uncertainty from this source, which is 0.93%.

4.7.2 Signal model

The nominal signal shape is described by two single-sided Crystal Ball function for both signal channel and also normalization channel. To estimate the systematic uncertainty due to the signal model, we use the Hypatia distribution as the alternative parameterization of the signal shape. For the signal shape, we float only the mean value and the width parameter, and

other parameters are fixed to MC. The projection plots are given in Figure 4.28. The change of relative branching fraction is 0.48%.

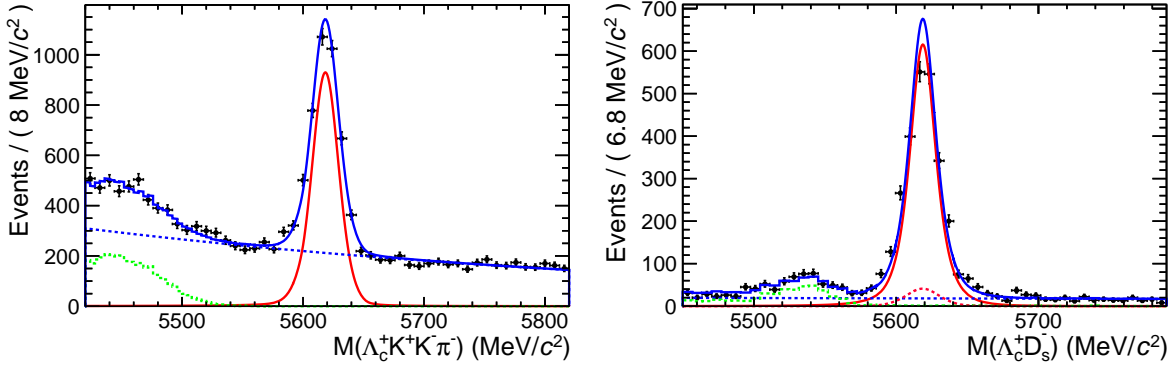


Figure 4.28 Invariant mass distributions for the $\Lambda_b^0 \rightarrow \Lambda_c^+ K^+ K^- \pi^-$ sample(left) and $\Lambda_b^0 \rightarrow \Lambda_c^+ D_s^-$ sample(right) with fit and residuals. The signal shape is described by Hypatia function and background shape is the nominal one. The blue line is full fit, the blue dashed line is the combinatorial background, the red line is the signal shape, the pink dashed line is $\Lambda_b^0 \rightarrow \Lambda_c^+ K^+ K^- \pi^-$ background.

4.7.3 MC statistics

The limited statistics of the simulated samples used to estimate efficiencies is considered as a source of systematic uncertainty, which can be calculated as the standard deviation of a binomial distribution:

$$\sigma_\epsilon = \sqrt{\epsilon(1 - \epsilon)/N} \quad (4.7)$$

where ϵ is the efficiency obtained from simulated events, and N stands for the total number of simulated events. This expression should be modified if each event has different weights, which is due to the reweight mentioned in Sec. 4.4.

The statistic uncertainty of ϵ is

$$\sigma_\epsilon = \frac{\sqrt{\sum_i \epsilon_i (1 - \epsilon_i) w_i^2}}{\sum_i w_i}, \quad (4.8)$$

where the w_i is the weight for every event. This uncertainty is about 2.48%.

4.7.4 p_T , y and nTracks reweight

The data and MC sample that we used to obtain the p_T , y and nTracks weights have finite statistic, which leads to an uncertainty of each single-event weight. A toy MC is used to propagate these uncertainties of single-event weights to the uncertainty of relative efficiency. For each toy experiment, all the weights are varied randomly according to their errors, then the

relative efficiency is evaluated. The toy tests result in a distribution of the relative efficiency, whose RMS is taken as uncertainty for the relative efficiencies. The systematic uncertainty is around 0.65% according to the toy study.

Another source of systematic uncertainty about the reweight is from the binning scheme of the weight table. We rebin the p_T , y table and calculate the relative efficiency of TOS lines again, the difference is taken as the systematic uncertainty of this source. The corresponding uncertainty is around 0.43%. The similar method is applied to the nTracks reweight, and the corresponding result is 0.84%.

4.7.5 Dalitz reweight

Toy experiments are used to study the uncertainty due the finite data and MC sample size. For each experiment, all the weights are varied randomly according to their errors, then the relative efficiency is evaluated. The toy tests result is a distribution of the relative efficiency, whose RMS is taken as uncertainty for the relative efficiencies. The estimated uncertainty is around 1.12%.

Another uncertainty source is the binning scheme of these two weight, we rebin the weight table randomly and recalculate the relative efficiencies, the difference between the new result and the default result as the systemic error from this source. This uncertainty is about 0.79%.

4.7.6 Trigger efficiency

The L0 Hardron TOS trigger efficiency is gained from efficiency tables, with error bar in every bin. We generate many similar table according to the value and error of bins, then the relative efficiency is evaluated. The toy tests result is a distribution, and we take the RMS as the uncertainty. This uncertainty is about 0.09%.

4.7.7 PID efficiency

The PID efficiency is obtained using a data driven method, and the finite statistic of the calibration samples leads to uncertainty of the PID efficiencies. The PIDCALIB package gives the 3-D histograms that shows the single-event PID efficiency as well as its uncertainty. A toy Monte Carlo method is applied to propagate these uncertainties to the average PID efficiency. The PID efficiencies of each tracks are set to be a random number with the Gaussian distribution $G(\epsilon_{PID}, \sigma_{PID})$, where ϵ_{PID} stands for the value of PID efficiency from PIDCALIB package, and σ_{PID} stands for the uncertainty. Due to lack of statistics in some bins of the efficiency tables.

PIDCALIB package sometimes gives unphysical efficiencies, which are smaller than zero, or larger than one. In the default treatment, we set negative PID efficiency as 0 and that larger than one as 1. So we estimate the systematic uncertainty of setting the larger 1 as 1. These efficiencies are replaced by uniform distribution random numbers ranged from 0 to 1. A new relative efficiencies are calculated with the same method and the differences are set to be the uncertainties.

Another source of systematic uncertainty about PID efficiency is from the binning scheme of the efficiency table, which is estimated by halve the bin size of momentum for all the particles. After this process, we find the relative efficiency get a negligible change, so we neglect this source here. The PID uncertainty is about 0.4%.

4.7.8 $\Lambda_c^+\pi$, K^+K^- and $\Lambda_c^+K^+K^-$ mass inconsistency and Λ_b^0 IP smearing

Figure. 4.24 and Figure. 4.25 show the comparison between some invariant mass distributions in data after background subtraction with the Splot technique and the MC sample generated by phase-space model. We see significant difference between data and the background subtracted data in the invariant mass distribution of $\Lambda_c^+\pi^-$. We apply a weight to the MC sample make it has same distribution with data sample in $\Lambda_c^+\pi$ spectrum. This uncertainty is about 1.33%.

Besides, we also find that the mass distributions of K^+K^- and $\Lambda_c^+K^+K^-$ are also inconsistent between the data and MC samples. In this case, we apply a weight to the MC sample according to the K^+K^- distribution, then to estimate the efficiency again, and this uncertainty is about 2.62%. Then we use the same method to estimate the effect from the $\Lambda_c^+K^+K^-$ inconsistency between the data and MC samples, and this uncertainty is about 2.03%. It is not reasonable to add these two uncertainties to the final results both, and we take the larger one as the uncertainty caused by the K^+K^- and $\Lambda_c^+K^+K^-$ distribution inconsistency.

We remove Λ_b^0 IP smearing and repeat all processes to recalculate the efficiency, and the difference are set to be the uncertainty. This uncertainty is about 0.09%.

4.7.9 Physical background effect

We change the mass region begins from 5500 MeV in $\Lambda_b^0 \rightarrow \Lambda_c^+K^+K^-\pi^-$ fitting to exclude the partial reconstructed background in the low mass sideband, and take the yield difference as one systematic uncertainty. This uncertainty is about 0.26%.

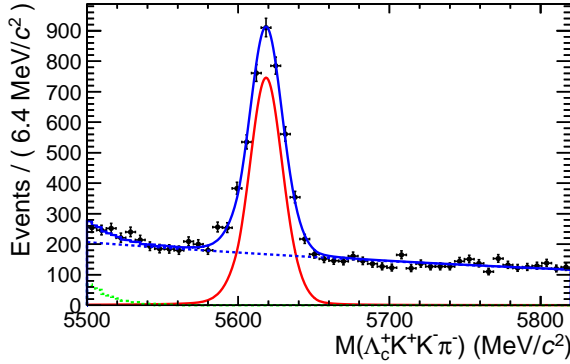


Figure 4.29 Invariant mass distributions for the $\Lambda_b^0 \rightarrow \Lambda_c^+ K^+ K^- \pi^-$ sample. The blue line is full fit, the blue dashed line is the combinatorial background, the red line is the signal shape.

4.7.10 $\Lambda_b^0 \rightarrow \Lambda_c^+ K^+ K^- \pi^-$ in normalization channel

When we estimate the yields of $\Lambda_b^0 \rightarrow \Lambda_c^+ D_s^-$, the number of $\Lambda_b^0 \rightarrow \Lambda_c^+ K^+ K^- \pi^-$ background is fixed to value obtained from sideband. In order to consider this uncertainty, we float the number of $\Lambda_b^0 \rightarrow \Lambda_c^+ K^+ K^- \pi^-$ within the margin of error and fit mass distribution again. The difference of the signal yield is considered as the systematic uncertainty. This uncertainty is about 0.77%.

4.7.11 Fraction of different MC sample

As we mixed three kinds of MC samples of $\Lambda_b^0 \rightarrow \Lambda_c^+ K^+ K^- \pi^-$ channel together to estimate the efficiency, and the fraction is obtained by fitting the two dimensional distributions of $K^+ K^- \pi^-$ and $K^+ \pi^-$. The fitting result is shown in the Figure. 4.23, and the corresponding numbers are listed in Tab. 4.10. Then we studied the effect of the fraction used in the $\Lambda_b^0 \rightarrow \Lambda_c^+ K^+ K^- \pi^-$ channel efficiency calculation. We change the number of different MC sample according to their errors independently, and recalculate the final efficiency, and find the corresponding uncertainties are 0.016%, 0.163% and 0.028%, this uncertainty is pretty small, and the total value is around 0.17%.

4.8 Conclusion

With the 3.0 fb^{-1} data collected in 2011 and 2012, an observation $\Lambda_b^0 \rightarrow \Lambda_c^+ K^+ K^- \pi^-$ decay channel has been performed. Taking $\Lambda_b^0 \rightarrow \Lambda_c^+ D_s^-$ as the normalization channel, the ratio of products of branching fraction and fragmentation fraction is measured to be

$$\frac{\mathcal{B}(\Lambda_b^0 \rightarrow \Lambda_c^+ K^+ K^- \pi^-)}{\mathcal{B}(\Lambda_b^0 \rightarrow \Lambda_c^+ D_s^-; D_s^- \rightarrow K^+ K^- \pi^-)} = 1.71 \pm 0.069 \text{ (stat)} \pm 0.077 \text{ (syst)}. \quad (4.9)$$

Including the branching fraction of $\mathcal{B}(D_s^- \rightarrow K^+ K^- \pi^-) = (5.45 \pm 0.17)\%$ from PDG, we can obtain the ratio of branching fraction between $\Lambda_b^0 \rightarrow \Lambda_c^+ K^+ K^- \pi^-$ and $\Lambda_b^0 \rightarrow \Lambda_c^+ D_s^-$:

$$\frac{\mathcal{B}(\Lambda_b^0 \rightarrow \Lambda_c^+ K^+ K^- \pi^-)}{\mathcal{B}(\Lambda_b^0 \rightarrow \Lambda_c^+ D_s^-)} = (9.33 \pm 0.38 \text{ (stat)} \pm 0.42 \text{ (syst)} \pm 0.29(\mathcal{B})) \times 10^{-2}, \quad (4.10)$$

where the uncertainties are statistical, systematic and systematic due to uncertainty of $\mathcal{B}(D_s^- \rightarrow K^+ K^- \pi^-)$.

The predicted pentaquark can be checked in the $\Lambda_c^+ K^+$ mass spectrum^[99]. Figure. 4.24 shows the invariant mass distribution of $\Lambda_c^+ \pi^-$, obtained with the background subtracted data. There is no significant peak in this distribution. Besides, there is no clear sign of Ξ_c from the invariant mass distribution of $\Lambda_c^+ K^-$.

Chapter 5 ECAL simualtion study for Upgrade II

5.1 Introduction

It is generally agreed within the LHCb collaboration and the community of flavour physics that an upgrade of the LHCb detector to make full exploitation of the High-Luminosity LHC (HLLHC), which provides an opportunity to investigate the open questions in flavour physics^[83,84,131]. This proposed upgrade is referred to as the LHCb Upgrade II, which should be capable of taking data at an instantaneous luminosity of up to $1.5 \times 10^{34} \text{ cm}^{-2} \cdot \text{sec}^{-1}$. The goal is to collect a data sample of an integrated luminosity of 300 fb^{-1} after Run 6^[84]. Among the biggest challenges for the Upgrade are the large number of proton-proton interactions in a single bunch crossing (pile-up) and the large amount of radiation that the detector has to tolerate.

The present ECAL has good performance with run1 and run2 luminosity. There is not a certaiy answer if it can handle a very high luminosity, it is necessary to take a look at the performance of current ECAL with high luminosity in the parameterized simulation first. From the parameterized simulaiton, the possible methods are studied to optimize the detector and let it conquer the pile-up effect. There are many factors that could affect the ECAL performance, like intrinsic energy resolution and so on. By improving these factors, the performance of ECAL might be promoted. Besides, it is commonly agreed that high precision time information is needed to deal with the pile-up, which is the major item studied in the simulation. And high granularity is another requirement for the Upgrade ECAL, which can greatly help reducing the occupancy due to the high luminosity.

For the calorimeter, the main idea is that it should allow for the reconstruction and analyses of the decay modes involving neutral particles. This chapter will discuss the requirements to ECAL for Upgrade II in the parameterized simulation first. A detailed silicon-tungsten (SiW) ECAL is discussed then, *i.e.* a sampling ECAL with silicon as the active material and tungsten as the absorbers.

5.2 Parameterized simulation

The parameterized simulation tool is developed to study the requirements to ECAL for Upgrade II with pretty high instananeus lominosity. This tool is based on GAUSS^[73] and

DELPHES^[135], GAUSS^[i]s used to produce generated level sample with different eventtypes ① and DELPHES is used to run detector simulation by parameterized way. Actually, the DELPHES does not have appropriate module easily used for ECAL simulation for LHCb, since the default geometry of calorimeter in DELPHES is bucket, while the geometry of ECAL at LHCb is a plane. Therefore, new parameterized simulation modules for LHCb is developed first. Then, the specific decay channels are reconstructed using the output from parameterized simulation. Finally, these simulation samples are analyzed. The frame to achieve the parameterized simulation for ECAL is shown in Figure. 5.1

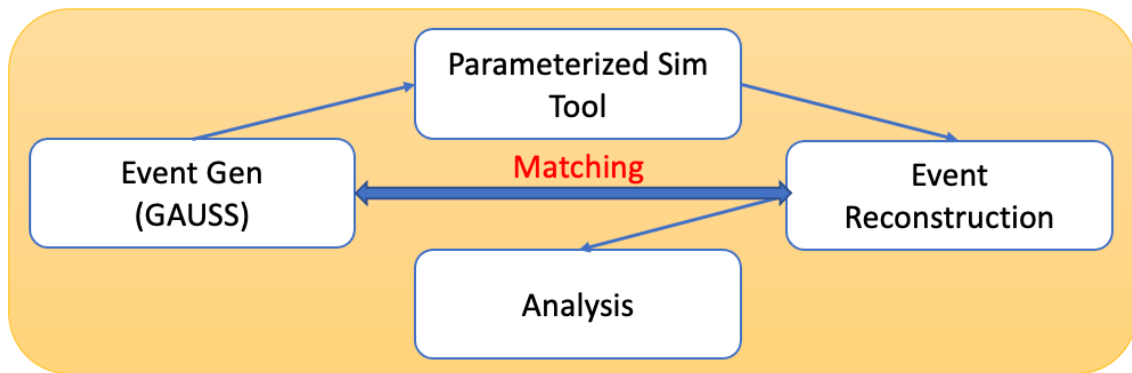


Figure 5.1 The simulation process in the parameterized simulation.

5.2.1 Parameterization of shower

A method to achieve parameterized simulation is introduced below briefly. The particles like photon or electron will transform into electromagnetic showers in ECAL, which are consisted of many electrons or photons. Two processes, photon pair production and electron bremsstrahlung, continue with the shower development until photons fall below the pair production threshold. Then mean longitudinal profile of the energy deposition in electromagnetic cascade can be described by this formula obtained from beam test^[104]:

$$F(x, y, f, \sigma, R) = \frac{f}{2\pi\sigma} e^{-\frac{x^2+y^2}{2\sigma^2}} + \frac{1-f}{2\pi} \frac{2R^2}{(x^2 + y^2 + z^2)^2} \quad (5.1)$$

where the first part is used to describe the tail of shower, and the second part to describe the main section. The parameters used can be obtained from the beam test, like σ , f and R . Above formula is utilized to distribute the energy of entering particle to the corresponding cells. In the parameterized simulation tool, the length of the cascade shape is not considered.

Next step is to smear the deposited energy in the cell, the parameterized energy resolution

① Different eventtypes present different decay channels.

formula is used:

$$\frac{\sigma}{E} = \frac{\alpha}{\sqrt{E}} \oplus \beta \quad (5.2)$$

where α is roughly equal to 10% and β is approximately equal to 1% for the current shashlik ECAL, as mentioned in Section 2.2.2. After Upgrade II at LHCb, the measuring unit of ECAL will have the ability to record precision time information, the time resolution is a given value in this simulation tool, it is convenient to set this value in the configuration file.

5.2.2 Reconstruction and calibration

The reconstruction method in the parameterized simulation tool follows the one utilized in the current shashlik ECAL, which is named as cellular automaton algorithm^[57,76]. This method is processed based on the seed cell, which has a local maximum energy. In this tool, the clusters are determined by the algorithm mentioned above, and reconstructed using 3×3 cells, the energy and position are calculated as:

$$\begin{aligned} E &= \sum_i^{cells} E_i \\ x_c &= (\sum_i^{cells} x_i \times E_i) / E \\ y_c &= (\sum_i^{cells} y_i \times E_i) / E \\ z_c &= z_i \\ t_c &= (\sum_i^{cells} t_i \times E_i) / E \end{aligned} \quad (5.3)$$

where the subscript i represents the cell belonging to the corresponding cluster.

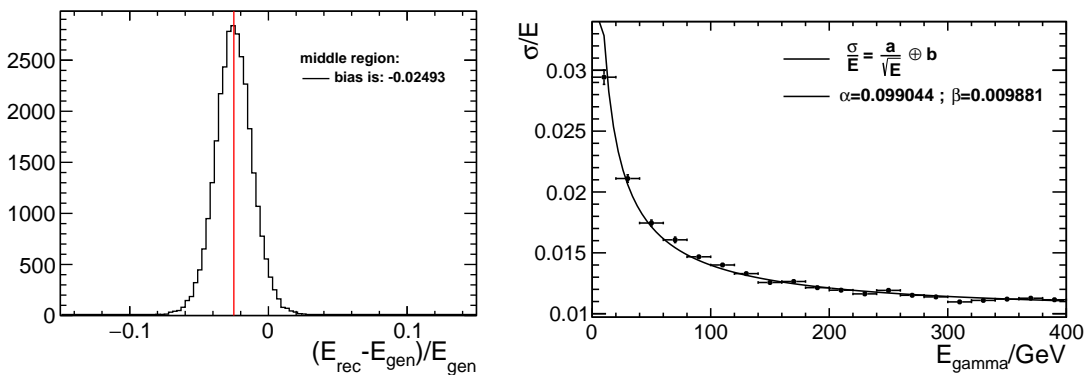


Figure 5.2 The difference between the reconstructed energy and generated level energy (left), and the relation between the energy resolution and particle energy after calibration (right).

In this tool, the calibration to the reconstructed variables are also imported. The energy need to be recalculated by multiplying with a factor due the energy leaking effect. The bias between the reconstructed energy and generated energy is shown in left of Figure. ???. In addition, the calibration to the position is achieved by using a correction formula:

$$x_{cali} = f \times b \times \text{asinh}\left(\frac{x_{rec}}{\Delta} \cosh \frac{\Delta}{b}\right) \quad (5.4)$$

where the x_{cali} is the x-coordinate in the frame of seed cell, x_{rec} the position obtained from Equation. 5.3, and other variables are calibration parameters. The performance of position calibration is shown in the Figure. ???, which is in the case of cell size equal to 6.06 cm. By the way, the calibration need to be applied indepently to the sample using different cell size.

To verify the credibility of this method, the energy resolution is checked by γ gun events, as shown in the right of Figure. 5.2, which is consistent to the performance of current ECAL.

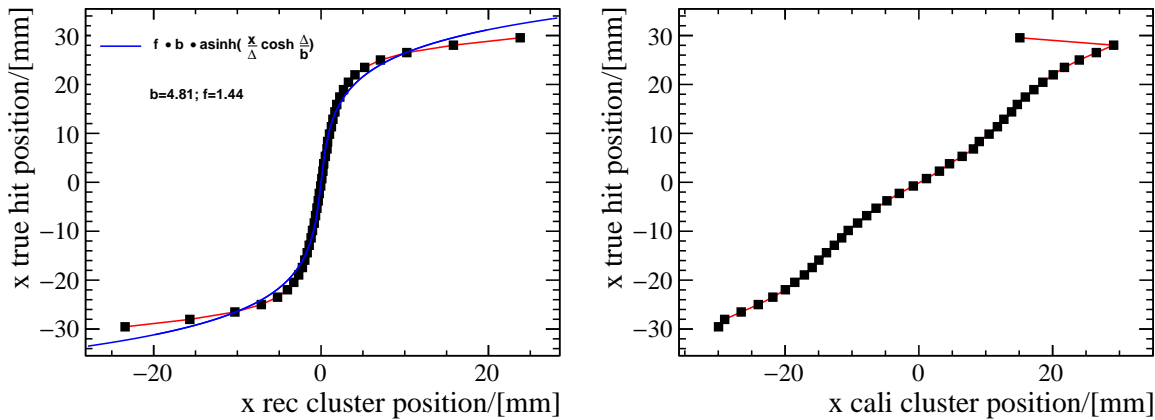


Figure 5.3 The relation between the true position and reconstructed position before (left) and after (right) calibration.

5.2.3 Neutral particle identification

5.2.3.1 Removal of charged particles

Some charged particles can also deposit energy in ECAL, we can removed this effect by an anti-coincidence between the cluster ($E_T > 250$ MeV) position and the extrapolation of the reconstructed tracks ($p_T > 150$ MeV) up to the calorimeter. The distance between the reconstructed cluster and the nearest tracks is calculated, if the position resolution of tracks is overlooked, the required distance is larged than half of the cell size. If the futher trackers and ECAL both have ability to record precision time, the time matching between track arrival time and shower reconstructed time can also help to identify the cluster arised from charged

particle.

5.2.3.2 Characteristics of γ, π^0 and overlapping cluster

γ/π^0 seperation is an important prerequisite for many physics analysis^[62]. Many photons detected by the ECAL are originated from π^0 decays. Two photons of the π^0 has possibility to be reconstructed as one cluster due to the granularity, especially for the π^0 with pretty large momentum, as shown in the Figure. 5.4. If the distance between 2γ decayed from the π^0 in the ECAL plane is large enough, the π^0 can be reconstructed as resolved one, otherwise, it will be reconstructed as merged particle, which means the showers from the 2γ are overlapping together.

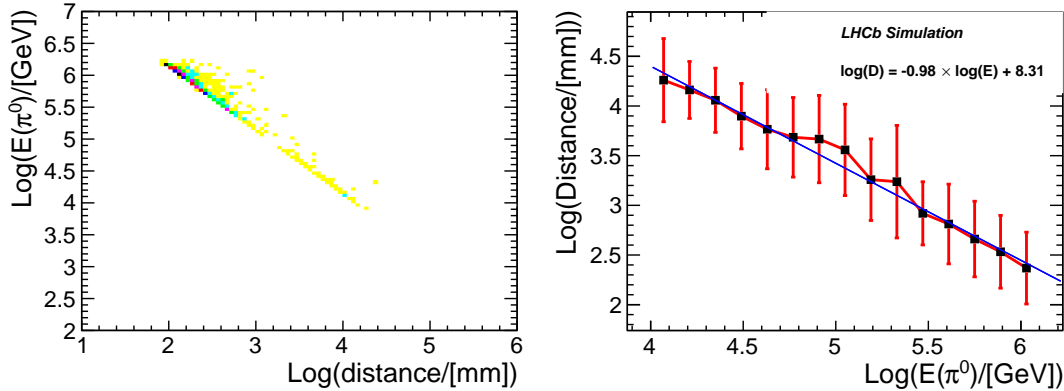


Figure 5.4 The relation between the π^0 energy and the distance of two γ on the ECAL plane.

As the luminosity will become pretty high after Upgrade II, it is possible to increase the chances of overlapping clusters. And beyond that, Identifying the random overlapping cluster is another important task.

The method for γ, π^0 and overlapping cluster seperation is based on the shape of cluster. As the timing information will be recorded after Upgrade II, it also has possibility to seperate the clusters from different sources. The position spread matrix elements are defined as:

$$\begin{aligned} S_{XX} &= \frac{\sum_{i=1}^N E_i (x_i - x_c)^2}{\sum_{i=1}^N E_i} \\ S_{YY} &= \frac{\sum_{i=1}^N E_i (y_i - y_c)^2}{\sum_{i=1}^N E_i} \\ S_{XY} &= \frac{\sum_{i=1}^N E_i (x_i - x_c)(y_i - y_c)}{\sum_{i=1}^N E_i} \end{aligned} \quad (5.5)$$

where (x_c, y_c) is the position of the cluster, as defined in Equation 5.3, and (x_i, y_i) is the position of used cell for a given cluster of N cells. In this simualtion, seven separation variables are

constructed including timing information:

- The size of the cluster, also explained as second order of moments, referred to as $r2$:

$$r2 = \langle r^2 \rangle = S_{XX} + S_{YY} \quad (5.6)$$

- The importance of the tails, referred to as $r2r4$:

$$r2r4 = 1 - \frac{\langle r^2 \rangle^2}{\langle r^4 \rangle} \quad (5.7)$$

- Ratio of the eigenvalues of the matrix S :

$$\kappa = \sqrt{1 - 4 \frac{S_{XX}S_{YY} - S_{XY}^2}{(S_{XX} + S_{YY})^2}} \quad (5.8)$$

- The orientation of the correlation between X and Y coordinates, referred to as $asym$:

$$asym = \frac{S_{XY}}{\sqrt{S_{XX}S_{YY}}} \quad (5.9)$$

- The energy fraction of the seed cell in the cluster:

$$E_{seed}/E_{cluster} \quad (5.10)$$

- The second order of moments about timing information, referred to as $t2$:

$$t2 = \langle t^2 \rangle = \frac{\sum_{i=1}^N E_i(t_i - t_c)^2}{\sum_{i=1}^N E_i} \quad (5.11)$$

- The importance of the tails of timing, referred to as $t2t4$:

$$t2t4 = 1 - \frac{\langle t^2 \rangle^2}{\langle t^4 \rangle} \quad (5.12)$$

The variables constructed above are taken as input for the multi-variable analysis tool, several methods are compared, and the BDTG is taken as the default training algorithm.

5.2.3.3 γ, π^0 and overlapping cluster separation

The discriminant variables introduced above are taken as input for Multivariate Analysis (TMVA)^[97]. Photons in LHCb acceptance with $E \in [10, 400]$ GeV events are taken as signal sample (EventType=56000400). The π^0 particle gun decaying to two γ events are generated used for the merged π^0 sample (EventType==56200100). Furthermore, the random overlapping cluster sample is created base on the gamma gun events, with a gamma particle is inserted in the generated level. The energy of accompanying gamma with the exponential distribution, with the mean value equal to 10 GeV, which is estimated from the minimum bias sample. The generated position and time of this accompanying gamma follow the character of primary vertex

distribution. Besides, $E_T > 250$ MeV is applied to all γ candidates before being imported in the TMVA tool. Considering the energy scale of γ and π^0 is different, $E < 200$ GeV is also applied to γ and random overlapping samples.

Discrimination between γ and merged π^0 is studied first. Figure. 5.5 shows these discriminant variables used in the multivariable analysis, while Figure. 5.6 shows the distribution of BDTG, and no overtraining effect appears from this test. The receiver operating characteristic curve (ROC) is shown in Figure. 5.7, the left one is obtained with 8 discriminant variables are included, while the one shows the performance with only 6 variables (no $t2$ and $t2t4$). According to these plots, the timing information does not contribute much on the γ and merged π^0 separation.

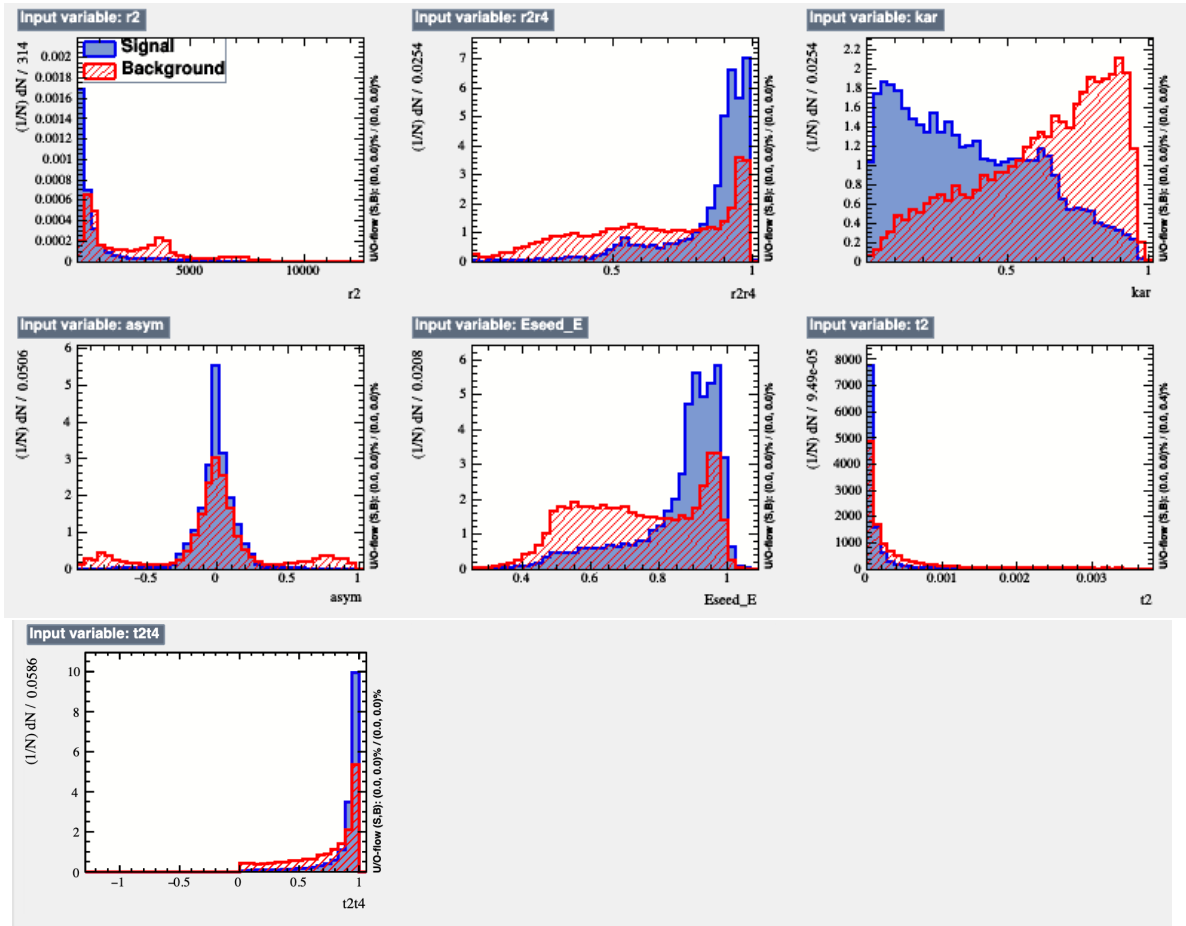


Figure 5.5 The distribution of discriminant variables used for cluster identification.

Another tests are performed to identify the single γ and merged π^0 from random overlapping clusters. Figure. 5.8 shows the identification ability between the pure γ and contaminated one, from this plot, it is found that the timing information plays a important role for this separation. Similar check is also performed on the merged π^0 and random overlapping cluster

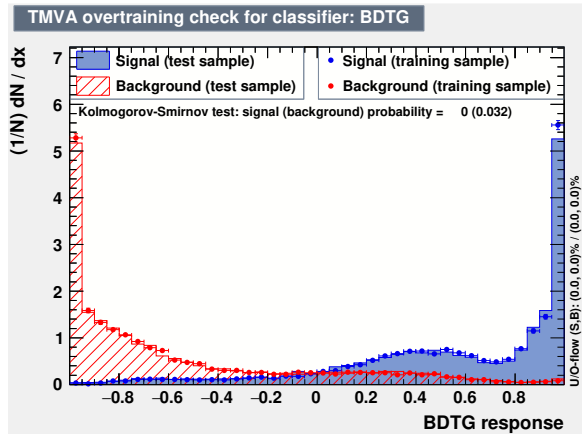


Figure 5.6 The distribution of BDTG of the signal sample (γ) and background sample (merged π^0).

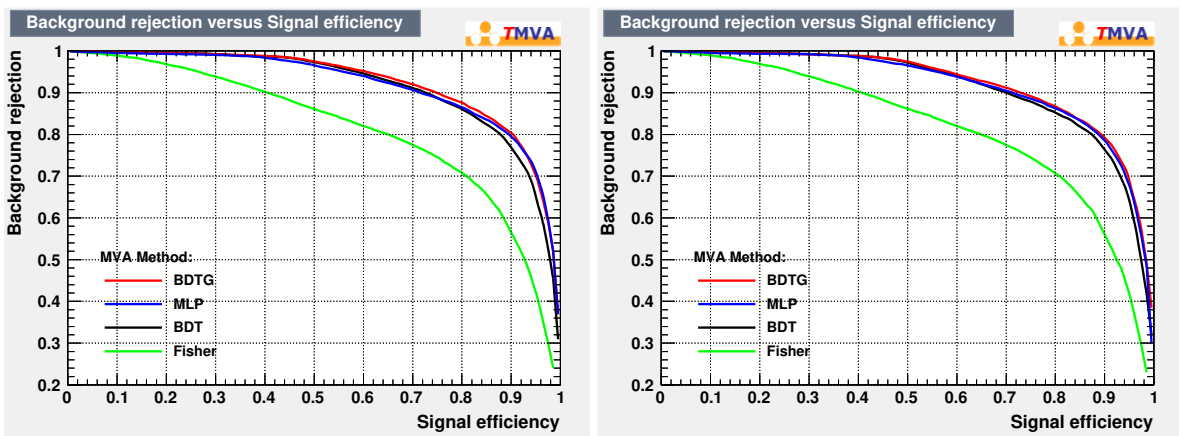


Figure 5.7 Performance of different methods used on the simulation samples. The left one presents the performance of γ and π^0 separation with the timing information included, right one with the timing information excluded.

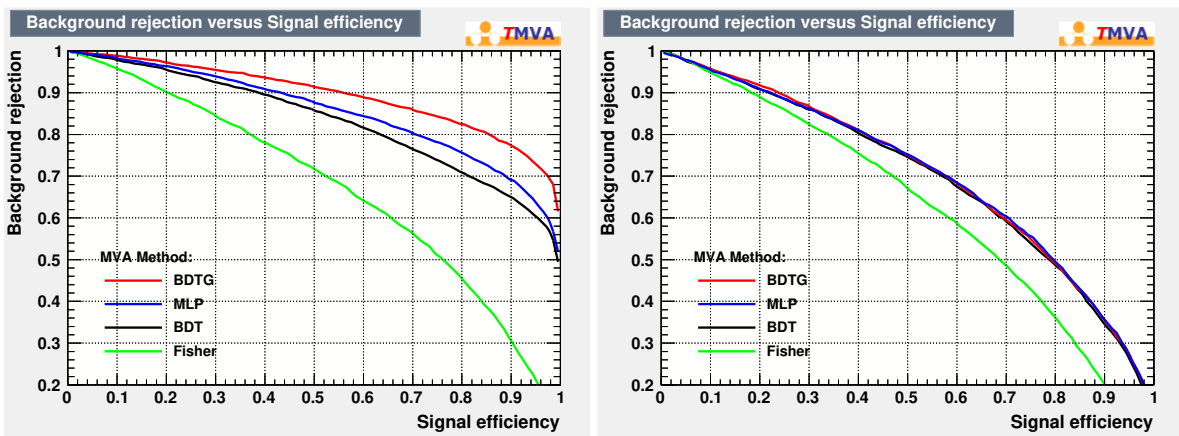


Figure 5.8 Performance of different methods used on the simulation samples. The left one presents the performance of γ and random overlapping cluster separation with the timing information included, right one with the timing information excluded.

samples, the result is shown in the Figure. 5.9. It is obvious that BDTG method has a good

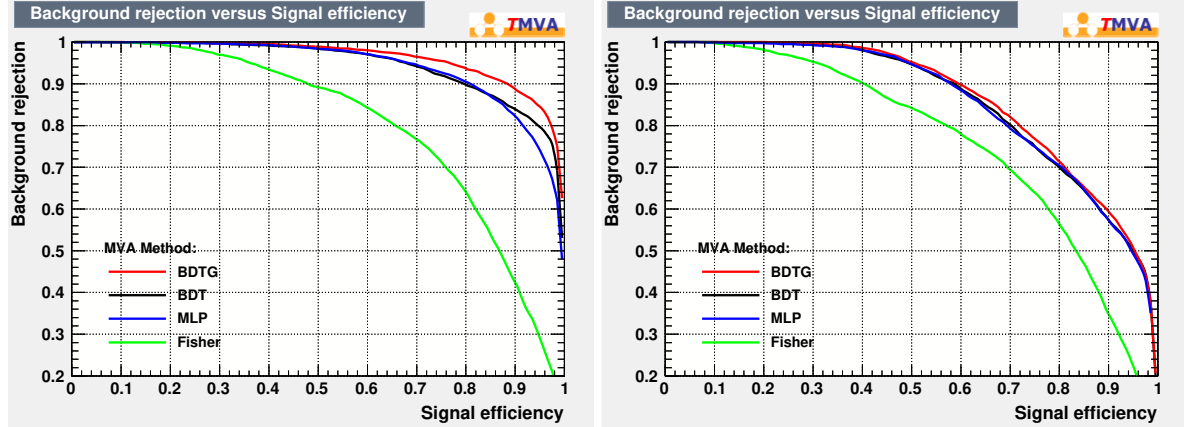


Figure 5.9 Performance of different methods used on the simulation samples. The left one presents the performance of π^0 and random overlapping cluster separation with the timing information included, right one with the timing information excluded.

Table 5.1 Identification variables and corresponding functions.

Variables	function
PID_g_piz	Is a pure γ rather than a merged π^0
PID_g_conta	Is a pure γ without contamination
PID_piz_conta	Is a merged π^0 without contamination
Dis_charge	Is a neutral particle rather than coming from charged track

performance, three different variables are constructed to identify reconstructed cluster based on BDTG, as listed in Table. 5.1

5.2.4 Performance in $B_s^0 \rightarrow \phi\gamma$ decay

The decay channel of $B_s^0 \rightarrow \phi\gamma$ is studied with different ECAL cell size configuration or luminosity condition. In the reconstruction, the ϕ particle information is obtained from generated samples. Thus, the final performance is only related to the different configuration of ECAL in simulation. Table. 5.2 lists all selections used in this channel reconstruction, the transverse energy of reconstructed gamma is larger than 2600 MeV and the transverse of the B_s^0 candidates greater than 3000 MeV. Table. 5.2 lists the selection applied to the simulation samples, we name them basic selections here.

Table 5.2 Selection criteria in $B_s^0 \rightarrow \phi\gamma$ channel.

Quantity	Selections
p_T of γ	> 2.6 GeV
p_T of B_s^0	> 3.0 GeV

5.2.4.1 Luminosity effect

As mentioned above, the luminosity will increase markedly after Upgrade II, the physical performances in this channel with different luminosities are studied first. 20000 simulation samples for each luminosities were generated by this parameterized simulation tool, and by the way, the current ECAL cell segmentation is used for these samples. Figure. 5.10 shows the $\phi\gamma$ invariant mass distribution with different luminosities. $\mathcal{L} = 4 \times 10^{32} \text{ cm}^{-2} \text{ s}^{-1}$ is the instantaneous luminosity during Run 1 and Run 2 at LHCb, and this value can reach up to $\mathcal{L} = 1.5 \times 10^{34} \text{ cm}^{-2} \cdot \text{s}^{-1}$ after Upgrade II. Two other luminosity cases are also studied, since the instantaneous luminosity descends as time goes by in one beam injection,

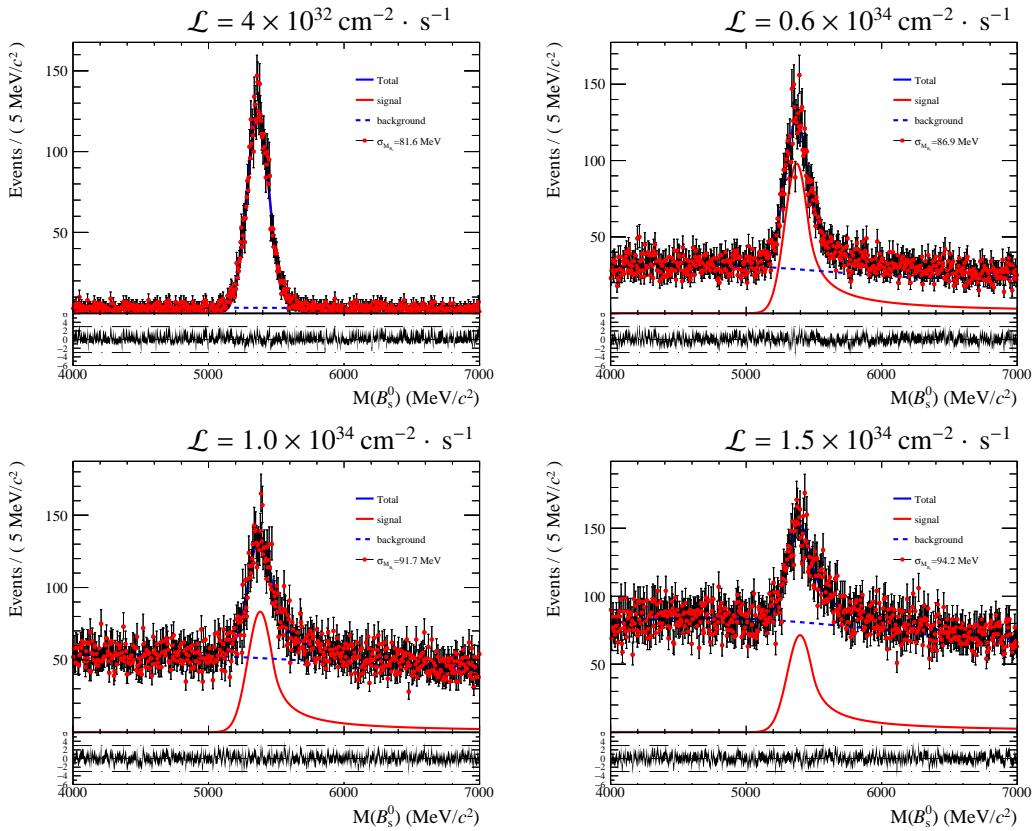


Figure 5.10 The mass distribution of B_s^0 in $B_s^0 \rightarrow \phi\gamma$ decay with different luminosities.

The yields of signal and background are estimated by fitting the mass distribution for each sample, where the crystal ball function is used to describe the shape of signal and the background is described 3 order chebyshev polynomial function. The fitting results are listed in Table. 5.3. Comparing these four plots, the distinguishing feature is that the yields of combinatorial background increases rapidly along with the increase of luminosity, and we found that this increase is linear roughly. In addition, the significance is diminished due to the high-background. By the way, the significance is defined as $S/\sqrt{S+5B}$ here. The background

yield is multiplied with a factor of 5 as this value is underestimated from simulation sample, and this factor was obtained by comparing to previous study^[5].

Besides, the mass resolution of B_s^0 becomes larger with luminosity increased. Most clearly, a long tail appears in B_s^0 mass distribution in high luminosity case due to overlapping effect. Thus, we need to improve the properties of ECAL to meet these challenges.

5.2.4.2 Smaller cell size to remove overlapping effect

In order to remove the overlapping clusters, two other cell size segmentations are studied in parameterized simulation. The first one is designed according to the rediation⁽²⁾, as shown in Figure. 5.11. The other one is very high granularity silicon-tungsten ECAL, all cells are squares with width equal to 1 cm, as shown in Figure. 5.18.

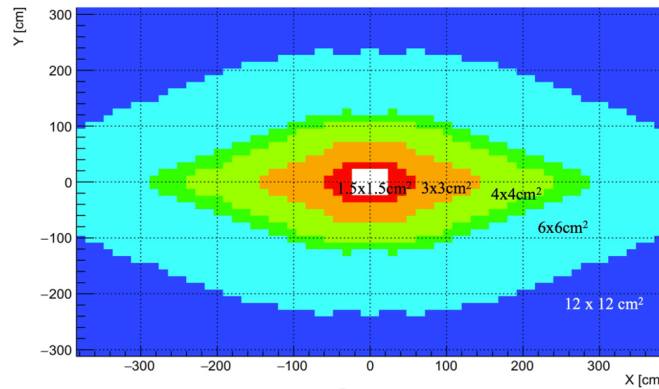


Figure 5.11 The diagram of ECAL cell size segmentation proposed by Phillip Roloff for LHCb.

In these parameterized simulations, the energy resolution of Phillip's segmentation is set to be $\sigma(E)/E = 0.1/\sqrt{E} \oplus 0.024$ ⁽³⁾, while the energy resolution of Si-W ECAL is $\sigma(E)/E = 0.2/\sqrt{E} \oplus 0.007$ ⁽⁴⁾. All results with different simulation configurations are summarized in Table. 5.3. According to these simulation samples, we find that the reconstruction efficiencies do not change significantly. The significance of smaller cell size is a little better than the value obtained from current segmentation. Most obviously, the number of background candidates becomes larger with higher luminosity.

5.2.4.3 Precision timing to remove pile-up effect

The surge of combinatorial background comes from pile-up effect in high luminosity situation. In order to remove this kind of background candidates, the time information is

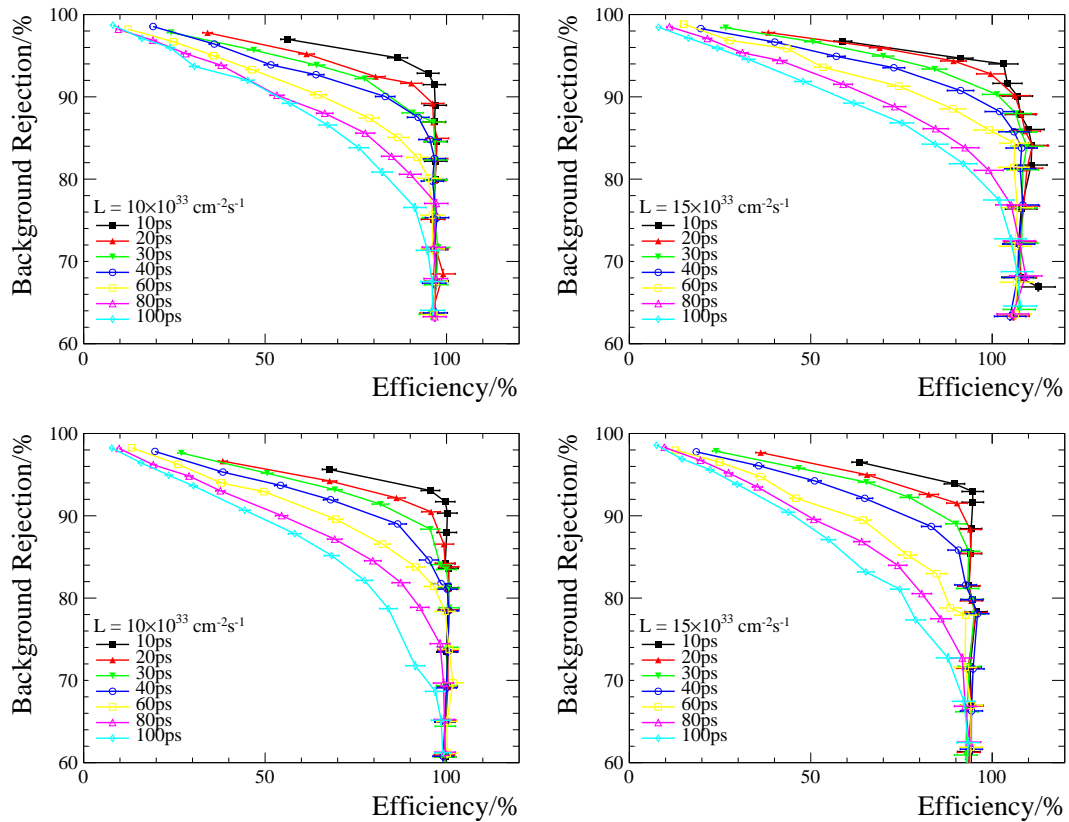
(2) This configuration was proposed by Philipp Roloff for LHCb.

(3) According to GEANT4 simulation of spaghetti ECAL from other colleagues in LHCb.

(4) Obtained from GEANT4 simulation of Si-W, details are shown in next section.

Table 5.3 The physical performance in different luminosities with different ECAL cell segmentation.

Segmentation	Luminosity ($\text{cm}^{-2} \cdot \text{s}^{-1}$)	Efficiency	Bkg ($\times 1000$)	Significance	Mass resolution (MeV)
Current	4×10^{32}	0.25	1.9	62	82
	0.6×10^{34}	0.23	16.6	33	87
	1.0×10^{34}	0.21	29.8	23	92
	1.5×10^{34}	0.19	46.7	17	94
Phillip's	4×10^{32}	0.25	1.6	61	109
	0.6×10^{34}	0.23	13.9	33	104
	1.0×10^{34}	0.21	22.4	24	105
	1.5×10^{34}	0.21	31.1	22	105
Si-W	4×10^{32}	0.28	1.8	62	89
	0.6×10^{34}	0.27	15.5	38	90
	1.0×10^{34}	0.27	22.8	35	85
	1.5×10^{34}	0.24	30.2	27	88

Figure 5.12 The relation between signal efficiency and combinatorial background rejection fraction with different Δt cuts applied, in Phillip's segmentation (top) and Si-W segmentation (bottom) respectively.

used to distinguish the primary vertices. Considering the ECAL can record the precision time information, the shower time reconstructed from ECAL is named as t_1 . Assuming the further VELO at LHCb has ability to detect the vertex time, named as t_2 . The time difference between

the shower and vertex can be obtained as $\Delta t = t_1 - t_2 - l/c$, where l/c represents the γ flight time. In current simulation, the time resolution of vertex is overlooked and the ECAL time resolution is given value. In this way, we can study the requirement of ECAL time resolution.

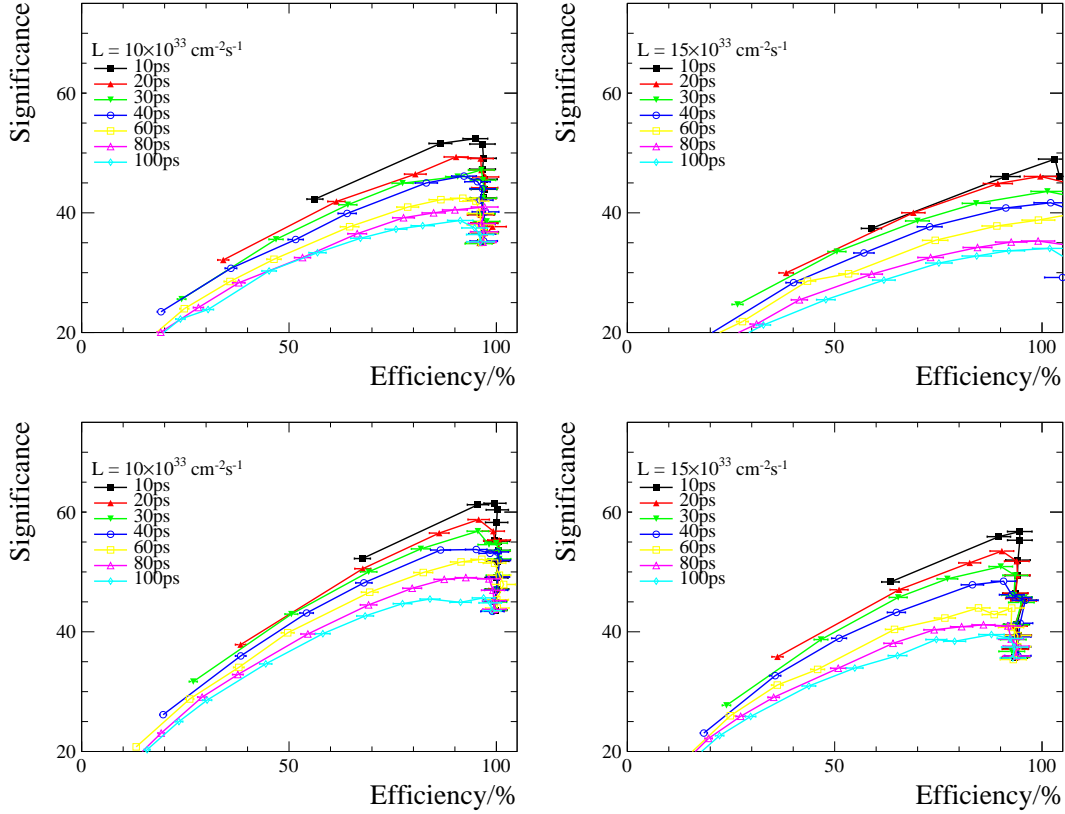


Figure 5.13 The relation between signal efficiency and significance with different Δt cuts applied, in Phillip's segmentation (top) and Si-W segmentation (bottom) respectively.

The performances of this additional selection value Δt in this decay channel is studied then. The relation between selection efficiency and background rejection fraction after time matching applied with different time resolutions is shown in Figure. 5.12. It is clearly that most of combinatorial background candidates can be removed with the time resolution equal to tens of picosecond for both cell size segmentation. The signal significance of 20000 events simulation sample was also studied, as shown in Figure. 5.13. Based on the research described above, there is not a big challenge for this channel reconstruction in high luminosity situation, tens of picosecond can help to reject most of combinatorial background candidates due to high pile-up effect. Both Phillip's segmentation and Si-W segmentation have good performances. Nevertheless, we need to keep in mind that this channel can be studied during Run 1 and Run 2 at LHCb, the mentioned requirements to ECAL for this channel cannot expand study scope at LHCb.

5.2.5 Performance in $B_s^0 \rightarrow J/\psi\pi^0$ decay

Another interesting decay channel is $B_s^0 \rightarrow J/\psi\pi^0$, which has not been observed yet. Besides, the channel $B^0 \rightarrow J/\psi\pi^0$ has similar topology to this one, we can estimate the both channel together using same simulation samples for this pre-study. The decay channel of $B_s^0 \rightarrow J/\psi\pi^0$ is studied with different ECAL cell size configuration or luminosity condition. Similar to the $B_s^0 \rightarrow \phi\gamma$ decay study, J/ψ information is obtained from generated samples. Table. 5.4 lists all selections used in this channel reconstruction, the transverse energy of reconstructed gamma is larger than 0.5 GeV and the transverse of the π^0 candidates greater than 2 GeV. Besides, the π^0 candidates with mass in 2.5σ of π^0 mass resolution are used to reconstruct B_s^0 . In addition, the transverse energy of B_s^0 is required to be larger than 2 GeV.

Table 5.4 Selection criteria in $B_s^0 \rightarrow J/\psi\pi^0$ channel.

Quantity	Selections
p_T of γ	> 0.5 GeV
p_T of π^0	> 2 GeV
mass window of π^0	$2.5\sigma_M$
p_T of B_s^0	> 2.0 GeV

5.2.5.1 Luminosity effect

The physical performances in this channel with different luminosities are studied first. 20000 simulation samples for each luminosities were generated by this parameterized simulation tool. Figure. 5.14 shows the $J/\psi\pi^0$ invariant mass distribution with different luminosities. The yields of signal and background are estimated by fitting the mass distribution for each sample, where the gaussian function is used to describe the shape of signal and the background is described 2 order chebyshev polynomial function. The fitting results are listed in Table. 5.5. This channel is different from $B_s^0 \rightarrow \phi\gamma$, the number of background candidates grows even faster as luminosity increases, especially in the $\mathcal{L} = 1.5 \times 10^{34} \text{ cm}^{-2} \cdot \text{s}^{-1}$ case. The reason is that two γ candidates are used in reconstruction for this channel, and average energy of γ in this channel is usually smaller than the value in $B_s^0 \rightarrow \phi\gamma$ decay. By the way, the significance is defined as $S/\sqrt{S + 20B}$ here. The background yield is multiplied with a factor of 20⁽⁵⁾ as this value is underestimated from signal simulation sample.

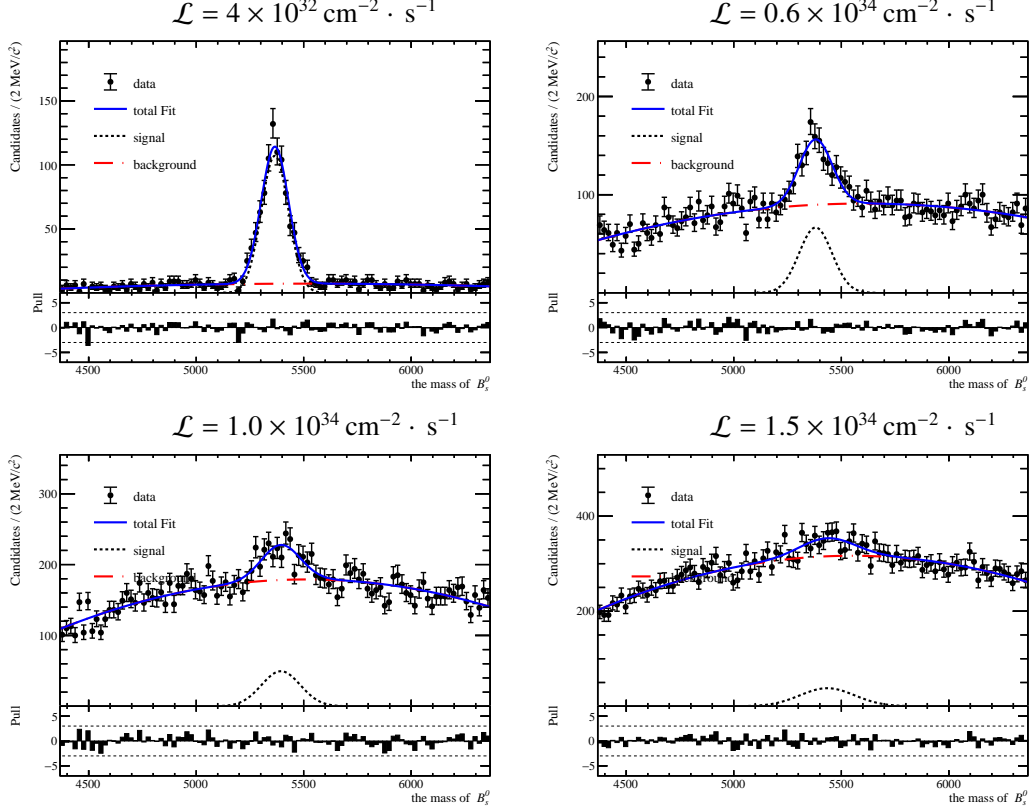


Figure 5.14 The mass distribution of B_s^0 in $B_s^0 \rightarrow J/\psi\pi^0$ decay with different luminosities.

Table 5.5 The physical performance in different luminosities with different ECAL cell segmentation.

Segmentation	Luminosity ($\text{cm}^{-2} \cdot \text{s}^{-1}$)	Efficiency	Bkg ($\times 1000$)	Significance	Mass resolution (MeV)
Current	4×10^{32}	0.042	0.6	15	63
	0.6×10^{34}	0.032	8.1	3	77
	1.0×10^{34}	0.028	16.0	2	90
	1.5×10^{34}	—	—	—	—
Phillip's	4×10^{32}	0.071	0.7	21	65
	0.6×10^{34}	0.059	7.5	7	68
	1.0×10^{34}	0.059	13.0	5	70
	1.5×10^{34}	0.039	21.7	3	64
Si-W	4×10^{32}	0.168	1.3	34	82
	0.6×10^{34}	0.153	12.4	13	77
	1.0×10^{34}	0.147	21.1	9	79
	1.5×10^{34}	0.137	33.7	7	77

5.2.5.2 Smaller cell size to improve the reconstruction efficiency

Similar to the study of $B_s^0 \rightarrow \phi\gamma$ decay, all results with different simulation configurations are summarized in Table. 5.5. According to these simulation samples, we find that the recon-

⑤ The factor of 20 is obtained from internal $B^0 \rightarrow J/\psi\pi^0$ analysis at LHCb.

struction efficiencies change significantly, which is much different from the decay of $B_s^0 \rightarrow \phi\gamma$. The signal reconstruction efficiency of Si-W small cell size segmentation is around 4 times larger than the number of current ECAL segmentation. Besides, the number of background candidates are pretty large in high luminosity situation for each case. There is no chance to study this channel if the combinatorial background candidates cannot be rejected.

5.2.5.3 Precision timing to remove pile-up effect

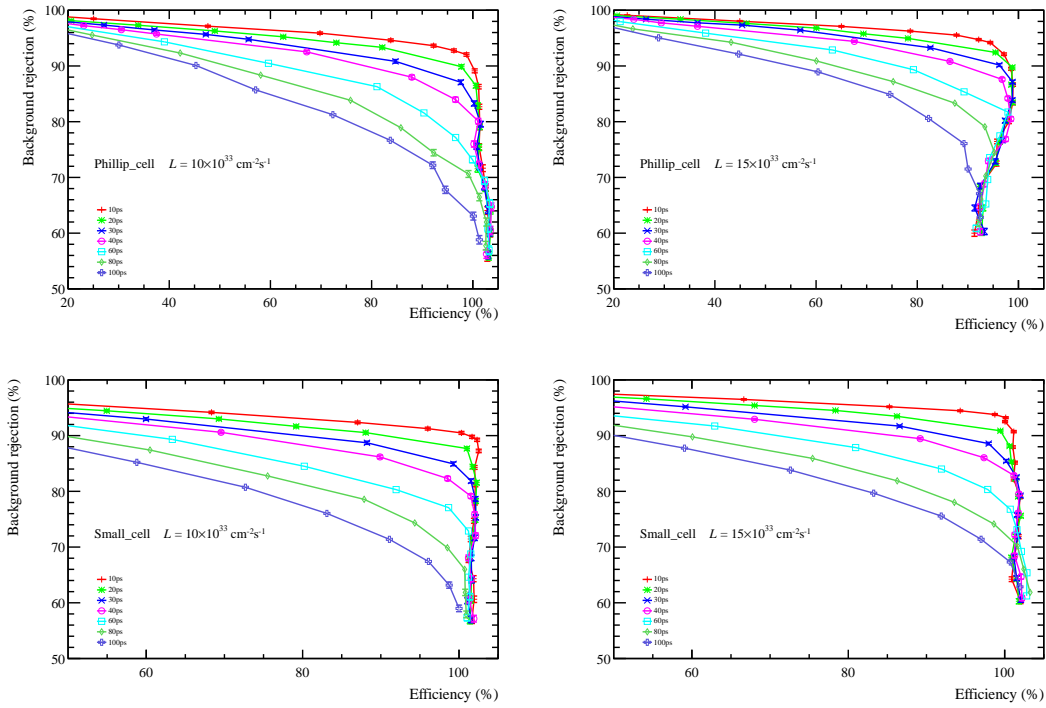


Figure 5.15 The relation between signal efficiency and combinatorial background rejection fraction with different $R(t)$ cuts applied, in Phillip's segmentation (top) and Si-W segmentation (bottom) respectively.

High luminosity leads to a pretty high combinatorial background level. In order to remove this kind of background candidates, the time information is used to distinguish the primary vertices. Unlike the $B_s^0 \rightarrow \phi\gamma$, two γ are used in this channel reconstruction. A new variable $R(t)$ is used to reject background candidates, which is defined as $R(t) = \sqrt{\Delta(t_1)^2 + \Delta(t_2)^2}$, where the $\Delta(t_1)$ is the difference between the J/ψ vertex time and expected γ generated time measured by ECAL, $\Delta(t_2)$ denotes the time difference of the other γ .

The performances of this additional selection value $R(t)$ in this decay channel is studied then. The relation between selection efficiency and background rejection fraction after time matching applied with different time resolutions is shown in Figure 5.15. It is clearly that most of combinatorial background candidates can be removed with the time resolution equal to tens of

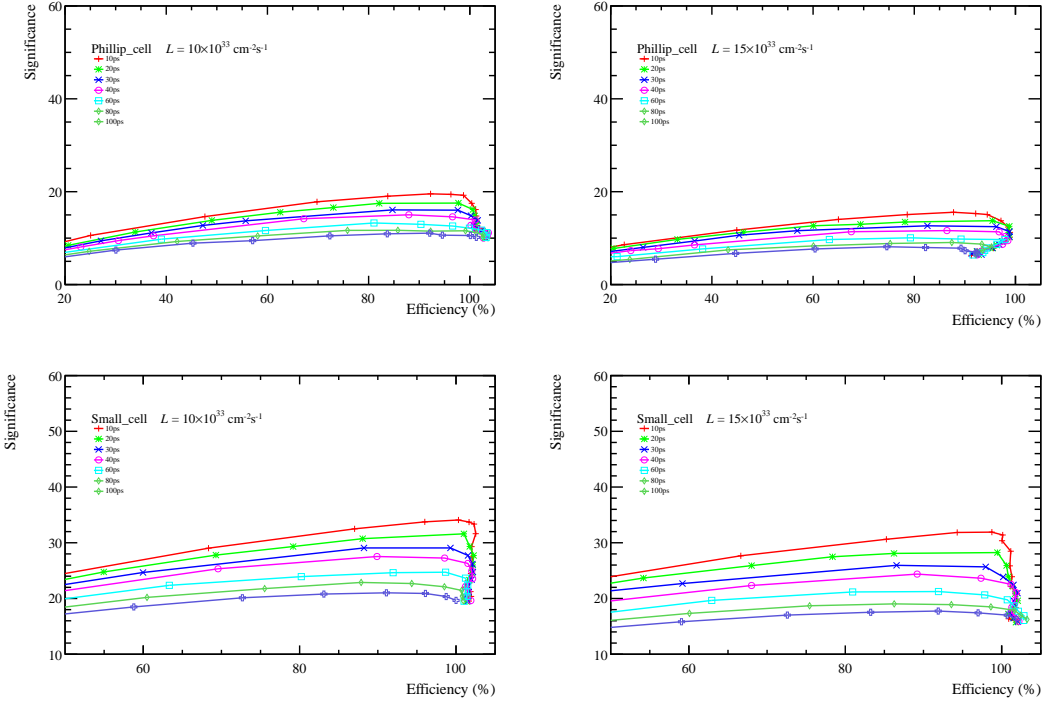


Figure 5.16 The relation between signal efficiency and significance with different $R(t)$ cuts applied, in Phillip's segmentation (top) and Si-W segmentation (bottom) respectively.

picosecond for both cell size segmentation. The signal significance of 20000 events simulation sample was also studied, as shown in Figure. 5.16. When comparing the performances with different cell size segmentation, the signal significance of Si-W ECAL improves a lot comparing to the Phillip's segmentation due to larger reconstruction efficiency. It also means that smaller cell configuration can help improve the reconstruction efficiency of π^0 .

5.2.6 From parameterized simulation to GEANT4 simulation

From parameterized simulation, we find that overlapping effect is the biggest challenge after Upgrade II as high pile-up effect. This causes a bad performance in the cluster reconstruction and particle identification. Smaller cell size ECAL can reduce this effect, which leads to a better reconstruction efficiency and mass resolution in some physical channels. Besides, smaller cell size configuration can improve the reconstruction efficiency of resolved π^0 , which also results in a better mass resolution in the physical channel containing π^0 .

In addition to smaller cell size, timing information can also help eliminate high pile-up effect significantly. On the one hand, timing information can be used in the physical channel reconstruction, the shower time should be coincident to the vertex time that the neutral particle decaying from, a lot of combinatorial background candidates are removed by

the timing matching. On the other hand, timing information can also be used in the cluster reconstruction and identification level, help to identify the neutral particles from charged tracks by timing matching and removed random overlapping cluster effect according to the cell's time distribution in one cluster. By studying the physical performance with different time resolution, the timing resolution requirement for futher ECAL is around 20 ps for the particle with energy larger than 10 GeV.

The technical proposal is not studied in the parameterized simualtion, a possible technolgy chioce is using silicon sensor to measure shower time out of the experience of CMS, which can meet the requirement to time resolution. In this next section, we will discuss this performance of silicon-tungsten ECAL at LHCb. In the GEANT4 model, the idea by inserting several silicon layers to measure time in the shashlik or crystal ECAL is also discussed.

5.3 Silicon-tungsten ECAL simulation

A standalone Geant4 package is developed to study the performance of the SiW ECAL. Figure 5.17 shows a flowchart of the simulation, reconstruction, and analysis. For the study of energy resolution and the determination of the calibration parameters, the input of the Geant4 simulation is simply provided by G4ParticleGun. For the simulation of the benchmark decay channels, the Gauss package (v51r2) is used to produce the input for the full simulation of the SiW ECAL. In the Gauss simulation the beam condition of Upgrade II is used, and the information of all particles before entering the calorimeter is recorded and is used later as the input of the standalone ECAL simulation. In this case, apart from the SiW ECAL nothing else exists in the standalone simulation. In order to study the Bremsstrahlung effect of electrons, a simplified tracking system with the magnetic field before the ECAL is implemented in the simulation. The amount of material is around $0.6X_0$. In this case the input of the standalone simulation is the output of Gauss at generator level with the Upgrade II beam condition.

5.3.1 Simulation model in GEANT4

The multi-layer SiW detector model is constructed in a standalone Geant4 framework. Details of the detector are described below.

5.3.1.1 Geometry

The default geometry of the SiW ECAL is as follows. It contains 26 layers of tungsten as the absorbers interleaved with 26 silicon layers as the active material. The thickness of each

silicon (tungsten) layer is 0.4 mm (3.5 mm). The cell size of the Si layers is $1.01\text{ cm} \times 1.01\text{ cm}$. Figure 5.18 shows a side-view of the SiW ECAL with a shower of a 50 GeV photon. When studying the energy resolution, the thickness of each layer and the cell size are varied.

5.3.1.2 Detection efficiency of sensors

During the development of a shower some energies will deposit in the cells. It is assumed here that the sensor will not be triggered if the deposited energy in one cell is less than 0.5 MeV. We define the detection efficiency of sensors as the fraction of the cells with deposited energy greater than 0.5 MeV. One can imagine that this efficiency should be close to unit in the first stage of the shower development, while it will be small in the far-end part of the shower. Figure 5.19 presents the efficiency varies with the energy and the direction of the incident particle. It shows that the dependence of the efficiency on the incident angle is almost negligible, while the efficiencies for the layers in the end part of the ECAL strongly depend on the energy of the incident photon. One can conclude from these plots that if only a few silicon layers will be used to obtain time information of the shower, they should not be placed in the end part of the ECAL.

5.3.1.3 Parameterized silicon sensor time resolution

The silicon sensor provides the information of time-of-arrival (ToA). From the CMS TDR (CERN-LHCC-2017-023)^[146], the precision of the overall timing measurement depends on the intrinsic performance of the silicon sensor, together with the preamplifier and the discriminator. Results from the CMS beam tests^[37] have shown that the timing resolution obtained with silicon sensors does not vary significantly with sensor thickness when the resolution is measured as a

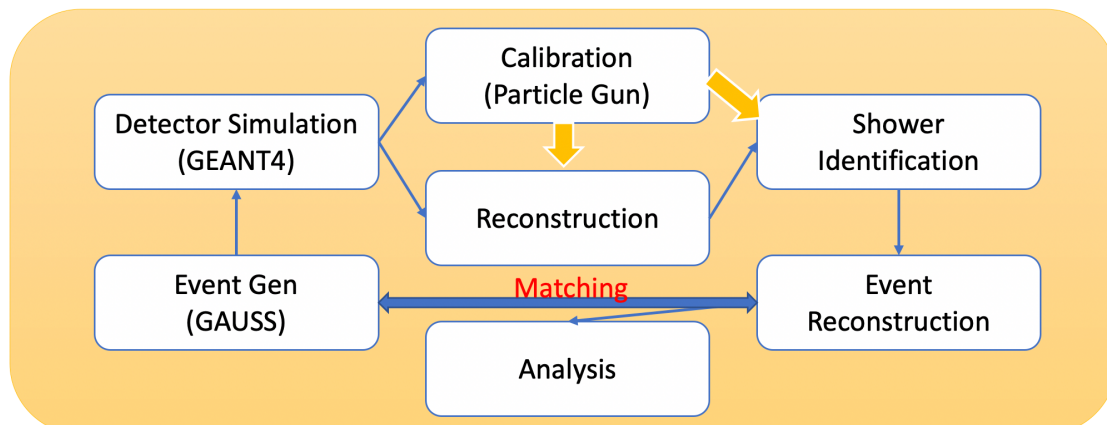


Figure 5.17 The simulation process with Si-W ECAL model in GEANT4.

function of the signal-to-noise ratio, S/N .

The timing resolution can be expressed as

$$\sigma_t = \sigma_{jitter} \oplus \sigma_{floor}, \quad \sigma_{jitter} = \frac{A}{S/N}, \quad (5.13)$$

where σ_{floor} is a constant term, and the symbol \oplus denotes quadratic summation. The constant

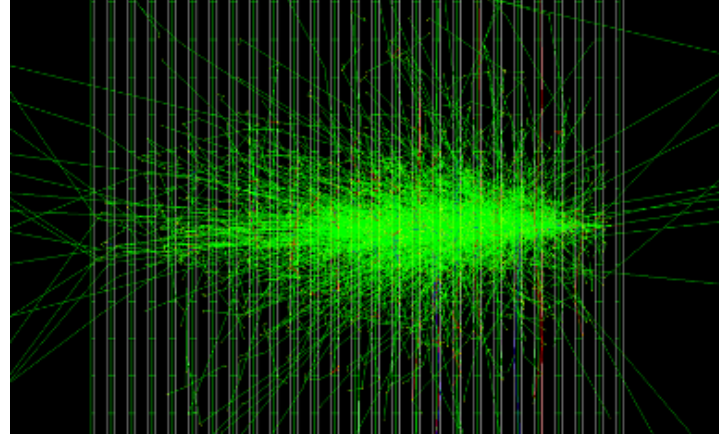


Figure 5.18 Geometry of the SiW ECAL used in the Geant4 simulation. Displayed is a shower of a 50 GeV photon.

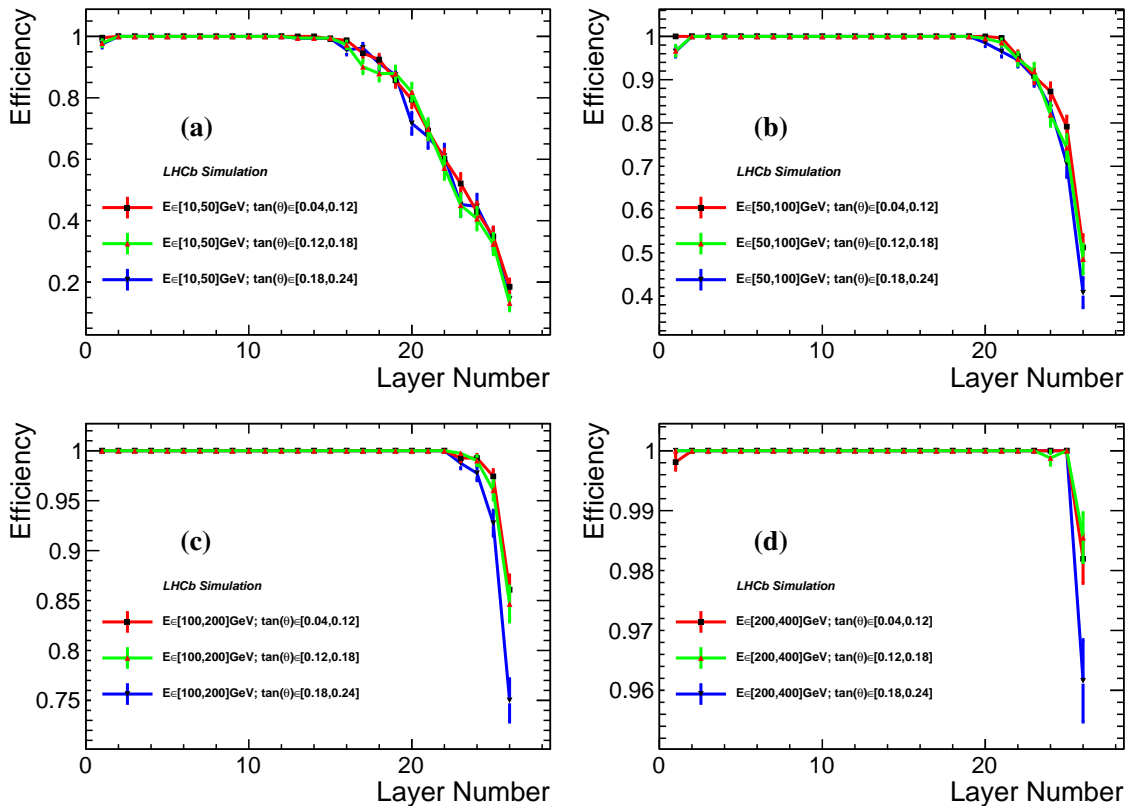


Figure 5.19 The detection efficiency of sensors for γ with different energy and incident directions to the ECAL plane.

A is fixed by the response time and noise characteristics of the sensor and the preamplifier. According the test by CMS, the expected parameters are: $A = 5 \text{ ns}$, $\sigma_{floor} = 20 \text{ ps}$ and the S/N for MIP is equal to 12. The deposited energy MIP in a 0.4 mm-thick silicon for is around 0.16 MeV, so the parameterized function can be written as

$$\sigma_t = \frac{5 \text{ ns}}{12 \times \sqrt{E/0.16}} \oplus 0.02 \text{ ns}, \quad (5.14)$$

where E is the deposited energy in MeV. For safety, the parameterized time resolution used in this simulation is

$$\sigma_t = \frac{5 \text{ ns}}{12 \times \sqrt{E/0.2}} \oplus 0.02 \text{ ns}. \quad (5.15)$$

5.3.2 Reconstruction and calibration

The cell energy smaller than 0.5 MeV is neglected in the clustering. There are many different clustering algorithms to reconstruct the cluster for different kinds of calorimeters, *e.g.* Arbor, ML, APRIL, *et al.*^[49,110,133]. The main idea is to fully exploit the advantage of the shower characteristics for a given calorimeter. A simple but effective algorithm is used for preliminary analyses. The algorithm used this study is similar to the method used in the current LHCb calorimeter with an extension to multi-layer configuration. It is simple and effective for preliminary analyses. In this algorithm, the seed cell for each layer (26 layers in total), which is used as a starting point for the aggregation, is first searched for according to the energy distribution. The cell energies around the seed cell are then added for each layer. Finally, these energies in all layers are summed to form a shower if they are in a similar position in the x - y plane.

5.3.2.1 Shower reconstruction

The cluster layer energy is obtained by adding all cell's energy together:

$$E_{layer} = \sum_i^{cells} E_i \quad (5.16)$$

and the layer cluster position are estimated:

$$\begin{aligned} x_{layer} &= (\sum_i^{cells} x_i \times E_i) / E_{layer} \\ y_{layer} &= (\sum_i^{cells} y_i \times E_i) / E_{layer} \\ z_{layer} &= z_i \end{aligned} \quad (5.17)$$

$$z_{layer} = z_i$$

As the thickness of silicon sensor is very small, 4 μm here, the silicon sensor z position is taken as the layer cluster position.

The layer time is also obtained from the cell in the same layer:

$$T_{layer} = \left(\sum_i^{cells} T_{i,cali} \times E_i \right) / E_{layer} \quad (5.18)$$

considering the developing time of the shower, usually, the measured time from the cells around seed cell is larger than the seed cell time, therefore, the used time in the above formula is calibrated, the calibration method will be addressed later.

The shower information is estimated from the each layer cluster calibrated, with the layer energy weight. In the current reconstruction algorithm, the layer cluster energy smaller then 3 MeV is overlooked, considering the random effect.

5.3.2.2 Energy calibration

The method to calibrate the reconstruct shower energy is similar to the previous study, by a lineareer function:

$$E_{cali} = \alpha \times E_{rec} + \beta \quad (5.19)$$

In the real experiment, the calibrated parameters are obtained from beam test or real running, we estimate these numbers in from particle gun simulation here. From the γ event, we get the relation between the true particle energy and the reconstructed one, as shown in Figure .5.20, and fitted by a linear function. The obtained values will be taken as the calibration parameters. After the calibration is finished, the energy resolution is studied, as shown in Figure. 5.21, where the thicknesses of silicon is 4 mm.

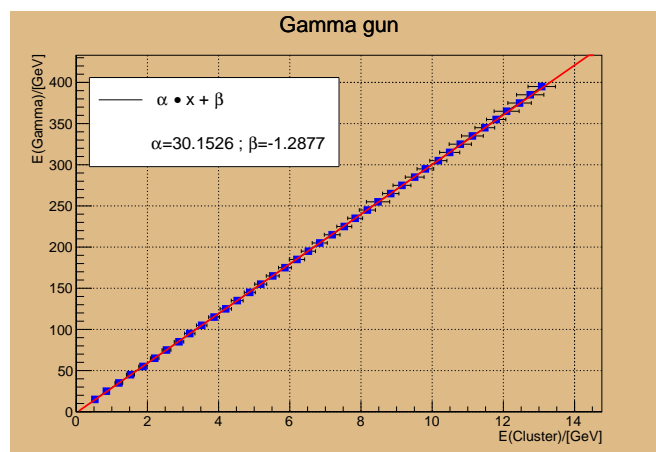


Figure 5.20 The relation between particle true energy and reconstructed cluster shower energy.

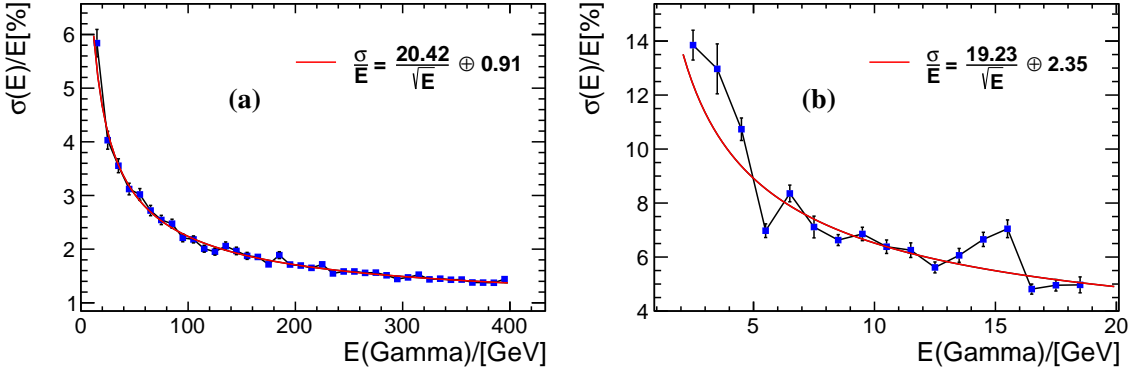


Figure 5.21 The energy resolution in different particle energy regions.

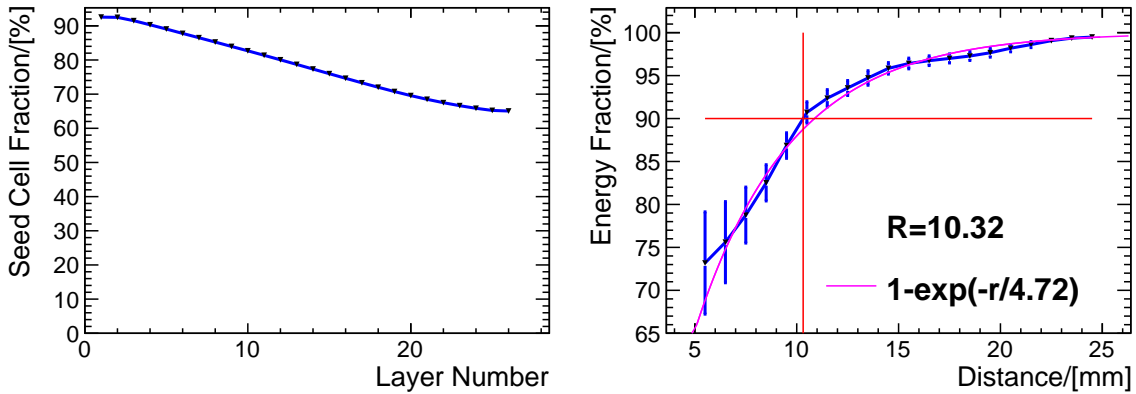


Figure 5.22 The seed cell energy fraction for each layer (left). The estimated Moliere radius (right).

The seed cell energy fraction in one layer cluster for each layer is shown in left of Figure. 5.22, according to this plot, we know that most of shower energy deposit in the seed cell, which is also the reason why we use current method to cluster. Besides, the seed energy fraction becomes smaller as the shower development.

A check to the Moliere radius is also performed, as shown in right of Figure. 5.22, which is obtained from the reconstructed shower energy from the silicon sensors. The estimated Moliere radius is around 10.3 mm, which is a little larger than the value of tungsten from PDG as the silicon and gap in the current Multi-layer Si-W ECAL model. Besides, this plot also shows the lateral development of shower in Si-W ECAL, the distribution is parameterized by this function:

$$f = 100(1 - e^{r/A}) \quad (5.20)$$

where r is the cell distance to the shower energy baryon axis, $A = 4.73$ is obtained from fitting, which is a free parameters.:q Actually, the relations between energy fraction and distance in each layers are little different, not go too far into this in the preliminary study.

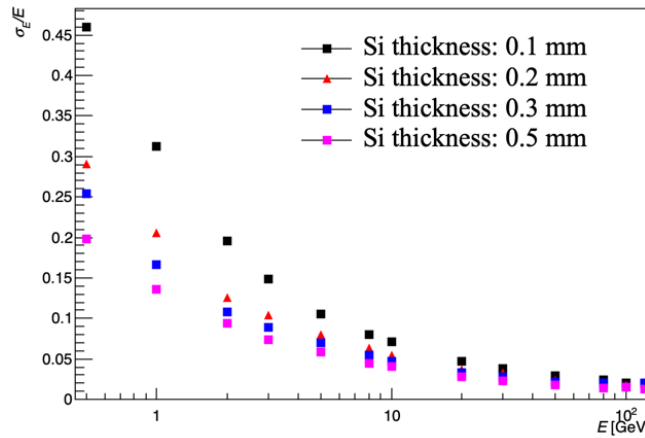


Figure 5.23 Energy resolution of electron showers as a function of the incident electron energy for different thicknesses of the silicon layers. The cell size is $1.0 \times 1.0 \text{ cm}^2$ and the thickness of the tungsten layers is 3.5 mm.

Figure 5.23 shows the energy resolution as a function of the incident electron energy for different thicknesses of the silicon layers with the cell size of $1.0 \times 1.0 \text{ cm}^2$ and the thickness of 3.5 mm for the tungsten layers. It shows that the energy resolution improves as the Si thickness increases. The dependence of the energy resolution on the cell size of the silicon layer and the thickness of the tungsten layer is almost negligible. The energy resolution is around 15% (5%) when the energy of the electron is 1 GeV (10 GeV).

5.3.2.3 Position calibration

The method to calibrate the layer cluster position is similar to the one used in current ECAL. And the position calibration is performed according to the relative position in one cell. As shown in the left of Figure. 5.24, the reconstructed position is not exactly equal to the true position, the relation of these values is estimated by Function. 5.4, also used in parameterized simulation. the left plot of Figure. 5.24 is a example to the 15th layer, actually, every layer is studied separately, as shower shape changes with depth of the incident.

We also take a look at the position resolution with the different particle energy in each layer. As shown in the right Figure. 5.24, the 5-17 layer performed better than other layers within a large particle gun energy region.

5.3.2.4 Timing calibration

The method to calibrate time information is also studied. As mentioned in the Section. 5.3.1.3, the parameterized method is used to simulate the silicon sensor time, which also

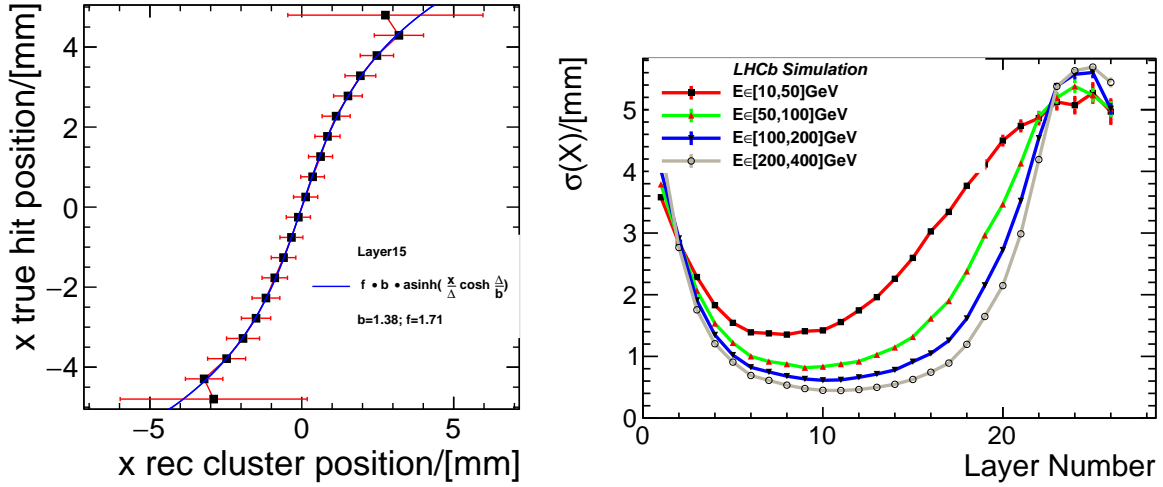


Figure 5.24 The relative position to the cell between true layer cluster and true layer cluster of the 15th layer (left). The position resolution (right).

rest with the development characters of shower in Si-W ECAL. Usually, the measured time around the seed cell perform a "time-lag" effect comparing to the value obtained from the seed cell. As shown in Figure. 5.25, the time difference measured from the seed cell and around cells is related to the distance, in this case, we calibrate the cell time using a linear function:

$$\Delta(T_{cell}) = a \times d + b \quad (5.21)$$

where the $\Delta(T_{cell})$ is the time difference to the seed cell, d is the distance, and a, b are the calibration parameters. We study the time calibration for each layer separately.

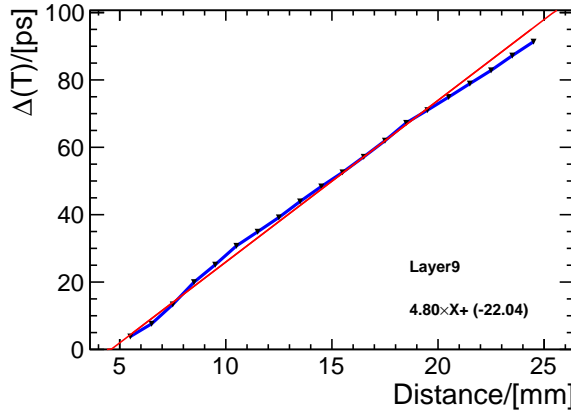


Figure 5.25 The time difference between the seed cell time with the measured value around cells in 9th layer

The time resolutions of every layer are shown in Figure. 5.26, which are different with each other as the shower deposited energy distribution in the z-direction. According to the energy resolution results in every layer mentioned above, we find that the layer with larger

deposited energy leads to better energy and time resolution.

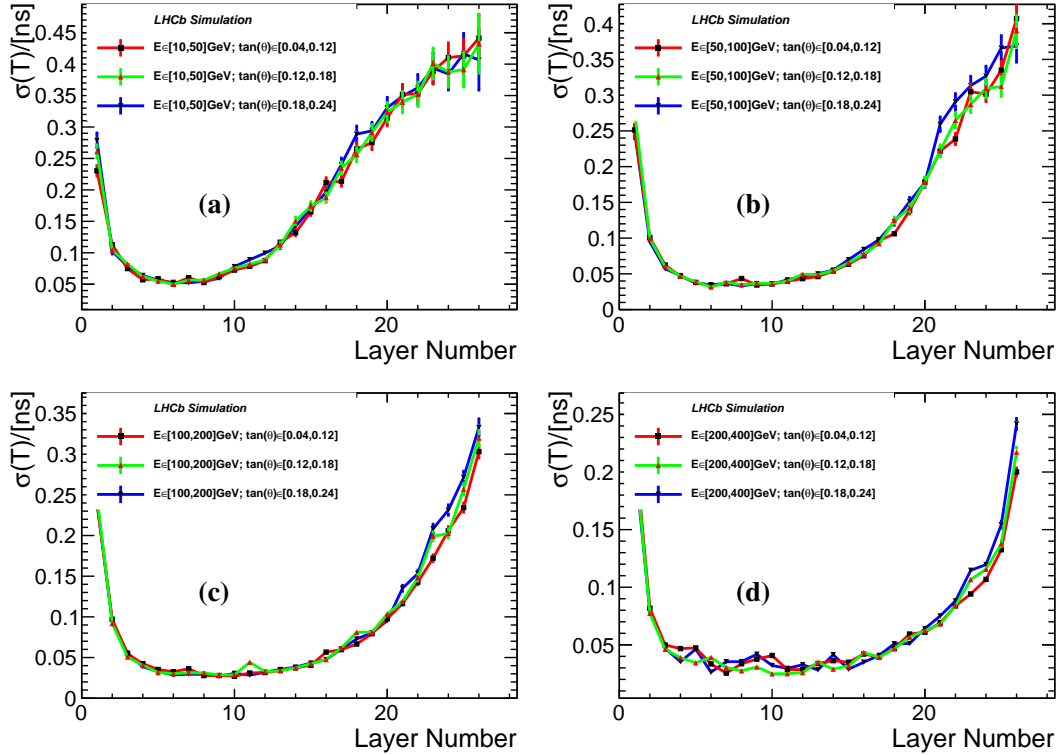


Figure 5.26 The time resolution of each layer with different γ energy and incident angle.

Figure. 5.27 shows the time resolution in layer 4-14 before and after the cell time calibration, the time distribution peak becomes narrow, especially for the rear layers.

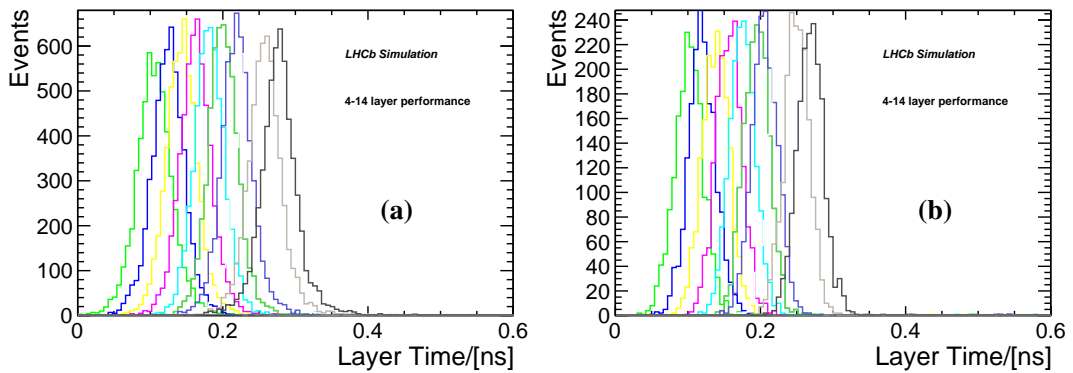


Figure 5.27 The time distribution for each layer before(a) and after(b) calibration.

The shower time is reconstructed based on the measured time from each layer, the time recorded in each layer is different as shower developing in the longitudinal direction. As shown in Figure. 5.28, the slope of this linear function obtained from fitting is around equal the value if assume the shower development speed is exactly equal to light speed, from this study, which

is around 2% smaller than the light speed. Besides, we use this parameter to calibrate the measured layer time when reconstruct the shower time.

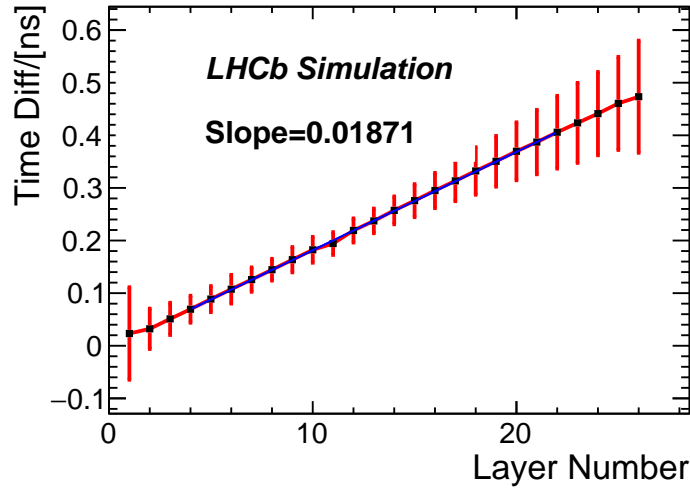


Figure 5.28 The time difference measured in each layer.

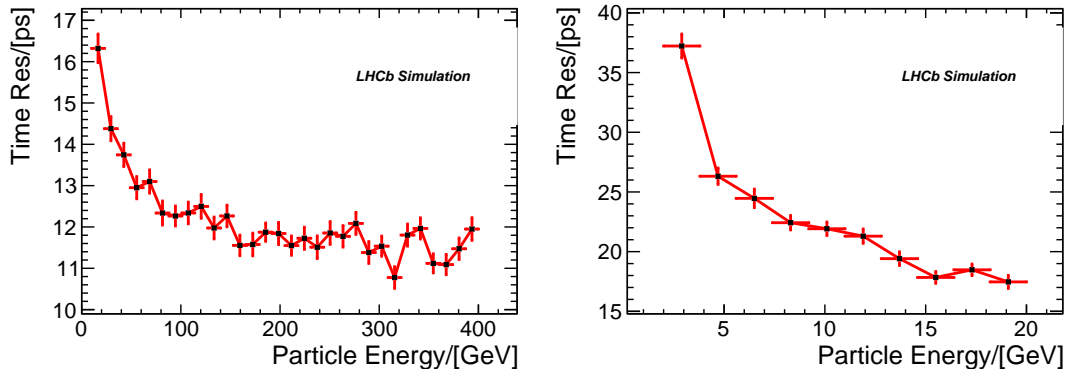


Figure 5.29 The shower time resolution with three layers to measure shower time, the right plot shows the low energy result.

After time calibration, the shower time resolution is shown in Figure. 5.29, which is related to the particle energy, and the shower time resolution is constructed from 4th, 5th and 6th layers. If only three layers have the ability to record the time information, the shower time resolution will reach to 15 ps. This number can meet the requirement obtained from parameterized simulation.

5.3.3 Physical performance with silicon of different thickness

As the known, the silicon sensors have to work at around -30°C , to reliably operate silicon sensors after irradiation, and to keep low electronic noise causing from leakage current. The

evaporative CO₂ is popularly used to cool the silicon sensors, which go through the pipes in the copper cooling plane as the copper can provide excellent thermal conductivity. In order to study the effect to the performance of copper plane cryostat, we change the geometry to each layer, with 6 mm copper plane added, which is attached to the silicon sensors. This is a safe estimation, usually 26 cooling layers are not necessary, according to the study from CMS HGCAL group, five plants are employed to cool the system totally. The physical performances with copper cryostat are also studied.

5.3.3.1 $B_s^0 \rightarrow \phi\gamma$ performance

The simulation sample of this decay channel was generated in $\mathcal{L} = 4 \times 10^{32} \text{ cm}^{-2} \cdot \text{s}^{-1}$ situation, details procedure is shown in Figure 5.17. The reconstruction method for this channel is as same as the one performed in parameterized simulation. Figure 5.30 presents the mass distributions of B_s^0 mesons which are constructed in $B_s^0 \rightarrow \phi\gamma$ channel with different thickness of silicon sensor. It is obvious that the Si-W with copper cooling included leads to a worse B_s^0 mass resolution. Besides, these results are consistent to these obtained from parameterized simulation.

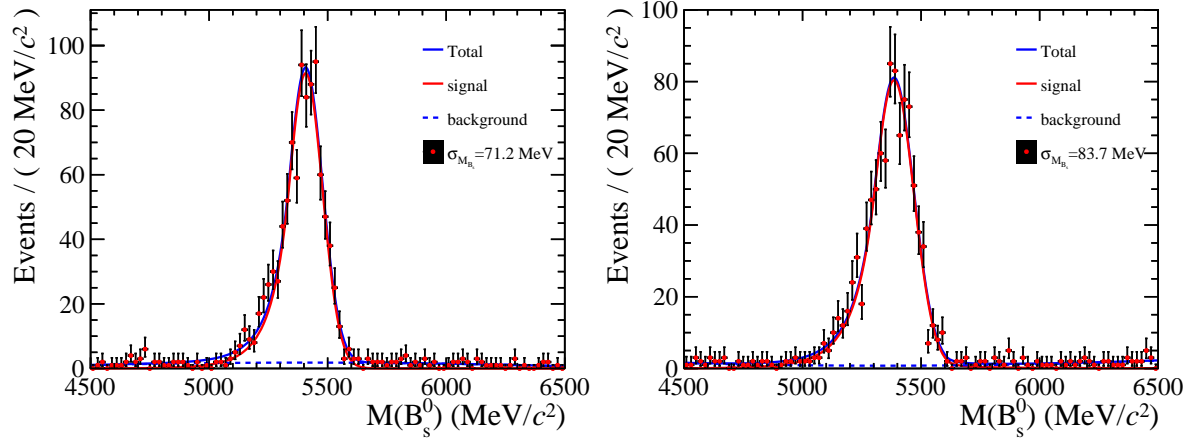


Figure 5.30 Mass distributions of the B_s^0 mesons from $B_s^0 \rightarrow \phi\gamma$ decays. The thickness of silicon sensor is 2 mm, no copper cryostat applied (left). The thickness of silicon sensor is 2 mm, 26 cooling copper plane added against silicon layers.

5.3.3.2 $B_s^0 \rightarrow J/\psi\pi^0$ performance

The decay channel $B_s^0 \rightarrow J/\psi\pi^0$ is used to study the performance for π^0 mesons. Figure 5.31 shows the mass distributions of the π^0 mesons from $B_s^0 \rightarrow J/\psi\pi^0$ decays. Besides, the B_s^0 mass resolution is also studied. Figure 5.32 shows the B_s^0 mass distributions with $\mathcal{L} = 4 \times 10^{32} \text{ cm}^{-2} \cdot \text{s}^{-1}$. The left one is the result with the thickness of silicon sensor equal to

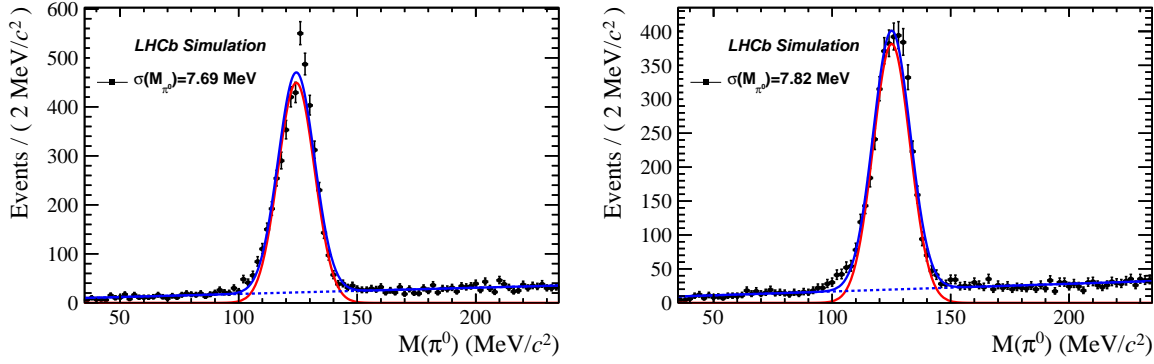


Figure 5.31 Mass distributions of the π^0 mesons from $B_s^0 \rightarrow J/\psi\pi^0$ decays. The thickness of silicon sensor is 2 mm, no copper cryostat applied (left). The thickness of silicon sensor is 2 mm, 26 cooling copper plane added against silicon layers.

2 mm, while the right one shows the result with copper cooling plane applied. Similarly, the results from GEANT4 simulation are consistent to the parameterized simulation conclusion.

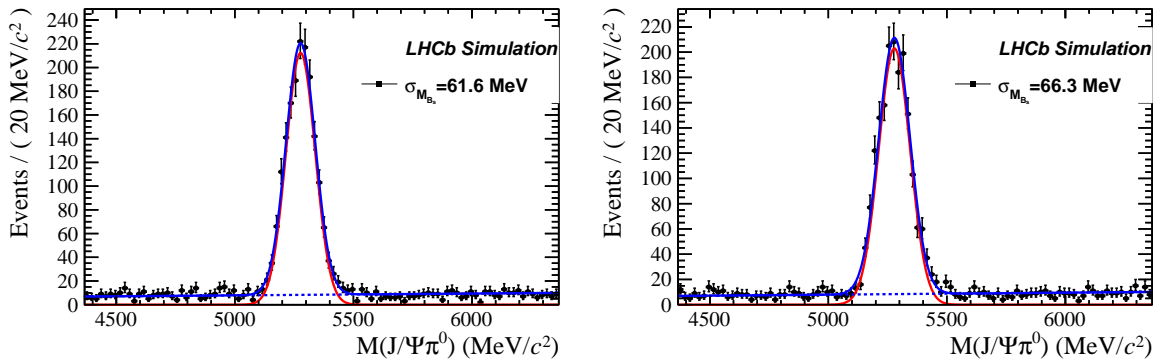


Figure 5.32 The B_s^0 mass distribution reconstructed from $B_s^0 \rightarrow J/\psi\pi^0$ decay. The thickness of silicon sensor is 2 mm, no copper cryostat applied (left). The thickness of silicon sensor is 2 mm, 26 cooling copper plane added against silicon layers.

5.3.4 Bremsstrahlung recovery and $B^0 \rightarrow K^* e^- e^+$ performance

In consideration of the detector material budget before the ECAL, the electron has possibility to interact with trackers from bremsstrahlung, which cause the energy measurement to electron is not accurate, especially the reaction happening before the magnet. In this case, we want to study the method to recover the electron energy by adding the radiated γ .

The decay channel $B^0 \rightarrow K^* e^- e^+$ is taken as a benchmark channel, which can be used to study the bremsstrahlung effect. The electron energy and transverse momentum distribution are shown in Figure. 5.33.

We take a look at the distance between the electron and the bremsstrahlung photon on the ECAL plane, as shown in the Figure. 5.34.

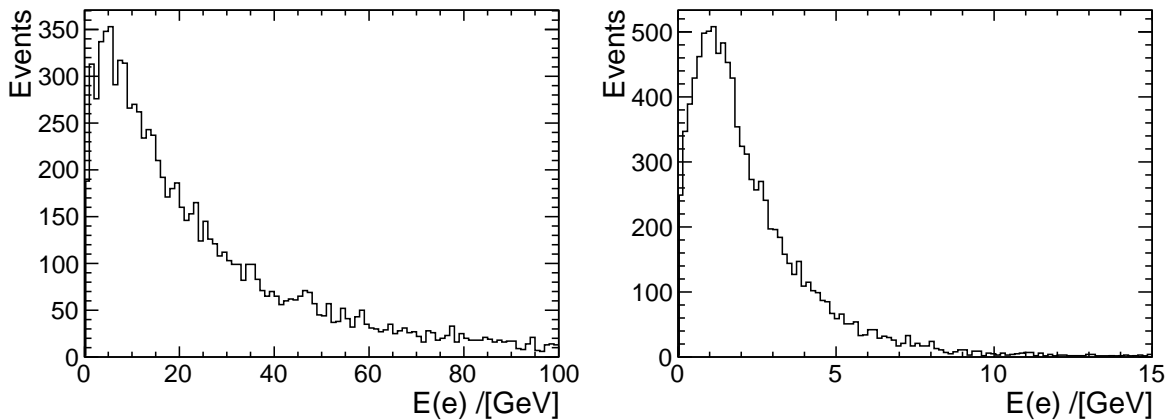


Figure 5.33 The electron energy(left) and transverse momentum(right) distribution in $B^0 \rightarrow K^* e^- e^+$ decay.

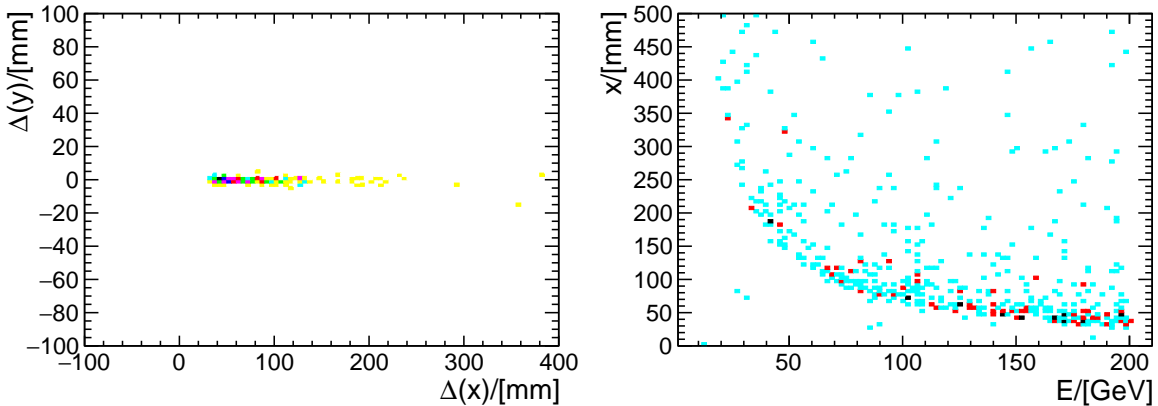


Figure 5.34 Left: the distance between the electron and bremsstrahlung photon on the ECAL plane; Right: the relation between the electron energy and the x distance on the ECAL plane.

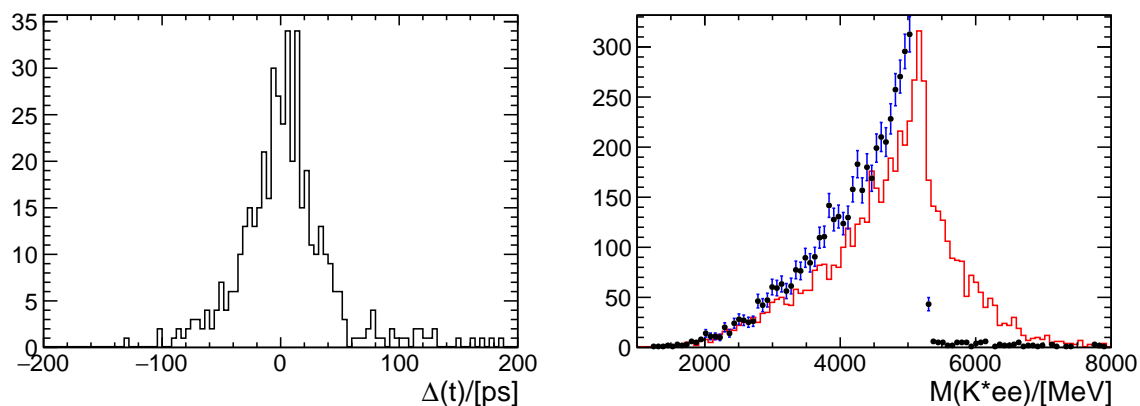


Figure 5.35 Left: the time difference between the electron and bremsstrahlung photon. Right: the B^0 mass distribution before(blue point) or after bremsstrahlung recovery with time-matching included(red line).

The time difference between the electron and bremsstrahlung photon is shown in the left plot of Figure. 5.35, we hope the time information can help improve the mass resolution of B^0 reconstructed from $B^0 \rightarrow K^* e^- e^+$ decay, the mass distribution is shown in the right plot of Figure. 5.35. However, there is no significant improvement for the invariant mass resolution of $K^* e^+ e^-$ when time information is used.

5.4 Conclusions

The parameterized simulation tool for ECAL upgrade was developed based on GAUSS and DELPHES. By studing two decay channels, we found the high luminosity causes a very level of combinatorial background. The precision timing can help to remove many background candidates, and the needed time resolution is around several tens of picosecond. Besides, the smaller cell size is necessary for Upgrade II, as it has a great impact to reconstruction efficiency.

Then, a detailed Si-W ECAL simulation is performed with a stand-alone GEANT4 package. The energy resolution and time resolution are obtained from this simulation, and these values can meet the requirements for ECAL Upgrade II at LHCb. Two decay chennels are studied in this simulation tool, and these results fall in line with parameterized simulation findings.

Chapter 6 Summary and Implication

6.1 Exotic hadrons study at LHCb

The first observation of exotic states with a new quark content $c\bar{c}u\bar{s}$ decaying to the $J/\psi K^+$ final state is reported with high significance from an amplitude analysis of the $B^+ \rightarrow J/\psi \phi K^+$ decay in Chapter. 3. The analysis is carried out using proton-proton collision data corresponding to a total integrated luminosity of 9 fb^{-1} collected by the LHCb experiment at centre-of-mass energies of 7, 8 and 13 TeV. The most significant state, $Z_{cs}(4000)^+$, has a mass of $4003 \pm 6^{+4}_{-14} \text{ MeV}$, a width of $131 \pm 15 \pm 26 \text{ MeV}$, and spin-parity 1^+ , where the quoted uncertainties are statistical and systematic, respectively. A new $1^+ X(4685)$ state decaying to the $J/\psi \phi$ final state is also observed with high significance. In addition, the four previously reported $J/\psi \phi$ states are confirmed and two more exotic states, $Z_{cs}(4220)^+$ and $X(4630)$, are observed with significance exceeding five standard deviations.

The $Z_{cs}(4220)^+$ observed at LHCb is not as same as the one discovered at BESIII, we need to examine them in future experiments carefully. Besides, the neutral isospin particle of $Z_{cs}(4000)^+$ and $Z_{cs}(4220)^+$ can be searched in an akin decay channel, $B^0 \rightarrow J/\psi \phi K_S^0$, which can be studied at LHCb.

The first observation of $\Lambda_b^0 \rightarrow \Lambda_c^+ K^+ K^- \pi^-$ decay is reported in Chapter. 4, and the ratio branching fraction to $\Lambda_b^0 \rightarrow \Lambda_c^+ D_s^-$ decay is measured to be $(9.26 \pm 0.29 \pm 0.46 \pm 0.26) \times 10^{-2}$. Though no obvious open charm pentaquark signal is observed from the $\Lambda_c^+ K^+$ mass distribution, some analogous decay channels can be explored to search this kind of states at LHCb. It is very likely that the open-charm pentaquark states can be found in further studies as the open-charm tetraquark state was observed at LHCb recently^[21].

In addition, there are many other open questions related pentaquark sector. The J^P of observed pentaquarks have not been determined yet, we expect these important parameters can be explored at LHCb. Considering the pentaquark states are only found in $\Lambda_b^0 \rightarrow J/\psi p K^-$ at LHCb, it is necessary to confirm these observations in different decay channels or different experiments.

6.2 ECAL simulation for Upgrade II at LHCb

This dissertation discusses the simulation study of ECAL for LHCb Upgrade II. Two simulation tool were developed from this research. According to two decay channels, it is found that the precision timing and smaller cell size are keys for Upgrade II of ECAL. Besides, the high granularity Si-W ECAL can meet these requirements.

As the final upgrade plan of ECAL for Upgrade II at LHCb has not been decided yet, it is important to continue detailed simulation study for ECAL Upgrade II. For example, the final cell size segmenation should be optimized based on some key decay channels, the precision timing is used to identify different kinds of shower, the detailed reconstruction algorithms need to be optimized and so on. When the final scheme is chosen, the detailed detector model can be imported in LHCb software framework.

Appendix A Hiddern-charm pentaquark states in $\Lambda_b^0 \rightarrow J/\psi p K^-$ decay

A.1 Selection

This analysis uses all the pp collision data in Run 1 and Run 2 stage, corresponding to an integrated luminosity of 3 fb^{-1} (6 fb^{-1}) in Run 1 (Run 2). The simulation samples of the $\Lambda_b^0 \rightarrow J/\psi p K^-$ decay are generated by PYTHIA with pp collisions at $\sqrt{s} = 7\text{ TeV}$, 8 TeV and 13 TeV respectively, with the ratio of the numbers of events roughly one to two between Run 1 and Run 2. Both PYTHIA 6 and PYTHIA 8 generators are used. The Monte Carlo event type is **15144001**, in which Λ_b^0 is forced to decay into the $J/\psi p K^-$ final state with the PHSP model.

A.1.1 Reconstruction and pre-selection

In this analysis the reconstruction of the Λ_b^0 candidate starts from the stripping line **FullDSTDiMuonJpsi2MuMuDetachedLine** in the **DiMuon** stream of the stripping reconstruction, which different version, S21r1 for 2011, S21 for 2012, S24 for 2015, S28 for 2016, S29r2 for 2017, and S34 for 2018. The selection criteria in this stripping line is summarized in Table A.1. The J/ψ candidate is formed by two oppositely charged tracks consistent with muon hypotheses (IsMuon) with $p_T > 550\text{ MeV}/c$ and good track fit quality $\chi^2/\text{ndf} < 4$. The J/ψ candidate is required to have an invariant mass within the $\pm 100\text{ MeV}/c^2$ window around the known J/ψ mass^[126], and to have a vertex fit quality $\chi^2_{\text{vtx}} < 20$. The J/ψ candidate is consistent with originating from b -hadron decays by requiring its decay length significance (DLS) to be greater than three.

Comparing to the previous study^[11], the selection criteria is optimized, all differences between the new selection criteria and old study are summarized in Table A.2. To select good J/ψ candidates, a tightened PID cut $\text{DLL}_{\mu\pi} > 0$ is required for both muon tracks in the final state, and the dimuon invariant mass window is reduced to $[-48, 43]\text{ MeV}/c^2$ around the known J/ψ mass^[156]. The J/ψ mass resolution is around $13\text{ MeV}/c^2$. To reconstruction the Λ_b^0 candidate, the J/ψ candidate is combined with two opposite charged tracks, consistent with pions and protons respectively. This is achieved by PID cuts on the ProbNN variables: $\text{ProbNN}_K(K) > 0.2$ and $\text{ProbNN}_p(p) > 0.2$. The two hadronic tracks are required to have large transverse momenta, $p_T > 250\text{ MeV}/c$, inconsistent with originating from the primary vertex

(PV), $\chi^2_{\text{IP}} > 9$. The Λ_b^0 candidate is required to have a good vertex fit quality, $\chi^2/\text{ndf} < 10$, with a displayed decay vertex, flight distance to primary vertex is larger than 1.5 mm. It should be consistent with being produced from PV by requiring $\chi^2_{\text{IP}} < 25$ and cosine value of the direction angle, $\text{DIRA} > 0.999$. And the χ^2 of closet approach distance between p and K^- is smaller than 16. The Λ_b^0 candidates with mass $5.1 < M(J/\psi p \pi^-) < 6.5 \text{ GeV}/c^2$ are selected.

The $\Lambda_b^0 \rightarrow J/\psi p K^-$ decay chain is refitted with two sequential constraints using the `DecayTreeFitter` to improve the mass resolution: A) the J/ψ candidate mass constrained to its known value^[156] and the Λ_b^0 candidate constrained to originating from the PV; B) the invariant mass of the Λ_b^0 candidate constrained to its known value^[145], with the momenta of the J/ψ , p and K^- daughters re-calculated according to this constraint.

It should be noted that the PID requirements on the hadron tracks are not applied when reconstructing the Λ_b^0 candidates in the simulation sample. The effect, instead, is considered using weights from the PID calibration (`PIDCalib`). The pion track is calibrated using pion tracks from the D^* tagged $D^0 \rightarrow K^- \pi^+$ decay, while the proton track is calibrated using proton tracks from the $\Lambda_c^+ \rightarrow p K^- \pi^+$ decay.

Events with Λ_b^0 candidates in both the simulation and the data samples are required to fire (TOS) the trigger sequences: at the HLT1 level by either of the `Hlt1DiMuonHighMass`, `Hlt1TrackMuon` and `Hlt1TrackAllL0` for Run 1 sample, while `Hlt1DiMuonHighMass`, `Hlt1TrackMuon`, `Hlt1TwoTrackMVA` and `Hlt1TrackMVA` for Run 2 sample; and at the HLT2 level by either of the `Hlt2DiMuonDetachedJPsi` lines.

Table A.1 Stripping selections of J/ψ candidates in the line `FullDSTDiMuonJpsi2MuMuDetachedLine`.

Quantity	Selections
<code>IsMuon(μ)</code>	= TRUE
<code>DLL($\mu - \pi$)</code>	> 0
$p_T(\mu)$	$> 550 \text{ MeV}/c$
Track $\chi^2/\text{ndf}(\mu)$	< 4
$\Delta M(J/\psi)$	$< 100 \text{ MeV}/c^2$
Vertex $\chi^2(J/\psi)$	< 20
<code>DLS(J/ψ)</code>	> 3

A.1.2 Multivariate analysis

The multivariate analysis (MVA) is used to further suppress the background. All variables used are listed in Table. A.3. Besides, the Run 1 and Run 2 samples are studied separately. The distributions of these variables of Run 2 sample for the signal in the simulation sample and the background in the data sideband are shown in Figure. B.4,

Table A.2 Pre-selections of $\Lambda_b^0 \rightarrow J/\psi p \pi^-$ candidates between old Run 1 analysis and this one.

	Quantity	Old Run 1	This analysis
1	All tracks χ^2/ndf	< 4	same
2	clone track rejection	CloneDist cut	same
3	ghost rejection	ghost probability < 0.2	same
2	muon DLL(μ)	> 0 & ISMUON	same
5	vertex of J/ψ	$\chi^2 < 16$	same
6	mass window of J/ψ	[−48, 43] MeV	same
3	p_T of muon	> 550 MeV	> 500 MeV
4	p_T of hadron	> 250 MeV	same
4	$p_T(p) + p_T(K^-)$	> 900 MeV	same
7	χ_{VS}^2 of hadron	> 9	same
8	PID of K	DLL($K - \pi$) > 0 and DLL($p - K$) < 3	ProbNNk > 0.2
9	PID of p	DLL($p - \pi$) > 10 and DLL($p - K$) > 3	ProbNNp > 0.2
16	DOCA χ^2 of pK^-	< 16	same
11	Λ_b^0 vertex	$\chi_{\text{vtx}}^2/\text{ndf} < 10$	same
10	χ_{IP}^2 of Λ_b^0	< 25	same
12	DIRA of Λ_b^0	> 0.999	same
15	Flight distance of Λ_b^0	> 1.5 mm	same

The BDTG method is used as the default method, and the overtraining test for the BDTG method is given in the right plot of Figure. B.5 for Run 2 samples. The BDTG discriminant distributions for the training samples are consistent with those in the test samples. No effect of overtraining is observed. The working point of the BDTG value is optimized by maximizing the figure of merit (FoM) of the signal significance, defined as $S/\sqrt{S+B} \times \epsilon_S$. The ϵ_S is the signal efficiency for a specified BDTG cut and is determined from the simulation sample, while S (B) is the number of the signal (background) events in the $\pm 3\sigma$ region around the known Λ_b^0 .

Table A.3 Variables used in TMA study.

	Variables
1	χ_{vtx}^2 of Λ_b^0
2	$\log(1 - \cos\theta_p)$
3	χ_{IP}^2 of Λ_b^0
4	min χ_{IP}^2 of hadron
5	FD of Λ_b^0
6	p_T of Λ_b^0
7	sum p_T of hadrons
8	min PID of muon
9	ProbNNp of p
10	ProbNNk of K^-
11	momentum of p

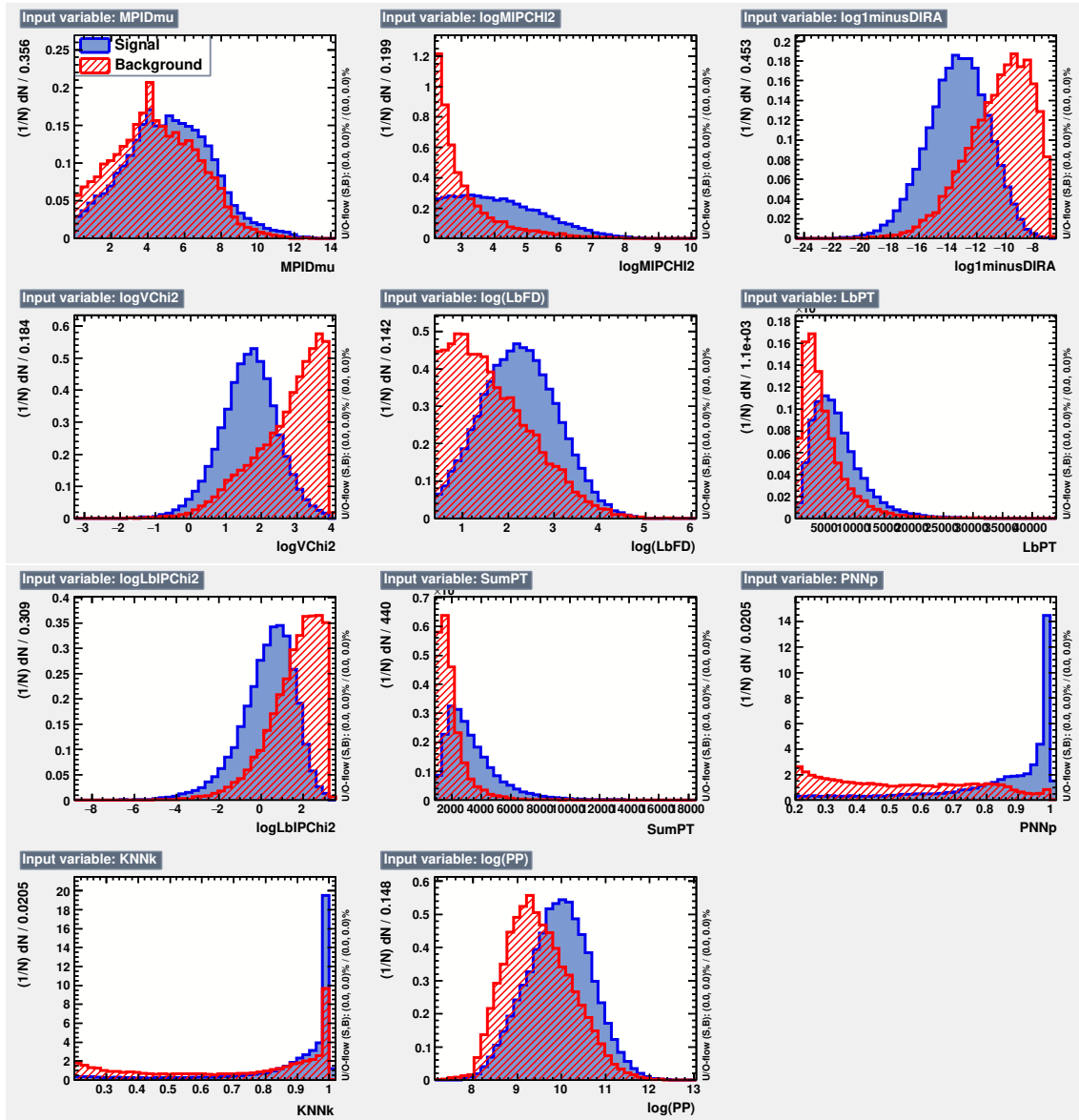


Figure A.1 Discriminating variables used in the MVA training of Run 2 sample.

mass in the $J/\psi p\pi$ invariant mass distribution of the data. The distribution of the FoM as a function of the BDTG cut value is given, and the value of 0 for Run 1 and -0.4 for Run 2 are determined as the default working points.

A.2 One dimensional fit and mass resolution

For the nominal results, the relativistic Breit-Wigner function (BW) of free pole mass (M) and width (Γ) is used for the signal shape:

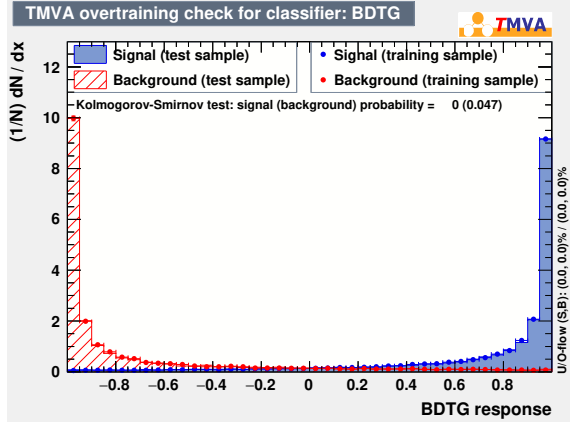


Figure A.2 The BDTG output distribution for signals and the background in the training sample and the test sample of Run 2 sample.

$$BW(m|M, \Gamma) = \frac{B_p B_q}{\frac{M^2 - m^2}{M\Gamma} - i} \times \frac{1}{\sqrt{\pi \frac{\Gamma}{2} I}} \quad (\text{A.1})$$

where B_p, B_q are optional Blatt-Weisskopf factors (the nominal fits assume S-wave production and decay, thus $B_p = B_q = 1$) and I is the normalization integral. The definition of I affects only the signal yield convention, and is given by:

$$I = \frac{1}{\pi} \left(\arctan\left(\frac{m_{max} - M}{\frac{\Gamma}{2}}\right) - \arctan\left(\frac{m_{min} - M}{\frac{\Gamma}{2}}\right) \right) \quad (\text{A.2})$$

where $[m_{min}, m_{max}]$ is the fit range. The latter is an accurate integral of the magnitude ($|BW|^2$) of non-relativistic Breit-Wigner function, in which

$$\frac{M^2 - m^2}{M\Gamma} \rightarrow \frac{M - m}{\frac{\Gamma}{2}} \quad (\text{A.3})$$

This formula is surprisingly accurate for the relativistic Breit-Wigner as well, especially when the fit boundaries are far from the pole mass as measured in units of the width. As seen from the equations above, we use mass-independent resonant width. We have checked that considering its mass dependence ($\Gamma \rightarrow \Gamma(m) = \Gamma \frac{q_0}{m} \frac{M}{m} B_q^2$) has negligible effect on our fits results, since the signal peaks are narrow. Besides, the Blatt-Weisskopf factor used here is similar to the one mentioned in $B^+ \rightarrow J/\psi \phi K^+$ amplitude analysis.

We use polynomial functions (pol) of various order to describe the smooth background under the P_c^+ peaks ($\Lambda_b^0 \rightarrow J/\psi \Lambda^*$ is the main background source). The polynomial coefficients are free fit parameters. Switching from the plain to Chebyshev polynomials improved numerical stability of the fits for high orders of the polynomial:

The Chebyshev polynomials (T_n) are orthogonal to each other, when the fit range is mapped to the $[1, +1]$ range (the x_m variable). This reduces correlations between the fitted polynomial coefficients, making convergence faster and avoiding round-off problems in the calculation of the covariance matrix.

The phase-space factor, pq , multiplies the signal and background functions added together, where $p(q)$ is the $P_c^+(J/\psi)$ momentum in the Λ_b^0 (P_c^+) rest frame. This factor is always included, even if we don't explicitly mention it in the figure captions. When overlapping signal peaks are fitted, we first add them incoherently when constructing the PDF function (P):

$$P(m) = p\dot{q} \left(\sum_j Y_j |BW(m|M_j, \Gamma_j)|^2 + pol(m|\vec{a}) \right) \quad (\text{A.4})$$

When allowing for their interference, a relative complex phase δ_j is added as a free parameter:

$$\left| \sum_{j=1} \sqrt{|Y_j|} e^{i\delta_j} BW(m|M_j, \Gamma_j) \right|^2 P(m) = p\dot{q} \left(\sum_j Y_j |BW(m|M_j, \Gamma_j)|^2 + pol(m|\vec{a}) \right) \quad (\text{A.5})$$

We parameterize the observed $m_{J/\psi p}$ dependence with a quadratic function, $\sigma_m(m)$, as shown in Figure. ??, and smear any fit function with a Gaussian of appropriate width:

$$P_{\text{smeared}}(m) = \sum_k P_k P(m + x_k \sigma_m(m)) \quad (\text{A.6})$$

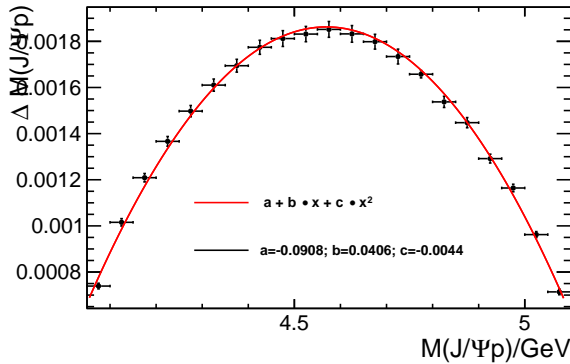


Figure A.3 The $m_{J/\psi p}$ resolution depended on the mass itself.

Appendix B Evidence of pentaquark states in $\Lambda_b^0 \rightarrow J/\psi p\pi^-$ decay

B.1 Study motivation

The Cabibbo-suppressed decay $\Lambda_b^0 \rightarrow J/\psi p\pi^-$ offers a new possibility to study these two states, as well as the other type of exotic state $Z_c^- \rightarrow J/\psi\pi^-$. The study of the relative branching fraction $R_{\pi^-/K^-} \equiv \mathcal{B}(\Lambda_b^0 \rightarrow \pi^- P_c^+)/\mathcal{B}(\Lambda_b^0 \rightarrow K^- P_c^+)$ could be useful to discriminate among their possible interpretations. Starting from Λ_b^0 , $ud(b)$, the Cabibbo-suppressed $b \rightarrow c\bar{c}d$ transition combined with the creation of a light quark pair $u\bar{u}$ yields a final state with the quark content $ud(c\bar{c}d)u\bar{u}$. The d quark in the P_c^+ state can be either directly from the content in the Λ_b^0 baryon or from the $b \rightarrow c\bar{c}d$ transition. This results in two interfering processes, referred as the external W -emission and the internal W -emission diagrams^[66]. The two diagrams are shown in Figure. B.1. While for the Cabibbo-favoured decay $\Lambda_b^0 \rightarrow K^- P_c^+$, only the external W -emission process exists, as the transition $b \rightarrow c\bar{c}s$ doesn't produce a d quark for the P_c^+ state. Assuming the internal W -emission process is zero, Ref. [66] predicted the relative branching fraction $R_{\pi^-/K^-} = 0.07 \sim 0.08$, due to the differences of CKM elements and the phase-space factors. A sizable internal W -emission process could modify (either increase or reduce) the predicted value and even the relative production phase between the two P_c states, resulting in different interference patterns between the two decays.

A different production mechanics is proposed. Ref. [98] argues that the P_c state in the $\Lambda_b^0 \rightarrow J/\psi pK^-$ decay is produced mainly by the charmless Λ_b^0 decay via the $b \rightarrow u\bar{u}s$ transition, in which the $c\bar{c}$ contents in P_c states arise from the intrinsic charms within the Λ_b^0 baryon. The Feynman diagram is shown in Figure. B.2. A very large value $R_{\pi^-/K^-} = 0.58 \pm 0.05$ is predicted.

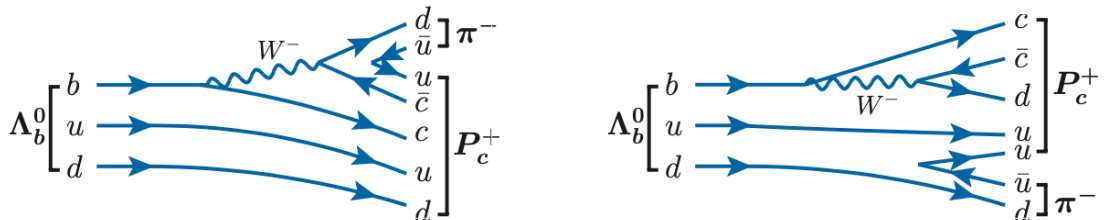


Figure B.1 Feynman diagrams of the $\Lambda_b^0 \rightarrow P_c\pi$ decay via (left) the external and (right) the internal W^- emissions.

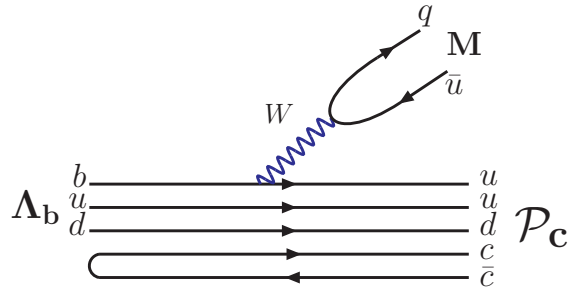


Figure B.2 Feynman diagram of $\Lambda_b^0 \rightarrow P_c^+ M$ via the charmless $b \rightarrow u\bar{u}q$ transition suggested by Ref. [98], where $M(q)$ can be $K^-(s)$ or $\pi^-(d)$.

The channel $\Lambda_b^0 \rightarrow J/\psi p\pi^-$ is expected to be produced via the intermedia resonances K^* , $\Lambda_b^0 \rightarrow J/\psi N^*$ with $N^* \rightarrow p\pi^-$. The transition of $\Lambda_b^0 \rightarrow J/\psi N^*$ is dominated by the flavor changing decay of $b \rightarrow c + \bar{c}d$. This suggests that the u and d quark in the Λ_b^0 should be a spectator, hence their isospin quantum number $I = 0$ should be conserved. As a consequence, if the ud pair is to be combined with a d quark to form a baryon, it will favor N baryons instead of Δ ones.

LHCb has measured the branching fraction of the overall Cabibbo-suppressed decay relative to the Cabibbo-favoured decay to be $\mathcal{B}(\Lambda_b^0 \rightarrow J/\psi p\pi^-)/\mathcal{B}(\Lambda_b^0 \rightarrow J/\psi pK^-) = 0.0824 \pm 0.0024 \pm 0.0042^{[7]}$, where the first uncertainty is statistical and the second systematic.

Actually, a full amplitude analysis of $\Lambda_b^0 \rightarrow J/\psi p\pi^-$ decay has been performed using LHCb Run 1 data sample^[13]. If including both types of the exotic resonances report in 2015^[12], the total significance for them is 3.1σ using a conservative model of N^* resonances and 6.6σ when only well established N^* states are allowed. Within the large statistical and systematic errors, the data are consistent with the $P_c(4450)^+$ and $P_c(4380)^+$ production rates expected from their previous observation and Cabibbo suppression. However, a new narrow $P_c(4312)^+$ state is discribed with a large statistical with Run 1 and Run 2 sample collected at LHCb^[19], and the previously reported $P_c(4450)^+$ structure contains two peaks, $P_c(4440)^+$ and $P_c(4457)^+$, which match the predictions for loosely bound and narrow molecular states. In this case, it is required to revisit this decay channel with both Run 1 and Run 2 data sample.

B.2 Selection

B.2.1 Dataset

This analysis uses all the pp collision data in Run 1 and Run 2 stage, corresponding to an integrated luminosity of 3 fb^{-1} (6 fb^{-1}) in Run 1 (Run 2). The simulation samples of the

$\Lambda_b^0 \rightarrow J/\psi p\pi^-$ decay are generated by PYTHIA with pp collisions at $\sqrt{s} = 7\text{ TeV}$, 8 TeV and 13 TeV respectively, with the ratio of the numbers of events roughly one to two between Run 1 and Run 2. Both PYTHIA 6 and PYTHIA 8 generators are used. The Monte Carlo event type is 15144021, in which Λ_b^0 is forced to decay into the $J/\psi p\pi^-$ final state with the PHSP model.

B.2.2 Reconstruction and pre-selection

In this analysis the reconstruction of the Λ_b^0 candidate starts from the stripping line `FullDSTDiMuonJpsi2MuMuDetachedLine` in the `DiMuon` stream of the stripping reconstruction, which different version, S21 for 2011, S21r1 for 2012, S24 for 2015, S28 for 2016, S29r2 for 2017, and S34 for 2018. The selection criteria in this stripping line is summarized in Table B.1. The J/ψ candidate is formed by two oppositely charged tracks consistent with muon hypotheses (`IsMuon`) with $p_T > 550\text{ MeV}/c$ and good track fit quality $\chi^2/\text{ndf} < 4$. The J/ψ candidate is required to have an invariant mass within the $\pm 100\text{ MeV}/c^2$ window around the known J/ψ mass^[126], and to have a vertex fit quality $\chi^2_{\text{vtx}} < 20$. The J/ψ candidate is consistent with originating from b -hadron decays by requiring its decay length significance (DLS) to be greater than three.

Comparing to the previous study^[13], the selection criteria is optimized, all differences between the new selection criteria and old study are summarized in Table B.2. To select good J/ψ candidates, a tightened PID cut $\text{DLL}_{\mu\pi} > 0$ is required for both muon tracks in the final state, and the dimuon invariant mass window is reduced to $[-48, 43]\text{ MeV}/c^2$ around the known J/ψ mass^[156]. The J/ψ mass resolution is around $13\text{ MeV}/c^2$. To reconstruction the Λ_b^0 candidate, the J/ψ candidate is combined with two opposite charged tracks, consistent with pions and protons respectively. This is achieved by PID cuts on the `ProbNN` variables: $\text{ProbNN}_\pi(\pi) > 0.2$ and $\text{ProbNN}_p(p) > 0.2$. The two hadronic tracks are required to have large transverse momenta, $p_T > 250\text{ MeV}/c$, inconsistent with originating from the primary vertex (PV), $\chi^2_{\text{IP}} > 9$. The Λ_b^0 candidate is required to have a good vertex fit quality, $\chi^2/\text{ndf} < 10$, with a displayed decay vertex, flight distance to primary vertex is larger than 1.5 mm . It should be consistent with being produced from PV by requiring $\chi^2_{\text{IP}} < 25$ and cosine value of the direction angle, $\text{DIRA} > 0.999$. And the χ^2 of closet approach distance between p and π^- is smaller than 20. The Λ_b^0 candidates with mass $5.1 < M(J/\psi p\pi^-) < 6.5\text{ GeV}/c^2$ are selected.

The $\Lambda_b^0 \rightarrow J/\psi p\pi^-$ decay chain is refitted with two sequential constraints using the `DecayTreeFitter` to improve the mass resolution: A) the J/ψ candidate mass constrained to its known value^[156] and the Λ_b^0 candidate constrained to originating from the PV; B) the invariant mass of the Λ_b^0 candidate constrained to its know value^[145], with the momenta of the

J/ψ , p and π^- daughters re-calculated according to this constraint.

It should be noted that the PID requirements on the hadron tracks are not applied when reconstructing the Λ_b^0 candidates in the simulation sample. The effect, instead, is considered using weights from the PID calibration (PIDCalib). The pion track is calibrated using pion tracks from the D^* tagged $D^0 \rightarrow K^-\pi^+$ decay, while the proton track is calibrated using proton tracks from the $\Lambda_c^+ \rightarrow pK^-\pi^+$ decay.

Events with Λ_b^0 candidates in both the simulation and the data samples are required to fire (TOS) the trigger sequences: at the HLT1 level by either of the `Hlt1DiMuonHighMass`, `Hlt1TrackMuon`, `Hlt1TrackMVADecision` and `Hlt1TwoTrackMVADecision` lines; and at the HLT2 level by either of the `Hlt2DiMuonDetachedJPsi` and `Hlt2TopoMu(2,3,4)BodyBBDT` lines.

Table B.1 Stripping selections of J/ψ candidates in the line `FullDSTDiMuonJpsi2MuMuDetachedLine`.

Quantity	Selections
<code>IsMuon(μ)</code>	= TRUE
$\text{DLL}(\mu - \pi)$	> 0
$p_T(\mu)$	$> 550 \text{ MeV}/c$
Track $\chi^2/\text{ndf}(\mu)$	< 4
$\Delta M(J/\psi)$	$< 100 \text{ MeV}/c^2$
Vertex $\chi^2(J/\psi)$	< 20
$\text{DLS}(J/\psi)$	> 3

Table B.2 Pre-selections of $\Lambda_b^0 \rightarrow J/\psi p\pi^-$ candidates between old Run 1 analysis and this one.

Quantity	Old Run 1	This analysis
1 All tracks χ^2/ndf	< 3	same
2 muon DLL(μ)	$> 0 \& \text{ISMUON}$	same
3 p_T of muon	$> 550 \text{ MeV}$	same
4 p_T of hadron	$> 250 \text{ MeV}$	same
5 vertex of J/ψ	$\chi^2 < 16$	same
6 mass window of J/ψ	$[-48, 43] \text{ MeV}$	same
7 χ_{vs}^2 of hadron	> 9	same
8 PID of π	$\text{ProbNNpi} \times (1 - \text{ProbNNpi}) > 0.5$	$\text{ProbNNpi} > 0.2$
9 PID of p	$\text{ProbNNpi} > 0.1$	$\text{ProbNNpi} > 0.2$
10 χ_{IP}^2 of Λ_b^0	< 25	same
11 Λ_b^0 vertex	$\chi_{\text{vtx}}^2/\text{ndf} < 10$	same
12 DIRA of Λ_b^0	> 0.9995	> 0.999
13 χ_{τ}^2 of Λ_b^0	> 9	-
14 $p(p)$	$> 10 \text{ GeV}$	-
15 Flight distance of Λ_b^0	-	$> 1.5 \text{ mm}$
16 DOCA χ^2 of $p\pi^-$	-	< 20

B.2.3 Reflections vetoing

Since the decays of $B^0 \rightarrow J/\psi K\pi$, $B_s^0 \rightarrow J/\psi K^+K^-$, $\Lambda_b^0 \rightarrow J/\psi pK^-$ have much larger branching fractions than the $\Lambda_b^0 \rightarrow J/\psi p\pi^-$ decay, even after the PID requirements on the hadron tracks, the $\Lambda_b^0 \rightarrow J/\psi p\pi^-$ sample is still potentially contaminated by these decays. To investigate the effects of the reflections from these decays, the invariant mass of the Λ_b^0 candidate in the $\Lambda_b^0 \rightarrow J/\psi p\pi^-$ sample is re-calculated with the proton assumed as a pion or kaon and/or the pion assumed as a kaon or proton. Figure B.3 shows these re-calculated invariant mass distributions for those $\Lambda_b^0 \rightarrow J/\psi p\pi^-$ candidates within the $\pm 20 \text{ MeV}/c^2$ mass window ($\approx 3\sigma$) around the known Λ_b^0 mass^[156]. Clear contamination with the $B^0 \rightarrow J/\psi K\pi$, $B_s^0 \rightarrow J/\psi KK$ and $\Lambda_b^0 \rightarrow J/\psi pK^-$ decays are observed, as shown by the narrow peaks around the known B^0 , B_s^0 and Λ_b^0 masses in the top right, bottom left and bottom middle plots in Fig. B.3. The contribution of $B_{(s)}^0 \rightarrow J/\psi \pi\pi$ decays is insignificant. The contamination from $B^0 \rightarrow J/\psi K\pi$ is vetoed if: $M(J/\psi[p \rightarrow K]\pi)$ sits in the $\pm 22 \text{ MeV}/c^2$ window around the known B^0 mass^[156], or $M(J/\psi[p \rightarrow \pi][\pi \rightarrow K])$ sits in the $\pm 22 \text{ MeV}/c^2$ window around the known B^0 mass and $\text{ProbNNpi}(p) > 0.1 \& \text{ProbNNk}(\pi) > 0.1$. The contamination with the $\Lambda_b^0 \rightarrow J/\psi pK^-$ decay is vetoed if: $M(J/\psi p[\pi^- \rightarrow K])$ sits in the $\pm 22 \text{ MeV}/c^2$ window around the known Λ_b^0 mass^[156] and $\text{ProbNNk}(\pi) > 0.2$, or $M(J/\psi[p \rightarrow K][\pi \rightarrow p])$ sits in the $\pm 22 \text{ MeV}/c^2$ window around the known B^0 mass and $\text{ProbNNk}(p) > 0.1 \& \text{ProbNNp}(\pi) > 0.1$. Besides, the reflection of $B_s^0 \rightarrow J/\psi K^+K^-$ decay is removed in this case: $M(J/\psi[p \rightarrow K][\pi^- \rightarrow K])$ sits in the $\pm 22 \text{ MeV}/c^2$ window around the known B_s^0 mass^[156].

A large fraction of $\Lambda_b^0 \rightarrow J/\psi p\pi^-$ candidates come from the decay $\Lambda_b^0 \rightarrow J/\psi \Lambda^0$ with $\Lambda^0 \rightarrow p\pi^-$, which is not interesting in this analysis. These events are removed if the invariant mass $M(p\pi^-)$ locates in the $\pm 5 \text{ MeV}/c^2$ window around the known Λ^0 mass^[156].

During the invariant mass vetoing, the mass resolutions are determined by fitting the invariant mass distribution in a narrow region around the signal peak; the signal mass shape is described by double-sided crystal ball function (DSCB) with tail parameters fixed to the $\Lambda_b^0 \rightarrow J/\psi p\pi^-$ simulation, while the background is simply described by a linear function.

B.2.4 Multivariate analysis

The multivariate analysis (MVA) is used to further suppress the background. In the MVA training the signal sample is from the $\Lambda_b^0 \rightarrow J/\psi p\pi^-$ simulation using the PHSP model, while the background sample is from the upper sideband of the $\Lambda_b^0 \rightarrow J/\psi p\pi^-$ invariant mass distribution, $M(J/\psi p\pi) \in [5.67, 5.80] \text{ GeV}/c^2$. These samples are randomly split into two

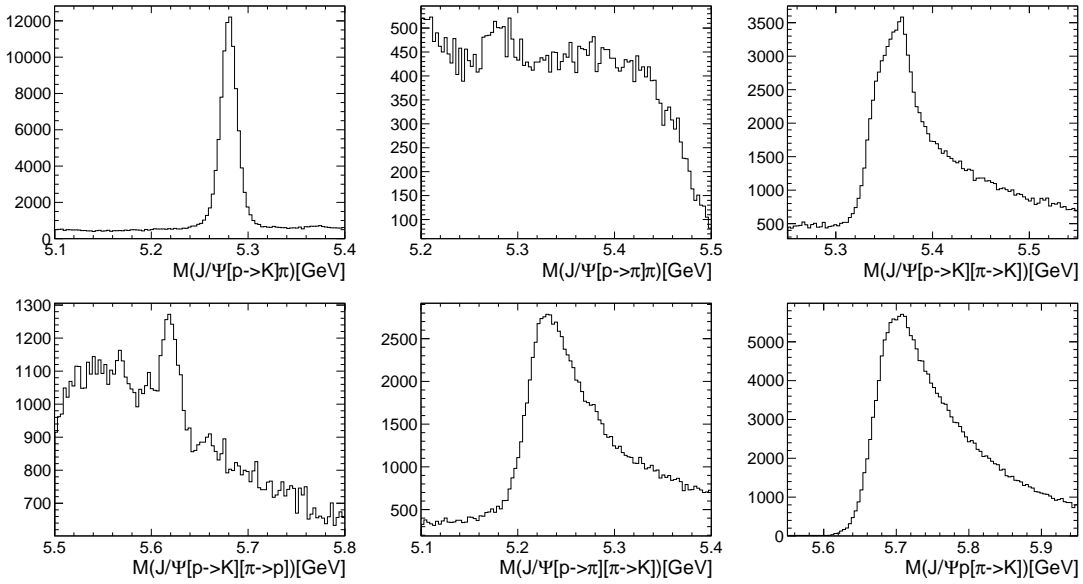


Figure B.3 Invariant mass distributions of the $\Lambda_b^0 \rightarrow J/\psi p\pi^-$ candidate with the p and the π^- assumed to be other hadrons for those Λ_b^0 candidates in the ± 20 MeV/ c^2 mass window around the known Λ_b^0 mass. The labels $h \rightarrow h'$ indicate that the h hadron in the $\Lambda_b^0 \rightarrow J/\psi p\pi^-$ decay is assumed as a h' hadron.

halves, one for the training and the other for the test. Different from the previous study, the PID information variables are included in the MVA classification. All used variables are listed in Table. B.3. The smaller value of the two muon PID variables ($DLL_{\mu\mu}$); the smaller value of the χ^2_{IP} of the two muon tracks; the smaller value of the χ^2_{IP} of the two hadron tracks; the arithmetic addition of the p_T of the two hadrons; the DIRA, the flight distance (FD), the p_T , the χ^2_{IP} and the vertex fit quality (χ^2_{vtx}/ndf) of the Λ_b^0 candidate. the PID variables of hadrons. Besides, the Run 1 and Run 2 samples are studied separately. The distributions of these variables of Run 1 sample for the signal in the simulation sample and the background in the data sideband are shown in Figure. B.4, corresponding Run 2 distributions are shown in Appendix. ??.

The BDTG method is used as the default method, and the overtraining test for the BDTG method is given in the right plot of Figure. B.5 for both Run 1 and Run2 samples. The BDTG discriminant distributions for the training samples are consistent with those in the test samples. No effect of overtraining is observed. The working point of the BDTG value is optimized by maximizing the figure of merit (FoM) of the signal significance, defined as $\epsilon_S/\sqrt{S+B}$. The ϵ_S is the signal efficiency for a specified BDTG cut and is determined from the simulation sample, while S (B) is the number of the signal (background) events in the $\pm 3\sigma$ region around the known Λ_b^0 mass in the $J/\psi p\pi^-$ invariant mass distribution of the data. In Figure. B.6, the distribution of the FoM as a function of the BDTG cut value is given, and the value of 0.88 for Run 1 and 0.9 for Run 2 are determined as the default working points.

Table B.3 Variables used in TMA between previous Run1 and this study.

	Previous Run 1	This analysis
1	χ_{vtx}^2 of Λ_b^0	same
2	sum p_T of hadrons	same
3	χ_{IP}^2 of Λ_b^0	same
4	DIRA of Λ_b^0	same
5	min χ_{IP}^2 of hadrons	same
6	min χ_{IP}^2 of muon	same
7	FD of Λ_b^0	same
8	p_T of Λ_b^0	same
9	min PID of muon	same
10	-	ProbNNp of p
11	-	ProbNNpi of π^-
12	-	momentum of p

B.3 Invariant B mass fit and Dalitz plot distributions

After the selections, the sample of $\Lambda_b^0 \rightarrow J/\psi p\pi^-$ decays consists of the signal, the combinatorial background and the $\Lambda_b^0 \rightarrow J/\psi pK^-$ relections. The invariant mass distribution of the signal is described by a DSCB function, an alternative fit with the Hypatia model is also performed; the shape of the combinatorial background is described by an exponential function; and the shapes of the $\Lambda_b^0 \rightarrow J/\psi pK^-$ reflections are determined from simulation. A simulation $\Lambda_b^0 \rightarrow J/\psi pK^-$ sample is used to determine the shapes of the reflections. The candidate is reconstructed as $\Lambda_b^0 \rightarrow J/\psi p[K^- \rightarrow \pi^-]$, and all selections except the PID requirements used to select $\Lambda_b^0 \rightarrow J/\psi p\pi^-$ candidates in this analysis are applied to these candidates. Each event that passes the selections is assigned a weight to account for the PID efficiency, and the weight is determined from the PIDCalib package. By filling the invariant mass under $J/\psi p\pi^-$ hypotheses into histograms with the PID weight, the shapes are determined, as shown in Fig. B.7. The histogram is converted to a histogram-PDF in the fit. It should be noted that the shape is found to be insensitive to the decay model ^①, so the shape determined from the simulation with the PHSP decay model is good enough to represent the complicated Dalitz distribution seen in the data.

In Figure. B.8, the fitted invariant mass distributions of the $\Lambda_b^0 \rightarrow J/\psi p\pi^-$ candidate are shown for both Run 1 and Run 2 samples. The signal yields given by the fit are 1960 ± 53 for Run1 and 8607 ± 111 for Run2, The $J/\psi p\pi^-$ signal peak has a mean value of $5620.1 \pm 0.1 \text{ MeV}/c^2$.

The invariant mass fit result is used to calculate the *sWeights* for both the signal and background components. In Figure. B.9, the “Dalitz” plots using the invariant mass squared

^① The shape determined in different slices of $M(p\pi)$ is very similar.

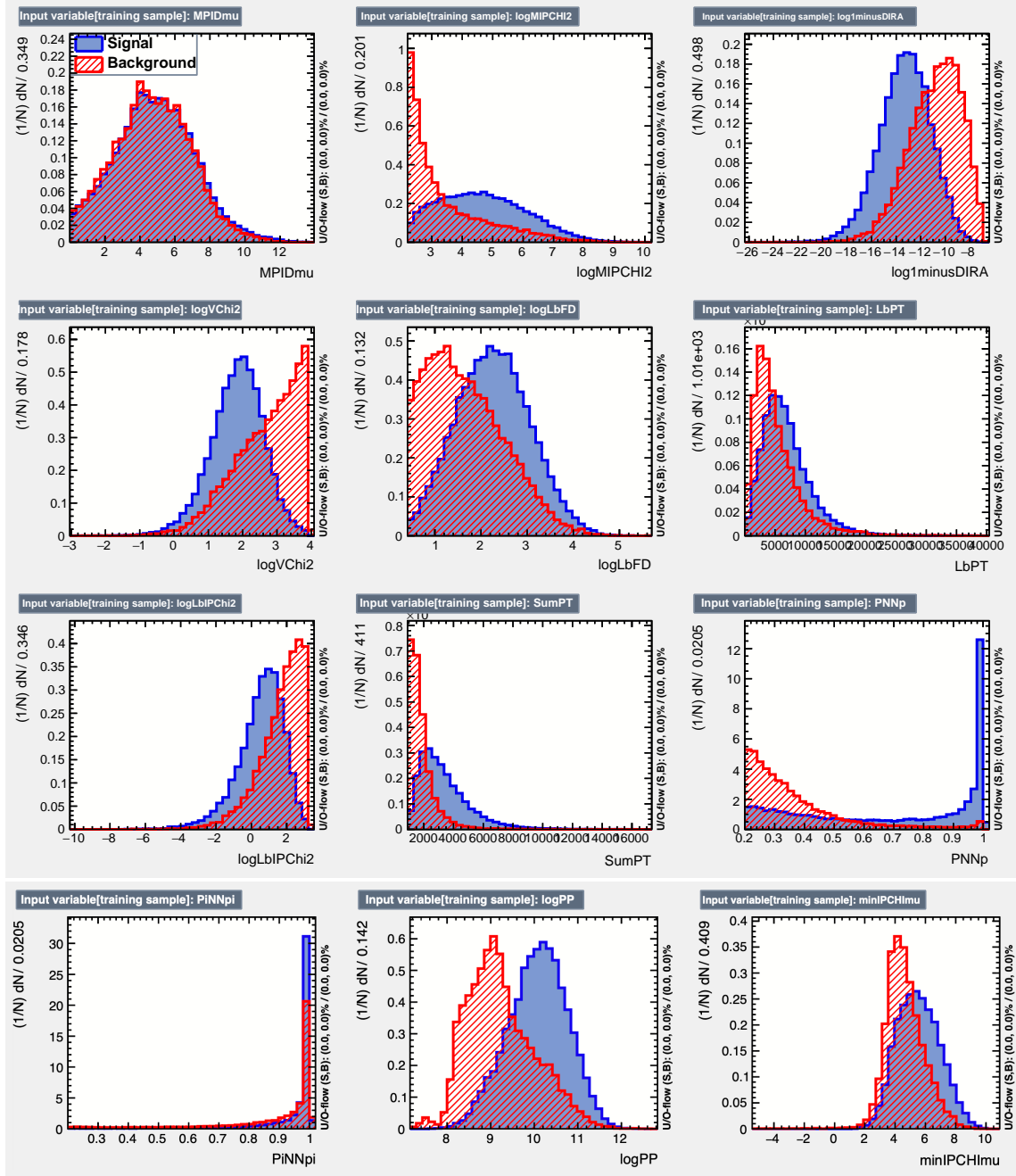


Figure B.4 Discriminating variables used in the MVA training of Run 1 sample.

are shown, $m_{p\pi^-}^2$ vs $m_{J/\psi p}^2$, and $m_{p\pi^-}^2$ vs $m_{J/\psi\pi}^2$ as independent variables. Here, the Run 1 and Run 2 are put together. As expected, significant N^* contributions are seen, especially in the region around $m^2 p\pi^- = 2 \text{ GeV}^2/c^4$. It seems that narrow belt around the $P_c(4450)$ region at about $20 \text{ GeV}^2/c^4$ in the $J/\psi p$ mass-squared is visible. While many events concentrate in a limited window around $m_{p\pi}^2 = 6 \text{ GeV}^2/c^4$ and $m_{J/\psi p}^2$ between 18 to $20 \text{ GeV}^2/c^4$, which could be due to the P_c contribution. These events are also presented at the region of $m_{J/\psi\pi^-}^2$ around $17 \text{ GeV}^2/c^4$ with $m_{p\pi}^2$ around $6 \text{ GeV}^2/c^4$.

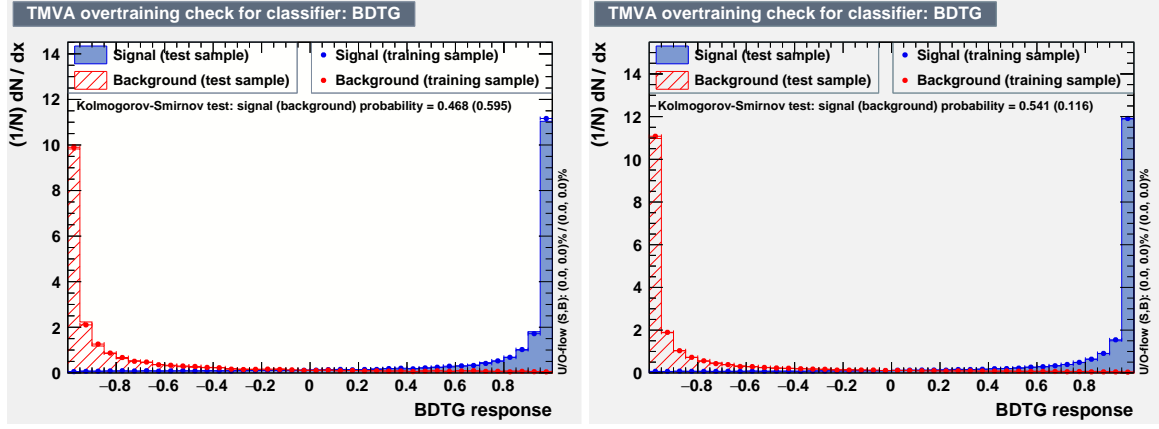


Figure B.5 The BDTG output distribution for signals and the background in the training sample and the test sample of Run 1(left) and Run 2(right) samples.

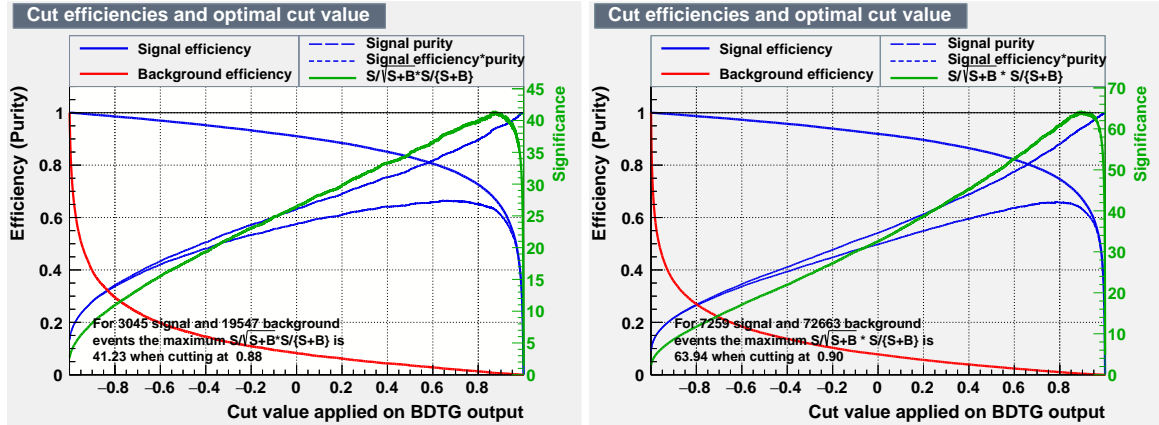


Figure B.6 Signal significance (arbitrary unit) for different BDTG cut values of Run 1(left) and Run 2(right) samples.

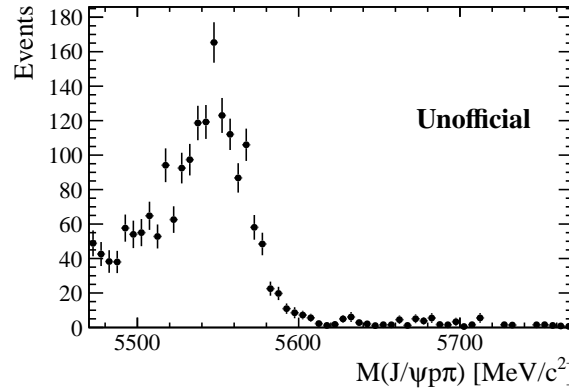


Figure B.7 Distribution of the invariant mass of $\Lambda_b^0 \rightarrow J/\psi p K^-$ candidates reconstructed as $\Lambda_b^0 \rightarrow J/\psi p\pi^-$.

B.4 Amplitude analysis

Then, a full amplitude analysis is performed to examine the contributions of the two P_c states and possible Z_c state. Isobar model approach is used in which each resonance is described

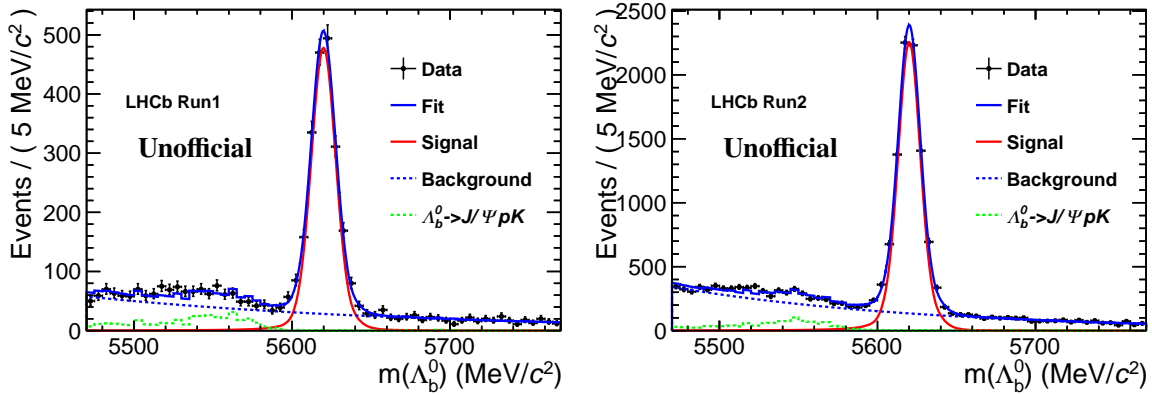


Figure B.8 Invariant mass distribution of the $\Lambda_b^0 \rightarrow J/\psi p\pi^-$ decay and the fitted curve for Run 1(left) and Run 2(right) samples.

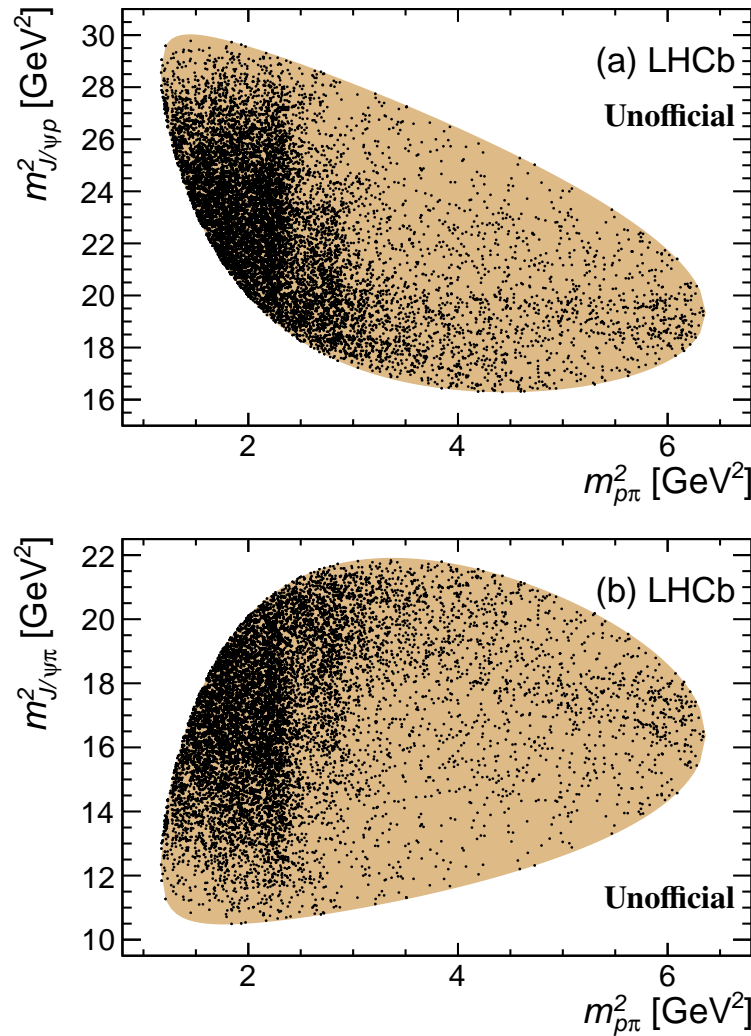


Figure B.9 Invariant mass squared of $p\pi$ versus either $J/\psi p$ (top) or $J/\psi \pi$ (bottom) for candidates with $sWeights$ to subtract background contribution. The hatched area shows the kinematic allowed region.

by a Breit-Wigner. The amplitude formalism has been described in the $B^+ \rightarrow J/\psi pK^+$ analysis above, Section 3.4, by replacing variables with the particle K^+ by these of the π^- , the p by these of the ϕ , and B^+ by these of the Λ_b^0 . There are 6 fitting observables: invariant mass of $p\pi$, $m(p\pi)$, and five decay angles denoted as Ω , including (i) cosine of helicity angle of the Λ_b^0 decays $\cos \theta_{\Lambda_b^0}$; (ii) cosine of helicity angle of the N^* decays $\cos \theta_{N^*}$; (iii) cosine of helicity angle of the J/ψ decays $\cos \theta_{J/\psi}$; (iv) angle between Λ_b^0 and N^* decay planes ϕ_π ; and (iv) angle between Λ_b^0 and J/ψ decay planes ϕ_μ .

Except for the exotic baryonic P_c states, exotic mesonic states $Z_c^- \rightarrow J/\psi\pi^-$ could also contribute to this decay. The matrix elements for the $J/\psi N^*$, $P_c^+\pi^-$ and $J/\psi\pi^-$ decay chains, are similar to that in the previous $\Lambda_b^0 \rightarrow J/\psi p\pi^-$ study^[13]. Furthermore, the proton and muon helicity states in each of the exotic decay chains must be expressed in the basis of helicities in the N^* decay chain, which is incorporated in the total decay matrix element as follows

$$|\mathcal{M}|^2 = \sum_{\lambda_{\Lambda_b^0}} \sum_{\lambda_p} \sum_{\Delta\lambda_\mu} \left| \mathcal{M}_{\lambda_{\Lambda_b^0}, \lambda_p, \Delta\lambda_\mu}^{N^*} + e^{i\Delta\lambda_\mu\alpha_\mu} \sum_{\lambda_p^{P_c}} d_{\lambda_p^{P_c}, \lambda_p}^{\frac{1}{2}}(\theta_p) \mathcal{M}_{\lambda_{\Lambda_b^0}, \lambda_p^{P_c}, \Delta\lambda_\mu}^{P_c} \right. \\ \left. + e^{i\Delta\lambda_\mu\alpha_\mu^{Z_c}} \sum_{\lambda_p^{Z_c}} e^{i\lambda_p^{Z_c}\alpha_p^{Z_c}} d_{\lambda_p^{Z_c}, \lambda_p}^{\frac{1}{2}}(\theta_p^{Z_c}) \mathcal{M}_{\lambda_{\Lambda_b^0}, \lambda_p^{Z_c}, \Delta\lambda_\mu}^{Z_c} \right|^2, \quad (\text{B.1})$$

where the matrix element for each of the decay chains is denoted by the superscripts, and θ_p ($\theta_p^{Z_c}$) is the polar angle in the p rest frame between the boost directions from the N^* and P_c^+ (Z_c^-) rest frames, and α_μ ($\alpha_\mu^{Z_c}$) is the azimuthal angle correcting for the difference between the muon helicity states in the N^* and P_c^+ (Z_c^-) decay chains. Unlike in the P_c^+ chain, the azimuthal angle ($\alpha_\mu^{Z_c}$) aligning the two proton helicity frames is not zero.

B.4.1 Likelihood construction with sPlot technique

A so-called *sFit* approach is used in this analysis. In such approach the total PDF is equal to the signal PDF, as the background is subtracted from the log-likelihood sum using the *sWeights*. The signal PDF is obtained by multiplying the decay matrix element \mathcal{M} squared with the selection efficiency, $\epsilon(m_{p\pi}, \Omega)$,

$$\mathcal{P}_{\text{sig}}(m_{p\pi}, \Omega | \vec{\omega}) = \frac{1}{I(\vec{\omega})} |\mathcal{M}(m_{p\pi}, \Omega | \vec{\omega})|^2 \Phi(m_{p\pi}) \epsilon(m_{p\pi}, \Omega), \quad (\text{B.2})$$

where $\Phi(m_{p\pi})$ is the phase space function equal to $p \cdot q$, with p being the momentum of the $p\pi$ system (*i.e.* K^*) in the Λ_b^0 rest frame, and q being the momentum of π^- in the K^* rest frame, and $I(\vec{\omega})$ is the normalization integral. The fitting parameters, $\vec{\omega}$, represent independent helicity

or LS couplings, and masses and widths of resonances (or Flatté parameters).

This quasi-log-likelihood sum is scaled by a constant factor, $s_W \equiv \sum_i W_i / \sum_i W_i^2$ to account for the effect of the background subtraction on the statistical uncertainty. To determine $\vec{\omega}$,

$$\begin{aligned} -2 \ln \mathcal{L}(\vec{\omega}) &= -2s_W \sum_i W_i \ln \mathcal{P}_{\text{sig}}(m_{p\pi i}, \Omega_i | \vec{\omega}) \\ &= -2s_W \sum_i W_i \ln |\mathcal{M}(m_{p\pi i}, \Omega_i | \vec{\omega})|^2 + 2s_W \ln I(\vec{\omega}) \sum_i W_i \\ &\quad - 2s_W \sum_i W_i \ln [\Phi(m_{p\pi i}) \epsilon(m_{p\pi i}, \Omega_i)]. \end{aligned} \quad (\text{B.3})$$

is minimized. The last term does not depend on the fitted parameters $\vec{\omega}$ and is therefore dropped. The efficiency still appears in the normalization integral. The integration is done without the need to parameterize the efficiency, by summing the matrix element squared over the simulated events that are generated uniformly in phase space and pass through the detector modelling and the data selection procedure,

$$\begin{aligned} I(\vec{\omega}) &\equiv \int |\mathcal{M}(m_{p\pi}, \Omega | \vec{\omega})|^2 \Phi(m_{p\pi}) \epsilon(m_{p\pi}, \Omega) dm_{p\pi} d\Omega \\ &\propto \sum_j^{N_{\text{MC}}} w_j^{\text{MC}} |\mathcal{M}(m_{p\pi j}, \Omega_j | \vec{\omega})|^2, \end{aligned} \quad (\text{B.4})$$

where w_j^{MC} are the weights given to the simulated events to improve the agreement between data and simulations.

As described above, the PID cuts on the hadron tracks, p, π candidates are not applied in the simulation sample, instead their effect is considered by the PID weights determined using the `PIDCalib` package. The PID weight is the probability (efficiency) of a track passing a specific PID requirement, and is a function of the track momentum, pseudo-rapidity and event multiplicity. For each Λ_b^0 candidate, the weight is determined as the product of the two PID weights on p and π .

B.4.2 N^* resonances

The conventional resonances contributing to the Λ_b^0 channel are excited N^* states that decay to $p\pi^-$. The isospin violated decay $\Lambda_b^0 \rightarrow J/\psi \Delta^*$, $\Delta^* \rightarrow p\pi^-$ is expected to be suppressed. A preliminary study on similar decay gives the isospin violated decay to the allowed decay $\Gamma(\Lambda_b^0 \rightarrow J/\psi \Sigma)/\Gamma(\Lambda_b^0 \rightarrow J/\psi \Lambda) < 1\%$ at 95% confidence level. Thus Δ^* is not considered in this study.

Table B.4 lists total 14 N^* states that we consider. They are all established resonances (overall status 3 or 4 stars). The Breit-Wigner amplitude is used for all the resonances, except for the $N(1535)$ state, that is described by a Flatté function. Because the resonance has significant coupling to ηN channel whose open threshold is very close to the mass of the state. In the πN elastic scattering, the resonance is shown by a sharp cusp^[44,45]. Since the angular momenta in the two coupling channels are all zero, the Flatté function can be simplified as

$$F(m|M_0, g_{N\pi}, g_{n\eta}) = \frac{1}{M_0^2 - m^2 - i(g_{N\pi}^2 \rho_{N\pi}(m) + g_{n\eta}^2 \rho_{n\eta}(m))}, \quad (\text{B.5})$$

where $\rho_k(m) = 2q_k(m)/m$ is the phase-space factor, g_k is the coupling, and q_k is the momentum of either π or η in the K^* rest frame for channel $k = N\pi$ or $n\eta$. Here N can be either a proton p or a neutron n ; their mass difference is ignored and use the proton mass instead. When $m < m_n + m_\eta$, $q_{n\eta}$ becomes imaginary for continuance, *i.e.*

$$q_k(m) = i \frac{\sqrt{|(m^2 - (m_n + m_\eta)^2)(m^2 - (m_n - m_\eta)^2)|}}{2m}, \quad (\text{B.6})$$

where m_n and m_η are the masses of n and η , respectively. According to Ref [43], $g_k^2 \rho_k(M_0) = M_0 \mathcal{B}_k \Gamma_0$, where M_0 and Γ_0 are the Breit-Wigner mass and width of the resonance respectively, while \mathcal{B}_k is the branching fraction of the resonance decaying to the channel k . $\mathcal{B}_{n\eta}/\mathcal{B}_{N\pi} = (0.95 \pm 0.03)\%$ is used^[145], and assume that the two channels saturate the full decay width of the resonance.

An S-wave non-resonant (NR) contribution for $J^P = 1/2^- p\pi^-$ is included. The mass dependent term is described by the form $1/m^2$ which is found to be significant improving the fit.

Due to the limited sample size, the fit cannot converge including all resonances with all helicity couplings. Each N^* resonance is described by maximum 4 (6) independent LS couplings for the spin equal to (great than) $1/2$, where L is the orbital angular momentum of the Λ_b^0 decay and S is the total spin of the $J/\psi N^*$ system. High L couplings are expected to be suppressed by the angular momentum barrier, so the couplings is selected by first allowing low L contribution. Table B.4 lists the models including N^* states with independent LS couplings used. The "Nominal Model" (NM) contains 10 N^* resonances and a NR component described by 40 free parameters, in which each L component of each resonance that improves the $-2 \ln \mathcal{L}$ great than 9 units. "Extended Model" (EM) contains the maximum number free parameters that can achieve a converged fit. As the "Extended" model have too many parameters and hard to obtain accuracy uncertainty, it will be used as the systematic study and the significance

evaluation.

Table B.4 The N^* resonances used in the different fits. Parameters are taken from the PDG^[145]. The number of LS couplings is also listed for the “Nominal Model” (NM) and “Extended Model” (EM). To fix overall phase and magnitude conventions, which otherwise are arbitrary, the $N(1535)$ coupling of lowest LS is set to be (1,0). A zero entry means the state is excluded from the fit.

State	J^P	M_0 (MeV)	Γ_0 (MeV)	NM	EM
$N(1440)$	$1/2^+$	1430	350	4	4
$N(1520)$	$3/2^-$	1515	115	3	3
$N(1535)$	$1/2^-$	1535	150	3	3
$N(1650)$	$1/2^-$	1655	140	4	4
$N(1675)$	$5/2^-$	1675	150	5	5
$N(1680)$	$5/2^+$	1685	130	3	3
$N(1700)$	$3/2^-$	1700	150	3	3
$N(1710)$	$1/2^+$	1710	100	4	4
$N(1720)$	$3/2^+$	1720	250	5	5
$N(1875)$	$3/2^-$	1875	250	3	3
$N(1900)$	$3/2^+$	1900	200	0	3
$N(2190)$	$7/2^-$	2190	500	0	3
$N(2300)$	$1/2^+$	2250	400	0	3
NR $p\pi$	$1/2^-$	-	-	4	4
Free parameters				82	100

B.4.3 Parameters describing the P_c^+ states

Because of limited statistics, the strategy is to check whether or not the data is consistent with the $\Lambda_b^0 \rightarrow J/\psi p K^-$ decays studied previously^[19], thus it is required to use constraints as many as possible from that study.

Each P_c^+ state is described by total 10 parameters: 2 parameters for mass and width, 6 for independent helicity couplings of the $P_c^+ \rightarrow J/\psi p$ decay, $\mathcal{H}_{\lambda_\psi^{P_c}, \lambda_p^{P_c}}^{P_{cj} \rightarrow \psi p}$, and 2 for the complex LS coupling ratio of the $\Lambda_b^0 \rightarrow P_c^+ \pi^-$ decays, $B_{L=J_{P_c}+1/2}/B_{L=J_{P_c}-1/2}$. To obtain a reliable fit, some free parameters are reduced: for each P_c^+ state, the mass and width to the measured values from the $\Lambda_b^0 \rightarrow J/\psi p K^-$ decay is fixed^[19]. Besides, the smallest allowed orbital angular momentum is $L = 2$ for P_c^+ states. Then, totally 2 free parameters for P_c^+ states are obtained.

In the nominal model, all the P_c^+ states have negative parity according to the prediction of molecular model, $J^P = 1/2^-$ for $P_c(4312)$ and $P_c(4400)$, and $J^P = 3/2^-$ for $P_c(4380)$ and $P_c(4457)$ ^[114], this spin-parity assignment is used in this analysis.

Appendix C Z_{cs} states in $B^+ \rightarrow J/\psi \phi K^+$ decay

C.1 Angular moments

The unnormalized Legendre moments defined as

$$\langle P_\ell^U \rangle = \sum_{i=1}^{N_{\text{events}}} \frac{1}{\epsilon_i} P_\ell(\cos \theta), \quad (\text{C.1})$$

where $P_\ell(\cos \theta)$ is the Legendre polynomial of order ℓ and ϵ_i is the efficiency for each event, depending on its phase-space location. Structures related to a spin J resonance described by the helicity angle θ , can show up in the Legendre moments of rank up to $l = 2J$, or up to $l = J + J'$ in interferences of J and J' amplitudes. Mass dependence of the Legendre moments can provide hints about resonances present in the data, since their quantum numbers restrict J values. Unfortunately, reflections of decays from the other decay chain(s) can generate mass dependent variations of the moments at any rank, obscuring interpretation of the data.

The moments distribution is obtained by weighting each events by a weight $\frac{1}{\epsilon_i} P_\ell(\cos \theta)$. The background contribution in the data is subtracted, and the signal contribution is achieved as the moments distribution of events in the signal region minus the moments distribution of sideband events, the latter is scaled by the ratio of background yields between the signal and the sideband regions. In Fig. C.1 we show the Legendre moments vs. $m_{J/\psi \phi}$ using cosine helicity angle of $J/\psi \phi$ as the argument of the polynomial. The nominal model describes the data reasonably well. Improvements over the old Run 1 model are clearly visible in several moments.

In Fig. C.2, the Legendre moments vs. $m_{\phi K}$ using cosine helicity angle of ϕK are shown. The agreement is again reasonable, but the differences between the nominal and old Run 1 model are smaller.

The Legendre moments vs $m_{J/\psi K}$ using cosine helicity angle of $J/\psi K$ are shown in Fig. C.3. Some improvements of the nominal model as compared to the old Run 1 model are see.

C.2 Model-independent

To cross-check the results obtained with the Breit-Wigner sum approach, we replace selected partial waves, one at a time, with a model-independent (MI) description of the

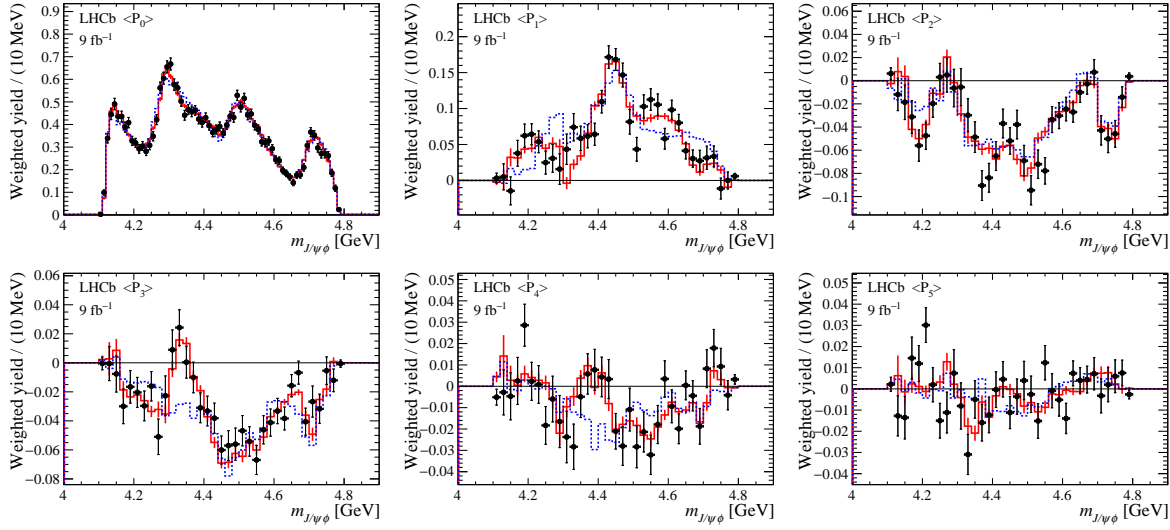


Figure C.1 Angular moments of $J/\psi\phi$ helicity angle as a function of $m_{J/\psi\phi}$ compared between the background subtracted data, and PDFs from run1 model (blue dashed) and the nominal model (red solid). The $\chi^2/n\text{bin}$ for the fit of nominal model (run1 model) are 83(136)/69, 59(117)/35, 48(89)/35, 33(89)/35, 42(81)/35, 55(65)/35 for order from 0 to 5, respectively.

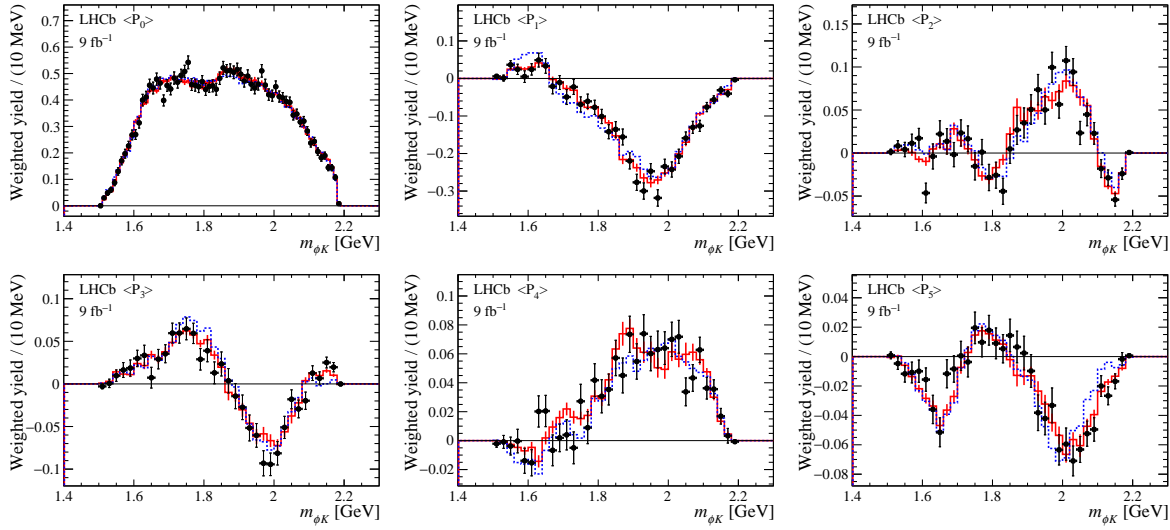


Figure C.2 Signal angular moments of ϕK helicity angle as a function of $m_{\phi K}$ compared between the background subtracted data, and PDFs from run1 model (blue dashed) and the nominal model (red solid). The $\chi^2/n\text{bin}$ for the fit of nominal model (run1 model) are 66(79)/69, 37(86)/35, 49(48)/35, 35(59)/35, 46(44)/35, 36(74)/35 for order from 0 to 5, respectively.

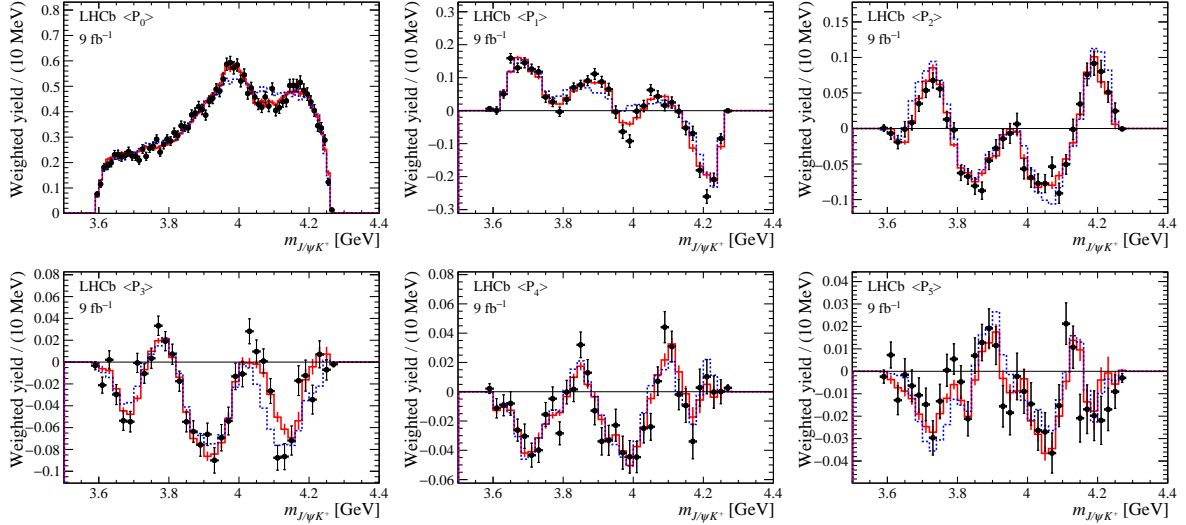


Figure C.3 Angular moments of $J/\psi K$ helicity angle as a function of $m_{\phi K}$ compared between the background subtracted data, and PDFs from run1 model (blue dashed) and the nominal model (red solid). The χ^2/n_{bin} for the fit of nominal model (run1 model) are 77(138)/69, 50(108)/35, 30(75)/35, 60(81)/35, 31(41)/35, 44(68)/35 for order from 0 to 5, respectively.

complex amplitude describing the mass dependence. We first investigate $J^P = 1^+ Z \rightarrow J/\psi K$ partial wave in which we use two BW poles in the nominal model. The other resonances are described by BW as done in the nominal fit, since the data are unable to constraint many waves in MI approach at the same time. i The BW functions for the two $1^+ Z$'s are replaced by complex numbers c_i , where $i = 1, \dots, 25$, representing this wave in 27 MeV bins of $m_{J/\psi K}$. The MI amplitude at any value of $m_{J/\psi K}$ is returned by two cubic splines for the Real and Imaginary parts of c_i . To be more specific, the mass dependent term R for a wave of Z_j is reformed as

$$R_{Z_j}(m_{J/\psi K}) = B'_{L_B^{Z_j}}(p, p_0, d) \left(\frac{p}{M_B} \right)^{L_B^{Z_j}} c_i(m_{J/\psi K}) \quad (\text{C.2})$$

Here p_0 is calculated using the center mass of $m_{J/\psi K}$ (*i.e.* $(m_{J/\psi K}^{\min} + m_{J/\psi K}^{\max})/2$), and L_B takes the lowest allowed value. Comparing the above equation with Eq. (3.19), the MI complex amplitude include BW function and the Blatt-Weisskopf function of resonance decay.

To simplify, one MI is used to represent all LS partial waves of $1^+ Z$ contributions. We compare this fit and the model-dependent nominal BW-sum results for the amplitude squared and complex phase in a function of $m_{J/\psi K}$ in Fig. C.4. The corresponding Argand plot is shown in Fig. C.5. The MI study confirms that two Z states are needed in 1^+ partial wave.

Next, we examine X waves, one at a time. The amplitude squared and phase motivation of the smallest L wave are shown Fig. C.6 and C.7 for the 1^+ and 0^+ ⁽¹⁾ components, respectively.

⁽¹⁾ The 0^+ result is obtained without the $Z(4220)$ state, to remove strong negative interference between $0^+ X$ and $Z(4220)$.

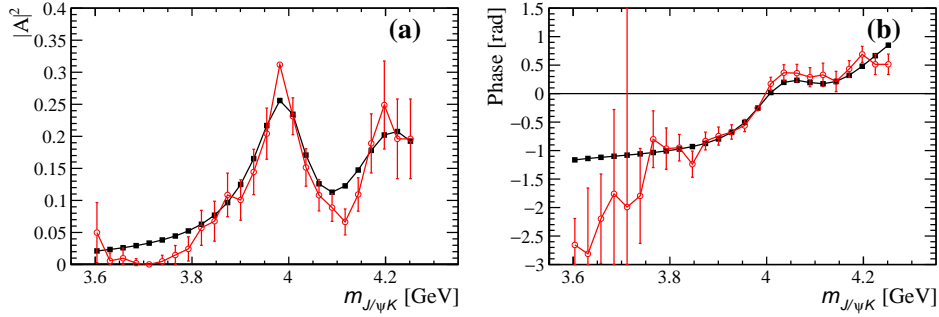


Figure C.4 (a) Amplitude squared and (b) phase motion for $1^+ Z$ wave obtained from the model-independent method (red open) and the nominal BW-sum fit (black solid). The BW-sum model has poles at $M_0 - i\Gamma_0/2 = 4003 - i131/2$ and $4216 - i233/2$ MeV, obtained from sum of the lowest L waves for a reference.

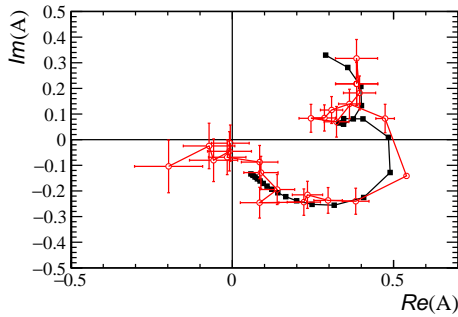


Figure C.5 Argand plot of $1^+ Z$ waves obtained from the model-independent method (red open) and the nominal BW-sum fit (black solid). The BW-sum model has poles at $M_0 - i\Gamma_0/2 = 4003 - i131/2$ and $4216 - i233/2$ MeV, obtained from sum of the lowest L waves for a reference.

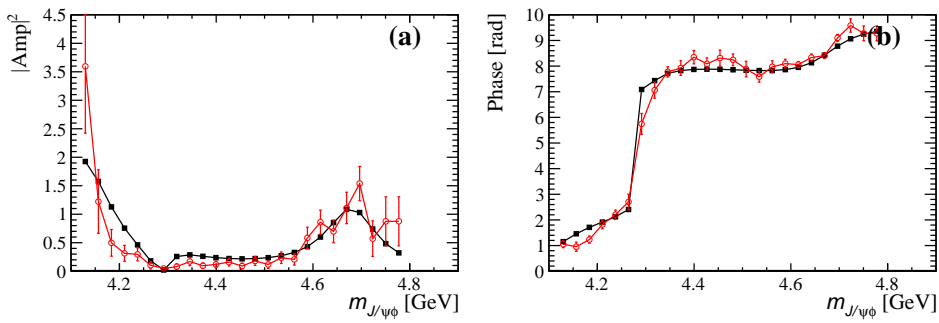


Figure C.6 (a) Amplitude squared and (b) phase motion for $1^+ X$ lowest L wave obtained from the model-independent method (red open) and the nominal BW-sum fit (black solid). The BW-sum model has poles at $M_0 - i\Gamma_0/2 = 4118 - i162/2$, $4294 - i53/2$ and $4684 - i126/2$ MeV, obtained from sum of the lowest L waves for a reference.

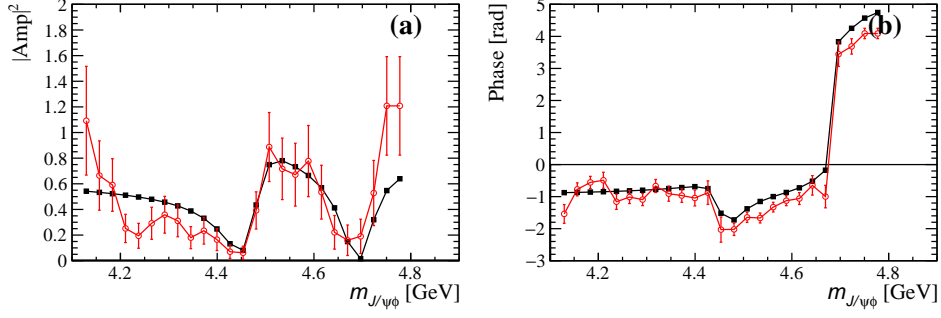


Figure C.7 (a) Amplitude squared and (b) phase motion for 0⁺ X lowest L wave obtained from the model-independent method (red open) and the nominal BW-sum fit (black solid). The BW-sum model has poles at $M_0 - i\Gamma_0/2 = 4474 - i 77/2, 4694 - i 87/2$ MeV and the NR contribution, obtained from sum of the lowest L waves for a reference.

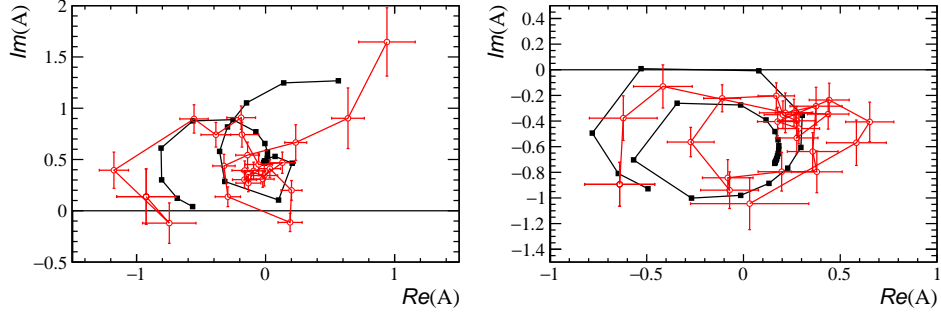


Figure C.8 (Left) Argand plot of 1⁺ X waves obtained from the model-independent method (red open) and the nominal BW-sum fit (black solid). The BW-sum model has poles poles at $M_0 - i\Gamma_0/2 = 4118 - i 162/2, 4294 - i 53/2$ and $4684 - i 126/2$ MeV, obtained from sum of the lowest L waves for a reference. (Right) Argand plot of 0⁺ X waves obtained from the model-independent method (red open) and the nominal BW-sum fit (black solid). The BW-sum model has poles poles at $M_0 - i\Gamma_0/2 = 4118 - i 162/2, 4294 - i 53/2$ and $4684 - i 126/2$ MeV, obtained from sum of the lowest L waves for a reference.

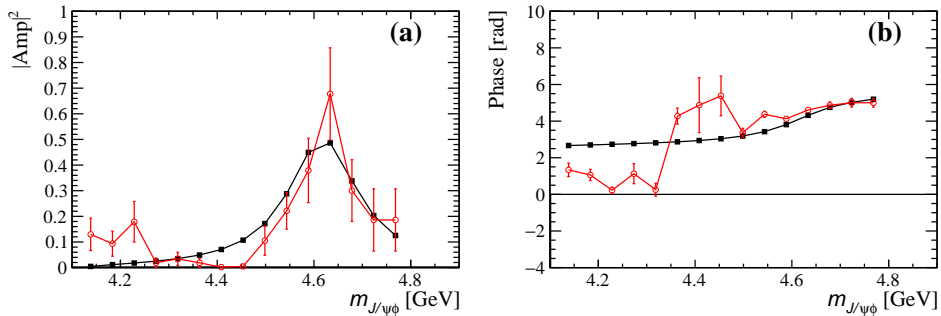


Figure C.9 (a) Amplitude squared and (b) phase motion for 1⁻ X wave obtained from the model-independent method (red open) and the nominal BW-sum fit (black solid). The BW-sum model has one pole at $M_0 - i\Gamma_0/2 = 4626 - i 174/2$ MeV.

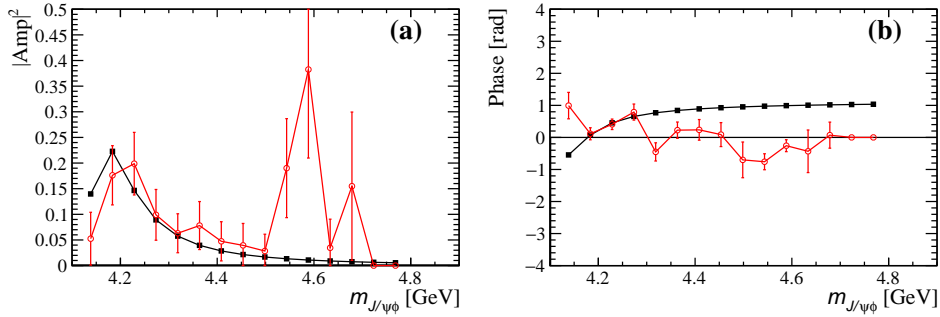


Figure C.10 (a) Amplitude squared and (b) phase motion for 2^- X wave obtained from the model-independent method (red open) and the nominal BW-sum fit (black solid). The BW-sum model has one pole at $M_0 - i\Gamma_0/2 = 4146 - i 135/2$ MeV.

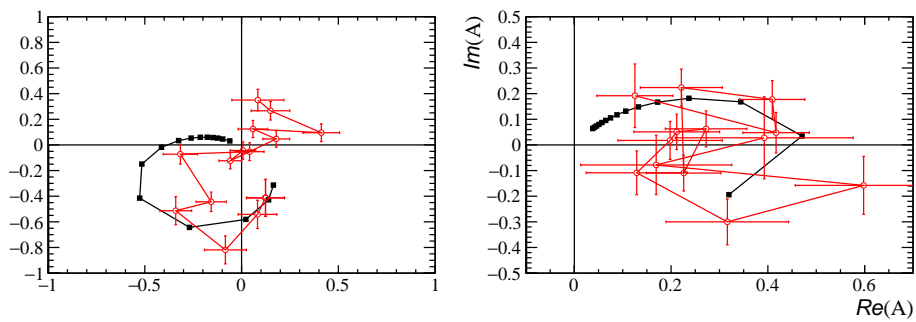


Figure C.11 (Left) Argand plot of 1^- X waves obtained from the model-independent method (red open) and the nominal BW-sum fit (black solid). The BW-sum model has poles at $M_0 - i\Gamma_0/2 = 4626 - i 174/2$ MeV. (Right) Argand plot of 2^- X waves obtained from the model-independent method (red open) and the nominal BW-sum fit (black solid). The BW-sum model has poles at $M_0 - i\Gamma_0/2 = 4146 - i 135/2$ MeV.

The MI results and the nominal BW fit are in good agreement in both magnitude and phase. The MI fit confirms the existence of the new $1^+ X(4685)$ state at about 4.7 GeV, in addition to the $X(4140)$ and $X(4274)$ identified in the previous amplitude analysis. An amplitude peak is obtained in this region with the phase motion is consistent with the BW fit (Fig. C.6). The corresponding Argand plots for both waves are shown in Fig. C.8.

Next we show the tests for small X contribution of one J^P , in Figs. C.9 and C.10 for 1^- and $2^- X$ contributions, respectively. The MI results also supports activities at of 1^- at 4.6 GeV and 2^- at 4.2 GeV found in the sum of BW approach, particular for 1^- state. The corresponding Argand plots for both waves are shown in Fig. C.11.

C.3 Check on the non- ϕ sideband

The B^\pm candidates with $1050 < m_{KK} < 1100$ MeV are selected, and referred to as the ϕ sideband sample. The yields of $B \rightarrow J/\psi KKK$ signal and of combinatorial background in the ± 15 MeV mass range around the peak are summarized in Table.C.1.

Table C.1 The signal and combinatorial background yields in the ± 15 MeV range around the B mass peak for $B \rightarrow J/\psi KKK$ candidates in the ϕ sideband (see the text).

type	yields
signal	3766 ± 73
combinatorial background	2609 ± 65

The $m_{J/\psi K}, m_{J/\psi \phi}$ and $m_{\phi K}$ distributions are shown in Fig.C.12. The $m_{J/\psi K}$ distribution for the $m_{J/\psi \phi} \in (4.25, 4.35)$ MeV slice is shown in Fig.C.13. There is no sign of any mass peaking, in particular of $Z(4000)$. The Dalitz plots in the ϕ sideband sample are shown in Fig.C.14. The $J/\psi \phi$ mass structures, which are prominent in the $B \rightarrow J/\psi \phi K$ sample, are not present when the m_{KK} is selected in the ϕ sideband.

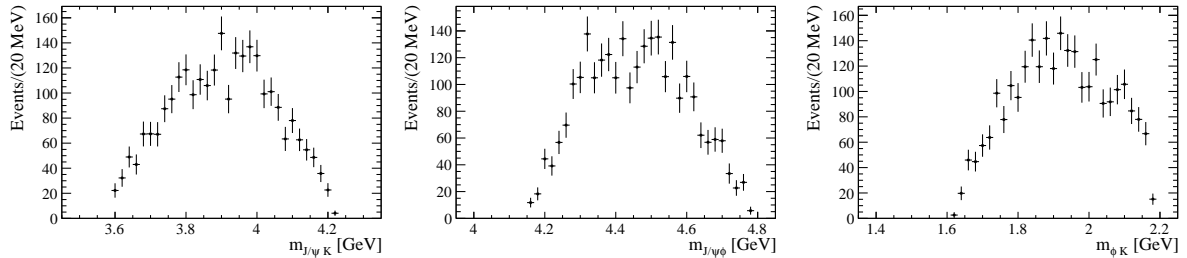


Figure C.12 The mass distribution of $m_{J/\psi K}, m_{J/\psi \phi}$ and $m_{\phi K}$ with phi sideband sample.

components. Otherwise, $Z(4420)$ gets very broad and FF is unphysically large at 150%.

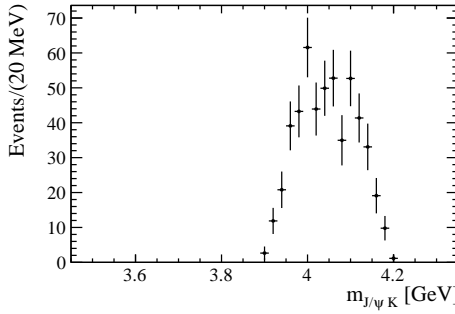
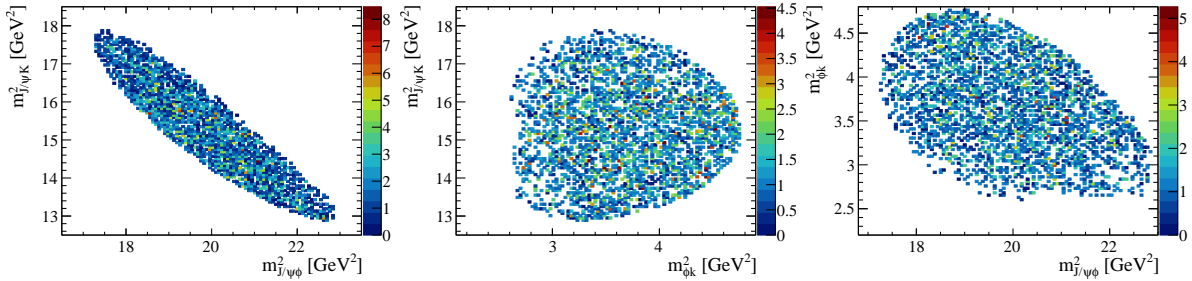
Figure C.13 The mass distribution of $m_{J/\psi K}$ with $m_{J/\psi \phi} \in (4.25, 4.35)$ MeV.

Figure C.14 The dalitz plot with phi sideband sample.

C.4 Kmatix model

Since many K^* resonances with the same J^P are overlapping (1^+ , 1^- and 2^- waves), the BW sum may not be their best representation. As an alternative, we use a simplified K-Matrix formula to describe them. The $\text{BW}(m_{K\phi}|M_0^{K_n^*}, \Gamma_0^{K_n^*})$ term in Eq. (3.19) is replaced by:

$$RKM_n(m|M_{0n}, \Gamma_{0n}) = \frac{\frac{1}{M_{0n}^2 - m^2}}{1 - i(\sum_j \frac{M_{0j}\Gamma_{0j}(m)}{M_{0j}^2 - m^2} + f_{sc} \cdot \rho(m))}, \quad (\text{C.3})$$

where the denominator sums over the same J^P K^* resonances, and f_{sc} accounts for a possible non-resonance contribution, phase space factor $\rho(m) = 2p/m$. For the non-resonance function, if including it, f_{sc} is a free parameter in the fit, and the numerator in Eq. (C.3) is 1 instead of $1/(M_{0n}^2 - m^2)$. Here we set $f_{sc} = 0$, as the non-resonances are modelled by tail of lower mass K^* 's.

We use the same K^* resonant masses and widths as those used in the nominal fit. The conclusions for the exotic states are unchanged, and the results are taken as the systematic uncertainty. The projections of this fit onto masses are shown in Fig. C.15.

The KMatrix model with two coupling channels are tested, which are used to describe the 2^1P_1 and 2^3P_1 K^* resonances, as the two states overlapping with each other. And the detailed formula can be found in 95, 124, 145. We replace the BW to this model to describe 2^1P_1

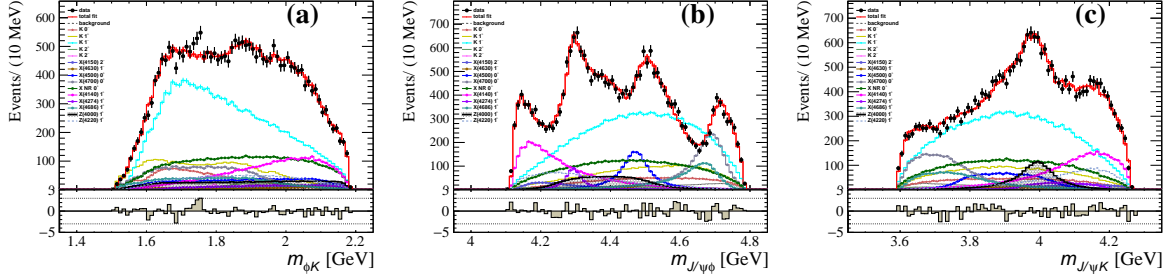


Figure C.15 Fit projections of (a) $m_{\phi K}$, (b) $m_{J/\psi \phi}$, (c) $m_{J/\psi K}$ from the nominal $K+5X+2X+2Z$ model with K-Matrix for describing the K^* resonances.

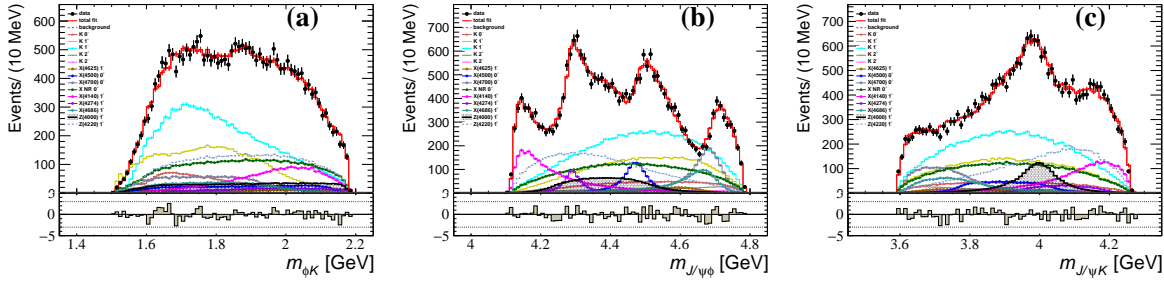


Figure C.16 Fit projections of (a) $m_{\phi K}$, (b) $m_{J/\psi \phi}$, (c) $m_{J/\psi K}$ from the nominal $2K(K\text{Matrix})+7K+5X+2X+2Z$ model.

and 2^3P_1 states, which overlapping with each other. The floating value in the fitting includes resonance pole mass, coupling and physical background parameters. We test this model in the nominal fitting, and the change of $\ln(L)$ is around 10, which is pretty small. The projections of this fit onto masses are shown in Fig. C.16.

C.5 Check of the background PDF on B mass sidebands

As described before, the 6D background PDF is constructed using the B mass sideband events, assuming that it can be factorized into a product of 2D functions of $m_{\phi K}$ and decay angles in the K^* decay chain. Such constructed 6D background density is then divided by similarly constructed 6D selection efficiency parametrization, worked out using the simulated events, and then added to the signal matrix element squared in a proportion constrained by the background fraction in the real data sample. To cross-check how well such background PDF describes the sideband distributions we show in Fig. C.17 its projections onto the masses and decay angles from all three chains superimposed on the sideband data. The projections are achieved by weighting the phase-space MC events, passed through the selection criteria, by the parameterized background PDF. Since the X and Z decay chain variables are not used in the parameterization of the background PDF, the cross-check is non-trivial. The cross-check

also depends on the cancellation of the parameterized efficiency in the background PDF by the unparameterized efficiency encoded in the MC events, which is a part of our cFit approach. The agreement is fairly reasonable.

Among the systematic variations we include an alternative way to parameterize the background PDF. Instead of assuming factorization, we use decomposition of the background density and of the efficiency into their multidimensional moments in the K^* decay chain variables. For examples, the efficiency parametrization becomes:

$$\begin{aligned} \epsilon(m_{\phi K}, \Omega) = & \sum_{a,b,c,d,e,f} \epsilon^{abcdef} \mathcal{P}_a(\cos \theta_{K^*}) Y_{bc}(\cos \theta_\psi, \phi_{(\psi K^*)}) \\ & \times \mathcal{P}_d \left(2 \frac{m_{\phi K} - m_{\phi K}^{\min}}{m_{\phi K}^{\max} - m_{\phi K}^{\min}} - 1 \right) \mathcal{P}_e(\cos \theta_\phi) \mathcal{P}_f \left(\frac{\phi_{K^+}}{\pi} \right), \end{aligned} \quad (\text{C.4})$$

where \mathcal{P} is Legendre polynomial, Y_{bc} are spherical harmonics, and $m_{\phi K}^{\min}$ and $m_{\phi K}^{\max}$ are the minimum and maximum allowed values for $m_{\phi K}$, respectively. The Y_{bc} functions are complex functions. To ensure that the efficiency function is real, we set $\epsilon^{abcdef} = -\epsilon^{ab(-c)def}$. The values of ϵ^{abcdef} are determined by summing over the fully simulated phase-space events or sideband events

$$\begin{aligned} \epsilon^{abcdef} = & \frac{1}{\sum_i w_i} \sum_i w_i \frac{2a+1}{2} \frac{2d+1}{2} \frac{2e+1}{2} \frac{2f+1}{2} \mathcal{P}_a(\cos \theta_{K^*,i}) Y_{bc}(\cos \theta_{\psi,i}, \phi_{(\psi K^*)}, i) \\ & \times \mathcal{P}_d \left(2 \frac{m_{\phi K,i} - m_{\phi K}^{\min}}{m_{\phi K}^{\max} - m_{\phi K}^{\min}} - 1 \right) \mathcal{P}_e(\cos \theta_{\phi,i}) \mathcal{P}_f \left(\frac{\phi_{K^+,i}}{\pi} \right) \frac{1}{g_i}, \end{aligned} \quad (\text{C.5})$$

where the weights w_i^{mc} account for GB weights for B^+ , p_T and multiplicity (for background $w_i^{\text{bkg}} = 1$, and g_i is the value of the phase-space probability density for event i). This approach allows the description of multidimensional correlations without assuming factorization. In practice, the sum is over a finite number of terms ($a \leq 10$, $b \leq 4$, $-2 \leq c \leq 2$, $d, e, f \leq 8$) and only coefficients with a statistical significance larger than three standard deviations (σ) from zero are retained. The fit results obtained with this approach are included in the tables of systematic errors in Sec. ???. We also show comparison of this paramaterization to the sideband data in Fig. C.12.

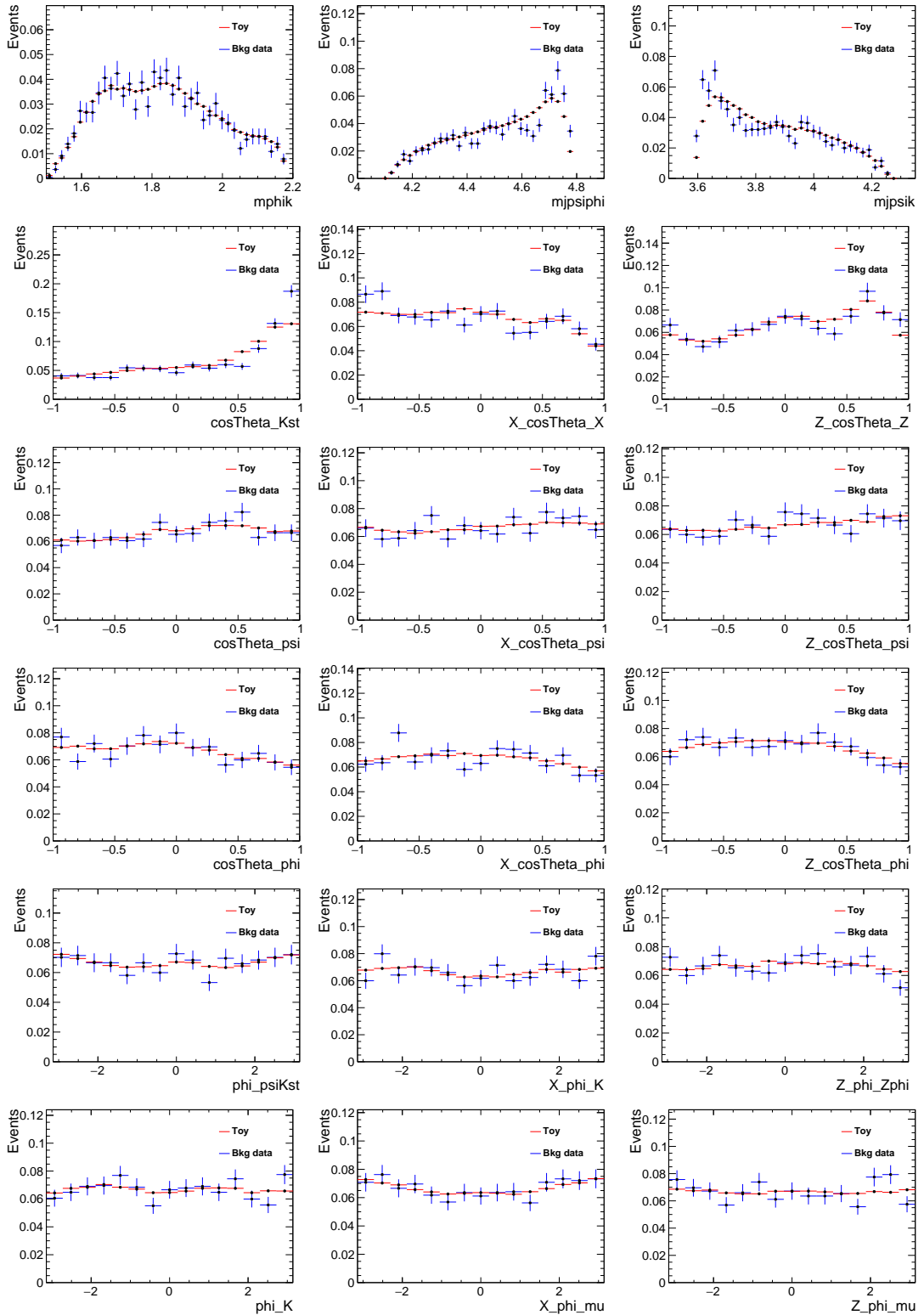


Figure C.17 Comparison between the parametrized background PDF used in the default cFit (red dots) with the B sideband data (blue dots) for all masses and angles used in nominal fit, for K^* chain (left) X chain (middle) and Z_{cs} chain (right).

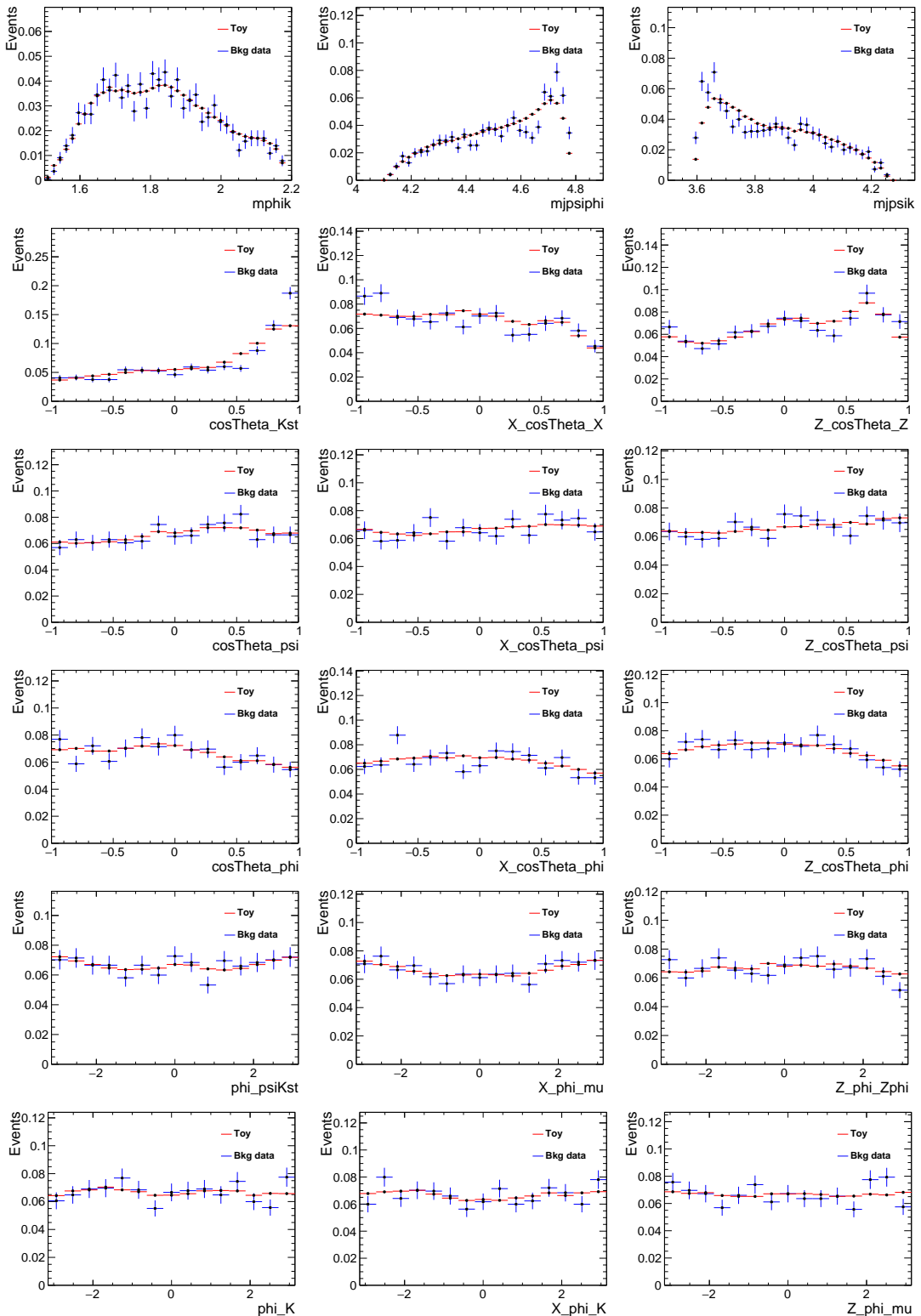


Figure C.18 Comparison between the alternative parametrized background PDF (red dots) with the B sideband data (blue dots) for all masses and angles used in nominal fit, for K^* chain (left) X chain (middle) and Z_{cs} chain (right).

References

- [1] R. Aaij *et al.* “Measurements of the branching fractions for $B_{(s)} \rightarrow D_{(s)}\pi\pi\pi$ and $\Lambda_b^0 \rightarrow \Lambda_c^+\pi\pi\pi$ ”. *Phys. Rev.* **2011**, *D84*: 092001.
- [2] R. Aaij *et al.* “Search for the $X(4140)$ state in $B^+ \rightarrow J/\psi\phi K^+$ decays”. *Phys. Rev.* **2012**, *D85*: 091103(R).
- [3] R. Aaij *et al.* “Determination of the $X(3872)$ meson quantum numbers”. *Phys. Rev. Lett.* **2013**, *110*: 222001.
- [4] R. Aaij *et al.* “Evidence for the decay $B^0 \rightarrow J/\psi\omega$ and measurement of the relative branching fractions of B_s^0 meson decays to $J/\psi\eta$ and $J/\psi\eta'$ ”. *Nucl. Phys.* **2013**, *B867*: 547.
- [5] R. Aaij *et al.* “Measurement of CP observables in $B^0 \rightarrow DK^{*0}$ with $D \rightarrow K^+K^-$ ”. *JHEP*, **2013**, *03*: 067.
- [6] R. Aaij *et al.* “Evidence for the decay $X(3872) \rightarrow \psi(2S)\gamma$ ”. *Nucl. Phys.* **2014**, *B886*: 665.
- [7] R. Aaij *et al.* “Observation of the $\Lambda_b^0 \rightarrow J/\psi p\pi^-$ decay”. *JHEP*, **2014**, *07*: 103.
- [8] R. Aaij *et al.* “Observation of the resonant character of the $Z(4430)^-$ state”. *Phys. Rev. Lett.* **2014**, *112*: 222002.
- [9] R. Aaij *et al.* “Study of beauty hadron decays into pairs of charm hadrons”. *Phys. Rev. Lett.* **2014**, *112*: 202001.
- [10] R. Aaij *et al.* “LHCb detector performance”. *Int. J. Mod. Phys.* **2015**, *A30*: 1530022.
- [11] R. Aaij *et al.* “Measurement of the branching fraction ratio $\mathcal{B}(B_c^+ \rightarrow \psi(2S)\pi^+)/\mathcal{B}(B_c^+ \rightarrow J/\psi\pi^+)$ ”. *Phys. Rev.* **2015**, *D92*: 057007.
- [12] R. Aaij *et al.* “Observation of $J/\psi p$ resonances consistent with pentaquark states in $\Lambda_b^0 \rightarrow J/\psi p K^-$ decays”. *Phys. Rev. Lett.* **2015**, *115*: 072001.
- [13] R. Aaij *et al.* “Evidence for exotic hadron contributions to $\Lambda_b^0 \rightarrow J/\psi p\pi^-$ decays”. *Phys. Rev. Lett.* **2016**, *117*: 082003.
- [14] R. Aaij *et al.* “Model-independent evidence for $J/\psi p$ contributions to $\Lambda_b^0 \rightarrow J/\psi p K^-$ decays”. *Phys. Rev. Lett.* **2016**, *117*: 082002.
- [15] R. Aaij *et al.* “Amplitude analysis of $B^+ \rightarrow J/\psi\phi K^+$ decays”. *Phys. Rev.* **2017**, *D95*: 012002.
- [16] R. Aaij *et al.* “Observation of exotic $J/\psi\phi$ structures from amplitude analysis of $B^+ \rightarrow J/\psi\phi K^+$ decays”. *Phys. Rev. Lett.* **2017**, *118*: 022003.
- [17] R. Aaij *et al.* “Observation of the decay $\Lambda_b^0 \rightarrow \Lambda_c^+ p\bar{p}\pi^-$ ”. *Phys. Lett.* **2018**, *B784*: 101.
- [18] R. Aaij *et al.* “Studies of the resonance structure in $D^0 \rightarrow K^\mp\pi^\pm\pi^+\pi^-$ decays”. *Eur. Phys. J.* **2018**, *C78*: 443.
- [19] R. Aaij *et al.* “Observation of a narrow pentaquark state, $P_c(4312)^+$, and of two-peak structure of the $P_c(4450)^+$ ”. *Phys. Rev. Lett.* **2019**, *122*: 222001.

- [20] R. Aaij *et al.* “Evidence of a $J/\psi\Lambda$ structure and observation of excited Ξ^- states in the $\Xi_b^- \rightarrow J/\psi\Lambda K^-$ decay”. **2020**, to appear in Science Bulletin.
- [21] R. Aaij *et al.* “First observation of the decay $B^0 \rightarrow D^0\bar{D}^0K^+\pi^-$ ”. *Phys. Rev.* **2020**, *D102*: 051102.
- [22] R. Aaij, S. Akar, J. Albrecht *et al.* “Design and performance of the LHCb trigger and full real-time reconstruction in Run 2 of the LHC”. *Journal of Instrumentation*, 2019-04, *14*(04): P04013–P04013. <http://dx.doi.org/10.1088/1748-0221/14/04/P04013>.
- [23] T. Aaltonen *et al.* “Evidence for a Narrow Near-Threshold Structure in the $J/\psi\phi$ Mass Spectrum in $B^+ \rightarrow J/\psi\phi K^+$ Decays”. *Phys. Rev. Lett.* **2009**, *102*: 242002.
- [24] T. Aaltonen *et al.* “Observation of the $Y(4140)$ structure in the $J/\psi\phi$ Mass Spectrum in $B^\pm \rightarrow J/\psi\phi K$ decays”. **2011**.
- [25] Victor Mukhamedovich Abazov *et al.* “Search for the $X(4140)$ state in $B^+ \rightarrow J/\psi\phi K^+$ decays with the D0 detector”. *Phys. Rev.* **2014**, *D89*: 012004.
- [26] Victor Mukhamedovich Abazov *et al.* “Inclusive Production of the $X(4140)$ State in $p\bar{p}$ Collisions at D0”. *Phys. Rev. Lett.* **2015**, *115*: 232001.
- [27] K. Abe, I. Adachi, H. Aihara *et al.* “Observation of a Charmoniumlike State Produced in Association with a J/ψ in e^+e^- Annihilation at $\sqrt{s} \approx 10.6$ GeV”. *Phys. Rev. Lett.* 2007-02, *98*: 082001. <https://link.aps.org/doi/10.1103/PhysRevLett.98.082001>.
- [28] M. Ablikim, M. N. Achasov, S. Ahmed *et al.* “Precise Measurement of the $e^+e^- \rightarrow \pi^+\pi^-J/\psi$ Cross Section at Center-of-Mass Energies from 3.77 to 4.60 GeV”. *Phys. Rev. Lett.* 2017-03, *118*: 092001. <https://link.aps.org/doi/10.1103/PhysRevLett.118.092001>.
- [29] M. Ablikim, M. N. Achasov, X. C. Ai *et al.* “Observation of a Charged Charmoniumlike Structure in $e^+e^- \rightarrow \pi^+\pi^-J/\psi$ at $\sqrt{s}=4.26$ GeV”. *Phys. Rev. Lett.* 2013-06, *110*: 252001. <https://link.aps.org/doi/10.1103/PhysRevLett.110.252001>.
- [30] M. Ablikim, M. N. Achasov, X. C. Ai *et al.* “Observation of $e^+e^- \rightarrow \pi^0\pi^0h_c$ and a Neutral Charmoniumlike Structure $Z_c(4020)^0$ ”. *Phys. Rev. Lett.* 2014-11, *113*: 212002. <https://link.aps.org/doi/10.1103/PhysRevLett.113.212002>.
- [31] M. Ablikim, M. N. Achasov, X. C. Ai *et al.* “Observation of $Z_c(3900)^0$ in $e^+e^- \rightarrow \pi^0\pi^0J/\psi$ ”. *Phys. Rev. Lett.* 2015-09, *115*: 112003. <https://link.aps.org/doi/10.1103/PhysRevLett.115.112003>.
- [32] M. Ablikim, M. N. Achasov, X. C. Ai *et al.* “Observation of a Neutral Charmoniumlike State $Z_c(4025)^0$ in $e^+e^- \rightarrow (D^*\bar{D}^*)^0\pi^0$ ”. *Phys. Rev. Lett.* 2015-10, *115*: 182002. <https://link.aps.org/doi/10.1103/PhysRevLett.115.182002>.
- [33] M. Ablikim, M. N. Achasov, O. Albayrak *et al.* “Observation of a Charged Charmoniumlike Structure $Z_c(4020)$ and Search for the $Z_c(3900)$ in $e^+e^- \rightarrow \pi^+\pi^-h_c$ ”. *Phys. Rev. Lett.* 2013-12, *111*: 242001. <https://link.aps.org/doi/10.1103/PhysRevLett.111.242001>.
- [34] M. Ablikim, M. N. Achasov, O. Albayrak *et al.* “Observation of a Charged $(D\bar{D}^*)^\pm$ Mass Peak in $e^+e^- \rightarrow \pi D\bar{D}^*$ at $\sqrt{s} = 4.26$ GeV”. *Phys. Rev. Lett.* 2014-01, *112*: 022001. <https://link.aps.org/doi/10.1103/PhysRevLett.112.022001>.

- [35] M. Ablikim, M. N. Achasov, O. Albayrak *et al.* “*Observation of a Charged Charmoniumlike Structure in $e^+e^- \rightarrow (D^*\bar{D}^*)^\pm\pi^\mp$ at $\sqrt{s} = 4.26$ GeV*”. *Phys. Rev. Lett.* 2014-04, **112**: 132001. <https://link.aps.org/doi/10.1103/PhysRevLett.112.132001>.
- [36] Medina Ablikim *et al.* “*Observation of a near-threshold structure in the K^+ recoil-mass spectra in $e^+e^- \rightarrow K^+(D_s^-D^{*0} + D_s^{*-}D^0)$* ”. 2020-11.
- [37] N. Akchurin *et al.* “*First beam tests of prototype silicon modules for the CMS High Granularity Endcap Calorimeter*”. *JINST*, **2018**, *13*(10): P10023.
- [38] Raphael M. Albuquerque, Mirian E. Bracco and Marina Nielsen. “*A QCD sum rule calculation for the $Y(4140)$ narrow structure*”. *Physics Letters B*, **2009**, *678*(2): 186–190. <http://www.sciencedirect.com/science/article/pii/S0370269309006935>.
- [39] A. A. Alves Jr. *et al.* “*The LHCb detector at the LHC*”. *JINST*, **2008**, *3*(LHCb-DP-2008-001): S08005.
- [40] A. A. Alves Jr. *et al.* “*The LHCb detector at the LHC*”. *JINST*, **2008**, *3*: S08005.
- [41] P. del Amo Sanchez, J. P. Lees, V. Poireau *et al.* “*Evidence for the decay $X(3872) \rightarrow J/\psi\omega$* ”. *Phys. Rev. D*, 2010-07, *82*: 011101. <https://link.aps.org/doi/10.1103/PhysRevD.82.011101>.
- [42] Irina Machikhiliyan and. “*The LHCb electromagnetic calorimeter*”. *Journal of Physics: Conference Series*, 2009-04, *160*: 012047. <https://doi.org/10.1088/1742-6596/160/1/012047>.
- [43] A. V. Anisovich, R. Beck, E. Klempert *et al.* “*Properties of baryon resonances from a multichannel partial wave analysis*”. *Eur. Phys. J.* **2012**, *A48*: 15.
- [44] R. A. Arndt, W. J. Briscoe, T. W. Morrison *et al.* “*Low-energy eta N interactions: Scattering lengths and resonance parameters*”. *Phys. Rev.* **2005**, *C72*: 045202.
- [45] R. A. Arndt, W. J. Briscoe, I. I. Strakovsky *et al.* “*Extended partial-wave analysis of piN scattering data*”. *Phys. Rev.* **2006**, *C74*: 045205.
- [46] B. Aubert, R. Barate, M. Bona *et al.* “*Evidence of a Broad Structure at an Invariant Mass of 4.32 GeV/c² in the Reaction $e^+e^- \rightarrow \pi^+\pi^-\psi(2S)$ Measured at BABAR*”. *Phys. Rev. Lett.* 2007-05, *98*: 212001. <https://link.aps.org/doi/10.1103/PhysRevLett.98.212001>.
- [47] B. Aubert, R. Barate, D. Boutigny *et al.* “ *$e^+e^- \rightarrow \pi^+\pi^-\pi^+\pi^-$, $K^+K^-\pi^+\pi^-$, and $K^+K^-K^+K^-$ cross sections at center-of-mass energies 0.5–4.5 GeV measured with initial-state radiation*”. *Phys. Rev. D*, 2005-03, *71*: 052001. <https://link.aps.org/doi/10.1103/PhysRevD.71.052001>.
- [48] V. E. Barnes, P. L. Connolly, D. J. Crennell *et al.* “*Observation of a Hyperon with Strangeness Minus Three*”. *Phys. Rev. Lett.* 1964-02, *12*: 204–206. <https://link.aps.org/doi/10.1103/PhysRevLett.12.204>.
- [49] D. Belayneh, F. Carminati, A. Farbin *et al.* “*Calorimetry with Deep Learning: Particle Simulation and Reconstruction for Collider Physics*”. *ArXiv*, **2019**, *abs/1912.06794*.
- [50] I. Belyaev *et al.* “*Handling of the generation of primary events in Gauss, the LHCb simulation framework*”. *J. Phys. Conf. Ser.* **2011**, *331*: 032047.
- [51] M. Benayoun, L. DelBuono, S. Eidelman *et al.* “*Radiative decays, nonet symmetry, and SU(3) breaking*”. *Phys. Rev. D*, 1999-05, *59*: 114027. <https://link.aps.org/doi/10.1103/PhysRevD.59.114027>.

- [52] S. Bethke. “*Experimental tests of asymptotic freedom*”. *Progress in Particle and Nuclear Physics*, **2007**, 58(2): 351–386. <http://www.sciencedirect.com/science/article/pii/S0146641006000615>.
- [53] C. Bignamini, B. Grinstein, F. Piccinini *et al.* “*Is the $X(3872)$ Production Cross Section at $\sqrt{s}=1.96$ TeV Compatible with a Hadron Molecule Interpretation?*” *Phys. Rev. Lett.* 2009-10, **103**: 162001. <https://link.aps.org/doi/10.1103/PhysRevLett.103.162001>.
- [54] J.M. Blatt and V.F. Weisskopf. *Theoretical Nuclear Physics*. Springer-Verlag, **1979**.
- [55] Geoffrey T. Bodwin, Eric Braaten, Tzu Chiang Yuan *et al.* “ *P -wave charmonium production in B -meson decays*”. *Phys. Rev. D*, 1992-11, **46**: R3703–R3707. <https://link.aps.org/doi/10.1103/PhysRevD.46.R3703>.
- [56] Tanja Branz, Thomas Gutsche and Valery E. Lyubovitskij. “*Hadronic molecule structure of the $Y(3940)$ and $Y(4140)$* ”. *Phys. Rev. D*, 2009-09, **80**: 054019. <https://link.aps.org/doi/10.1103/PhysRevD.80.054019>.
- [57] V. Breton, N. Brun and P. Perret. “*A clustering algorithm for the LHCb electromagnetic calorimeter using a cellular automaton*”. 2001-09.
- [58] Thomas Britton. *First amplitude analysis of $B^+ \rightarrow J/\psi \phi K^+$ decays* [phdthesis]. **2016**, <https://surface.syr.edu/etd/510>.
- [59] J. Brodzicka. “*Heavy flavour spectroscopy*”. In: *24th International Symposium on Lepton-Photon Interactions at High Energy (LP09), 2009*. **2009**. <https://indico.desy.de/event/1761/contributions/27653/>.
- [60] D V Bugg. “*How resonances can synchronize with thresholds*”. *Journal of Physics G: Nuclear and Particle Physics*, 2008-05, **35**(7): 075005. <https://doi.org/10.1088/0954-3899/35/7/075005>.
- [61] Nicola Cabibbo. “*Unitary Symmetry and Leptonic Decays*”. *Phys. Rev. Lett.* 1963-06, **10**: 531–533. <https://link.aps.org/doi/10.1103/PhysRevLett.10.531>.
- [62] Miriam Calvo Gomez, Eric Cogneras, Olivier Deschamps *et al.* *A tool for γ/π^0 separation at high energies* [techreport]. Geneva, 2015-08. <https://cds.cern.ch/record/2042173>.
- [63] A Cardini. “*The LHCb Muon Upgrade*”. *Journal of Instrumentation*, 2014-02, **9**(02): C02014–C02014. <https://doi.org/10.1088/1748-0221/9/02/c02014>.
- [64] Serguei Chatrchyan *et al.* “*Observation of a peaking structure in the $J/\psi \phi$ mass spectrum from $B^\pm \rightarrow J/\psi \phi K^\pm$ decays*”. *Phys. Lett.* **2014**, *B734*: 261–281.
- [65] Dian-Yong Chen, Xiang Liu and Takayuki Matsuki. “*Predictions of Charged Charmoniumlike Structures with Hidden-Charm and Open-Strange Channels*”. *Phys. Rev. Lett.* **2013**, *110*(23): 232001.
- [66] Hai-Yang Cheng and Chun-Khiang Chua. “*Bottom baryon decays to pseudoscalar meson and pentaquark*”. *Phys. Rev.* **2015**, *D92*: 096009.
- [67] Shen Cheng-Ping. “*XYZ particles at Belle*”. *Chin. Phys.* **2010**, *C34*: 615–620.
- [68] K. Chilikin *et al.* “*Experimental constraints on the spin and parity of the $Z(4430)^+$* ”. *Phys. Rev.* **2013**, *D88*: 074026.
- [69] K. Chilikin, I. Adachi, H. Aihara *et al.* “*Observation of an alternative $\chi_{c0}(2P)$ candidate in $e^+e^- \rightarrow J/\psi D\bar{D}$* ”. *Phys. Rev. D*, 2017-06, **95**: 112003. <https://link.aps.org/doi/10.1103/PhysRevD.95.112003>.

- [70] K. Chilikin, R. Mizuk, I. Adachi *et al.* “*Observation of a new charged charmoniumlike state in $\bar{B}^0 \rightarrow J/\psi K^- \pi^+$ decays*”. *Phys. Rev. D*, 2014-12, **90**: 112009. <https://link.aps.org/doi/10.1103/PhysRevD.90.112009>.
- [71] S.-K. Choi, S. L. Olsen, K. Abe *et al.* “*Observation of a Narrow Charmoniumlike State in Exclusive $B^\pm \rightarrow K^\pm \pi^+ \pi^- J/\psi$ Decays*”. *Phys. Rev. Lett.* 2003-12, **91**: 262001. <https://link.aps.org/doi/10.1103/PhysRevLett.91.262001>.
- [72] S.K. Choi *et al.* “*Observation of a resonance-like structure in the $\pi^\pm \psi'$ mass distribution in exclusive $B \rightarrow K \pi^\pm \psi'$ decays*”. *Phys. Rev. Lett.* **2008**, *100*: 142001.
- [73] M Clemencic *et al.* “*The LHCb simulation application, Gauss: Design, evolution and experience*”. *J. Phys. Conf. Ser.* **2011**, *331*: 032023.
- [74] T. E. Coan, Y. S. Gao, F. Liu *et al.* “*Charmonium Decays of $Y(4260)$, $\psi(4160)$, and $\psi(4040)$* ”. *Phys. Rev. Lett.* 2006-04, **96**: 162003. <https://link.aps.org/doi/10.1103/PhysRevLett.96.162003>.
- [75] *Computing Model of the Upgrade LHCb experiment*. Geneva, **2018**.
- [76] O Deschamps, F P Machefert, M H Schune *et al.* *Photon and neutral pion reconstruction* [techreport]. Geneva, 2003-09. <https://cds.cern.ch/record/691634>.
- [77] Jorgivan M. Dias, Xiang Liu and Marina Nielsen. “*Prediciton for the decay width of a charged state near the $D_s \bar{D}^*/D_s^* \bar{D}$ threshold*”. *Phys. Rev. D*, **2013**, *88*(9): 096014.
- [78] Gui-Jun Ding. “*Possible Molecular States of $D^*(s)$ anti- $D^*(s)$ System and $Y(4140)$* ”. *Eur. Phys. J. C*, **2009**, *64*: 297–308.
- [79] Yubing Dong, Amand Faessler, Thomas Gutsche *et al.* “ *$J/\psi \gamma$ and $\psi(2S)\gamma$ decay modes of the $X(3872)$* ”. *Journal of Physics G: Nuclear and Particle Physics*, 2010-11, **38**(1): 015001. <https://doi.org/10.1088/0954-3899/38/1/015001>.
- [80] S. Dubynskiy, A. Gorsky and M.B. Voloshin. “*Holographic hadro-quarkonium*”. *Physics Letters B*, **2009**, *671*(1): 82–86. <https://www.sciencedirect.com/science/article/pii/S0370269308014226>.
- [81] Estia Eichten and Brian Hill. “*An effective field theory for the calculation of matrix elements involving heavy quarks*”. *Physics Letters B*, **1990**, *234*(4): 511–516. <https://www.sciencedirect.com/science/article/pii/0370269390920490>.
- [82] Estia J. Eichten, Kenneth Lane and Chris Quigg. “*Charmonium levels near threshold and the narrow state $X(3872) \rightarrow \pi^+ \pi^- J/\psi$* ”. *Phys. Rev. D*, 2004-05, **69**: 094019. <https://link.aps.org/doi/10.1103/PhysRevD.69.094019>.
- [83] Richard Keith Ellis *et al.* “*Physics Briefing Book: Input for the European Strategy for Particle Physics Update 2020*”. 2019-10.
- [84] *Expression of Interest for a Phase-II LHCb Upgrade: Opportunities in flavour physics, and beyond, in the HL-LHC era*. Geneva, **2017**.
- [85] E. Fermi and C. N. Yang. “*Are Mesons Elementary Particles?*” *Phys. Rev.* 1949-12, **76**: 1739–1743. <https://link.aps.org/doi/10.1103/PhysRev.76.1739>.

- [86] J. Ferretti and E. Santopinto. “*Hidden-charm and bottom tetra- and pentaquarks with strangeness in the hadro-quarkonium and compact tetraquark models*”. *JHEP*, **2020**, 04: 119.
- [87] Massimiliano Fiorini. “*The upgrade of the LHCb RICH detectors*”. *Nuclear Instruments and Methods in Physics Research Section A: Accelerators, Spectrometers, Detectors and Associated Equipment*, **2020**, 952, 10th International Workshop on Ring Imaging Cherenkov Detectors (RICH 2018): 161688. <http://www.sciencedirect.com/science/article/pii/S0168900218318011>.
- [88] *Framework TDR for the LHCb Upgrade: Technical Design Report*. Geneva, **2012**.
- [89] William R. Frazer and Archibald W. Hendry. “*S-Matrix Poles Close to Threshold*”. *Phys. Rev.* 1964-06, **134**: B1307–B1314. <https://link.aps.org/doi/10.1103/PhysRev.134.B1307>.
- [90] Murray Gell-Mann. “*A schematic model of baryons and mesons*”. *Phys.Lett.* **1964**, 8: 214–215.
- [91] Feng-Kun Guo, Christoph Hanhart, Qian Wang *et al.* “*Could the near-threshold XYZ states be simply kinematic effects?*” *Phys. Rev. D*, 2015-03, **91**: 051504. <https://link.aps.org/doi/10.1103/PhysRevD.91.051504>.
- [92] Feng-Kun Guo, Xiao-Hai Liu and Shuntaro Sakai. “*Threshold cusps and triangle singularities in hadronic reactions*”. *Progress in Particle and Nuclear Physics*, **2020**, **112**: 103757. <https://www.sciencedirect.com/science/article/pii/S0146641020300041>.
- [93] Peng Guo, Tochtli Yépez-Martínez and Adam P. Szczepaniak. “*Charmonium meson and hybrid radiative transitions*”. *Phys. Rev. D*, 2014-06, **89**: 116005. <https://link.aps.org/doi/10.1103/PhysRevD.89.116005>.
- [94] Julie Haffner. “*The CERN accelerator complex. Complexe des accélérateurs du CERN*”. 2013-10, General Photo. <https://cds.cern.ch/record/1621894>.
- [95] V.K. Henner and T.S. Belozerova. “*Analysis of Overlapping Resonances Using the K-Matrix and Breit–Wigner Methods*”. *Phys. Part. Nucl.* **2020**, **51**(4): 673–677.
- [96] Emiko Hiyama, Atsushi Hosaka, Makoto Oka *et al.* “*Quark model estimate of hidden-charm pentaquark resonances*”. *Phys. Rev. C*, 2018-10, **98**: 045208. <https://link.aps.org/doi/10.1103/PhysRevC.98.045208>.
- [97] Andreas Hoecker *et al.* “*TMVA 4 — Toolkit for Multivariate Data Analysis with ROOT. Users Guide.*” **2009**.
- [98] Y. K. Hsiao and C. Q. Geng. “*Pentaquarks from intrinsic charms in Λ_b^0 decays*”. *Phys. Lett.* **2015**, **B751**: 572–575.
- [99] P. Z. Huang, Y. R. Liu, W. Z. Deng *et al.* “*Heavy pentaquarks*”. *Phys. Rev.* **2004**, **D70**: 034003.
- [100] Marek Karliner and Jonathan L. Rosner. “*Exotic resonances due to exchange*”. *Nuclear Physics A*, **2016**, 954, Recent Progress in Strangeness and Charm Hadronic and Nuclear Physics: 365–370. <http://www.sciencedirect.com/science/article/pii/S0375947416300434>.
- [101] Willis E. Lamb. “*Fine Structure of the Hydrogen Atom*”. *Science*, **1956**, **123**(3194): 439–442. <https://science.sciencemag.org/content/123/3194/439>.
- [102] Su Houng Lee, Marina Nielsen and Ulrich Wiedner. “ *$D(s)D^*$ molecule as an axial meson*”. *J. Korean Phys. Soc.* **2009**, **55**: 424.

- [103] J. P. Lees *et al.* “Study of $B^{\pm,0} \rightarrow J/\psi K^+ K^- K^{\pm,0}$ and search for $B^0 \rightarrow J/\psi \phi$ at BABAR”. *Phys. Rev.* **2015**, *D91*: 012003.
- [104] Itamar Levy. “Measurement of shower development and its Molière radius with a four-plane LumiCal test set-up”. Ed. by Paolo Checchia *et al.* *PoS*, **2017**, *EPS-HEP2017*: 502.
- [105] *LHCb PID Upgrade Technical Design Report*. Geneva, **2013**.
- [106] *LHCb Tracker Upgrade Technical Design Report*. Geneva, **2014**.
- [107] *LHCb Trigger and Online Technical Design Report*. Geneva, **2014**.
- [108] *LHCb Upgrade GPU High Level Trigger Technical Design Report*. Geneva, **2020**.
- [109] *LHCb Upgrade Software and Computing*. Geneva, **2018**.
- [110] B. Li, R. Été, G. Grenier *et al.* “APRIL : a novel Algorithm for Particle Reconstruction at ILC”. *JINST*, **2020**, *15*(05): C05016.
- [111] Bai-Qing Li and Kuang-Ta Chao. “Higher charmonia and X, Y, Z states with screened potential”. *Phys. Rev. D*, 2009-05, **79**: 094004. <https://link.aps.org/doi/10.1103/PhysRevD.79.094004>.
- [112] Tianbo Liu, Yajun Mao and Bo-Qiang Ma. “Present status on experimental search for pentaquarks”. *International Journal of Modern Physics A*, **2014**, *29*(13): 1430020. <https://doi.org/10.1142/S0217751X14300208>.
- [113] Xiang Liu and Shi-Lin Zhu. “ $Y(4143)$ is probably a molecular partner of $Y(3930)$ ”. *Phys. Rev. D*, 2009-07, **80**: 017502. <https://link.aps.org/doi/10.1103/PhysRevD.80.017502>.
- [114] Yan-Rui Liu, Hua-Xing Chen, Wei Chen *et al.* “Pentaquark and Tetraquark States”. *Progress in Particle and Nuclear Physics*, **2019**, *107*: 237–320. <http://www.sciencedirect.com/science/article/pii/S0146641019300304>.
- [115] Z. Q. Liu, C. P. Shen, C. Z. Yuan *et al.* “Study of $e^+e^- \rightarrow \pi^+\pi^- J/\psi$ and Observation of a Charged Charmoniumlike State at Belle”. *Phys. Rev. Lett.* 2013-06, **110**: 252002. <https://link.aps.org/doi/10.1103/PhysRevLett.110.252002>.
- [116] Qi-Fang Lü and Yu-Bing Dong. “ $X(4140)$, $X(4274)$, $X(4500)$, and $X(4700)$ in the relativized quark model”. *Phys. Rev. D*, 2016-10, **94**: 074007. <https://link.aps.org/doi/10.1103/PhysRevD.94.074007>.
- [117] Namit Mahajan. “ $Y(4140)$: Possible options”. *Physics Letters B*, **2009**, *679*(3): 228–230. <http://www.sciencedirect.com/science/article/pii/S0370269309008776>.
- [118] L. Maiani, F. Piccinini, A. D. Polosa *et al.* “ $Z(4430)$ and a new paradigm for spin interactions in tetraquarks”. *Phys. Rev. D*, 2014-06, **89**: 114010. <https://link.aps.org/doi/10.1103/PhysRevD.89.114010>.
- [119] Luciano Maiani, Antonio D. Polosa and Veronica Riquer. “A theory of X and Z multiquark resonances”. *Physics Letters B*, **2018**, *778*: 247–251. <https://www.sciencedirect.com/science/article/pii/S0370269318300479>.
- [120] A. Martínez Torres and E. Oset. “Novel Interpretation of the “ $\Theta^+(1540)$ Pentaquark” Peak”. *Phys. Rev. Lett.* 2010-08, **105**: 092001. <https://link.aps.org/doi/10.1103/PhysRevLett.105.092001>.

- [121] A. Massafferri. “*SciFi, the new Tracker of the LHCb experiment*”. *JINST*, **2020**, 15(08): C08006.
- [122] R. Molina and E. Oset. “*Y(3940), Z(3930), and the X(4160) as dynamically generated resonances from the vector-vector interaction*”. *Phys. Rev. D*, 2009-12, 80: 114013. <https://link.aps.org/doi/10.1103/PhysRevD.80.114013>.
- [123] T. Nakano, D. S. Ahn, J. K. Ahn *et al.* “*Evidence for a Narrow $S = +1$ Baryon Resonance in Photoproduction from the Neutron*”. *Phys. Rev. Lett.* 2003-07, 91: 012002. <https://link.aps.org/doi/10.1103/PhysRevLett.91.012002>.
- [124] M. Nauenberg and A. Pais. “*Woolly Cusps*”. *Phys. Rev.* 1962-04, 126: 360–364. <https://link.aps.org/doi/10.1103/PhysRev.126.360>.
- [125] Jason Nielsen. “*Fundamentals of LHC Experiments*”. *String Theory and Its Applications*, 2011-11. http://dx.doi.org/10.1142/9789814350525_0003.
- [126] K. A. Olive *et al.* “*Review of particle physics*”. *Chin. Phys.* **2014**, C38, and 2015 update: 090001.
- [127] Stephen Lars Olsen, Tomasz Skwarnicki and Daria Ziemska. “*Nonstandard heavy mesons and baryons: Experimental evidence*”. *Rev. Mod. Phys.* 2018-02, 90: 015003. <https://link.aps.org/doi/10.1103/RevModPhys.90.015003>.
- [128] Stephen Lars Olsen, Tomasz Skwarnicki and Daria Ziemska. “*Nonstandard heavy mesons and baryons: Experimental evidence*”. *Rev. Mod. Phys.* **2018**, 90(1): 015003.
- [129] Pablo G. Ortega, Jorge Segovia, David R. Entem *et al.* “*Canonical description of the new LHCb resonances*”. *Phys. Rev. D*, 2016-12, 94: 114018. <https://link.aps.org/doi/10.1103/PhysRevD.94.114018>.
- [130] P. Pakhlov, I. Adachi, H. Aihara *et al.* “*Production of New Charmoniumlike States in $e^+e^- \rightarrow J/\psi D^{(*)}\overline{D}^{(*)}$ at $\sqrt{s} \approx 10.6$ GeV*”. *Phys. Rev. Lett.* 2008-05, 100: 202001. <https://link.aps.org/doi/10.1103/PhysRevLett.100.202001>.
- [131] “*Physics case for an LHCb Upgrade II — Opportunities in flavour physics, and beyond, in the HL-LHC era*”. **2018**(CERN-LHCC-2018-027 LHCb-PUB-2018-009).
- [132] *Proceedings, 24th International Workshop on Vertex Detectors (Vertex 2015): Santa Fe, New Mexico, USA, June 1-5, 2015*. SISSA, **2015**.
- [133] Manqi Ruan. *Arbor, a new approach of the Particle Flow Algorithm*. **2014**.
- [134] Matthew Scott Rudolph. “*The LHCb Upstream Tracker Upgrade*”. *PoS*, **2020**, *Vertex2019*: 013.
- [135] Michele Selvaggi, J. Favereau, C. Delaere *et al.* “*DELPHES 3: A modular framework for fast-simulation of generic collider experiments*”. *Journal of Physics: Conference Series*, 2014-06, 523: 012033.
- [136] C. P. Shen, C. Z. Yuan, H. Aihara *et al.* “*Evidence for a New Resonance and Search for the Y(4140) in the $\gamma\gamma \rightarrow \phi J/\psi$ Process*”. *Phys. Rev. Lett.* 2010-03, 104: 112004. <https://link.aps.org/doi/10.1103/PhysRevLett.104.112004>.
- [137] Torbjörn Sjöstrand, Stephen Mrenna and Peter Skands. “*A brief introduction to PYTHIA 8.1*”. *Computer Physics Communications*, **2008**, 178(11): 852–867. <http://www.sciencedirect.com/science/article/pii/S0010465508000441>.

- [138] Torbjörn Sjöstrand, Stephen Mrenna and Peter" Skands. "PYTHIA 6.4 physics and manual". *JHEP*, **2006**, 05: 026.
- [139] Tomasz Skwarnicki. *A study of the radiative cascade transitions between the Upsilon-prime and Upsilonon resonances* [phdthesis]. **1986**, DESY-F31-86-02.
- [140] Fl Stancu. "Can $Y(4140)$ be a $c\bar{c}$ $s\bar{s}$ tetraquark?" *Journal of Physics G: Nuclear and Particle Physics*, 2010-06, 37(7): 075017. <https://doi.org/10.1088/0954-3899/37/7/075017>.
- [141] Peter Svihra. "The Design and Construction of LHCb VELO Upgrades Modules". 2020-08, Poster-2020-1041. <https://cds.cern.ch/record/2727215>.
- [142] E. S. Swanson. "Z_b and Z_c exotic states as coupled channel cusps". *Phys. Rev. D*, 2015-02, 91: 034009. <https://link.aps.org/doi/10.1103/PhysRevD.91.034009>.
- [143] Eric S. Swanson. "Diagnostic decays of the X(3872)". *Physics Letters B*, **2004**, 598(3): 197–202. <http://www.sciencedirect.com/science/article/pii/S0370269304011463>.
- [144] Eric S. Swanson. "Short range structure in the X(3872)". *Physics Letters B*, **2004**, 588(3): 189–195. <http://www.sciencedirect.com/science/article/pii/S0370269304004599>.
- [145] M. Tanabashi *et al.* "Review of particle physics". *to be published in Prog. Theor. Exp. Phys.* 2020, 083 C01 (2020), and 2020 update.
- [146] *The Phase-2 Upgrade of the CMS Endcap Calorimeter* [techreport]. Geneva, 2017-11. <https://cds.cern.ch/record/2293646>.
- [147] S. Uehara, T. Aushev, A. M. Bakich *et al.* "Observation of a Charmoniumlike Enhancement in the $\gamma\gamma \rightarrow \omega J/\psi$ Process". *Phys. Rev. Lett.* 2010-03, 104: 092001. <https://link.aps.org/doi/10.1103/PhysRevLett.104.092001>.
- [148] A. Vinokurova *et al.* "Search for B decays to final states with the η_c meson". *JHEP*, **2015**, 06, [Erratum: JHEP 02, 088 (2017)]: 132.
- [149] M.B. Voloshin. "Strange hadrocharmonium". *Phys. Lett. B*, **2019**, 798: 135022.
- [150] X. L. Wang, C. Z. Yuan, C. P. Shen *et al.* "Observation of Two Resonant Structures in $e^+e^- \rightarrow \pi^+\pi^-\psi(2S)$ via Initial-State Radiation at Belle". *Phys. Rev. Lett.* 2007-10, 99: 142002. <https://link.aps.org/doi/10.1103/PhysRevLett.99.142002>.
- [151] Zhi-Gang Wang, Zhi-Cheng Liu and Xiao-Hong Zhang. "Analysis of the $Y(4140)$ and related molecular states with QCD sum rules". *Eur. Phys. J. C*, **2009**, 64: 373–386.
- [152] C. Z. Yuan, C. P. Shen, P. Wang *et al.* "Measurement of the $e^+e^- \rightarrow \pi^+\pi^-J/\psi$ Cross Section Via Initial-State Radiation at Belle". *Phys. Rev. Lett.* 2007-11, 99: 182004. <https://link.aps.org/doi/10.1103/PhysRevLett.99.182004>.
- [153] Zhi-Yong Zhou, Zhiguang Xiao and Hai-Qing Zhou. "Could the X(3915) and the X(3930) Be the Same Tensor State?" *Phys. Rev. Lett.* 2015-07, 115: 022001. <https://link.aps.org/doi/10.1103/PhysRevLett.115.022001>.
- [154] SHI-LIN ZHU. "PENTAQUARKS". *International Journal of Modern Physics A*, **2004**, 19(21): 3439–3469. <https://doi.org/10.1142/S0217751X04019676>.

- [155] G Zweig. “*An SU_3 model for strong interaction symmetry and its breaking; Version 2*”. **1964**(CERN-TH-412). <http://cds.cern.ch/record/570209>.
- [156] P. A. Zyla *et al.* “*Review of particle physics*”. *to be published in Prog. Theor. Exp. Phys.* **2020**, 6: 083C01.

Acknowledgements

Vita

Declaration

原创性声明

本人郑重声明：所呈交的学位论文，是本人在导师的指导下，独立进行研究工作所取得的成果。除文中已经注明引用的内容外，本论文不含任何其他个人或集体已经发表或撰写过的作品或成果。对本文的研究做出重要贡献的个人和集体，均已在文中以明确方式标明。本声明的法律结果由本人承担。

论文作者签名： 日期： 年 月 日

学位论文使用授权说明

(必须装订在提交学校图书馆的印刷本)

本人完全了解北京大学关于收集、保存、使用学位论文的规定，即：

- 按照学校要求提交学位论文的印刷本和电子版本；
- 学校有权保存学位论文的印刷本和电子版，并提供目录检索与阅览服务，在校园网上提供服务；
- 学校可以采用影印、缩印、数字化或其它复制手段保存论文；
- 因某种特殊原因须要延迟发布学位论文电子版，授权学校在 一年 / 两年 / 三年以后在校园网上全文发布。

(保密论文在解密后遵守此规定)

论文作者签名： 导师签名： 日期： 年 月 日